Ion dynamics in solid-state batteries - A ^{7}Li NMR study

Ionendynamik in Festkörperakkumulatoren - Eine ^{7}Li NMR Studie
Zur Erlangung des Grades eines Doktors der Naturwissenschaften (Dr. rer. nat.)
genehmigte Dissertation von Michael Haaks, M.Sc. aus Schwetzingen
Tag der Einreichung: 15.01.2018, Tag der Prüfung: 14.02.2018
Darmstadt — D 17

1. Gutachten: Prof. Dr. Michael Vogel
2. Gutachten: Prof. Dr. Roland Böhmer

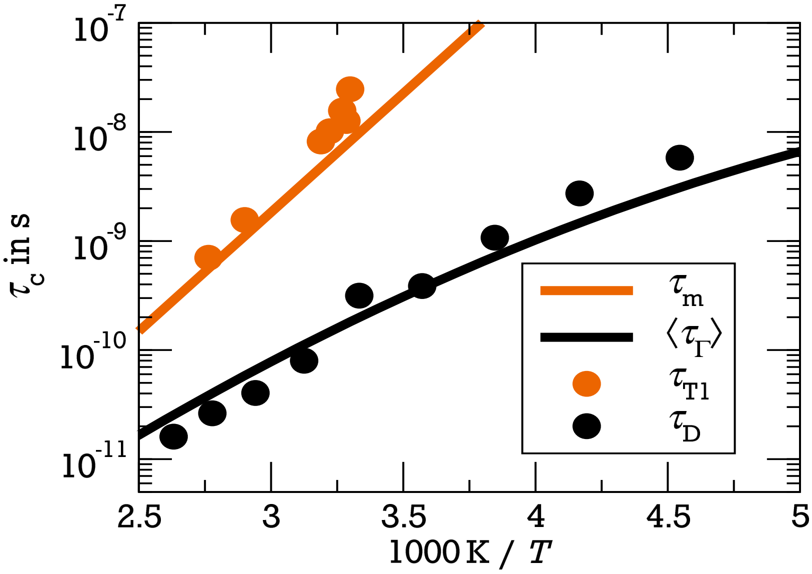

TECHNISCHE
UNIVERSITÄT
DARMSTADT

Fachbereich Physik
Condensed Matter Physics
AG Vogel

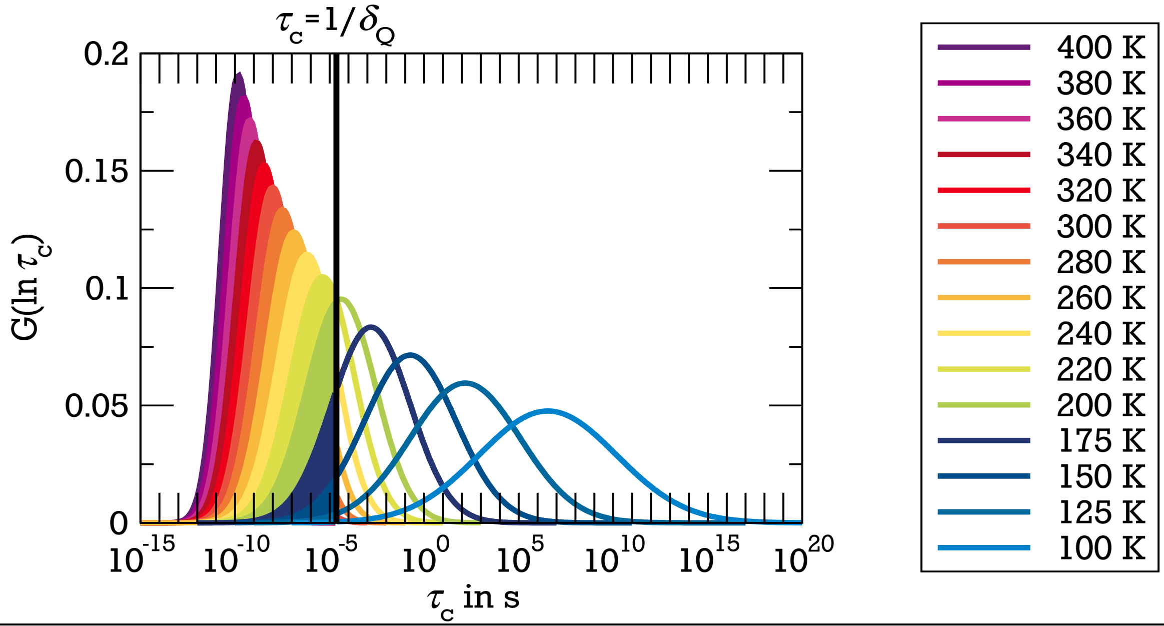

Ion dynamics in solid-state batteries - A ^{7}Li NMR study
Ionendynamik in Festkörperakkumulatoren - Eine ^{7}Li NMR Studie

Genehmigte Dissertation von Michael Haaks, M.Sc. aus Schwetzingen

1. Gutachten: Prof. Dr. Michael Vogel
2. Gutachten: Prof. Dr. Roland Böhmer

Tag der Einreichung: 15.01.2018
Tag der Prüfung: 14.02.2018

Version: 19.04.2018

Darmstadt — D 17

Bitte zitieren Sie dieses Dokument als:
URN: urn:nbn:de:tuda-tuprints-73638
URI: http://tuprints.ulb.tu-darmstadt.de/id/eprint/7363

Erklärung zur Dissertation

Hiermit versichere ich, die vorliegende Dissertation ohne Hilfe Dritter nur mit den angegebenen Quellen und Hilfsmitteln angefertigt zu haben. Alle Stellen, die aus Quellen entnommen wurden, sind als solche kenntlich gemacht. Diese Arbeit hat in gleicher oder ähnlicher Form noch keiner Prüfungsbehörde vorgelegen.

Darmstadt, den 15.01.2018

(Michael Haaks)

Zusammenfassung

Aufgrund des steigenden Energiebedarfs, in Verbindung mit einer mobilen Gesellschaft, wird es immer wichtiger Energie zu speichern, wenn sie verfügbar ist, und zur Verfügung zu stellen, wenn sie benötigt wird. Viele kleine Geräte, wie Smartphones und Digitalkameras, werden heutzutage mit wiederaufladbaren Lithium-Ionen-Batterien betrieben. Sollen diese Batterien zukünftig auch Elektrofahrzeuge mit Strom versorgen, müssen jedoch noch einige Verbesserungen erreicht werden. Ein Ziel ist die Entwicklung einer Festkörperbatterie, bei der das entflammbare flüssige Elektrolyt durch ein Festelektrolyt ersetzt wird. Vor einigen Jahren war die geringe Leitfähigkeit der größte Nachteil von Festkörper-Materialien. Inzwischen konnten Festkörper mit Leitfähigkeiten entwickelt werden, die denen von verwendeten Flüssig-Elektrolyten entsprechen. Allerdings sind die dynamischen Eigenschaften der Lithium-Ionen in diesen amorphen Materialien noch nicht verstanden.

Das Ziel dieser Arbeit ist die Analyse der Dynamik von Lithium-Ionen in solchen schnell leitenden Festkörpern über große Zeit- und Längenskalen hinweg. Zu diesen Zweck wurde eine Kombination aus etablierten und neu entwickelten ^{7}Li NMR Methoden verwendet.

Die in dieser Arbeit neu entwickelte Verbindung aus ^{7}Li Diffusionsmessungen und field-cycling Experimenten hat sich als ideale Komination herausgestellt. Während Erstere den langreichweitigen Ionentransport auf mesoskopischer Skala untersucht, liefern Letzere Informationen über lokale Sprünge der Lithium-Ionen auf mikroskopischer Skala im selben Temperaturbereich. Zusätzlich erlauben die field-cycling Messungen die Bestimmung der wahren Aktivierungsenergie dieser Dynamik durch Messung von temperaturabhängigen Suszeptibilitäts- bzw. Relaxationsraten-Maxima.

Die hier präsentierte Studie zeigt, dass viele Proben bei Annäherung an die Glasübergangstemperatur T_g Veränderungen aufweisen, welche teilweise gegensätzliche Auswirkungen haben. Während das $0.7Li_2S–0.3P_2S_5$ System dafür bekannt ist, dass sich die Dynamik der Lithium-Ionen durch diese Art der Keramisierung erhöht, führt das Erhitzen der $0.7Li_2S–0.3B_2S_3$ Proben zum Auftreten einer zweiten Lithium-Spezies mit einer verringerten Dynamik. Zudem liefert der Vergleich mit der Literaur den Hinweis, dass die Art der Probenpräparation einen nicht geringen Einfluss auf die Ergebnisse hat. Außerdem wird gezeigt, dass eine breite Gauß-Verteilung von Aktivierungsenergien in den untersuchten Materialien vorhanden ist. Diese Verteilung beeinflusst nicht nur die lokale Dynamik, sondern auch den langreichweitigen Ionentransport. Zudem ist sie auch verantwortlich für die unterschiedlichen Aktivierungsenergien, die üblicherweise von verschiedenen Methoden ermittelt werden. Dies ist der Tatsache geschuldet, dass jeweils andere Mittelwerte der resultierenden Verteilung von Korrelationszeiten untersucht werden. Daher ist es nicht nötig ein spezielles Modell anzuwenden, um die Unstimmigkeit der Aktivierungsenergien, ermittelt durch z. B. Leitfähigkeits- und NMR-Messungen, zu beschreiben. Diese Erkenntnis konnte durch erneute Auswertung von Literaturdaten bestätigt werden.

Abstract

Rising energy demand, in combination with a mobile society, makes it more and more important to store energy when available and release it upon demand. Rechargeable lithium ion batteries are widely used today for powering small devices, e.g., smartphones and cameras. However, further improvements are required, if lithium ion batteries are supposed to power electric vehicles. One requirement to achieve this task is the development of an all-solid state battery. Here, the flammable liquid electrolyte is replaced by a solid material. A few years ago, the main drawback of solid materials was the relatively low conductivity in comparison to that of their liquid counterparts. While the conductivity of solid electrolytes could be enhanced to the level of liquid electrolytes used in modern lithium ion batteries, the mechanism of lithium ion dynamics in those amorphous solids is still not understood.

The aim of this work is to analyse the dynamics of lithium ions in highly conducting solid materials on broad time and length scales. For this purpose, a combination of well established and newly developed ^{7}Li NMR methods are used.

The new conjunction of ^{7}Li diffusion measurements and ^{7}Li field-cycling relaxometry achieved in this work turns out to be an ideal combination. While the former probes the long-range transport on a mesoscopic length scale, the latter gives insight into local lithium ion jump dynamics on a microscopic length scale in the same temperature range. Additionally, field-cycling experiments allow the determination of the true activation energy by measuring temperature dependent susceptibility or relaxation-rate maxima.

The present research study reveals heat induced changes of the investigated samples when approaching their glass-transition temperatures T_g with partly opposite effects. While the $0.7Li_2S–0.3P_2S_5$ system is known for an enhanced dynamics due to this kind of ceramization, the heat treatment of the $0.7Li_2S–0.3B_2S_3$ samples leads to an occurance of a second lithium species with reduced dynamics. Additionally, comparison with literature reveals that the results strongly depend on details of the methods used to prepare the samples. Furthermore, it is shown in this work that a broad Gaussian distribution of activation energies exists in all studied solid lithium ion conductors, which is responsible not only for the local lithium ion jump dynamics, but also for the long-range diffusion. This indicates that the difference of activation energies usually obtained from distinct methods is a mere consequence of probing various averages of the resulting logarithmic distribution of correlation times. Hence, no specific model is necessary to describe the activation energy discrepancy often observed when comparing results of DC conductivity and NMR experiments. These findings are comfirmed by re-analyzing data given in the literature.

Contents

1 Introduction

After the nuclear disaster of Fukushima Daiichi on March 11, 2011 the public awareness of the risks and danger of nuclear power sources hasn't been higher since the Chernobyl incident on April 26, 1986, and the urge on usage of alternative power sources has risen. For example, the German renewable energies act (Erneuerbare-Energien-Gesetz) has been updated and the Japanese government adopted a similar act. In their International Energy Outlook 2016 the Energy Information Administration expected an increase in the world energy consumption especially in the field of renewable energy sources [EIA16, p.9]. There is also a rising demand in the field of electromobility and in today's information-rich, mobile society the requirement of portable equipment is enlarging steadily. Combining all these factors it is more and more important to be able to store energy when available and make it accessible upon demand. Lithium ion batteries (LIBs) are widely used for this purpose today and are promising candidates to fulfill this task in the near future.

Since decades there has been a great interest in developing a battery with Li metal as anode because of the fact Li is the lightest (molar mass $M_{\mathrm{Mol}} = 6.941\,\mathrm{g/mol}$, density $\varrho = 0.53\,\mathrm{g/cm^3}$) and most electropositive (-3.045 V standard electrode potential) metal resulting in a huge difference in capacity between Li metal (3860 Ah/kg) and negative electrodes (less than 1000 Ah/kg) [Tar01]. First promising developments lead to primary (non-rechargeable) batteries like the 1972 patented lithium-iodine PVP battery with the basic cell reaction $2\mathrm{Li} + \mathrm{I_2} \rightarrow 2\mathrm{LiI}$. This highly reliable and long-lived power source is providing currents in the microampere range which make it ideal for the use in implantable cardiac pacemakers [Hol07] and other small devices (wachtes, calculators, smoke alarms, etc.). In the following years other primary Li cells have found use in medical devices [Boc12] but the development of secondary (rechargeable) batteries has been hampered by dendrites growth on the lithium metal anode which can cause explosion hazards. As a consequence, research has been shifted towards LIBs where both electrodes and the electrolyte contain lithium ions. Many inorganic compounds react with alkali metals in a reversible way (intercalation compounds) which make them suitable for development of high-energy rechargeable LIBs in which lithium ions move from cathode and anode and vice versa to operate the battery. Because of this rocking motion this battery type is also called rocking-chair battery [Scr95]. In 1991, the first commercial secondary LIB has entered the market [Blo17] using $\mathrm{LiCoO_2}$ as cathode, as suggested by the group of Goodenough [Miz81]. This successfull design, as depicted in Fig. 1.1, has not changed much in the last two and a half decades. Today, most rechargeable LIBs consist of lithium cobalt dioxide as cathode, carbon (graphite) as anode and a liquid electrolyte, which usually consists of an optimized solvent mixture with dissolved binary salts and possibly further electrolyte additives.

The flammable nature of the alkyl carbonates in liquid electrolytes is the biggest disadvantage of the current battery design as it can cause the explosion of the cell. Several attempts have been made to exchange the liquid electrolyte, for example, in lithium solid polymer electrolyte batteries. As they require temperatures up to 80 °C, they are not useful for portable devices. Other

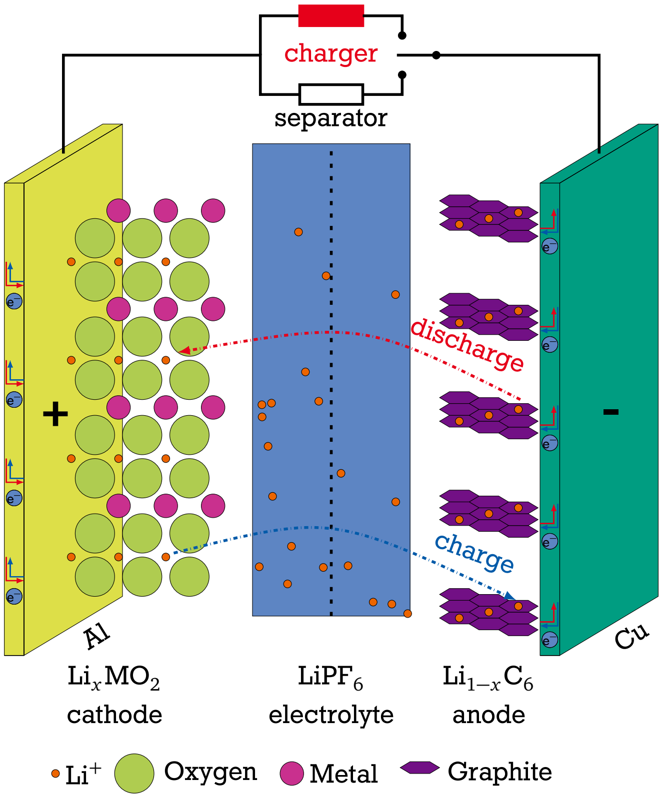

Figure 1.1.: Scheme of a lithium ion cell; a lithium ion battery is a collection of multiple cells.

designs are the all-solid state battery (ASSB) and the Li-air battery. The former is a battery where both electrodes and the electrolyte are made of solid materials and the latter consists of lithium metal as cathode and air as anode. To prevent the reaction of the metallic lithium with the oxygen of the air, the Li-air battery also requires a solid electrolyte. Therefore, the development of suitable solid electrolytes is one of the key challenges in modern battery research.

The objective of this work is to investigate the dynamics of lithium ions in materials which are promising candidates for the usage as solid electrolytes in ASSBs or Li-air batteries. Many studies on these so-called fast ion conductors (FICs) have been published, but there is still no consensus relating to the mechanism for ion conduction in disordered solids. For example, the jump relaxation model assumes a repulsive time-dependent interaction between mobile ions, resulting in a cage effect [Fun97]. By contrast, in the random potential energy model, it is assumed the ions feel a randomly varying potential energy resulting from the amorphous structure of the glass [Dyr88]. Not only the models trying to explain lithium ion dynamics in FICs are numerous, also the results obtained from different experiments and preparation techniques differ. For example, activation energies from DC conductivity measurements are usually lower than that of NMR experiments. This phenomenon has tried to be explained with the help of the coupling model [Nga93] and the use of percolation theory [Sva93, Dyr00]. While the former assumes a larger coupling parameter for NMR resulting in an enhanced activation energy, the latter reckons that conductivity depends only on lower barriers of a distribution of activation energies truncated at the percolation limit p_c. However, both interpretations are subject to controversal scientific debate.

Here, ^{7}Li NMR is utilized in order to determine the dynamics of lithium ions in FICs. ^{7}Li NMR is a capable tool to analyse dynamical properties in solid materials on broad time and length scales [Böh07a, Böh18]. By combining several techniques local lithium ion jump dynamics, yielding information on a microscopic length scale, can be observed over at least ten orders of magnitude in time from sub-nanoseconds to seconds. Furthermore, the long-range lithium ion transport on a mesoscopic length scale is accessible through the measurement of the lithium self-diffusion coefficient, using magnetic field gradient experiments. The applied ^{7}Li NMR techniques are a combination of well established methods, e.g., spin-lattice relaxation and line-shape analysis, with recently developed experiments, i.e., measurement of multi-time correlation functions. In the latter experiment, dynamical heterogeneities are probed. Additionally, the self-diffusion coefficient of lithium ions was obtained with the static field gradient technique for the first time ever.

While the conductivity of some solid materials is comparable to that of liquid electrolytes, there are still attempts to increase it even further. One possibility to enhance the dynamics is the mixed glass former effect (MGFE) [Kim06]. Here, two network formers are used to decrease the energy barriers lithium ions have to overcome during local jumps. Another strategy of increasing the conductivity is ceramization of glasses. While dynamics in crystals is usually slowed down, there are some systems where partial crystallization leads to enhanced movements in this so-called glass-ceramics [Miz05]. To analyze the lithium ion dynamics in those structural heterogeneous materials, $0.7Li_2S$–$0.27B_2S_3$–$0.03B_2O_3$ has been chosen as an example of an mixed glass former and the MGFE is studied by comparing the results of this sample with that of $0.7Li_2S$–$0.3B_2S_3$ containing only one glass former. The influence of ceramization on lithium ion dynamics is investigated in $0.7Li_2S$–$0.3P_2S_5$, which is the solid with the highest measured conductivity so far [Sei14].

This thesis is structured as follows. First, a brief overview of ionic transport in solids with a focus on diffusion phenomena is given in chapter 2. In chapter 3, ^{7}Li NMR is introduced, the method of choice in this work to analyse the dynamics of lithium ions in solids. The used experimental setups are described in chapter 4. Additionally, the investigated samples are presented. The results of the experiments performed on $Li_{10}SnP_2S_{12}$ are discussed in chapter 5. This sample was mainly chosen as a guinea-pig system to establish all the different NMR experiments described in chapter 3. Chapter 6 deals with silicon oxycarbide ceramics. In contrast to the other samples, SiOC is not a potential electrolyte, but an anode material. Here, the dynamics of a lithiated and a delithiated sample are compared. In chapter 7, the MGFE in the $0.7Li_2S$–$0.3B_2S_3$ system is analyzed and chapter 8 investigates the influence of ceramization on lithium ion dynamics using the example of $0.7Li_2S$–$0.3P_2S_5$. Finally, in chapter 9 the key findings of this work are summarized.

2 Ionic transport in solids

This chapter gives a brief overview of ionic transport in solids. Several diffusion mechanisms are introduced and the connection between diffusion and conductivity is discussed. A comprehensive description of diffusion mechanisms in solids can be found in several reviews [Gao16, Hei03, Hau87, Sou81] and textbooks [Hei05, Meh07, Mur06].

2.1 Diffusion

Diffusion is the transport of matter induced by stochastic movements and is described by Fick's laws. Fick's first law connects the flux $\mathbf{j}(\mathbf{r},t)$ of particles to a concentration gradient $\vec{\nabla} c$ [Fic55],

$$\mathbf{j}(\mathbf{r},t) = -\mathfrak{D}\vec{\nabla} c. \tag{2.1}$$

In case of isotropic diffusion, the second rank diffusivity tensor $\mathfrak{D}$ reduces to the diffusion coefficient D. With the continuity equation describing the conservation of mass, $\partial c/\partial t = -\vec{\nabla}\mathbf{j}(\mathbf{r},t)$, Fick's second law is derived from Fick's first law:

$$\frac{\partial c\left(\mathbf{r},t\right)}{\partial t} = \vec{\nabla}\left[D\vec{\nabla} c\left(\mathbf{r},t\right)\right] = D\Delta c\left(\mathbf{r},t\right), \tag{2.2}$$

where it is assumed that D is independent of the position and Δ denotes the Laplace operator. Einstein applied Fick's idea to the case without a macroscopic concentration gradient. Here, the movement is induced by thermal energy. In this case the diffusion is also called self diffusion. Einstein ascribed Fick's laws an interpretation based on probabilities [Ein05]

$$\frac{\partial p\left(\mathbf{r},t\right)}{\partial t} = D\Delta p\left(\mathbf{r},t\right). \tag{2.3}$$

Here, $p\left(\mathbf{r},t\right)$ is the probability to find a certain particle at position $\mathbf{r}$ at the time t. In order to obtain a solution to the diffusion equation (2.3), initial and boundary conditions have to be established. Here, an initial placement of the particle at the origin and a vanishing probability far away from this point is assumed. If the diffusing particle is allowed to spread into two identical samples of infinite thickness (sandwich geometry), the one-dimensional thin-film solution is given by

$$p\left(x,t\right) = \left(4\pi D t\right)^{-1/2} \exp\left(-\frac{x^2}{4Dt}\right), \tag{2.4}$$

where $2\sqrt{Dt}$ denotes the diffusion length. In three dimensions, the Gaussian solution reads

$$p\left(\mathbf{r},t\right) = \left(4\pi D t\right)^{-3/2} \exp\left(-\frac{\mathbf{r}^2}{4Dt}\right). \tag{2.5}$$

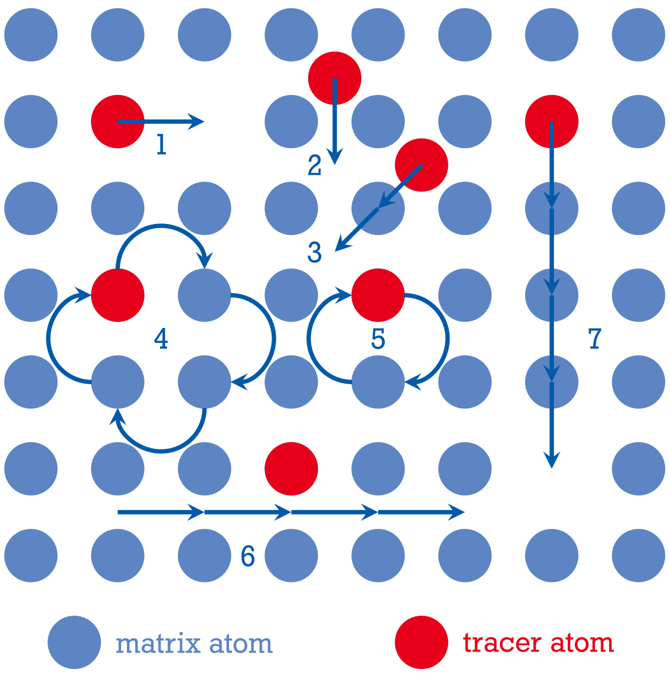

Figure 2.1.: Diffusion mechanisms in a crystal lattice: 1) vacancy mechanism, 2) interstitial mechanism, 3) intersticialcy mechanism, 4) ring diffusion mechanism, 5) direct exchange, 6) crowdian mechanism, 7) caterpillar mechanism. Modified from [Sha15]. Apart from mechanisms 2) and 3) tracer atoms are also matrix atoms.

The mean square displacement (MSD) of this probability is given by the Einstein relation

$$\langle \mathbf{r}^2 \rangle = 6Dt. \tag{2.6}$$

In solids, diffusion can be ascribed to jumps of individual atoms. In crystals, these jumps are either between regular lattice sites or between interstitial sites of the crystal lattice, q.v. Fig. 2.1. This elementary jump process can be described by only two physical quantities, the jump length l and the jump rate Γ_r. With these two quantities, the self-diffusion coefficient for uncorrelated, successive nearest-neighbor jumps (Markov process) in solids reads

$$D = \frac{1}{6}\Gamma_\mathrm{r} l^2. \tag{2.7}$$

For a thermally activated process, the jump rate is given by[1]

$$\Gamma_\mathrm{r}(T) = \Gamma_0 \exp\left(-\frac{E_\mathrm{a}}{k_\mathrm{B} T}\right). \tag{2.8}$$

Here, the activation energy E_a is the potential barrier between two sites, k_B is Boltzmann's constant, and T is the absolute temperature. The value of the pre-exponential factor Γ_0 de-

---

[1] Usually, the Gibbs free energy of migration is connected to the jump rate. Then, the pre-exponential factor can be ascribed to the attempt frequency ν_0 with which a particle tries to overcome the potential barrier between the two sites. ν_0 is typically in the range of the Debye frequency ($10^{12} - 10^{13}$ Hz).

pends on the diffusion mechanism and on the material under consideration. Consequently, the temperature dependence of the diffusion coefficient obeys the Arrhenius law:

$$D(T) = D_0 \exp\left(-\frac{E_\mathrm{a}}{k_\mathrm{B} T}\right). \tag{2.9}$$

The mean residence time of a particle at any given site, $\tau = 1/\Gamma_\mathrm{r}$, is approximately the correlation time τ_c measured in NMR experiments (see next chapter). Therefore, the temperature dependence of τ_c is also given by an Arrhenius equation

$$\tau_\mathrm{c} = \tau_0 \exp\left(\frac{E_\mathrm{a}}{k_\mathrm{B} T}\right). \tag{2.10}$$

In contrast to crystals, lithium ions in amorphous solids experience different environments. Furthermore, no regular sites exist in glassy materials. Hence, the barrier heights and the distance between various positions are randomly distributed, q.v. Fig. 2.2. Usually, the distribution of activation energies $g(E_\mathrm{a})$ is assumed to be of Gaussian shape. Moreover, ionic back-and-forth jumps between neighboring lithium sites can occur, leading to a delay of the macroscopic charge transport. Consequently, the jump length l and jump rate Γ_r in Eq. (2.7) have to be replaced by the mean jump length of an ion a and the mean hopping rate $\langle\Gamma_\mathrm{r}\rangle$, resulting in

$$D = \frac{1}{6}\langle\Gamma_\mathrm{r}\rangle a^2. \tag{2.11}$$

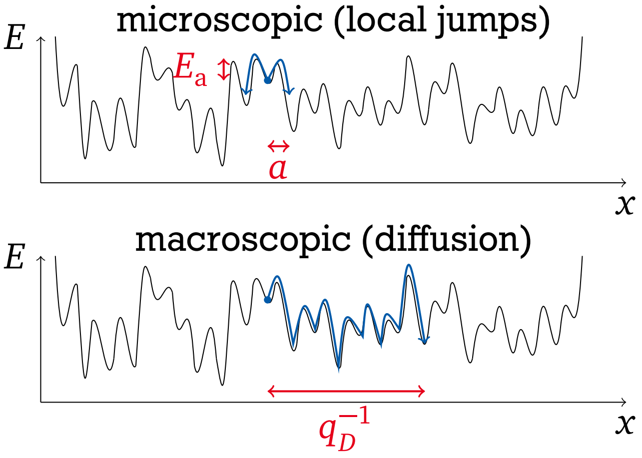

Figure 2.2.: Microscopic transport of lithium ions in amorphous solids is governed by local jumps over a barrier height E_a between two neighboring sites of distance a. Macroscopic transport is due to diffusion on a length scale determined by the inverse of the generalized scattering vector q_D.

Table 2.1.: Methods for studying diffusion in solids. Applied from [Hei03].

	Macroscopic	Microscopic
Nuclear	tracer diffusion field gradient NMR	NMR relaxation quasielastic neutron scattering
Non-nuclear	DC conductivity	AC conductivity

2.2 Conductivity

Two aspects are essential for the conductivity, the concentration of the mobile charge carriers n and their mobility μ. For μ, the potential barrier that has to be overcome by a jump plays an important role. The conductivity of a carrier is then given by the product of n, μ and its charge ze, where e is the charge of an electron and z is an integer. The total conductivity of a sample is the sum of all individual conductivities

$$\sigma = \sum_{\mathrm{i}} z_{\mathrm{i}} e \mu_{\mathrm{i}} n_{\mathrm{i}}. \tag{2.12}$$

In the materials discussed in this work, only lithium ions are mobile, while the anionic framework is considered to be rigid. In solid electrolytes the transference number[2] of lithium ions is almost 1, indicating a negligible electronic conductivity. Therefore, σ in solid electrolytes is given by the conductivity of the lithium ions. Conductivity and the diffusion coefficient of conduction D_σ are connected by the Nernst-Einstein equation

$$\sigma = \frac{ne^2}{k_{\mathrm{B}} T} D_\sigma. \tag{2.13}$$

Here, the charge of a lithium ion, $+e$, has been used. Usually, the diffusion coefficient D_σ calculated with the Nernst-Einstein equation (2.13) differs from the self-diffusion coefficient D of the ions obtained from other experiments, e.g., ^{7}Li SFG NMR. The deviation of this two coefficients is given by the Haven ratio [Imr07, Mur82]

$$H_{\mathrm{R}} \equiv \frac{D}{D_\sigma}. \tag{2.14}$$

The Haven ratio indicates correlation effects and collectivity and usually $H_{\mathrm{R}} < 1$ holds, but cases with $H_{\mathrm{R}} \gg 1$ have also been reported.

---

[2] The transference number is the fraction of the total electrical current carried by a certain ionic species.

3 ^{7}Li Nuclear magnetic resonance

Nuclear magnetic resonance (NMR) proved to be a powerful tool to ascertain structural features and dynamical properties of many liquid and solid materials. This non-invasive method is widely used in many different sciences, e.g., physics, chemistry, biology, and medicine. Using a combination of different techniques, NMR can probe the dynamics on a time scale of $10^{-10}\,\mathrm{s} \leq \tau \leq 10^{0}\,\mathrm{s}$, q.v. Fig. 3.1. Another strength is that NMR can probe both local dynamics and translational transport, i.e., dynamics on microscopic and mesoscopic length scales.

Time evolution of the spin system is determined by fluctuations of the spatial components of the dominant anisotropic interaction, $A_{l,m}$, which can be written in terms of a correlation function using the ensemble average $\langle \cdot \rangle$

$$F_{l,m}(|\tau|) = \langle A_{l,m}(t) A_{l,m}(t+\tau) \rangle. \tag{3.1}$$

This correlation function $F_{l,m}(|\tau|)$ decays with a characteristic time, which is called correlation time

$$\tau_{\mathrm{c}} = \int_0^\infty \frac{\langle A_{l,m}(t) A_{l,m}(t+\tau) \rangle}{\langle |A_{l,m}(t)|^2 \rangle} \,\mathrm{d}t. \tag{3.2}$$

In the simplest case, a single mono-exponential decay

$$F_{l,m}(|\tau|) \propto \exp\left(-\frac{t}{\tau_{\mathrm{c}}}\right) \tag{3.3}$$

describes the time dependence of $F_{l,m}(|\tau|)$ quite well. While the stimulated echo (STE) method allows a direct analysis of $F_{l,m}(|\tau|)$ in the time domain, relaxation methods work in the frequency domain. Therefore, the Fourier transform of $F_{l,m}(|\tau|)$, the spectral density

$$J_{l,m}(\omega) = \mathrm{Re} \int_0^\infty \langle A_{l,m}(t) A_{l,m}(t+\tau) \rangle \exp(i\omega\tau) \,\mathrm{d}t, \tag{3.4}$$

proved to be helpful in the analysis of relaxation experiments. The spectral density resulting from the mono-exponential correlation function given in Eq. (3.3) is named after Bloembergen, Purcell, and Pound (BPP) [Blo48]

$$J_{\mathrm{BPP}}(\omega_{\mathrm{L}}, \tau_{\mathrm{c}}) = \langle |A_{l,m}|^2 \rangle \frac{\tau_{\mathrm{c}}}{1 + \omega_{\mathrm{L}}^2 \tau_{\mathrm{c}}^2}. \tag{3.5}$$

Here, the Larmor frequency ω_{L}, q.v. Eq. (3.8), has been used in Eq. (3.5) to emphasize the fact, that in NMR relaxation experiments the spectral density is screened at this frequency. A mono-exponential decay of the correlation function is rarely seen in experiments. Often, a stretched exponential decay, named after Kohlrausch, Williams, and Watts (KWW) [Koh54, Wil70] is found

$$F_{l,m}(|\tau|) \propto \exp\left[-\left(\frac{t}{\tau_{\mathrm{c}}}\right)^{\beta}\right]. \tag{3.6}$$

Here, the stretching parameter $0 \leq \beta \leq 1$ describes the deviation from the mono-exponential behavior. There can be quite different origins of a stretched-exponential correlation function. In the homogeneous case, this stretching is an intrinsic characteristic, which is present in each spin subensemble. In the heterogeneous scenario, each subensemble experiences a mono-exponential correlation function but on a different time scale. Then, the superposition of the different correlation times τ_c leads to the stretching in $F_{l,m}(|\tau|)$. In this case, the measured stretching factor β can be used to derive the width of the distribution of correlation times $G(\tau_c)$. Following discussion is based on several common text books [Kim97b, Lev01, SR94] as well as a PhD thesis [Sto16] and two review articles [Böh07a, Böh18] as main references. They will not be referenced explicitly. In Sec. 3.1 the basic principles of NMR are briefly introduced, section 3.2 deals with the relevant internal interactions, and the experiments used during this work are described in Sec. 3.3. Finally, the effects of a distribution of correlation times on the measurements are discussed in Sec. 3.4.

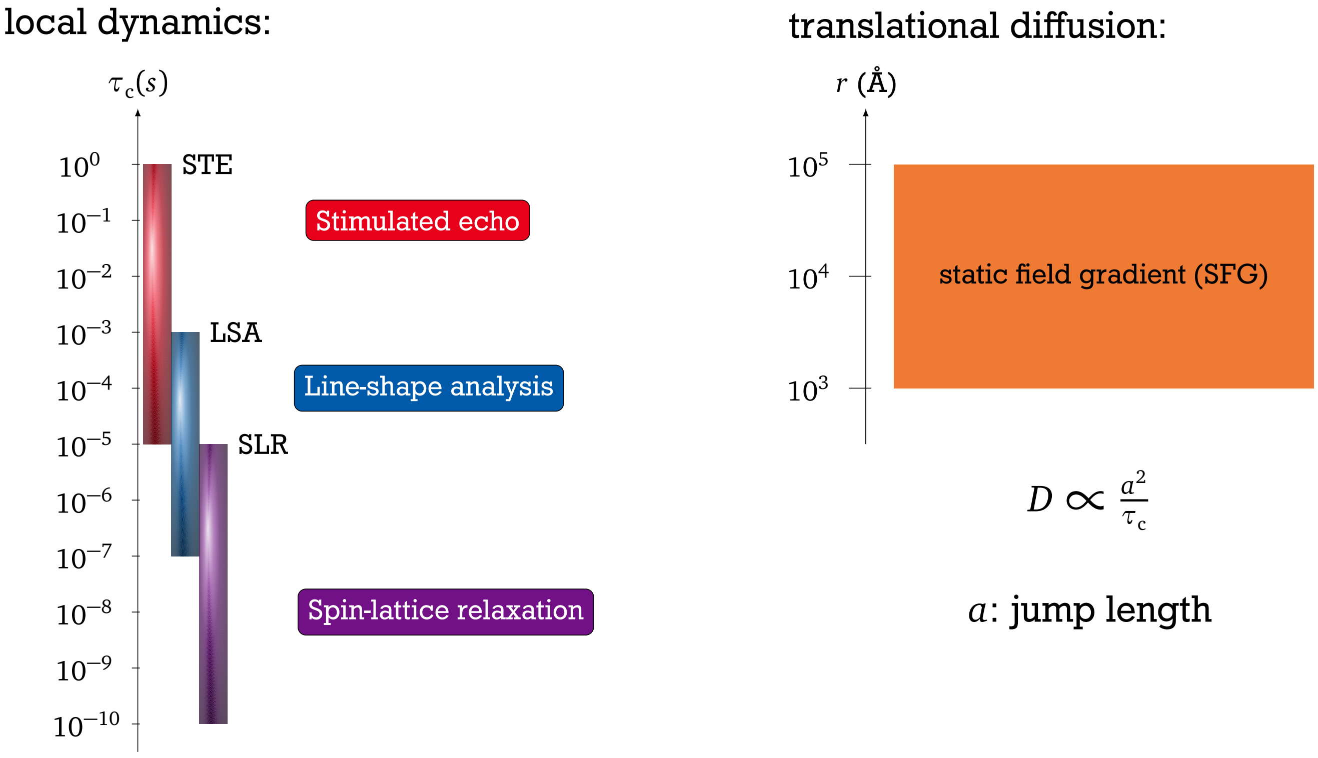

Figure 3.1.: Overview over the dynamical windows of different NMR techniques.

3.1 Basic principles

NMR is sensitive to the interaction of nuclei possessing a non-vanishing nuclear spin I with electro-magnetic fields. This can either be a strong external magnetic field, which is suitable to influence the total magnetization of the sample or weaker, internal electrical and magnetic fields, which depend on local characteristics of the system under investigation. When a spin I is under the influence of a strong external magnetic field $\mathbf{B}_0 = B\vec{e}_z$, the Zeeman interaction $\mathcal{H}_\mathrm{Z}$ deregulates the degeneracy of the $2I+1$ magnetic energy levels

$$E_m = -m_I \hbar\gamma B = -m_I \hbar\omega_\mathrm{L}. \tag{3.7}$$

The magnetic quantum number $m_I = I, I-1, \ldots, -I$ describes the projection of the spin angular momentum to the z-axis: $\hat{I}_\mathrm{z}\mathbf{B}_0 = m_I\hbar\mathbf{B}_0$; γ is called gyromagnetic ratio, and ω_L is the Larmor frequency which corresponds to the resonance condition of the spin system. In thermal equilibrium, the occupation numbers of the energy levels E_m are given by the Boltzmann distribution resulting in a majority of magnetic moments orientating along the magnetic field $\mathbf{B}_0$ and generating a macroscopic magnetization $\mathbf{M} \propto \mathbf{B}_0$ on the sample. The Larmor frequency

$$\omega_\mathrm{L} = -\gamma\,|\mathbf{B}_0| \tag{3.8}$$

describes the precession of the spins around the magnetic field axis. Transitions between different energy levels E_m can be induced with the help of radio frequency (RF) pulses of the frequency ω_L and a magnetic field $\mathbf{B}_1$ perpendicular to $\mathbf{B}_0$. These energy levels are further shifted by internal interactions. Therefore, it is possible to deduce characteristics of the sample from the response of RF pulses. The most important internal interactions in ^{7}Li solid-state NMR are the quadrupolar interaction $\mathcal{H}_\mathrm{Q}$ and the dipolar interaction $\mathcal{H}_\mathrm{D}$. The time evolution of the system

$$\mathcal{H} = \mathcal{H}_\mathrm{Z} + \mathcal{H}_\mathrm{RF} + \mathcal{H}_\mathrm{Q} + \mathcal{H}_\mathrm{D} \tag{3.9}$$

is usually described using the density operator

$$\rho\,(t) = \sum_i p_i\,|\Psi_i\,(t)\rangle\langle\Psi_i\,(t)| \tag{3.10}$$

with the one-particle states $\Psi_i\,(t)$ and $0 \le p_i \le 1$. For NMR, a decomposition of $\rho\,(t)$ into the $(2I+1)^2$ orthogonal, irreducible spherical tensor operators $T_{l,m}$ of rank $l \in [0, \ldots, 2I]$ and order of multiple-quantum transition $m \in [-l, \ldots, l]$ turned out to be useful. All Hamiltonians of spin interactions μ, which are based on second rank tensors, can be expressed in the general form

$$\mathcal{H}_\mu = C_\mu \sum_{l=0}^{2I} \sum_{m=-l}^{l} (-1)^m A_{l,-m} T_{l,m}, \tag{3.11}$$

where C_μ is a constant specific for the interaction and the $A_{l,-m}$ are spin-independent functions of the spatial orientation and distances. For a more detailed description of the density operator formalism as well as properties and tables of the spherical tensor operators, the reader is refered to the literature, e.g., [Bow86, Hub69].

3.2 Internal interactions

Usually, the interaction of nuclei with the external magnetic fields $\mathbf{B}_0$ and $\mathbf{B}_1$ are dominant, but only the internal interactions contain information about the structure and dynamics of the investigated samples. For reasons mentioned above, only the electrical quadrupolar and the magnetic dipolar interaction are discussed in this chapter and their typical parameters for ^{7}Li, as defined below, are given in Tab. 3.1.

Table 3.1.: Typical values of the quadrupolar coupling constant C_Q and the interaction frequencies ω_Q and ω_D given in kHz.

C_Q	$\frac{\omega_\mathrm{Q}}{2\pi}$	$\frac{\omega_\mathrm{D}}{2\pi}$
100	50	5

3.2.1 Quadrupolar interaction

Nuclei with a spin $I \geq 1$ have a non-vanishing nuclear electric quadrupole moment Q, which interacts with the electric field gradient (EFG). This EFG is generated by the other charges in the system and its magnitude is usually denoted as eq. Since the gradients are exclusively generated by the electrons and nuclei of molecules and crystals of the investigated sample, the size of the quadrupolar interaction experienced by a particular nucleus is a constant that is characteristic of the molecular or crystalline environment. Its value is called the quadrupolar coupling constant (QCC)

$$C_\mathrm{Q} = \frac{e^2 qQ}{h}, \tag{3.12}$$

where e and h are the charge of the electron and Planck's constant, respectively. By determining C_Q and using the nuclear quadrupole moment of ^{7}Li, -40 mb [Har07], the EFG q can be calculated. The nuclear spin Hamiltonian for the quadrupolar coupling reads

$$\mathcal{H}_\mathrm{Q} = \frac{eQ}{6I\,(2I-1)}\vec{I}\mathbf{V}\vec{I}, \tag{3.13}$$

with the symmetrical, traceless EFG tensor $\mathbf{V}$. In the principal axis system (PAS), $\mathbf{V}$ is diagonal

$$\mathbf{V} = \begin{pmatrix} V_{XX} & 0 & 0 \\ 0 & V_{YY} & 0 \\ 0 & 0 & V_{ZZ} \end{pmatrix} = eq \begin{pmatrix} -\frac{1}{2}\left(1-\eta_\mathrm{Q}\right) & 0 & 0 \\ 0 & -\frac{1}{2}\left(1+\eta_\mathrm{Q}\right) & 0 \\ 0 & 0 & 1 \end{pmatrix} \tag{3.14}$$

with the convention $|V_{XX}| \leq |V_{YY}| \leq |V_{ZZ}|$. As $\mathbf{V}$ is traceless, the Laplace equation $V_{XX} + V_{YY} + V_{ZZ} = 0$ holds. As seen from Eq. (3.14), only two independent parameters are required to describe the quadrupolar interaction:

$$eq = V_{ZZ}, \tag{3.15}$$

$$\eta_\mathrm{Q} = \frac{V_{YY}-V_{XX}}{V_{ZZ}}. \tag{3.16}$$

For the asymmetry parameter, $0 \leq \eta_\mathrm{Q} \leq 1$ holds. The QCC C_Q quantifies the strength of the quadrupolar interaction, but the shift of the spectral lines also depends on the spin I. Therefore, the anisotropy parameter

$$\delta_\mathrm{Q} = \frac{3e^2qQ}{2I\,(2I-1)\,\hbar} \overset{I=3/2}{=} \frac{1}{2}\frac{e^2qQ}{\hbar} \overset{\text{Eq. (3.12)}}{=} \pi C_\mathrm{Q} \tag{3.17}$$

has been introduced. The quadrupolar interaction leads to a deviation from the energy levels defined in Eq. (3.7). This quadrupolar splitting is connected with the orientation of the EFG via the quadrupolar frequency

$$\omega_\mathrm{Q} = \frac{\delta_\mathrm{Q}}{2}\left(3\cos^2\theta - 1 + \eta_\mathrm{Q}\sin^2\theta\cos 2\phi\right), \tag{3.18}$$

where the polar angle θ and the azimuthal angle ϕ define the orientation of the external magnetic field $\mathbf{B}_0$ in the PAS of the EFG. When dealing with the quadrupolar interaction as a perturbation of the Zeeman interaction, the shift of the transitions in first order is given by

$$\omega^{(1)}_{m\longleftrightarrow(m-1)} = (2m-1)\,\omega_\mathrm{Q}. \tag{3.19}$$

As seen from Eq. (3.19), the central line ($m = 1/2 \longleftrightarrow m = -1/2$) is not affected from first order perturbation. In second order perturbation a shift

$$\omega^{(2)} = \frac{4}{9}\left[\frac{2}{3}\left(1+\eta_\mathrm{Q}\right) + \frac{1}{24}\left(3+\eta_\mathrm{Q}\right)^2\right]\frac{\omega_\mathrm{Q}^2}{\omega_\mathrm{L}} \tag{3.20}$$

results. More details about quadrupolar coupling and its perturbation of the Zeeman interaction in first and second orders is given in some articles of the *Encyclopedia of Magnetic Resonance* [Man07, Bla07, Ash07, Veg07].

3.2.2 Dipolar interaction

The dipolar coupling represents the direct magnetic interactions of nuclear spins with each other. The interaction between these spins is mutual; each spin experiences the field generated by the other spins. Contrary to the J-coupling, the electron clouds are not involved in the direct dipolar coupling. The Hamiltonian of the dipole coupling of two spins i and j reads

$$\mathscr{H}_\mathrm{D} = \frac{\mu_0\gamma_\mathrm{i}\gamma_\mathrm{j}\hbar^2}{4\pi r_\mathrm{ij}^3}\vec{I}\mathbf{D}\vec{J}. \tag{3.21}$$

Here, $\mathbf{D}$ is a tensor which represents the orientational dependence of this interaction. Like $\mathbf{V}$, $\mathbf{D}$ is diagonal in the PAS, traceless and its isotropic mean is zero. The distance of spins i and j, $r_\mathrm{ij} = \left|\vec{r}_\mathrm{ij}\right|$, describes the dipolar axis; $\vec{I}$ and $\vec{J}$ are the spin angular momentum of spin i and j,

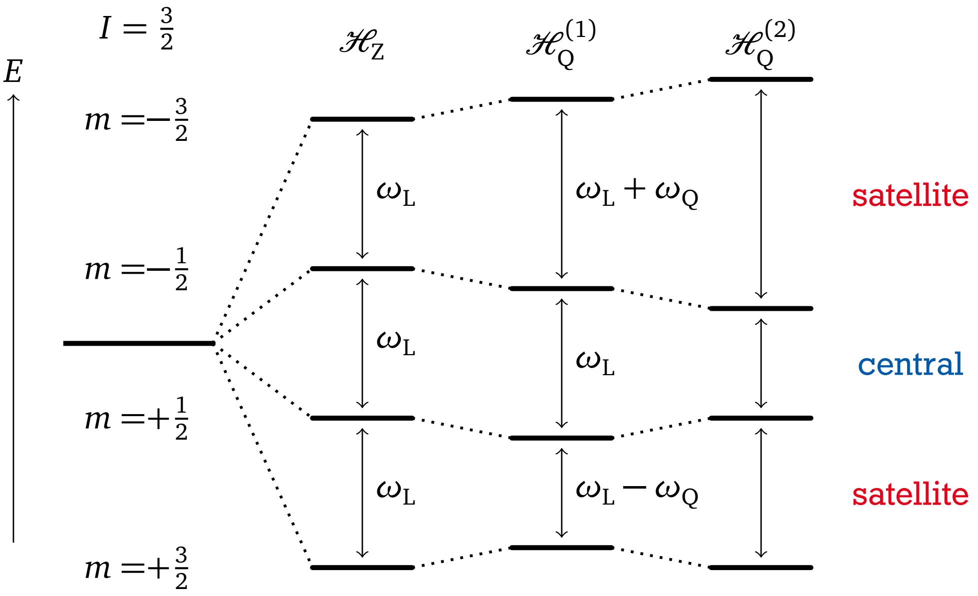

Figure 3.2.: Shift of the Zeeman niveaus caused by the quadrupolar interaction. The satellite transitions are shifted in first-order perturbation theory. In second order also the central transition is affected. The thickness of the drawn levels represents the strength of the dipolar coupling ω_D, q.v. Sec. 3.2.2.

respectively. With the help of the ladder operators $\hat{I}_\pm = \hat{I}_x \pm i\hat{I}_y$ and in polar coordinates, the Hamiltonian can be expressed using the dipolar alphabet:

$$\mathscr{H}_D = \frac{\mu_0\gamma_i\gamma_j\hbar^2}{4\pi r_{ij}^3}[\hat{A}+\hat{B}+\hat{C}+\hat{D}+\hat{E}+\hat{F}], \tag{3.22}$$

$$\hat{A} = \hat{I}_z\hat{J}_z\left(1-3\cos^2(\theta)\right), \tag{3.23}$$

$$\hat{B} = -\frac{1}{4}(\hat{I}_+\hat{J}_- + \hat{I}_-\hat{J}_+)\left(1-3\cos^2(\theta)\right), \tag{3.24}$$

$$\hat{C} = -\frac{3}{2}(\hat{I}_+\hat{J}_z + \hat{I}_z\hat{J}_+)\left(\sin(\theta)\cos(\theta)\exp(-i\phi)\right), \tag{3.25}$$

$$\hat{D} = -\frac{3}{2}(\hat{I}_-\hat{J}_z + \hat{I}_z\hat{J}_-)\left(\sin(\theta)\cos(\theta)\exp(i\phi)\right), \tag{3.26}$$

$$\hat{E} = -\frac{3}{4}\hat{I}_+\hat{J}_+\sin^2(\theta)\exp(-2i\phi), \tag{3.27}$$

$$\hat{F} = -\frac{3}{4}\hat{I}_-\hat{J}_-\sin^2(\theta)\exp(2i\phi). \tag{3.28}$$

The operator $\hat{A}$ leads to the line broadening and (in the homonuclear case, $I=J$) the operator $\hat{B}$ to energy conserving flip-flop processes (spin diffusion); the terms $\hat{C}$ to $\hat{F}$ describe relaxation processes, q.v. Sec. 3.3.1. The operators $\hat{C}$ and $\hat{D}$ lead to single and the operators $\hat{E}$ and $\hat{F}$ to double quantum coherences, respectively. Often, only the homonuclear dipole-dipole interaction, i.e., the case where I and J represent the same kind of nucleus, is relevant for ^{7}Li in solids. Then, the strength of the dipolar interaction, represented by the dipolar coupling frequency

$$\omega_{\mathrm{D}} = \frac{\mu_0 \gamma_{\mathrm{i}} \gamma_{\mathrm{j}} \hbar^2}{4\pi r_{\mathrm{ij}}^3} \frac{1}{2} \left(3\cos^2 \theta_{\mathrm{ij}} - 1 \right), \tag{3.29}$$

depends strongly on the density of the lithium ions $n = \langle 1/r_{\mathrm{ij}}^3 \rangle_{\mathrm{nn}}$ in the sample. Here, the index nn indicates that only next-neighbor distances are responsible for the density and θ_{ij} denotes the angle between r_{ij} and the external magnetic field $\mathbf{B}_0$.

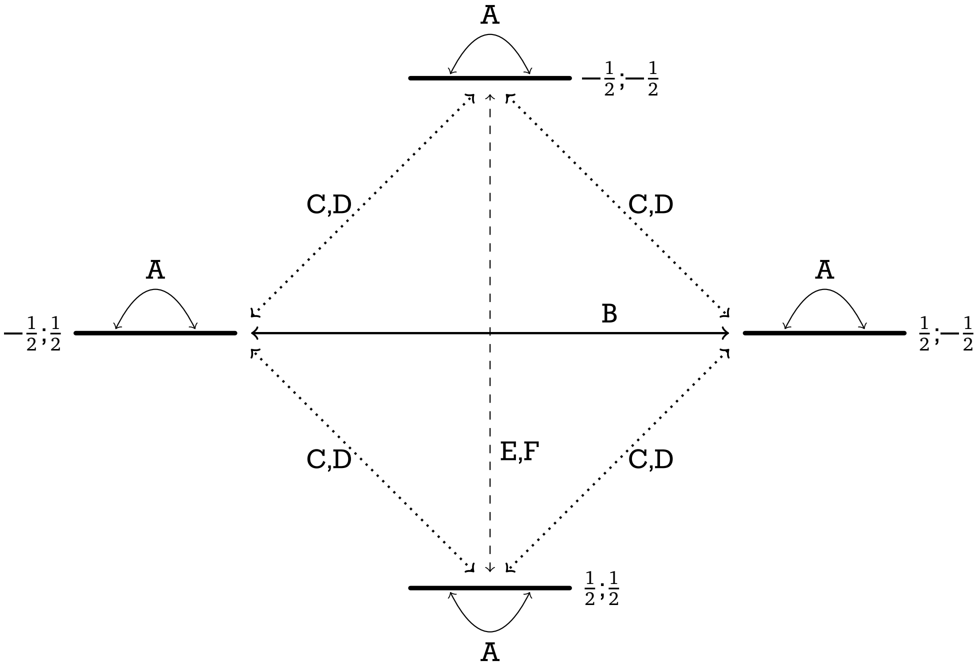

Figure 3.3.: Dipolar alphabet for a nucleus with spin $\frac{1}{2}$.

3.3 Pulse sequences

As mentioned above, RF pulses of a magnetic field $\mathbf{B}_1$ perpendicular to $\mathbf{B}_0$ can induce transitions between the nuclear states. With certain sequences of applied RF pulses and specific evolution times t_{p} these transitions, in combination with the internal interactions, are used to get access to dynamical processes on different time scales. The width of the excitation spectrum is given by

$$\Delta \nu_{\mathrm{p}} = \frac{c}{\Delta_{\mathrm{p}}}, \tag{3.30}$$

where Δ_{p} is the duration of the pulse and the factor c is on the order of unity; its exact value depends on the shape of the RF pulse. In this work pulse lengths of $2\,\mu\mathrm{s} \leq \Delta_{\mathrm{p}} \leq 2.5\,\mu\mathrm{s}$ have been used, resulting in $400\,\mathrm{kHz} \leq \Delta \nu_{\mathrm{p}} \leq 500\,\mathrm{kHz}$. For ^{7}Li this $\Delta \nu_{\mathrm{p}}$ is broader than the spectrum of the quadrupolar frequency ω_Q, leading to a non-selective excitation. Important for this non-selective excitation is the use of so-called hard pulses, i.e., pulses of high intensity resulting in $\mathscr{H}_\mathrm{RF} \gg \mathscr{H}_\mathrm{Q} + \mathscr{H}_\mathrm{D}$. Applying an on-resonant ($\omega_1 = \omega_\mathrm{L}$) hard pulse in direction I_Φ leads to a precession of the magnetization into the xy-plane

$$\mathscr{H}_\mathrm{RF} = \omega_1 I_\Phi = \omega_1 \left(I_x \sin\Phi + I_y \cos\Phi \right). \tag{3.31}$$

The flip angle φ is adjusted by the duration of the pulse Δ_p with

$$\varphi = \omega_1 \Delta_\mathrm{p}. \tag{3.32}$$

With the angle φ and the rotation axis Φ the notation of pulses in this work will be in the form φ_Φ.

3.3.1 Relaxation

The lifetime of the states induced by RF pulses is not infinite, but limited. Due to relaxation processes thermal equilibrium with Boltzmann distributed occupancy of the states will be reached sooner or later. This relaxation is described by the Bloch equations [Blo46]

$$\begin{aligned}
\frac{\mathrm{d}M_x(t)}{\mathrm{d}t} &= \gamma(\mathbf{M}\times\mathbf{B}_0)_x - \frac{M_x(t)}{T_2},\\
\frac{\mathrm{d}M_y(t)}{\mathrm{d}t} &= \gamma(\mathbf{M}\times\mathbf{B}_0)_y - \frac{M_y(t)}{T_2},\\
\frac{\mathrm{d}M_z(t)}{\mathrm{d}t} &= \gamma(\mathbf{M}\times\mathbf{B}_0)_z - \frac{M_z(t)-M_\infty}{T_1},
\end{aligned} \tag{3.33}$$

where $\mathbf{M}$ denotes the magnetization of the sample. The longitudinal relaxation in the z-direction is given by the relaxation rate T_1^{-1} and is also known as spin-lattice relaxation (SLR). In solids the transversal relaxation in the xy-plane is usually much faster than the SLR and its relaxation time T_2 is called spin-spin relaxation (SSR) time.

3.3.1.1 Spin-lattice relaxation

The SLR is caused by interaction with the lattice, i.e., spins flipping through fluctuations in a more favorable direction with respect to the external magnetic field $\mathbf{B}_0$ while exchanging energy with the lattice resulting finally in the equilibrium magnetization M_∞. In order to measure the SLR time T_1, the saturation recovery method can be used. Here, first the magnetization is destroyed by a sequence of several 90° pulses. As too few saturation pulses lead to a not completely destroyed magnetization and too many pulses heat up the sample, the number of saturation pulses has been restricted to the range of four to eight in this work. The SLR time is then monitored by screening the recovery of the magnetization after various delays t_d. In liquids, this is done by measuring the free induction decay (FID), i.e., the signal directly following a 90° pulse. Due to the very short T_2, the FID lies almost completely in the dead time of the receiver for solids, shown as the shaded area in Fig. 3.4. Therefore, the so-called solid echo pulse sequence depicted in Fig. 3.4 is used. In this sequence, a second pulse at a time t_p after the first pulse creates an echo of the signal occuring at t_p after the second pulse. Obviously, t_p has to be longer than the receiver dead time, on the other hand, a signal loss due to SSR prevents a usage of a too long t_p. The dead time of the receivers used for the measurements is ca. 10 µs, meaning that the decay of signals $\geq$ 100 kHz cannot be detected with an FID. For ^{7}Li this means that only the central transition is detectable without the measurement of an echo. Therefore, an evolution time of $t_\mathrm{p} = 20\,\mu\mathrm{s}$ has been used for all SLR measurements. To maximize the echo signal, a second pulse of 64° is used [Kan71]. The acquired magnetization recovery is often

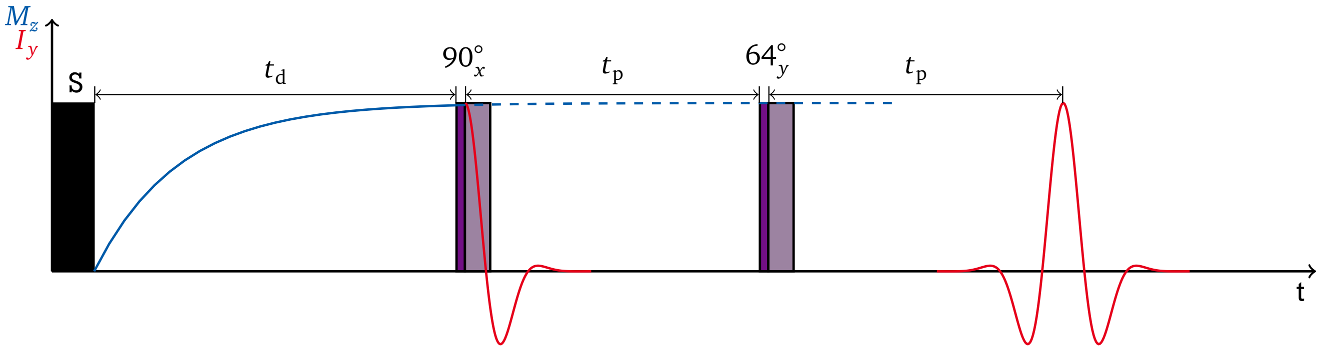

Figure 3.4.: Solid echo pulse sequence. This two-pulse sequence is used to measure the echo at the time t_p after the second pulse outside the receiver dead time (shaded area following the pulses). If not denoted otherwise, an evolution time of $t_\mathrm{p} = 20\,\mu\mathrm{s}$ has been used.

best described by a KWW function of the following form

$$M(t_\mathrm{d}) = M_\infty \left\{1 - \exp\left[-(t_\mathrm{d}/T_1)^{\beta_{\mathrm{T1}}}\right]\right\} + M_0. \tag{3.34}$$

Due to proper saturation the initial magnetization M_0 could be set to 0. Therefore, M_0 will be ignored for the remainder of this work. The deviation from the mono-exponential relaxation, characterized by a stretching factor $\beta_{\mathrm{T1}} < 1$, arises, if the spin system is no longer ergodic during the relaxation, i.e., if the time scale of the molecular dynamics is slower than T_1 and dynamical heterogeneities are no longer averaged out [Gei93]. A stretched relaxation is often connected to a distribution of relaxation times $G(T_1)$ and the mean of this distribution is given by

$$\langle T_1 \rangle = \int_0^\infty G(T_1) T_1 \,\mathrm{d}T_1 = \int_0^\infty \Phi(t)\,\mathrm{d}t = \int_0^\infty \exp\left[-\left(\frac{t_\mathrm{d}}{T_1}\right)^{\beta_{\mathrm{T1}}}\right] T_1 \,\mathrm{d}T_1 = \frac{T_1}{\beta_{\mathrm{T1}}} \Gamma\left(\frac{1}{\beta_{\mathrm{T1}}}\right), \tag{3.35}$$

where $\Phi(t) = (M_\infty - M(t_\mathrm{d}))/M_\infty$ and $\Gamma()$ denotes the gamma function.

Calculations have shown that, theoretically, there is a mono-exponential relaxation of the satellite transition and a bi-exponential relaxation for the central line [Maa03a, Maa03b]. However, in experiments usually only a single, mostly stretched exponential relaxation is observed leading to a harmonic mean relaxation rate $\langle T_1^{-1} \rangle$, which is given by [Blo99]

$$\langle T_1^{-1} \rangle = \int_0^\infty G(T_1) T_1^{-1} \,\mathrm{d}T_1 = -\lim_{t\to 0} \frac{\Phi(t)}{\mathrm{d}t} \tag{3.36}$$

and can be determined by analyzing the initial slope of the magnetization recovery. $\langle T_1^{-1}\rangle$ is connected to the spectral density via [Kan82, Cot07]

$$\begin{aligned}
\langle T_1^{-1}\rangle &= \frac{9}{160}\frac{2I+3}{I^2(2I-1)}\left(1+\frac{\eta_{\mathrm{Q}}^2}{3}\right)\left(\frac{e^2qQ}{\hbar}\right)^2\left[J_1(\omega_{\mathrm{L}},\tau_{\mathrm{c}})+J_2(2\omega_{\mathrm{L}},\tau_{\mathrm{c}})\right],\\
&\overset{J_2=4J_1\equiv 4J\,\text{[Jon66]}}{=} \frac{9}{160}\frac{2I+3}{I^2(2I-1)}\left(1+\frac{\eta_{\mathrm{Q}}^2}{3}\right)\left(\frac{e^2qQ}{\hbar}\right)^2\left[J(\omega_{\mathrm{L}},\tau_{\mathrm{c}})+4J(2\omega_{\mathrm{L}},\tau_{\mathrm{c}})\right],\\
&\overset{\eta_{\mathrm{Q}}=0,\,\text{Eq. (3.17)}}{=} \frac{9}{160}\frac{4}{9}(2I+3)(2I-1)\,\delta_{\mathrm{Q}}^2\left[J(\omega_{\mathrm{L}},\tau_{\mathrm{c}})+4J(2\omega_{\mathrm{L}},\tau_{\mathrm{c}})\right],\\
&\overset{I=3/2}{=} \frac{3\delta_{\mathrm{Q}}^2}{10}\left[J(\omega_{\mathrm{L}},\tau_{\mathrm{c}})+4J(2\omega_{\mathrm{L}},\tau_{\mathrm{c}})\right].
\end{aligned} \tag{3.37}$$

For the remainder of this work, the chevrons $\langle\cdot\rangle$ will often be omitted when dealing with relaxation times and rates, but it should be remembered that in a non-ergodic system $\langle T_1^{-1}\rangle > \langle T_1\rangle^{-1}$ holds. Figure 3.6 shows the dependence of the SLR time T_1 on τ_{c} in a double-logarithmic representation. If the correlation time τ_{c} obeys the Arrhenius law (2.10), a similar plot can be obtained with experimental data by using the inverse temperature T^{-1} as the x-coordinate. At a correlation time $\tau_{\mathrm{c}} \approx \omega_{\mathrm{L}}^{-1}$, T_1 passes through a minimum, the height of which is roughly given by $T_{1,\mathrm{min}} \approx \omega_{\mathrm{L}}/\omega_{\mathrm{Q}}^2$, q.v. Eq. (3.37). In the BPP model, the high- and low-temperature flanks are symmetrical and the activation energy E_{a} can be obtained directly from the slope of $T_1(\tau_{\mathrm{c}})$.

3.3.1.2 Spin-spin relaxation

The SSR is energy conservant and is caused by the slow dephasing of the spins due to interactions with each other. In the equilibrium state, the spins are evenly distributed in the xy-plane as there is no field to favor a direction and thus the magnetization in this plane is zero. The solid echo sequence described in the last section is characterized by a phase shift of 90° between the two pulses. To distinguish this sequence with a phase shift of 90° from the one without a phase shift between the two pulses, the former will be denoted as SE_+ and the latter as SE_-, as introduced in [Sto15]. Both, the SE_+ and the SE_- sequence suffer from the existence of oscillating quadrupolar transients, making it very difficult to obtain SSR parameters. By using the *exorcycle* $\mathrm{SE}_+{-}\mathrm{SE}_-$ with a flip angle $\varphi = 70.5°$, these transients are eliminated and the SSR time T_2 can be measured by monitoring the magnetization under variation of the evolution time t_{p}. The SSR of the central transition, $T_{2\mathrm{c}}$, differs from that of the satellite transition, $T_{2\mathrm{s}}$, and their connection to the spectral density reads [Bar73]

$$\frac{1}{T_{2\mathrm{c}}} = \frac{3\delta_{\mathrm{Q}}^2}{10}\left[J(\omega_{\mathrm{L}})+4J(2\omega_{\mathrm{L}})\right]+\left(\frac{\omega_{\mathrm{Q}}^2}{\omega_{\mathrm{L}}}\right)^2\tau_{\mathrm{c}}, \tag{3.38}$$

$$\frac{1}{T_{2\mathrm{s}}} = \frac{3\delta_{\mathrm{Q}}^2}{10}\left[10J(\omega_{\mathrm{L}})+4J(2\omega_{\mathrm{L}})+6J(0)\right]. \tag{3.39}$$

At high temperatures, i.e., sufficiently small τ_{c}, all contributions to the spectral density $J_m(m\omega_{\mathrm{L}})$ are approximately equal, resulting in $T_1 \approx T_{2\mathrm{s}} \approx T_{2\mathrm{c}}$. Near the T_1 minimum, the SSR time splits up in a central and a satellite contribution. The relaxation of the central transition first increases similar to T_1, reaches a maximum at $\tau_c \approx \omega_Q^{-1}$, and decreases again until it attains the inverse linewidth in the low temperature regime $T_{2c} \approx \omega_L/\omega_Q^2$, q.v. Sec. 3.3.2. The transversal relaxation time of the satellite transitions T_{2s} decreases till $\tau_c \approx \omega_Q^{-1}$ is reached. In this temperature regime $T_{2s} \approx \omega_Q^{-1}$ holds. Depending on the coupling strength ω_Q, the bi-exponentiality of the transversal relaxation can be seen in experimental data and analysis of the relaxation curves with

$$M(t_p) = M_0 \left\{ (1 - F_c) \exp\left[-\left(\frac{2t_p}{T_{2s}} \right)^{\beta_{T2s}} \right] + F_c \exp\left[-\left(\frac{2t_p}{T_{2c}} \right)^{\beta_{T2c}} \right] \right\} + M_\infty \tag{3.40}$$

is possible. Here, $0 \leq F_c \leq 1$ describes the fraction of the decay that arises due to the central relaxation T_{2c}. At low temperature, T_{2s} becomes very short and cannot be recorded. Therefore, the bi-exponential decay given in Eq. (3.40) is only obtainable at intermediate temperatures. The dependence on τ_c of both transversal relaxations as described above is also depicted in Fig. 3.6. Similar to the longitudinal relaxation, the bi-exponentiality of the SSR sometimes cannot be observed in experiments. In this case a single KWW function with a stretching parameter $1 \leq \beta_{T2} \leq 2$ often describes the data quite well.

3.3.1.3 Relaxation in the rotating frame

SLR measurements in the laboratory frame give insight into the molecular dynamics on a time scale near the inverse Larmor frequency ω_L^{-1}. A typical ^{7}Li Larmor frequency of approximately $2\pi \times 50\,\mathrm{MHz}$ results in a dynamical window in the nanosecond regime. This zone is usually outside the accessible temperature window for solid ion conductors. The glass transition or other phase transitions often prevent measurements at temperatures high enough to observe the T_1 minimum not to mention the high-temperature flank of $T_1(T)$. Alternatively, the relaxation can be measured in the rotating frame by using a so-called spinlock pulse P_lock which keeps the magnetization in the transverse plane. To measure the longitudinal relaxation time in the rotating frame $T_{1\rho}$, the pulse sequence shown in Fig. 3.5 is used. The spinlock pulse P_lock follows directly an initial 90° pulse. During the duration of the spinlock pulse, t_lock, the generated magnetization $\hat{I}_x$ decays with a relaxation rate $T_{1\rho}^{-1}$. By varying t_lock, this relaxation is screened. The connection between $T_{1\rho}$ and the spectral density is given by [Göb79]

$$\frac{1}{T_{1\rho}} = \frac{3\delta_Q^2}{10} \left[10J(\omega_L) + 4J(2\omega_L) + 6J(2\omega_1) \right]. \tag{3.41}$$

Therefore, $T_2 \leq T_{1\rho} < T_1$ holds and the relaxation in the rotating frame is sensitive to dynamics on a time scale $\tau_c \approx \omega_1^{-1}$, where $T_{1\rho}$ passes through a minimum. Using a P_lock with a strength of $\omega_1 \ll \omega_L$ gets access to dynamics in the microsecond regime.

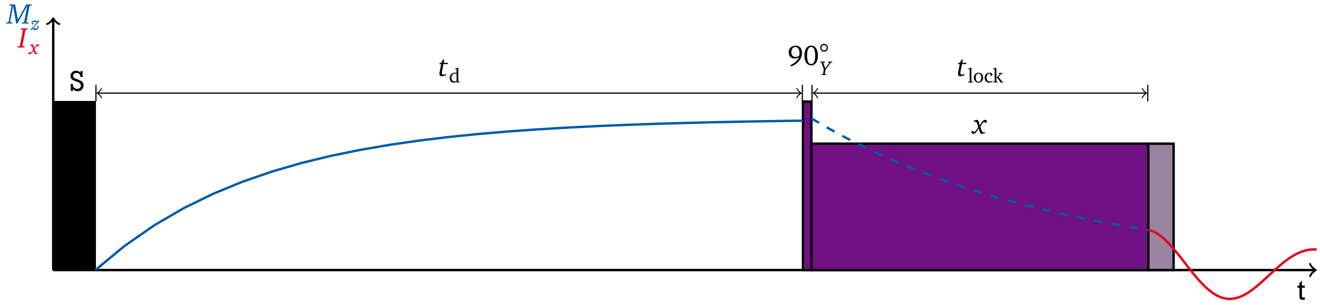

Figure 3.5.: Pulse sequence used to measure the relaxation time $T_{1\rho}$ in the rotating frame. The initial hard pulse and the spinlock pulse are characterized by a phase shift of 90°. If there is no phase shift between the two pulses, $T_{2\rho}$ can be measured.

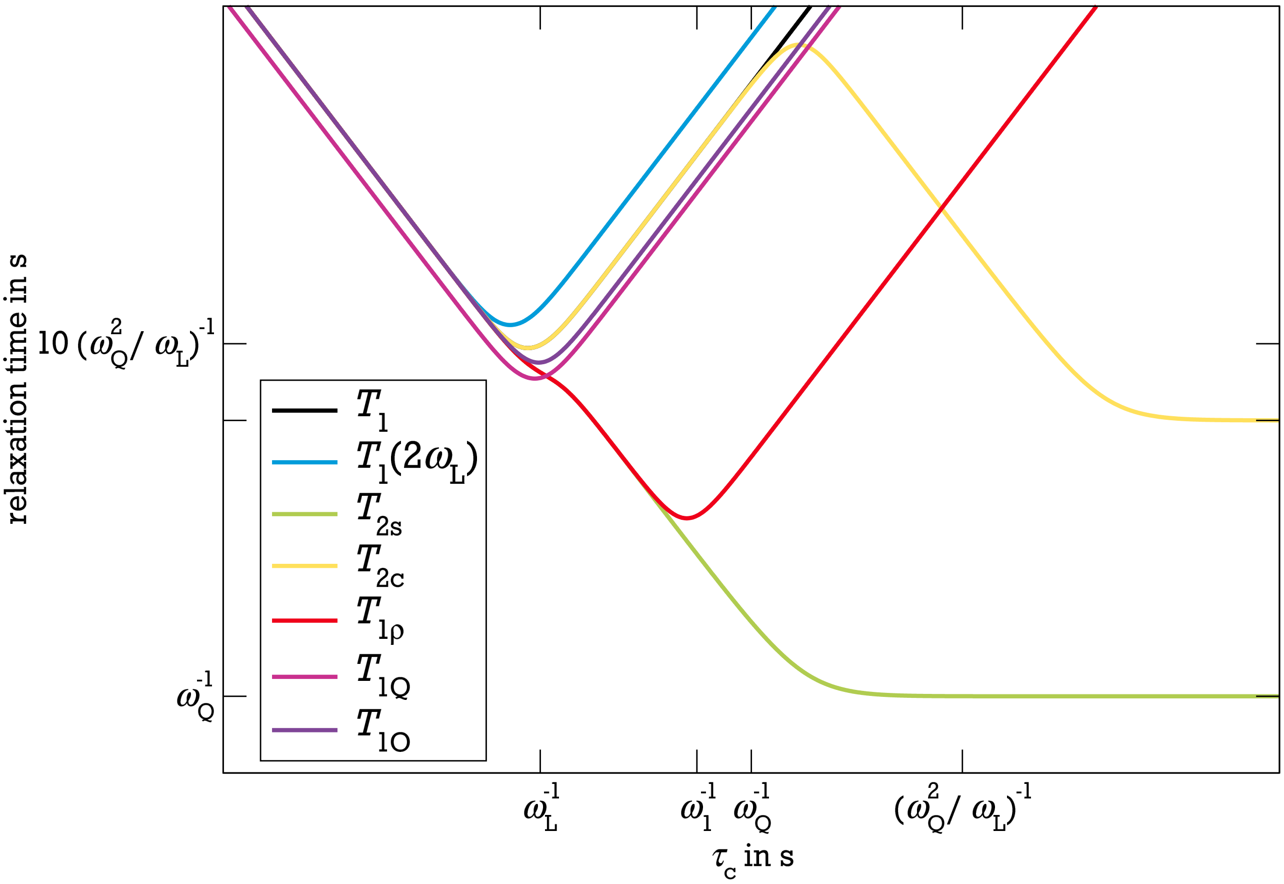

Figure 3.6.: NMR relaxation times as a function of the correlation time τ_c according to Eqs. (3.37), (3.38), (3.39), (3.41), (3.54), and (3.58). Modified from [Veg07].

3.3.1.4 Field-cycling relaxometry

A second possibility to overcome the problem of not observing the T_1 minimum in the accessible temperature range is to measure the SLR time at another Larmor frequency in order to fulfill the minimum condition $\omega_\mathrm{L}\tau_\mathrm{c} \approx 1$. Furthermore, the feasibility of performing the SLR measurements frequency dependent gives access to the spectral density, q.v. Eq. (3.37). In principle this can be done using standard equipment. Due to the limited availability of magnets in the laboratory, this time consuming approach has however been restricted to just a few frequencies [Kim97a, Kim96a, Sva93]. In contrast, using field-cycling (FC) relaxometry the dispersion of the SLR time T_1 and, thus, the spectral density $J(\omega_\mathrm{L}, \tau_\mathrm{c})$ can be monitored in a broad frequency range. This method is widely used to analyze dynamical processes in soft matter, e.g., viscous liquids and polymers [Kru12], but applications to ion dynamics in solid materials are still rare [Gra13, Gab15]. A typical cycle of the magnetic field $\mathbf{B}_0$ consists of polarization, relaxation, and detection periods as shown in Fig. 3.7. First, the sample is polarized for a sufficiently long time in a high magnetic field $\mathbf{B}_\mathrm{pol}$, whereupon a magnetization is built up inside the sample. Then, the field is rapidly switched to a low relaxation field $\mathbf{B}_\mathrm{rel}$, resulting in a relaxation from the equilibrium state in the polarization field towards that in the relaxation field. By variation of this relaxation period t_rel, the relaxation at $\mathbf{B}_\mathrm{rel}$ is monitored. For that, the field is switched again after t_rel to a very high detection field $\mathbf{B}_\mathrm{det}$ for maximizing the signal to noise ratio (SNR) and the amplitude of an FID following a $\pi/2$ pulse is read out. By analyzing the magnetization in dependence on t_rel, the SLR time $T_1(\omega_\mathrm{rel})$ can be obtained by using Eq. (3.34). When this whole procedure is repeated for different relaxation fields $\mathbf{B}_\mathrm{rel}$ the dispersion $T_1(\omega_\mathrm{rel} = \omega_\mathrm{L})$ is obtained. If the evolution and the polarization fields do not differ much, the polarization period can be omitted ($\mathbf{B}_\mathrm{pol} = 0$). Then, a magnetization buildup is measured similar to SLR experiments. In this way a higher contrast is achieved at high evolution fields, cf. [Kre16].

It proved useful not to use T_1 or the spectral density $1/T_1 \propto J(\omega_\mathrm{L}, \tau_\mathrm{c})$ but a generalized susceptibility representation, e.g., to enable a direct comparison with electrical or mechanical relaxation data. For this purpose, the NMR susceptibility $\chi''_\mathrm{NMR} = \omega_\mathrm{L}/T_1$ has been introduced [Kru12, Gra13, Gab15], which usually exhibits broad peaks allowing to obtain the time scale of the ionic hopping motion from the positions of those loss peaks according to $\tau_\mathrm{c} \approx 1/\omega_\mathrm{p}$. As a result of the reduced mobility of the ions at lower temperatures a shift of the maximum to smaller frequencies is observed upon cooling. If frequency-temperature superposition holds, the data obtained at different temperatures can be shifted to create a master curve [Kru12]. In this way, correlation times at temperatures showing no loss peak ω_p can be acquired by analyzing the temperature dependent shift factor s

$$\tau_\mathrm{c}(T) = 10^{s(T)}\tau_\mathrm{c}(\omega_\mathrm{p}). \tag{3.42}$$

Additionally, FC relaxometry is used to obtain diffusion coefficients from the low-frequency relaxation rates with [Har69, Sho81, Mei13]

$$R_1(\omega_\mathrm{L}) = R_1(0) - \frac{8\pi n\gamma^4\hbar^2 I(I+1)\cdot 0.555}{15D^{3/2}}\sqrt{\omega_\mathrm{L}}, \tag{3.43}$$

where n is the spin density.

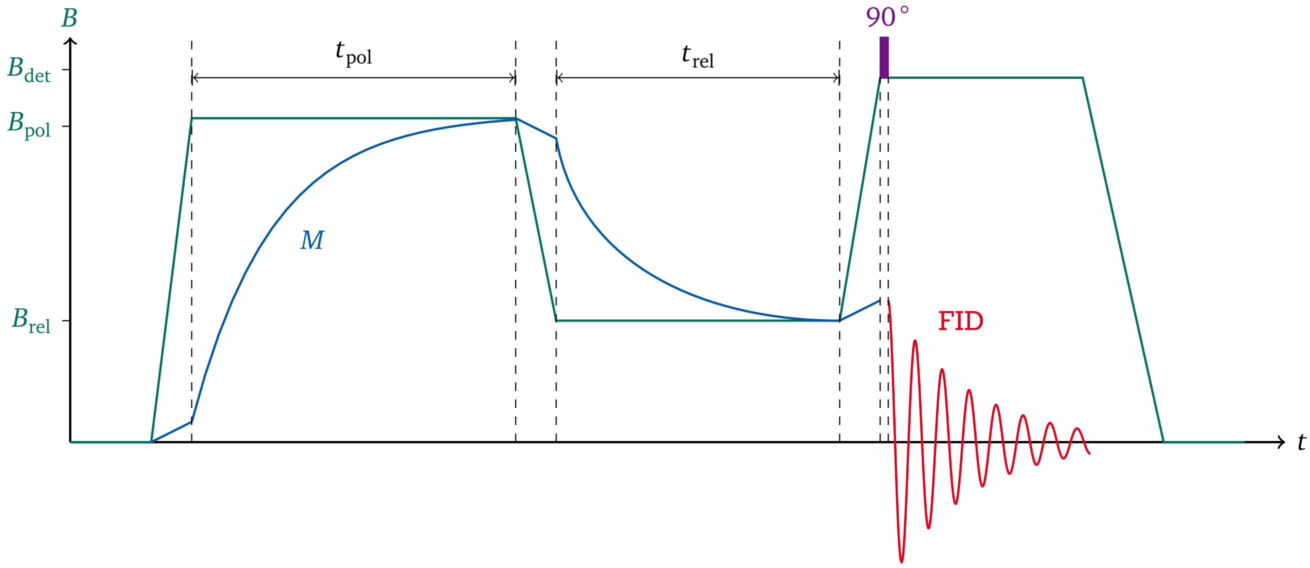

Figure 3.7.: Typical cycle of the magnetic field in an FC experiment. Modified from [Kre16].

3.3.2 Line shape analysis

Since the quadrupolar interaction is the dominant internal interaction for ^{7}Li, the quadrupolar frequency as given in Eq. (3.18) has great influence on the line shape. Several possible ^{7}Li NMR spectra in the rigid-lattice regime (RLR), i.e., at low temperatures, are depicted in Fig. 3.8. For a single crystal the ^{7}Li NMR spectrum consists of well separated lines (see upper panel of Fig. 3.8). For each distinguishable site i, a pair of satellite lines appears at $\pm\omega_Q^i$ on both sides from the central line. All lines are equally broadened due to the dipolar interaction. If the single crystal is grinded into a fine powder, all orientations, represented by the angle θ in Eq. (3.18), are present in the sample, resulting in the so-called Pake spectrum [Pak48] shown in the middle panel of Fig. 3.8. The strength of the quadrupolar coupling δ_Q can be clearly seen in powder spectra given by half the distance between the two edges ($\theta = 90°$) or, if the asymmetry parameter η_Q is zero, by the distance between the two horns ($\theta = 0°$).

The inherent heterogeneity in glassy solids leads to a distribution of nuclear quadrupole coupling constants, of asymmetry parameters, and of the orientation of the principal axes of the EFG tensors. As a result, the ^{7}Li NMR spectrum of a glassy solid at low temperature consists of two lines which are often well described by a superposition of a broad and a narrow Gaussian distribution as depicted in the lower panel of Fig. 3.8. The width of the satellite line represents the strength of the quadrupolar interaction while the central line is broadened due to the dipolar coupling. Ion diffusion from one site to another takes place with increasing temperature, resulting in an averaging of both the quadrupolar and dipolar interactions when the time scale of the local dynamics reaches the inverse of the coupling frequency. As a consequence, first the central and later the satellite line narrow when the temperature is increased. This process is known as motionally narrowing (MN) and finally leads to a single Lorentzian line in the extreme narrowing limit (ENL) for glasses at high temperatures.

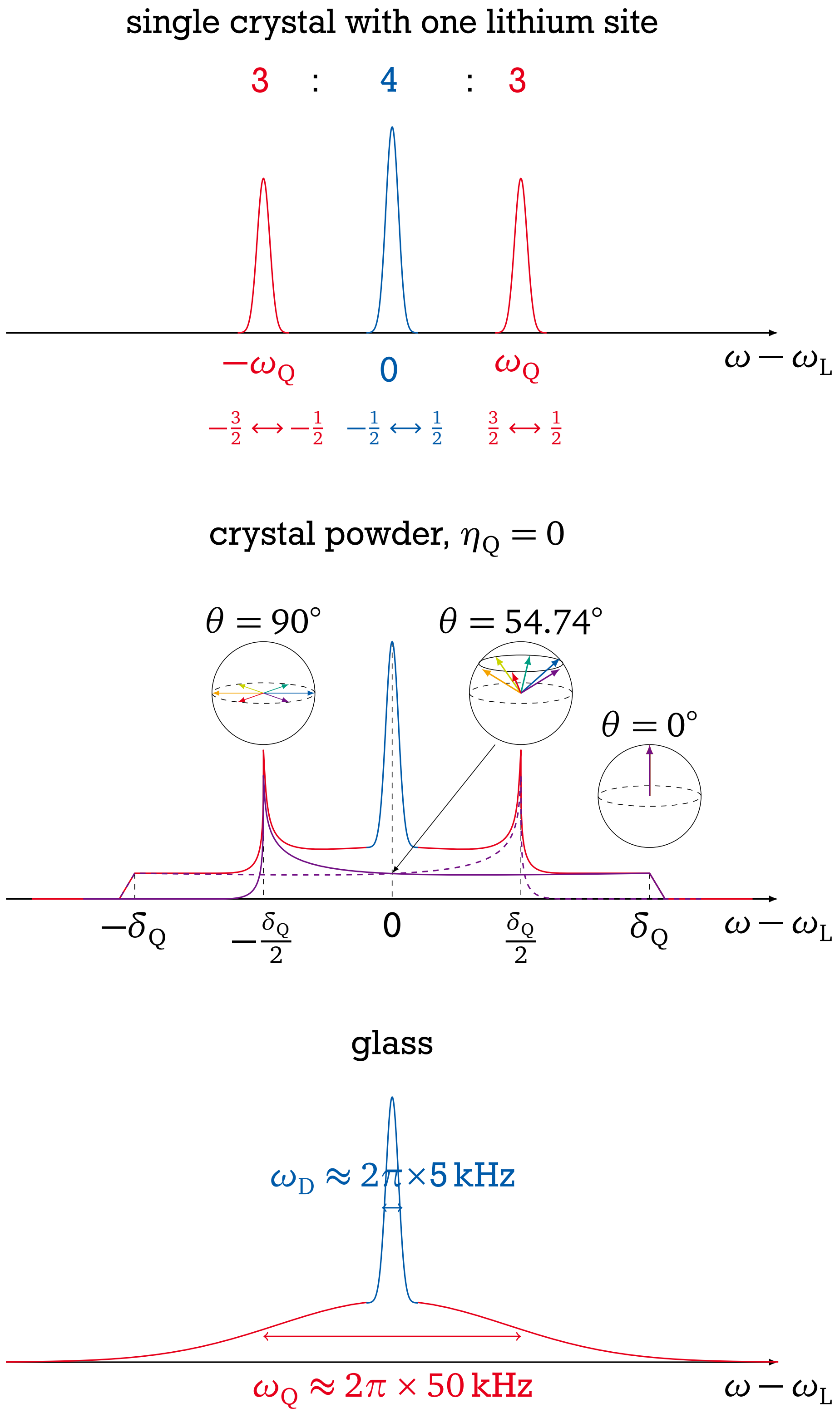

single crystal with one lithium site

crystal powder, $\eta_Q = 0$

glass

Figure 3.8.: ^{7}Li NMR spectra of a single crystal (upper panel), crystalline powder (middle panel), and glassy solid (lower panel). The satellite lines of the powder and glass spectrum are exaggerated by a factor of five for better visuality.

During the MN, and sometimes also in the RLR and ENL, the line is represented neither by a Gaussian nor a Lorentzian distribution. Therefore, the superposition of Gaussian and Lorentzian lines, the pseudo-Voigt (PV) function

$$PV(x) = R_{\mathrm{PV}} \frac{2\Sigma}{\pi \cdot \left[4(x-\mu_{\mathrm{PV}})^2 + \Sigma^2\right]} + (1-R_{\mathrm{PV}}) \sqrt{\frac{4\ln 2}{\pi \Sigma^2}} \exp\left(-4\ln 2 \frac{(x-\mu_{\mathrm{PV}})^2}{\Sigma^2}\right) \tag{3.44}$$

has been used to describe the glassy ^{7}Li NMR spectra. Here, Σ is the full width at half maximum (FWHM) of the line, μ_{PV} denotes the position of the peak, and the parameter R_{PV} describes the fraction of the Lorentzian line. Due to the much stronger quadrupolar interaction, the satellite line is often hardly seen in the MN regime, making a detailed analysis difficult. Therefore, mostly only the MN of the central line is analyzed.

The second moment of the resonance line $\langle\omega^2\rangle$ is related to the spectral density by [Abr61]

$$\langle\omega^2\rangle = \frac{1}{\pi}\int_0^\infty J_{1,1}(\omega)\,\mathrm{d}\omega, \tag{3.45}$$

$$= \langle\omega^2\rangle_\infty + \frac{2}{\pi}\left(\langle\omega^2\rangle_0 - \langle\omega^2\rangle_\infty\right)\tan^{-1}\left(\tau_{\mathrm{c}}\sqrt{\langle\omega^2\rangle}\right). \tag{3.46}$$

In Eq. (3.46) the fact that only frequencies smaller than the linewidth $\sqrt{\langle\omega^2\rangle}$ are contributing to the integral and the BPP spectral density $J_{\mathrm{BPP}}(\omega_{\mathrm{L}}, \tau_{\mathrm{c}})$ have been used. $\langle\omega^2\rangle_0$ and $\langle\omega^2\rangle_\infty$ are the second moment of the line in the RLR and ENL, respectively. Assuming an Arrhenius-like dependence of the correlation time and using the experimentally more easily accessible FWHM Σ makes it possible to calculate the correlation time from the line shape with

$$\tau_{\mathrm{LS}} = \frac{\tan\left(\frac{\frac{\pi}{2}\left(\Sigma^2(T)-\Sigma^2_\infty\right)}{\Sigma^2_{\mathrm{RL}}}\right)}{\Sigma(T)}. \tag{3.47}$$

Over the last decades, many other theories have been developed to obtain correlation times or activation energies from the line shape. Bjorkstam et al. [Bjo85] found an empirical relation for the correlation time at the temperature where the FWHM has reached half of its RLR value

$$\tau_{\mathrm{c}}(\Sigma_0/2) = \frac{0.3}{\Sigma_0}, \tag{3.48}$$

Waugh and Fedin (WF) [Wau63] related the activated energy with the onset of the MN

$$E_{\mathrm{a}}^{WF}/\mathrm{eV} = 1.617 \times 10^{-3} \cdot T_{\mathrm{onset}}/\mathrm{K}, \tag{3.49}$$

and Hendrickson and Bray (HB) [Hen73] developed a relation between the linewidth and the temperature to calculate the activation energy

$$\Sigma(T) = \frac{A}{1 + (A/B-1)\exp\left[-E_{\mathrm{a}}^{HB}/(k_{\mathrm{B}}T)\right]} + \Sigma_\infty, \tag{3.50}$$

where A is the broad line which denotes the non-excited state, B is the narrow line of the thermally activated ions and Σ_∞ is the FWHM in the ENL which also considers constant line-broadening terms. The spectral line in the ENL can be broadened due to instrumental problems, e.g., bad tuning, sample problems, e.g., sample inhomogeneities or temperature gradients across the sample, and field inhomogeneities.

Often the parameters obtained from this line-shape analysis (LSA) deviate from correlation times or activation energies acquired from other methods. The determination of $\tau_\mathrm{c}(T)$ from the line shape becomes even more difficult, when a distribution of activation energies is present as discussed in Sec. 3.4.5.

All spectra presented in this work have been recorded using the solid echo sequence SE_+ shown in Fig. 3.4.

3.3.3 Stimulated echo experiments

So far measurements which give access to the local dynamics in the nanosecond (SLR in laboratory frame) or microsecond (SLR in rotating frame, SSR, and LSA) regime have been discussed. STE experiments expand the accessible time scale to the slow dynamical regime ranging from milliseconds to seconds. The STE experiment consists of three pulses as depicted in Fig. 3.9. During the evolution time t_p the spins with their local frequencies accumulate a phase $\Phi(0) \equiv \Phi\left(0, t_\mathrm{p}\right) = \int_0^{t_\mathrm{p}} \omega_\mathrm{Q}(t)\,\mathrm{d}t$, which is then stored during the mixing time t_m. After the third pulse, this phase is correlated with the phase $\Phi(t_\mathrm{m}) \equiv \Phi\left(t_\mathrm{p}+t_\mathrm{m}, t_\mathrm{p}+t_\mathrm{m}+t_\mathrm{p}\right) = \int_{t_\mathrm{p}+t_\mathrm{m}}^{t_\mathrm{p}+t_\mathrm{m}+t_\mathrm{p}} \omega_\mathrm{Q}(t)\,\mathrm{d}t$. If a correlation between the two phases $\Phi(0)$ and $\Phi(t_\mathrm{m})$ exists, an echo appears at $t = t_\mathrm{p}$ after the third pulse, the stimulated echo [Hah50]. If $t_\mathrm{m} \gg t_\mathrm{p}$ is chosen, changes of ω_Q occur only during the mixing and not during the evolution time. Then, the phase is simply given by $\Phi\left(t, t_\mathrm{p}\right) = \omega_\mathrm{Q}(t)\,t_\mathrm{p}$ and an echo amplitude decay with increasing t_m can be identified with the correlation function $F_{l,0}(|t_\mathrm{m}|)$. Depending on the chosen phases of the pulses, the sine and cosine component of the two-time correlation function

$$F_2\left(t_\mathrm{p}, t_\mathrm{m}\right) = \langle \exp\left[i\Phi(0)\right] \exp\left[-i\Phi(t_\mathrm{m})\right]\rangle \tag{3.51}$$

can be measured independently. While the sine-correlation function F_2^SS, discussed in Sec. 3.3.3.1, has been obtained by the use of the spin-alignment echo (SAE) since many years [Böh00, Fas08], only recently the pulse sequence to acquire the cosine-correlation function F_2^CC for ^{7}Li has been developed [Sto15] and will be presented in Sec. 3.3.3.2. Both correlation functions can usually be described by a KWW function with the correlation time as the time constant. Usually, the logarithmic moments of a distribution $G(\tau_\mathrm{c})$ causing the non-exponentiality are of interest and the first moment of the KWW function in given by [Zor02]

$$\ln \tau_\mathrm{m} = \langle \ln \tau_\mathrm{c} \rangle = \ln \tau_2 + (1 - 1/\beta_\mathrm{F2})\,\mathrm{Eu}, \tag{3.52}$$

where τ_2 and β_F2 are the decay time and stretching parameter obtained from the KWW analysis of the correlation function, respectively, and Eu is Euler's constant (Eu = 0.5772).

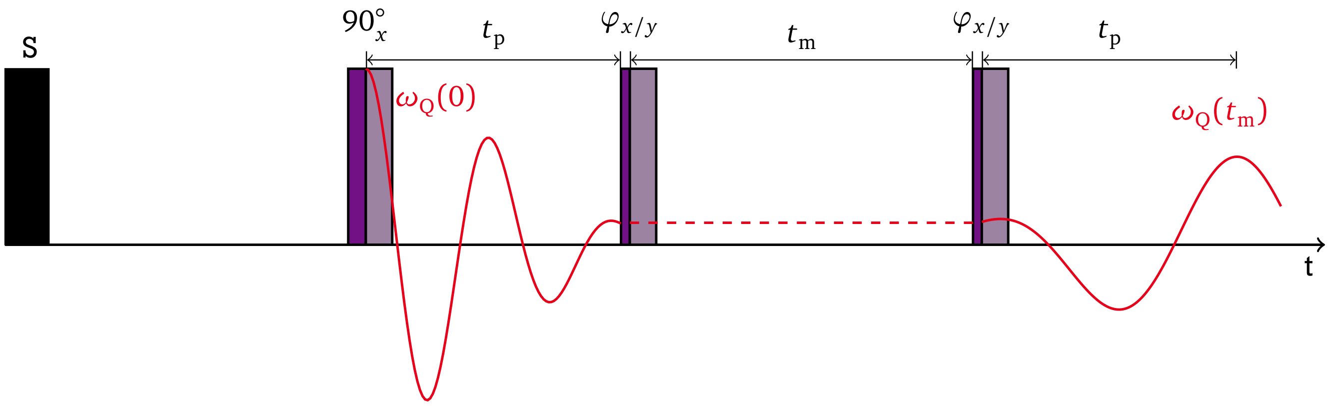

Figure 3.9.: Stimulated echo pulse sequence.

3.3.3.1 Spin-alignment echo

Using the Jeener-Broekaert pulse sequence $90^\circ_x - t_\mathrm{p} - 45^\circ_y - t_\mathrm{m} - 45^\circ_y$ [Jee67] and an adequate phase cycle, cf. [Qi04] or Appx. D, the sine-correlation function

$$F_2^{\mathrm{SS}}(t_\mathrm{p}, t_\mathrm{m}) = \frac{9}{20}\langle \sin[\omega_\mathrm{Q}(0)t_\mathrm{p}]\sin[\omega_\mathrm{Q}(t_\mathrm{m})t_\mathrm{p}]\rangle \tag{3.53}$$

is monitored. Here, $\omega_\mathrm{Q}(0)$ and $\omega_\mathrm{Q}(t_\mathrm{m})$ are the quadrupolar frequencies before and after the mixing time, respectively. During the mixing time t_m the phase information is stored in the spin-alignment state T_{20}, which decays with the time constant $T_{1\mathrm{Q}}$. The relaxation rate of this quadrupolar state is connected to the spectral density via [Car99]

$$\frac{1}{T_{1\mathrm{Q}}} = \frac{3\delta_\mathrm{Q}^2}{10}[5J(\omega_\mathrm{L}) + 5J(2\omega_\mathrm{L})], \tag{3.54}$$

leading to a ratio $T_{1\mathrm{Q}}/T_1 = 8/25$ for $\omega_\mathrm{Q}\tau_\mathrm{c} \gg 1$ and $T_{1\mathrm{Q}}/T_1 = 1/2$ for $\omega_\mathrm{Q}\tau_\mathrm{c} \ll 1$ [Böh07b] as shown in Fig. 3.6. N magnetically indistinguishable positions, i.e., equivalent sites in a crystal, lead to a residual correlation $F_\infty^{\mathrm{SS}} = 1/N$. Then, the obtained data points can usually be described by two non-exponential decays

$$F_2^{\mathrm{SS}}(t_\mathrm{m}) = \left\{(1 - F_\infty^{\mathrm{SS}})\exp\left[-\left(\frac{t_\mathrm{m}}{\tau_2}\right)^{\beta_{\mathrm{F2}}}\right] + F_\infty^{\mathrm{SS}}\right\}\exp\left[-\left(\frac{t_\mathrm{m}}{T_{1\mathrm{Q}}}\right)^{\beta_{\mathrm{T1Q}}}\right]. \tag{3.55}$$

3.3.3.2 Zeeman order

Using the Zeeman pulse sequence $90^\circ_x - t_\mathrm{p} - 43.5^\circ_x - t_\mathrm{m} - 43.5^\circ_x$ and an adequate phase cycle, q.v. Appx. D, the cosine-correlation function

$$F_2^{\mathrm{CC}}(t_\mathrm{p}, t_\mathrm{m}) = \frac{\sqrt{2}}{3}\langle \frac{2}{5} + \frac{3}{5}\cos[\omega_\mathrm{Q}(0)t_\mathrm{p}]\cos[\omega_\mathrm{Q}(t_\mathrm{m})t_\mathrm{p}]\rangle \tag{3.56}$$

is monitored. The term *Zeeman order* is misleading, as a mixture of dipolar (Zeeman) T_{10} and octupolar T_{30} states is present for $I = 3/2$ nuclei. But this term is used in analogy to the cos-cos experiments established in deuteron NMR. According to the different prefactors given in Eq. (3.56), a residual correlation of $F_\infty^{\text{CC}} = 0.4$ can be expected due to a constant contribution of the central line even for $N \to \infty$. Equivalent to the SAE, the F_2^{CC} is usually given by two non-exponential decays

$$F_2^{\text{CC}}(t_\text{m}) = \left\{ \left(1 - F_\infty^{\text{CC}}\right) \exp\left[-\left(\frac{t_\text{m}}{\tau_2} \right)^{\beta_{\text{F2}}} \right] + F_\infty^{\text{CC}} \right\} \exp\left[-\left(\frac{t_\text{m}}{T_{1\text{ZO}}} \right)^{\beta_{\text{T1ZO}}} \right], \tag{3.57}$$

where $T_{1\text{ZO}}$ is the relaxation time of the mixed Zeeman and ocupolar state. The purely octupolar state relaxes with [Böh07b]

$$\frac{1}{T_{1\text{O}}} = \frac{3\delta_\text{Q}^2}{10} \left[4J(\omega_\text{L}) + J(2\omega_\text{L}) \right], \tag{3.58}$$

resulting in a ratio $T_{1\text{O}}/T_1 = 8/17$ for $\omega_\text{Q}\tau_\text{c} \gg 1$; $T_1 = T_{1\text{O}}$ holds for $\omega_\text{Q}\tau_\text{c} \ll 1$ [Böh07b], q.v. Fig. 3.6.

3.3.4 Multi-time correlation functions

While the two-time correlation function observed with the STE method described in Sec. 3.3.3 approximately measures the probability of an ion to be at an equivalent site before and after the mixing time t_m, no statement can be made whether the ion stayed at the same site during t_m, made a jump to an equivalent site or even a forward-backward jump to another site and back to the original one. More insight into the jump dynamics and dynamic heterogeneities are possible with three- and four-, i.e., multi-time correlation functions (MTCFs). Here, the frequencies during three, respectively four, different evolution phases are correlated. This kind of experiment was first developed for deuteron NMR [SR94, Heu95, Hin98a, Hin98b, Böh96], was later adopted to $I = 1/2$ and other $I = 1$ nuclei like ^{109}Ag or ^{6}Li [Bri10, Vog04, Vog06], and has recently been developed for ^{7}Li NMR [Sto17]. The MTCF experiment consists of two STE sequences separated by an additional mixing time. Figure 3.10 shows the corresponding pulse sequence, which consists of seven pulses separated by three mixing times and four evolution times t_p of equal length. The correlation signal measured at t_p after the seventh pulse depends on the pulse length and phases, e.g., it is given by

$$E_4^{SSSS} = \frac{81}{320} \left\langle \sin\left[\omega_1 t_\text{p}\right] \sin\left[\omega_2 t_\text{p}\right] \sin\left[\omega_3 t_\text{p}\right] \sin\left[\omega_4 t_\text{p}\right] \right\rangle, \tag{3.59}$$

with $\omega_1 \equiv \omega_\text{Q}(0)$ and $\omega_i \equiv \omega_\text{Q}(t_{\text{m}(i-1)})$, $i = 2, 3, 4$. The stimulated echo experiment with first mixing time $t_{\text{m}1}$ acts as a dynamical low-pass filter by selecting a slow subensemble, if existent [Böh98]. The subsequent mixing time $t_{\text{m}2}$ separates the prior dynamic filter from another SAE pulse sequence which can be used to analyze the selected subensemble by varying the mixing times $t_{\text{m}2}$ or $t_{\text{m}3}$. Unfortunately, for ^{7}Li only this quadruple sine-modulated MTCF is accessible, while cosine-modulated ones, i.e., $E_4^{SSCC}, E_4^{CCSS}, E_4^{CCCC}$ cannot be obtained due to the occurance of quadrupolar transients and of constant magnetization terms which cannot simultaneously be eliminated in time-domain signals [Sto17]. As the entire dynamic exchange information is contained in E_4^{SSSS}, analysis of signals of the form given in Eq. (3.59) is sufficient. This quadruple sine modulated function can be recorded in many different ways, two of which are discussed in more detail in the following sections. A detailed analysis of the MTCF is usually done with the help of the parameters obtained from the two-time correlation function, τ_2 and β_{F2}, so that it is important to measure the SAE first.

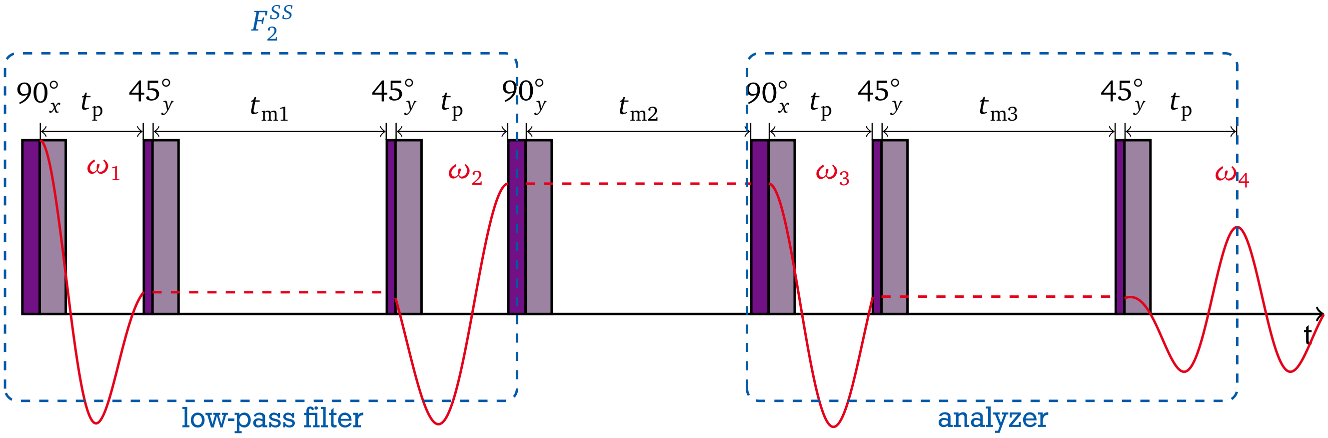

Figure 3.10.: Pulse sequence for measurement of multi-time correlation functions. The saturation pulses and relaxation regime has been omitted for better visuality. Modified from [Böh17].

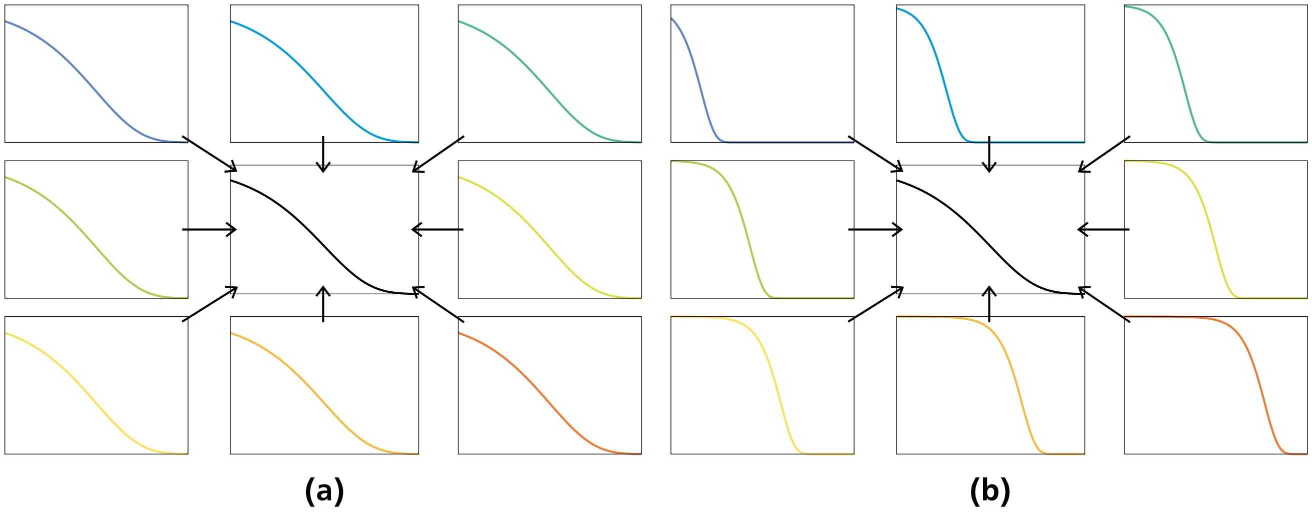

Figure 3.11.: Schematic illustration of the homogeneous (a) and heterogeneous (b) scenarios. The ensemle averaged correlation function (center) has the same non-exponential shape in both cases. In scenario (a) identical microscopic correlation functions are averaged, while in scenario (b) exponential correlation functions on different time scales result in the non-exponential average. Modified from [Ric93].

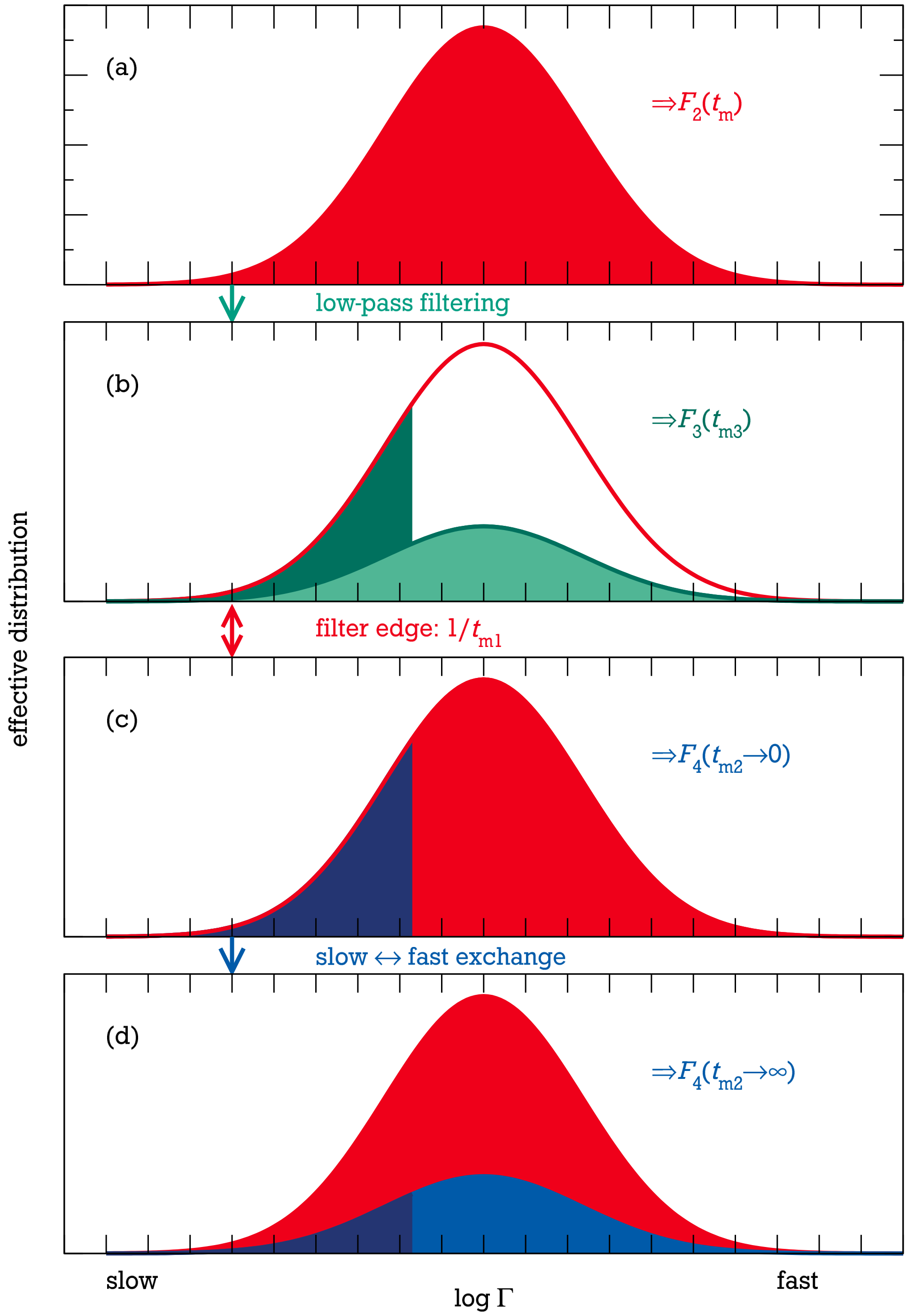

Figure 3.12.: Schematic illustration of some properties characterizing two-time and four-time correlation functions. (a) Effective distribution of ion hopping rates Γ that may be the origin of the non-exponential shape of $F_2(t_\mathrm{m})$. (b) Selection of small motional rates by applying a filter. The light green area represents the homogeneous limit, where only the amplitude and not the shape is altered. In the heterogeneous limit the mean is shifted to longer times (dark green area). The short- and the long-time limits of F_4 are illustrated in (c) and (d), respectively. Modified from [Sto17].

3.3.4.1 Three-time correlation function

With the three-time correlation function (3TCF) the origin of non-exponential relaxation can be determined, q.v. Fig. 3.11. This is done by setting the time of the low-pass filter to a constant value which is approximately the correlation time, $t_{\mathrm{m1}} \equiv t_{\mathrm{f}} \approx \tau_{\mathrm{c}}$. In this way ions residing at the same or equivalent sites before and after t_{m1} are selected. Additionally, the second mixing time is kept as short as possible ($t_{\mathrm{m2}} \to 0$), which yields $\omega_2 = \omega_3 \equiv \omega_{23}$. Finally, t_{m3} is varied resulting in the 3TCF

$$E_4^{SSSS}(t_{\mathrm{f}}, 0, t_{\mathrm{m3}}) \equiv F_3(t_{\mathrm{m3}}). \tag{3.60}$$

It should be noted that in the literature for this 3TCF often the symbol G_4 instead of F_3 is used [Sto17].

In the purely homogeneous scenario (Fig. 3.11a), all ions obey the same correlation function, which is intrinsically non-exponential, e.g., due to correlated forward-backward jumps [Bri10] and the 3TCF is given by [Vog04]

$$F_3^{\mathrm{hom}}(t_{\mathrm{m3}}) = \frac{1}{2}\left[F_2(t_{\mathrm{m1}} + t_{\mathrm{m3}}) + F_2(t_{\mathrm{m1}}) \cdot F_2(t_{\mathrm{m3}})\right]. \tag{3.61}$$

In the limit of purely heterogeneous dynamics (Fig. 3.11b), each ion has a mono-exponential correlation function but different time scales exist, resulting in a distribution of correlation times (DCT). In the heterogeneous case, different forms of F_3 exist for crystals and glasses [Bri10]. For ^{7}Li this difference is supposed to be negligible and the simple relation for glasses is used here:

$$F_3^{\mathrm{het}}(t_{\mathrm{m3}}) = F_2(t_{\mathrm{m1}} + t_{\mathrm{m3}}). \tag{3.62}$$

Another approach of analyzing the heterogeneity in glasses is simple using the filter efficiency (FE)

$$\mathrm{FE} = 1 - F_2(t_{\mathrm{m1}}) \tag{3.63}$$

and the parameters of the F_2 decay, τ_2 and β_{F2}. The stretching factor and time constant of the heterogeneous F_3 decay is then given by

$$\beta_{\mathrm{F3}}^{\mathrm{het}} = \beta_{\mathrm{F2}}\left[1 + f - f^{1/\beta_{\mathrm{F2}}}(1+f)^{1-1/\beta_{\mathrm{F2}}}\right] \text{ and} \tag{3.64}$$

$$\tau_3^{\mathrm{het}}/\tau_2 = (1+f)^{1/\beta_{\mathrm{F2}}} - f^{1/\beta_{\mathrm{F2}}}, \tag{3.65}$$

with $f = -\ln(1 - \mathrm{FE})$ [Sto17].

3.3.4.2 Four-time correlation function

If a DCT $G(\tau_\mathrm{c})$ exists, the four-time correlation function (4TCF) can monitor the time scale on which the ions exchange their correlation times. This is done by using the same dynamical filter during the first and second stimulated echo sequence ($t_\mathrm{m1} = t_\mathrm{m3} \equiv t_\mathrm{f}$). Therefore, only ions sufficiently slow ($\tau_\mathrm{c} > t_\mathrm{f}$) during the first and second filter contribute to the signal and $F_4(t_\mathrm{m2})$ decays when slow ($\tau_\mathrm{c} > t_\mathrm{f}$) ions become fast ($\tau_\mathrm{c} < t_\mathrm{f}$) during the mixing time t_m2. This decay can be described with

$$F_4(t_\mathrm{m2}) = F_2(t_\mathrm{m2}/\mathbb{Q} + 2t_\mathrm{f}) + \frac{[F_2(t_\mathrm{f}) - F_2(t_\mathrm{m2}/\mathbb{Q} + t_\mathrm{f})]^2}{1 - F_2(t_\mathrm{m2})}, \tag{3.66}$$

where $\mathbb{Q} \geq 1$ is the rate memory parameter [Heu97] describing the average number of jumps an ion has to take before it exhibits a random new rate from the distribution.

3.3.5 Diffusometry

While the experiments in homogeneous magnetic fields discussed above yield insights into ion dynamics on different time scales, they all are restricted to microscopic length scales, e.g., the distance between neighboring sites, usually a few Å. Contrarily, measurements in inhomogeneous magnetic fields provide access to ionic diffusion on mesoscopic length scales, typically some µm. Here, the proportionality of the Larmor frequency ω_L to the strength of the magnetic field is exploited, q.v. Eq. (3.8). When a pulsed field gradient (PFG) or static field gradient (SFG) is applied the resonance condition is given by

$$\omega_\mathrm{L}(z) = -\gamma\left(|\mathbf{B}_0| + gz\right), \tag{3.67}$$

where $g = \mathrm{d}B/\mathrm{d}z$ denotes the field gradient and z specifies the nuclear spin position in the inhomogeneous field for a static sample. Diffusion induced ionic motion results in time-dependent resonance frequencies, which can be probed by appropriate echo experiments [Gei98]. Due to the relatively slow diffusion in solids, SFG experiments are preferred as they take the advantage of the highest achievable field gradients of up to 180 T/m. Ionic diffusion is observed on long time scales by using the STE pulse sequence $90^\circ_x - t_\mathrm{p} - 90^\circ_x - t_\mathrm{m} - 90^\circ_x$ shown in Fig. 3.14. The echo height is reduced due to diffusion taking place during the mixing time t_m, as shown in Fig. 3.13, as well as SLR and SSR occuring during t_m and t_p, respectively, and it is read out either for constant t_p and various t_m or vice versa. In SFG experiments, the echo height due to unrestricted, three-dimensional diffusion is reduced according to

$$M\left(t_\mathrm{p}, t_\mathrm{m}\right) = M_0 \exp\left[-\left(\gamma g t_\mathrm{p}\right)^2 D\left(t_\mathrm{m} + \tfrac{2}{3}t_\mathrm{p}\right)\right] \exp\left[-(t_\mathrm{m}/T_1)^{\beta_\mathrm{T1}}\right] \exp\left[-2\left(t_\mathrm{p}/T_2\right)^{\beta_\mathrm{T2}}\right], \tag{3.68}$$

giving access to the self-diffusion coefficient D, which is probed on a length scale determined by the inverse of the generalized scattering vector $q_D = \gamma g t_\mathrm{p}$.

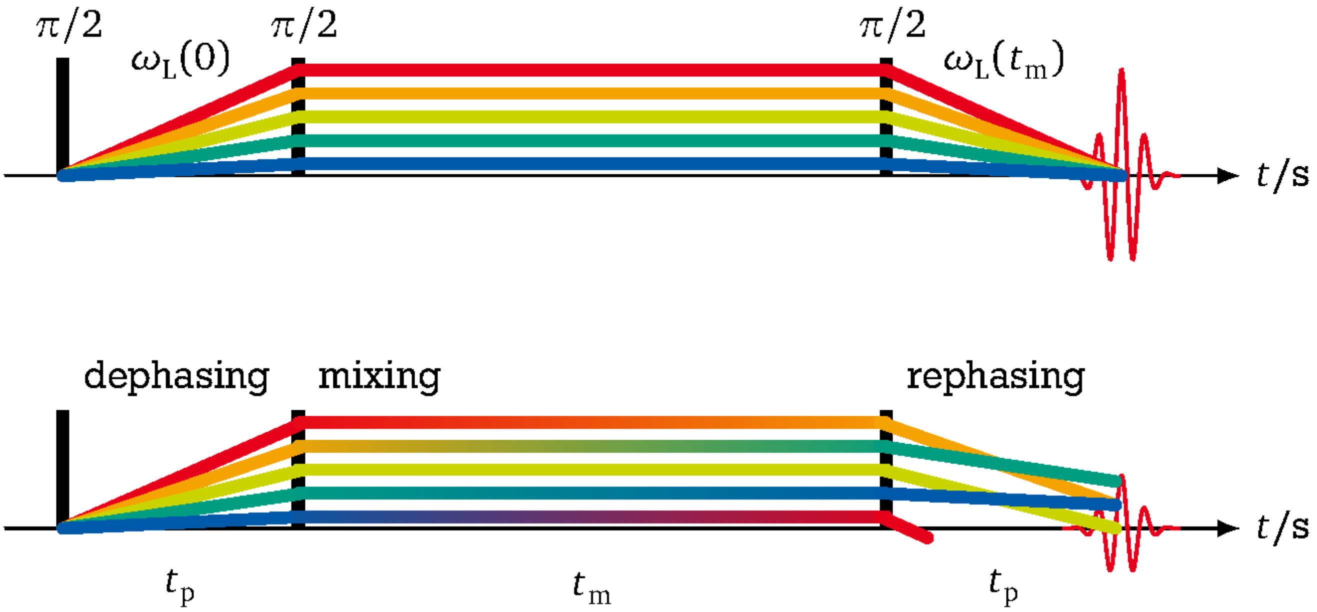

Figure 3.13.: STE experiment without (above) and with (below) the presence of diffusion. The colors indicate the position dependent ω_L and the slope visualizes the rapidity of the phase change during t_p. Diffusion during t_m changes ω_L, resulting in an imperfect rephasing and reduced echo height. Modified from [Ros12].

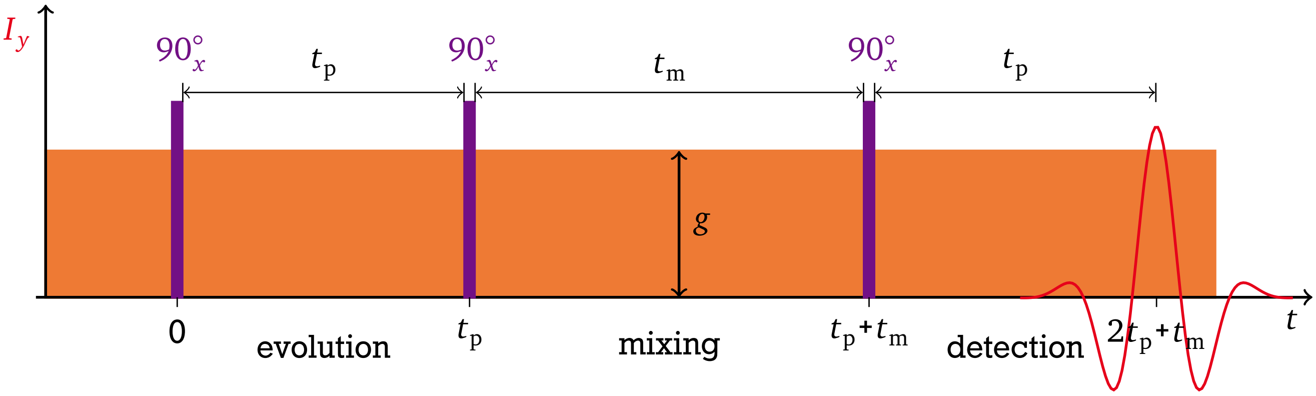

Figure 3.14.: Stimulated echo pulse sequence for static field gradient experiments.

3.4 Influence of a distribution of correlation times

As mentioned above, a stretched exponential correlation function is usually observed for ionic conductors. A stretching factor $\beta < 1$ measures the deviations from single exponential behavior. Possible reasons for $\beta < 1$ have been discussed in Sec. 3.3.4. If a distribution $G(\tau_\mathrm{c})$ exists, all observables O that depend on the correlation time τ_c are obtained from an average over this distribution,

$$O = \int_0^\infty O(\tau_\mathrm{c})\,G(\tau_\mathrm{c})\,\mathrm{d}\tau_\mathrm{c}. \tag{3.69}$$

3.4.1 Spectral densities

So far only the BPP spectral density $J_\mathrm{BPP}(\omega_\mathrm{L},\tau_\mathrm{c})$ has been mentioned. While this spectral density assumes a single correlation time, it can also be interpreted in terms of a distribution, when the $G(\tau_\mathrm{c})$ is equal to the Dirac delta function $\delta(\tau-\tau_\mathrm{c})$. $J_\mathrm{BPP}(\omega_\mathrm{L},\tau_\mathrm{c})$ is also known as the Debye spectral density as it follows directly from the assumption that the motion is random, i.e., obeys Poisson statistics. It is symmetric and has the limiting values

$$J_\mathrm{BPP}(\omega_\mathrm{L},\tau_\mathrm{c}) = \tau_\mathrm{c} \quad \text{for } \omega_\mathrm{L}\tau_\mathrm{c} \ll 1, \tag{3.70}$$

$$J_\mathrm{BPP}(\omega_\mathrm{L},\tau_\mathrm{c}) = \tau_\mathrm{c}^{-1}\omega_\mathrm{L}^{-2} \quad \text{for } \omega_\mathrm{L}\tau_\mathrm{c} \gg 1, \tag{3.71}$$

and the maximum value

$$J_\mathrm{BPP}(\omega_\mathrm{L},\tau_\mathrm{c})_\mathrm{max} = \omega_\mathrm{L}^{-1} \text{ for } \omega_\mathrm{L}\tau_\mathrm{c} = 1. \tag{3.72}$$

If an Arrhenius relationship between the correlation time τ_c and the activation energy E_a is assumed, q.v. Eq. (2.10), and $J_\mathrm{BPP}(\omega_\mathrm{L},\tau_\mathrm{c})$ is plotted vs. the inverse temperature T^{-1}, the slopes are $E_\mathrm{a}/k_\mathrm{B}$ and $-E_\mathrm{a}/k_\mathrm{B}$, respectively. In the following, two other spectral densities will be discussed briefly. First, a spectral density often used to describe dielectric relaxation data is introduced in Sec. 3.4.1.1. Then, the spectral density resulting from a Gaussian distribution of activation energies, often assumed to be present in solid ion conductors, is analyzed in Sec. 3.4.1.2. A detailed review of these and many other spectral densities has been written by Beckmann [Bec88].

3.4.1.1 Havriliak-Negami

A useful spectral density is the Havriliak-Negami (HN) spectral density

$$J_\mathrm{HN}(\omega_\mathrm{L},\tau_\mathrm{c}) = \frac{\sin\left[\epsilon \arctan\left(\frac{(\omega_\mathrm{L}\tau_\mathrm{c})^\alpha \sin(\alpha\pi/2)}{1+(\omega_\mathrm{L}\tau_\mathrm{c})^\alpha \cos(\alpha\pi/2)}\right)\right]}{\omega_\mathrm{L}} \left[1 + 2\,(\omega_\mathrm{L}\tau_\mathrm{c})^\alpha \cos(\alpha\pi/2) + (\omega_\mathrm{L}\tau_\mathrm{c})^{2\alpha}\right]^{-\epsilon/2}. \tag{3.73}$$

$J_{\mathrm{HN}}(\omega_{\mathrm{L}}, \tau_{\mathrm{c}})$ results from assuming both a distribution of motional barriers and the presence of correlated motions. The parameter α is a measure of the correlations and the product $\alpha\epsilon$ represents the spread of the barriers. The limiting values of $J_{\mathrm{HN}}(\omega_{\mathrm{L}}, \tau_{\mathrm{c}})$ are

$$J_{\mathrm{HN}}(\omega_{\mathrm{L}}, \tau_{\mathrm{c}}) \propto \tau_{\mathrm{c}}^{\alpha}\omega_{\mathrm{L}}^{-(1-\alpha)} \quad \text{for } \omega_{\mathrm{L}}\tau_{\mathrm{c}} \ll 1, \tag{3.74}$$

$$J_{\mathrm{HN}}(\omega_{\mathrm{L}}, \tau_{\mathrm{c}}) \propto \tau_{\mathrm{c}}^{-\alpha\epsilon}\omega_{\mathrm{L}}^{-(1+\alpha)} \quad \text{for } \omega_{\mathrm{L}}\tau_{\mathrm{c}} \gg 1. \tag{3.75}$$

Alvarez et al. have related the HN parameters to the KWW ones [Alv91]:

$$\alpha\epsilon = \beta^{1.23}. \tag{3.76}$$

The HN spectral density reduces to the symmetric Cole-Cole spectral density if $\epsilon = 1$ and to the asymmetric Cole-Davidson spectral density if $\alpha = 1$.

3.4.1.2 log-Gaussian

In a glassy solid the potential energy wells are assumed to differ in depth and shape from site to site which results in a distribution $g(E_{\mathrm{a}})$ of barrier heights and, hence, the ions hop with different rates. It is common practice to use a Gaussian distribution for $g(E_{\mathrm{a}})$ with the width parameter σ_{E} and center E_{m} [Ber05, Kim96a, Kim96b, Kim97a, Sto12, Fas08, Sva93, Sva00]:

$$g(E_{\mathrm{a}}) = \frac{1}{\sqrt{2\pi}\sigma_{\mathrm{E}}} \exp\left(-\frac{(E_{\mathrm{a}} - E_{\mathrm{m}})^2}{2\sigma_{\mathrm{E}}^2}\right). \tag{3.77}$$

The energy landscape is a characteristic of the disordered solid state of a sample. Therefore, it can be assumed that the distribution $g(E_{\mathrm{a}})$ and especially its variance σ_{E} is temperature independent. If the exchange process is thermally activated, a Gaussian distribution of activation energies (DAE) leads to a log-Gaussian distribution of correlation times $G(\ln\tau_{\mathrm{c}}) = k_{\mathrm{B}}T\,g(E_{\mathrm{a}})$:

$$G(\ln\tau_{\mathrm{c}}) = \frac{1}{\sqrt{2\pi}\sigma_{\tau}} \exp\left\{-\frac{1}{2}\left[\frac{1}{\sigma_{\tau}}\ln\left(\frac{\tau_{\mathrm{c}}}{\tau_{\mathrm{m}}}\right)\right]^2\right\}, \tag{3.78}$$

with $\sigma_{\tau} = \sigma_{\mathrm{E}}/(k_{\mathrm{B}}T)$. The correlation time τ_{m} is related to the mean energy E_{m} by the Arrhenius equation (2.10) which also connects the DCT $G(\tau_{\mathrm{c}}) = k_{\mathrm{B}}T/\tau_{\mathrm{c}} \cdot g(E_{\mathrm{a}})$ to the DAE:

$$G(\tau_{\mathrm{c}}) = \frac{1}{\sqrt{2\pi}\sigma_{\tau}\tau_{\mathrm{c}}} \exp\left\{-\frac{1}{2}\left[\frac{1}{\sigma_{\tau}}\ln\left(\frac{\tau_{\mathrm{c}}}{\tau_{\mathrm{m}}}\right)\right]^2\right\}. \tag{3.79}$$

The spectral density $J(\omega_{\mathrm{L}}, \tau_{\mathrm{c}})$ can be calculated via the DCT by integrating over all correlation times τ_{c}:

$$J_{\mathrm{Gauss}}(\omega_{\mathrm{L}}, \tau_{\mathrm{c}}) = \int_0^{\infty} G(\tau_{\mathrm{c}}) \frac{\tau_{\mathrm{c}}}{1 + \omega_{\mathrm{L}}^2\tau_{\mathrm{c}}^2} \mathrm{d}\tau_{\mathrm{c}}. \tag{3.80}$$

While the solution for integrals containing Gaussian functions given in Eqs. (3.77) and (3.78) (on linear and logarithmic scales, respectively) can be looked up in tables, it is faster to integrate

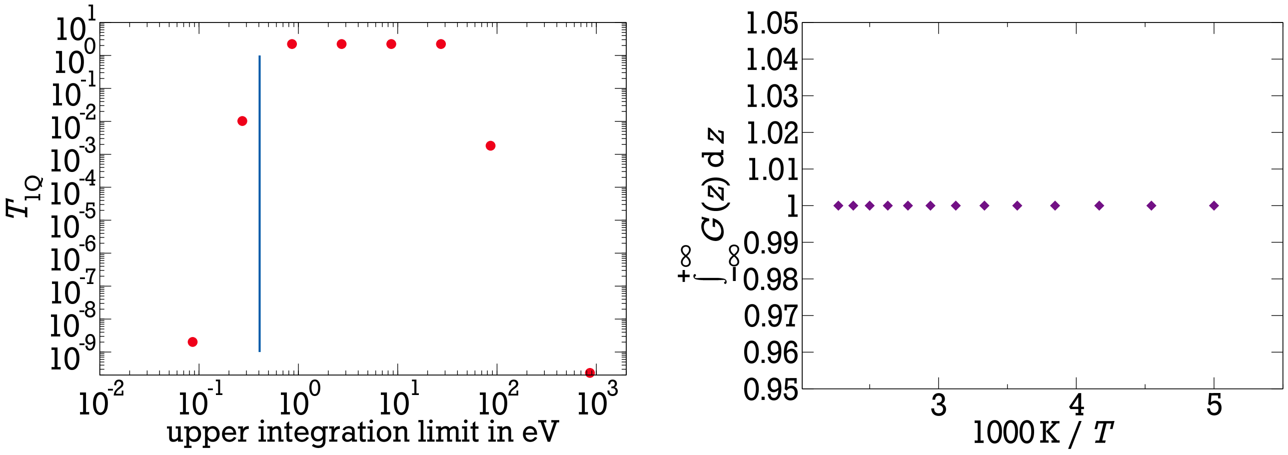

(a) **(b)**

Figure 3.15.: (a) Influence of the upper integration limit on numerical calculations for an exemplary calculation of $T_{1\mathrm{Q}}$ using a DAE with E_m = 0.40 eV and σ_E = 0.07 eV. If the upper integration limit is lower than E_m (represented by the blue line), the resulting $T_{1\mathrm{Q}}$ is too low. On the other hand, the result is also underestimating the true value of $T_{1\mathrm{Q}}$, if the upper integration limit is too high. The point on the very right represents a limit of $+\infty$. (b) In the calculation of the integral over the DCT with the parameter z as variable no numerical errors occur and the exact result, 1, is always computed.

them numerically using a modern computer. Under certain circumstances, this can become quite difficult and the result depends on the chosen upper integration limit, q.v. Appx. A and Fig. 3.15. Following substitution to a unitless parameter z turned out to be helpful in calculating integrals containing the DCT numerically:

$$z = \frac{E_\mathrm{a} - E_\mathrm{m}}{k_\mathrm{B} T} = \ln\left(\frac{\tau_\mathrm{c}}{\tau_\mathrm{m}}\right) \Leftrightarrow \tau_\mathrm{c} = \tau_\mathrm{m} e^z \Rightarrow \frac{\mathrm{d}\tau_\mathrm{c}}{\mathrm{d}z} = \tau_\mathrm{m} e^z \Rightarrow \mathrm{d}\tau_\mathrm{c} = \tau_\mathrm{m} e^z \mathrm{d}z = \tau_\mathrm{c}\mathrm{d}z. \tag{3.81}$$

With this substitution the integral of the DCT can be expressed as follows:

$$\begin{aligned}
1 = \int_0^\infty G(\tau_\mathrm{c})\mathrm{d}\tau_\mathrm{c} &\overset{(3.79)}{=} \int_0^\infty \frac{1}{\sqrt{2\pi}\sigma_\tau \tau_\mathrm{c}} \exp\left\{-\frac{1}{2}\left[\frac{1}{\sigma_\tau}\ln\left(\frac{\tau_\mathrm{c}}{\tau_\mathrm{m}}\right)\right]^2\right\}\mathrm{d}\tau_\mathrm{c} \\
&\overset{(3.81)}{=} \int_{-\infty}^\infty \frac{1}{\sqrt{2\pi}\sigma_\tau} \exp\left[-\frac{1}{2}\left(\frac{z}{\sigma_\tau}\right)^2\right]\mathrm{d}z \\
&\overset{\sigma_\tau = \sigma_\mathrm{E}/(k_\mathrm{B}T)}{=} \int_{-\infty}^\infty \frac{k_\mathrm{B}T}{\sqrt{2\pi}\sigma_\mathrm{E}} \exp\left[-\frac{1}{2}\left(\frac{z k_\mathrm{B} T}{\sigma_\mathrm{E}}\right)^2\right]\mathrm{d}z.
\end{aligned}$$

While the equations with the log-Gaussian distribution are often found in the literature, e.g., [Bec88] or [Kim96a], the equations containing the parameter z used during the calculations are hardly found. Therefore, these equations are presented in the following paragraphs.

Using the Arrhenius equation (2.10) to connect the maximum of the DCT with the maximum of the DAE, $\tau_\mathrm{m} = \tau_0 \exp[E_\mathrm{m}/(k_\mathrm{B}T)]$, the spectral density $J_\mathrm{Gauss}(\omega_\mathrm{L}, \tau_\mathrm{c})$ in Eq. (3.80) reads

$$J_\mathrm{Gauss}(\omega_\mathrm{L}, \tau_\mathrm{c}) = \int_{-\infty}^\infty \frac{\tau_\mathrm{m} k_\mathrm{B} T}{\sqrt{2\pi}\sigma_\mathrm{E}} \exp\left[z - \tfrac{1}{2}\left(\tfrac{z k_\mathrm{B} T}{\sigma_\mathrm{E}}\right)^2\right] \frac{1}{1 + \omega_\mathrm{L}^2 \tau_\mathrm{m}^2 e^{2z}}\mathrm{d}z. \tag{3.82}$$

The plot of $\ln J_{\text{Gauss}}(\omega_{\text{L}}, \tau_{\text{c}})$ vs. $\ln \tau_{\text{c}}$ is always symmetric about $\omega_{\text{L}}\tau_{\text{c}} = 1$ and the limiting values are

$$J_{\text{Gauss}}(\omega_{\text{L}}, \tau_{\text{c}}) \propto \tau_{\text{c}} \qquad \text{for } \omega_{\text{L}}\tau_{\text{c}} \ll 1, \tag{3.83}$$

$$J_{\text{Gauss}}(\omega_{\text{L}}, \tau_{\text{c}}) \propto \tau_{\text{c}}^{-1}\omega_{\text{L}}^{-2} \qquad \text{for } \omega_{\text{L}}\tau_{\text{c}} \gg 1. \tag{3.84}$$

The broader the distribution, the lower the height of $J_{\text{Gauss}}(\omega_{\text{L}}, \tau_{\text{c}})_{\max}$, which is always lower than $J_{\text{BPP}}(\omega_{\text{L}}, \tau_{\text{c}})_{\max}$ but occurs on the same $\tau_{\text{c}} = \omega_{\text{L}}^{-1}$.

3.4.2 Spin-lattice relaxation

As discussed in Sec. 3.3.1.1, a single correlation time τ_{c} leads to a symmetrical $T_1(T^{-1})$ plot, where the activation energy E_{a} can be obtained directly from the slopes of the high- and low-temperature flanks. When a distribution of energy barriers $g(E_{\text{a}})$ is present, the slope of the low-temperature side is reduced and a direct determination of E_{a} is no longer possible, q.v. Fig. 3.16. Usually, the E_{a} obtained from SLR experiments can be linked to the activation energy acquired from measurements of the two-time correlation function F_2 with

$$E_{\text{a}}^{T_1} = \beta_{\text{F2}} E_{\text{a}}^{F_2}, \tag{3.85}$$

where $E_{\text{a}}^{T_1}$ results from the low-temperature slope of the SLR measurements and β_{F2} and $E_{\text{a}}^{F_2}$ are obtained from SAE data. Equation (3.37) connects the SLR rate with the spectral density. Using the log-Gaussian spectral density with the substitution given in Eq. (3.81) this relation is given by [Pri02]

$$\frac{1}{T_1} = C \int_{-\infty}^{\infty} \frac{\tau_{\text{m}} k_{\text{B}} T}{\sqrt{2\pi}\sigma_{\text{E}}} \left(\frac{\exp\left[z - \frac{1}{2}\left(\frac{z k_{\text{B}} T}{\sigma_{\text{E}}}\right)^2\right]}{1 + \omega_{\text{L}}^2 \tau_{\text{m}}^2 e^{2z}} + \frac{4\exp\left[z - \frac{1}{2}\left(\frac{z k_{\text{B}} T}{\sigma_{\text{E}}}\right)^2\right]}{1 + 4\omega_{\text{L}}^2 \tau_{\text{m}}^2 e^{2z}} \right) \mathrm{d}z. \tag{3.86}$$

3.4.3 Susceptibility

A single relaxation time results in ω_{L}^{+1} and ω_{L}^{-1} behaviors on the low- and high- frequency flanks, respectively. With the existence of a DCT the slopes of a log-log representation are flattened and the susceptibility resulting from a log-Gaussian spectral density is given by

$$\chi_{\text{NMR}}'' = C\omega_{\text{L}} \int_{-\infty}^{\infty} \frac{\tau_{\text{m}} k_{\text{B}} T}{\sqrt{2\pi}\sigma_{\text{E}}} \left(\frac{\exp\left[z - \frac{1}{2}\left(\frac{z k_{\text{B}} T}{\sigma_{\text{E}}}\right)^2\right]}{1 + \omega_{\text{L}}^2 \tau_{\text{m}}^2 e^{2z}} + \frac{4\exp\left[z - \frac{1}{2}\left(\frac{z k_{\text{B}} T}{\sigma_{\text{E}}}\right)^2\right]}{1 + 4\omega_{\text{L}}^2 \tau_{\text{m}}^2 e^{2z}} \right) \mathrm{d}z. \tag{3.87}$$

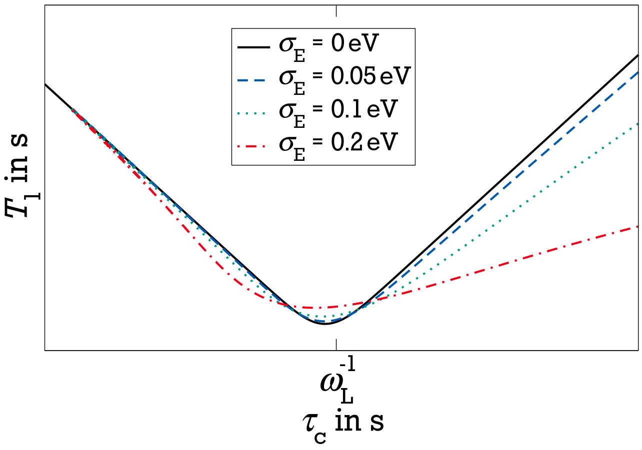

Figure 3.16.: The slope of the high frequency flank (low temperature flank in an Arrhenius graph) reduces and the T_1 minimum rises with increasing width of the DAE.

3.4.4 Correlation function

A DCT leads to a deviation from the mono-exponential correlation function given in Eq. (3.3). Usually, this deviation is analyzed in terms of a stretched-exponential decay of the KWW-form, q.v. Eq. (3.6), but a numerical calculation is possible, if the DCT is known. A log-Gaussian DCT for example leads to the following two-time correlation function

$$F_2(t_\mathrm{m}) = \int_{-\infty}^{\infty} \frac{k_\mathrm{B}T}{\sqrt{2\pi}\sigma_\mathrm{E}} \exp\left[-\tfrac{1}{2}\left(\tfrac{zk_\mathrm{B}T}{\sigma_\mathrm{E}}\right)^2\right] \exp\left(-\frac{t_\mathrm{m}}{\tau_\mathrm{m}e^z}\right) \mathrm{d}z. \tag{3.88}$$

3.4.5 Line shape

Usually, the treatment of the FWHM Σ instead of the second moment becomes even less effective if a DCT exists, resulting in correlation times obtained from LSA deviating significantly from τ_c acquired from other measurements. If the DCT is extremely broad, the situation changes drastically. Now, ions both faster and slower than the inverse coupling constant δ_Q^{-1} can be present at the same temperature. Beginning in the low-temperature limit the distribution of correlation times is completely on the slow side of the transition region (right hand side of Fig. 3.17). The fraction of the distribution on the fast side (left hand side of Fig. 3.17) increases with temperature until the whole distribution is shifted through this region. The fraction representing the part of the fast ions is called weighting factor $W(T)$ and is calculated by integrating the DCT from 0 to the experimental time scale τ^*

$$
\begin{aligned}
W(T) =& \int_0^{\tau^*} G(\tau_\mathrm{c}) \mathrm{d}\tau_\mathrm{c} \\
=& \int_{-\infty}^{\ln\left(\frac{\tau^*}{\tau_0}\right) - \frac{E_\mathrm{m}}{k_\mathrm{B}T}} G(z) \mathrm{d}z \\
=& \int_{-\infty}^{\ln\left(\frac{\tau^*}{\tau_0}\right) - \frac{E_\mathrm{m}}{k_\mathrm{B}T}} \frac{k_\mathrm{B}T}{\sqrt{2\pi}\sigma_\mathrm{E}} \exp\left[-\frac{1}{2}\left(\frac{z k_\mathrm{B} T}{\sigma_\mathrm{E}}\right)^2\right] \mathrm{d}z \\
=& \frac{1}{2} \operatorname{erf}\left(\frac{k_\mathrm{B} T z}{\sqrt{2}\sigma_\mathrm{E}}\right)\Bigg|_{-\infty}^{\ln\left(\frac{\tau^*}{\tau_0}\right) - \frac{E_\mathrm{m}}{k_\mathrm{B}T}} \\
=& \frac{1}{2} + \frac{1}{2} \operatorname{erf}\left(\frac{k_\mathrm{B} T \ln\left(\frac{\tau^*}{\tau_0}\right) - E_\mathrm{m}}{\sqrt{2}\sigma_\mathrm{E}}\right).
\end{aligned}
\tag{3.89}
$$

Here, the experimental time scale is given by $\tau^* = 1/\Sigma^\mathrm{s}_\mathrm{RL} \approx \delta_\mathrm{Q}^{-1}$, where $\Sigma^\mathrm{s}_\mathrm{RL}$ is the rigid-lattice width of the satellite transition and erf denotes the error function. In the transition region $W(T)$ rises from 0 to 1 with increasing temperature, which leads to a so called two-component spectrum. The shape of this two-component spectrum is a superposition of the RLR spectrum and the ENL spectrum. In the case of ^{7}Li studies on glassy samples the first usually consists of two Gaussian distributions and the latter is a Lorentzian, q.v. Sec. 3.3.2. Therefore, the spectrum can be fitted with the following function:

$$
\begin{aligned}
S(x) =& \frac{A_1 \cdot \Sigma}{2\pi\left(\frac{\Sigma^2}{4} + (x-\mu_1)^2\right)} + \frac{A_2 \cdot \exp\left(-\frac{(x-\mu_2)^2}{2\sigma_1^2}\right)}{\sqrt{2\pi}\sigma_1} + \frac{A_3 \cdot \exp\left(-\frac{(x-\mu_3)^2}{2\sigma_2^2}\right)}{\sqrt{2\pi}\sigma_2} \\
=& A \left\{ W(T) \frac{\Sigma_\infty}{2\pi\left(\frac{\Sigma_\infty^2}{4} + (x-\mu_1)^2\right)} \right. \\
& + (1 - W(T)) \left[f^\mathrm{c} \Sigma^\mathrm{c}_\mathrm{RL} \sqrt{\frac{4\ln(2)}{\pi}} \exp\left(-4\ln(2) \frac{(x-\mu_2)^2}{{\Sigma^\mathrm{c}_\mathrm{RL}}^2}\right) \right. \\
& + \left. \left. (1 - f^\mathrm{c}) \Sigma^\mathrm{s}_\mathrm{RL} \sqrt{\frac{4\ln(2)}{\pi}} \exp\left(-4\ln(2) \frac{(x-\mu_3)^2}{{\Sigma^\mathrm{s}_\mathrm{RL}}^2}\right) \right] \right\}.
\end{aligned}
\tag{3.90}
$$

Here, the A_n ($n = 1, 2, 3$) represent the intensities of each peak ($A = A_1 + A_2 + A_3$), the μ_n their centers and σ (Σ) their FWHM[1]. $\Sigma^\mathrm{c}_\mathrm{RL}$ and $\Sigma^\mathrm{s}_\mathrm{RL}$ are the FWHM of the central and satellite transitions of the RLR, respectively, Σ_∞ is the FWHM of the motionally narrowed spectrum, $f^\mathrm{c} = \frac{A_2}{A_2 + A_3}$ is the fraction of the central line in the static spectrum, and $W(T) = \frac{A_1}{A}$ is the

---

[1] The FWHM of a Gaussian distribution is given by $\Sigma = 2\sqrt{2\ln 2}\sigma$

weighting factor defined in Eq. (3.89). Neglecting contributions from ions with $\tau_\mathrm{c} \approx \tau^*$, the temperature-dependent normalized spectral shape $S(\omega, T)$ can also be written as

$$S(\omega, T) = W(T) S_\mathrm{f}(\omega) + [1 - W(T)] S_\mathrm{s}(\omega), \tag{3.91}$$

where $S_\mathrm{f}(\omega)$ and $S_\mathrm{s}(\omega)$ are the normalized line shapes in the limits of fast and slow dynamics, respectively.

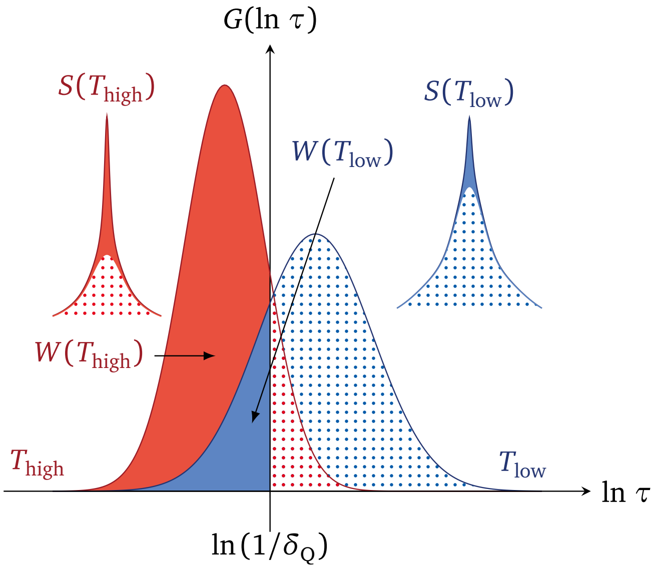

Figure 3.17.: Two-component spectrum resulting from a DCT. With increasing temperature the DCT shifts from right to left. For this reason, the weighting factor rises from 0 to 1. Consequently, the line shape of the spectra S becomes more and more Lorentzian-like while the fraction of the Gaussians decreases.

3.4.6 Diffusion

As discussed in Chap. 2, for a Markov process, the diffusion coefficient in solids can be expressed with the help of the jump distance a and the jump rate Γ of ionic hopping taking place between different sites in the solid matrix. In a first approach, the rate Γ can be expressed as the inverse of the correlation time τ_c leading to

$$D = \frac{a^2}{6\tau_\mathrm{c}} = \frac{a^2}{6} \int_0^\infty \frac{G(\tau_\mathrm{c})}{\tau_\mathrm{c}} \mathrm{d}\tau_\mathrm{c} = \frac{a^2}{6} \left\langle \frac{1}{\tau_\mathrm{c}} \right\rangle. \tag{3.92}$$

Equation (3.92) is consistent with the assumption that the diffusion coefficient depends on a mean hopping rate $\langle \Gamma_\mathrm{r} \rangle = \langle \tau_\Gamma \rangle^{-1} = \langle 1/\tau_\mathrm{c} \rangle$. Equivalent to the discussion for relaxation times in Sec. 3.3.1.1, the relation between the harmonic mean $\langle \tau_\Gamma \rangle$ and the arithmetic mean $\langle \tau \rangle$ reads $\langle \tau_\Gamma \rangle < \langle \tau \rangle$. The temperature dependence of the differing means following from thermally activated jumps and a log-Gaussian DCT as discussed in the next chapter is responsible for the diverse activation energies obtained from different methods.

3.4.7 Mode, arithmetic, and harmonic mean of a log-Gaussian distribution

This chapter mostly follows section 2.2 of [Vog02].

If there is a broad DCT, it is mandatory to consider by which kind of average the mean time constants are determined.

Assuming the NMR frequency after a jump is not correlated to the one before, the NMR two-time correlation function $F_2(t_\mathrm{m}) \propto \langle \omega(0)\omega(t_\mathrm{m})\rangle$ is given by:

$$F_2(t_\mathrm{m}) = \int_0^\infty g(\Gamma_\mathrm{r}) \exp(-\Gamma_\mathrm{r} t_\mathrm{m})\, \mathrm{d}\Gamma_\mathrm{r}. \tag{3.93}$$

The mean correlation time obtained by integration over $F_2(t_\mathrm{m})$ (see Eq. (3.1)) yields:

$$\langle \tau \rangle = \int_0^\infty F_2(t_\mathrm{m})\, \mathrm{d}t_\mathrm{m} = \int_0^\infty g(\Gamma_\mathrm{r})\, \mathrm{d}\Gamma_\mathrm{r} \int_0^\infty \exp(-\Gamma_\mathrm{r} t_\mathrm{m})\, \mathrm{d}t_\mathrm{m} = \int_0^\infty g(\Gamma_\mathrm{r}) \frac{1}{\Gamma_\mathrm{r}}\, \mathrm{d}\Gamma_\mathrm{r} = \left\langle \frac{1}{\Gamma_\mathrm{r}} \right\rangle. \tag{3.94}$$

The result shows, that the time constant in 2D NMR represents an average over times. In contrast, the MSD results from a rate average:

$$\langle r^2(\mathrm{t})\rangle = a^2 t \int_0^\infty g(\Gamma_\mathrm{r}) \Gamma_\mathrm{r}\, \mathrm{d}\Gamma_\mathrm{r} = a^2 t \langle \Gamma_\mathrm{r} \rangle = 6Dt. \tag{3.95}$$

In diffusion experiments, a mean time constant can be defined according to

$$\langle \tau_\Gamma \rangle = \frac{a^2}{6D} = \frac{1}{\langle \Gamma_\mathrm{r} \rangle} = \langle \tau^{-1} \rangle^{-1}. \tag{3.96}$$

Here, the subscript Γ indicates the rate average. For a logarithmic Gaussian distribution of jump rates $g(\ln \Gamma_\mathrm{r})$, which is characterized by a maximum at $\Gamma_\mathrm{r} = \Gamma_\mathrm{m}$ (the logarithmic mean $\langle \tau_\mathrm{lg} \rangle$ or mode) and a width parameter σ_Γ, both mean time constants are given by

$$\langle \tau_\Gamma \rangle = \frac{1}{\langle \Gamma_\mathrm{r} \rangle} = \frac{1}{\int_0^\infty g(\Gamma_\mathrm{r}) \Gamma_\mathrm{r}\, \mathrm{d}\Gamma_\mathrm{r}} = \frac{1}{\int_0^\infty \frac{1}{\sqrt{2\pi}\sigma_\Gamma} \exp\left(-\frac{\ln(\Gamma_\mathrm{r}/\Gamma_\mathrm{m})^2}{2\sigma_\Gamma^2}\right) \mathrm{d}\Gamma_\mathrm{r}} = \frac{1}{\Gamma_\mathrm{m} \exp\left(\frac{\sigma_\Gamma^2}{2}\right)} = \frac{\exp\left(-\frac{\sigma_\Gamma^2}{2}\right)}{\Gamma_\mathrm{m}}, \tag{3.97}$$

$$\langle \tau \rangle = \left\langle \frac{1}{\Gamma_\mathrm{r}} \right\rangle = \int_0^\infty g(\Gamma_\mathrm{r}) \frac{1}{\Gamma_\mathrm{r}}\, \mathrm{d}\Gamma_\mathrm{r} = \int_0^\infty \frac{1}{\sqrt{2\pi}\sigma_\Gamma \Gamma_\mathrm{r}^2} \exp\left(-\frac{\ln(\Gamma_\mathrm{r}/\Gamma_\mathrm{m})^2}{2\sigma_\Gamma^2}\right) \mathrm{d}\Gamma_\mathrm{r} = \frac{\exp\left(\frac{\sigma_\Gamma^2}{2}\right)}{\Gamma_\mathrm{m}}. \tag{3.98}$$

With a similar calculation for a logarithmic Gaussian DCT given by Eq. (3.78) the mean time constants (mode, harmonic mean, arithmetic mean) are given by

$$\langle \tau_\mathrm{lg} \rangle = \tau_\mathrm{m} = \tau_0 \exp\left[E_\mathrm{m}/(k_\mathrm{B} T)\right], \tag{3.99}$$

$$\langle \tau_\Gamma \rangle = \tau_\mathrm{m} \exp\left(-\frac{\sigma_\tau^2}{2}\right), \tag{3.100}$$

$$\langle \tau \rangle = \tau_\mathrm{m} \exp\left(\frac{\sigma_\tau^2}{2}\right). \tag{3.101}$$

Equation (3.100) is also known as *Bässler's law* [Ric90]. The logarithmic difference of $\langle\tau\rangle$ and $\langle\tau_\Gamma\rangle$ depends only on the width parameter σ_τ, which is related to the FWHM of the log-Gaussian distribution $\Sigma = \frac{2\sqrt{2\ln(2)}\sigma_\tau}{\ln(10)} \approx 1.02\sigma_\tau$:

$$\lg\left(\frac{\langle\tau\rangle}{\langle\tau_\Gamma\rangle}\right) = \frac{\sigma_\tau^2}{\ln(10)}. \tag{3.102}$$

Thus, for broad distributions, the mean time constants differ by several orders of magnitude. Figure 3.18a shows the time constants $\langle\tau\rangle$ and $\langle\tau_\Gamma\rangle$ for two selected temperatures together with the correspondent DCTs. The relation of Eq. (3.102) is clearly seen. At 150 K the DCT is very broad, consequently the difference of both time constants is more than twelve orders of magnitude. For high temperatures (here, exemplary shown is the DCT at 400 K) the difference is reduced extremely to less than two decades.

Figure 3.18b shows the temperature dependence of the different mean correlation times. At high temperatures all three mean times are approaching the pre-exponential factor of the correlation time τ_0. With decreasing temperature the means diverge from each other; while τ_m and $\langle\tau\rangle$ are approaching infinity in the limit of 0 K, a purely mathematical analysis of $\langle\tau_\Gamma\rangle$ reveals a maximum at $T = \sigma_\mathrm{E}^2/(E_\mathrm{m}\cdot k_\mathrm{B})$ and then $\langle\tau_\Gamma\rangle$ trends towards zero in the limit of 0 K. As $\langle\tau_\Gamma\rangle$ cannot become lower than τ_0, a phsyical analysis is possbile only for $T \geq \sigma_\mathrm{E}^2/(2E_\mathrm{m}\cdot k_\mathrm{B})$. As mentioned above, usually a Gaussian distribution of activation energies is found in glassy solids. Therefore, the temperature dependence of the mean correlation times, especially τ_m and $\langle\tau_\Gamma\rangle$, presented in Fig. 3.18b, will be used to explain the different E_a found by using different methods.

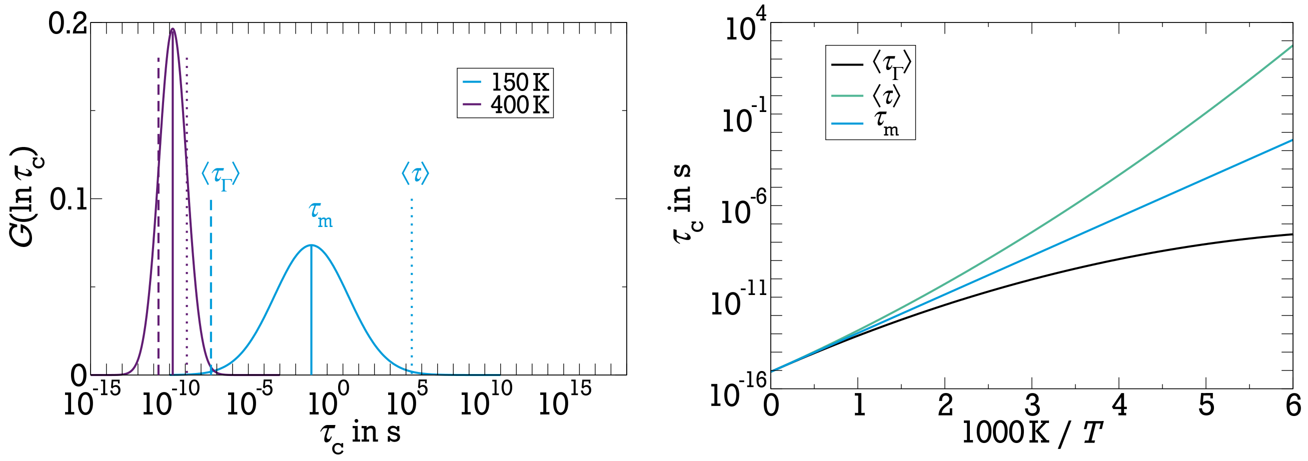

(a) (b)

Figure 3.18.: (a) Time constants of the DCT of two selected temperatures. The dotted lines represent $\langle\tau\rangle$ while $\langle\tau_\Gamma\rangle$ corresponds to the dashed lines. At 150 K the time constants differ more than twelve orders of magnitude. At 400 K the difference is reduced to approximately two orders of magnitude. (b) Comparison of the temperature dependence of the different time constants of the DCT. The data corresponds to an pre-exponential factor $\tau_0 = 8.4\times10^{-16}$ s and a DAE with E_m = 0.49 eV and σ_E = 0.08 eV. More details are given in the text.

4 Setup and samples

In the first part of this chapter the setups used for the ^{7}Li NMR experiments are introduced. At the beginning the general concepts of an NMR spectrometer are described. Then, specifications of the spectrometers used are given in detail, starting with the homogeneous field, followed by the FC, and concluding with the static field gradient spectrometers. The second part focuses on the investigated samples. Here, the preparation is discussed only briefly. For a more extensive description of the different preparation techniques, the reader is referred to the literature given in that section.

4.1 NMR spectrometers

As described in Sec. 3.3, various NMR methods are utilized in this thesis. Mostly ^{7}Li NMR in static fields is performed, additionally FC and diffusometry measurements are carried out. A sketch of the principle modus operandi of an NMR spectrometer is shown in Fig. 4.1. All spectrometers are operated by the Darmstadt Magnetic Resonance Instrument(ation) Software (DAMARIS) [Gäd07], which was developed at the TU Darmstadt to control home-built NMR spectrometers. With a front end based on the Python scripting language, DAMARIS offers the possibility to create and easily modify pulse programs. After the execution of a program, the script is translated into job-files which are used by the back end to control the pulse control card (SpinCore Pulsblaster PB24-100-32k). The frequency generator provokes the reference frequency ω_{R} which is amplified to high power RF pulses as stated by the pulse sequence defined in the script. The RF pulses are passed through a duplexer into the probe where also the NMR signal is induced. This signal (ω_{L}) is amplified and transported into the demodulator where it is split into two identical signals and mixed with ω_{R} and the 90° phase shifted ω_{R}. This quadrature detection enables a transformation into the rotating coordinate frame (RCF) and is done to distinguish between negative and positive frequencies relative to the carrier frequency which is possible as the real and imaginary part are accessible. Low pass filters ensure that only the differential component of the resulting signals (signals in the kHz regime) reach the analog to digital converter (ADC) card (Spectrum GmbH) which is synchronized with the pulse card. The results of the ADC card are written in result-files which then are utilized by the front end with the help of DAMARIS result scripts. A Programmed Test Sources (PTS) frequency synthesizer is used to generate the reference frequency ω_{R}. The nomenclature PTS #n is used in this work, where #n is a number that gives the upper limit of the working range of the PTS (in MHz). The phasing of the PTS is controlled by the DAMARIS software as part of the phase cycling listed in Appx. D. More information about DAMARIS can be found in the official online documentation [DAM] and more details about the functionality of an NMR spectrometer is given in [Fuk81].

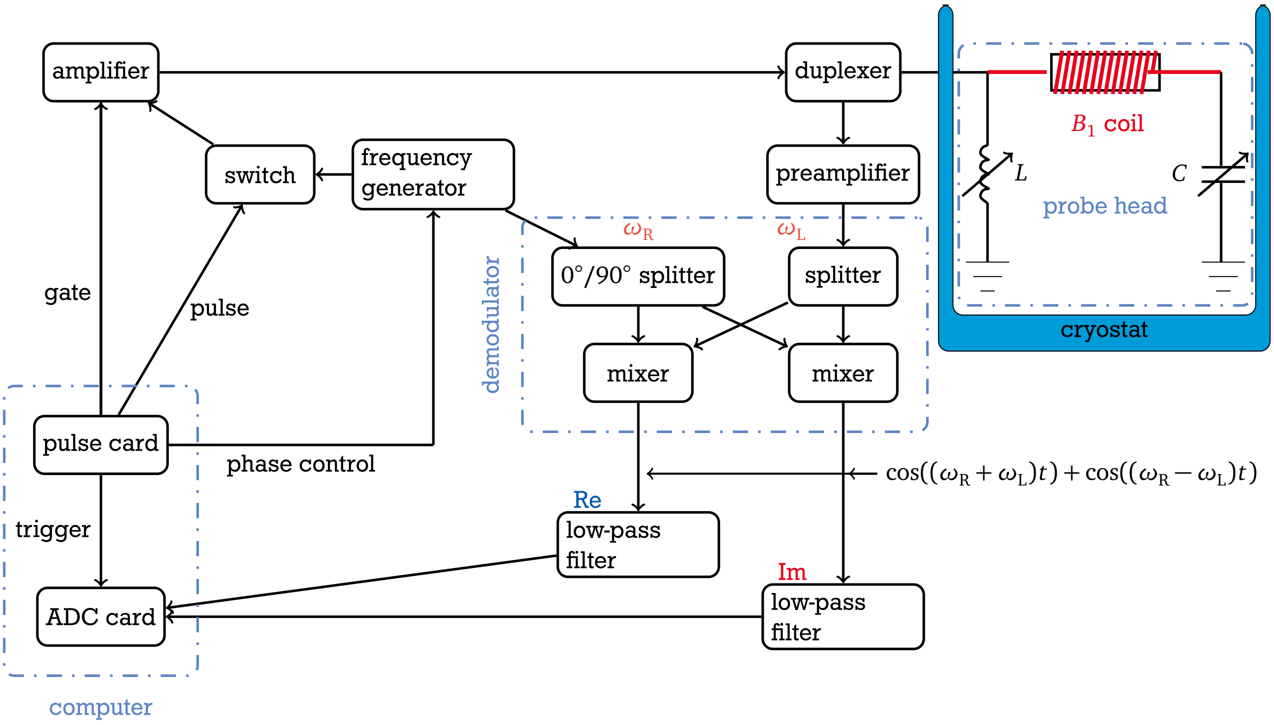

Figure 4.1.: Sketch of an FT-NMR spectrometer; see text for more details. Modified from [Pet13].

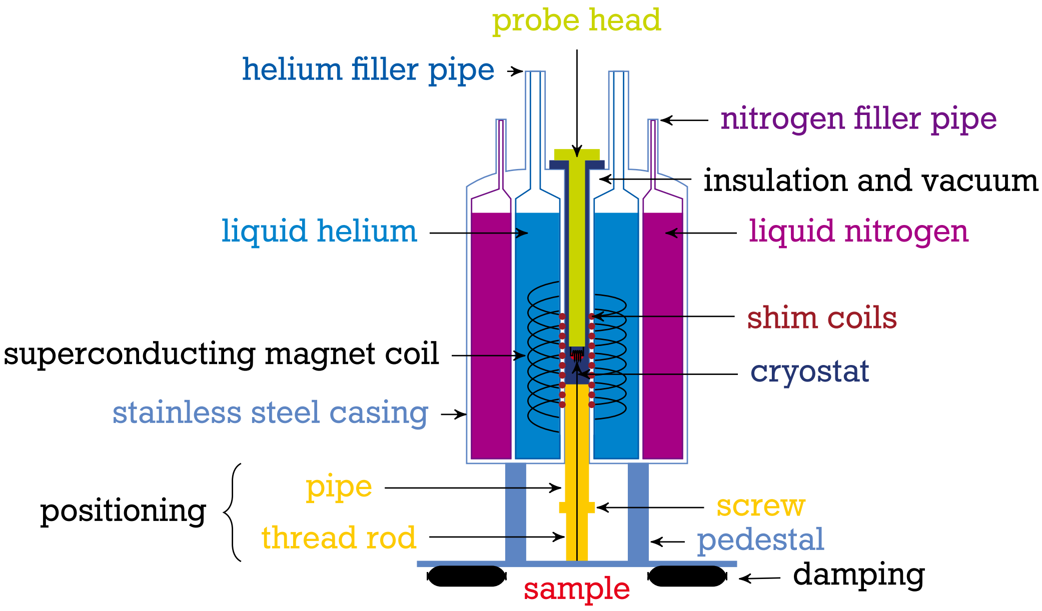

Figure 4.2.: Sketch of an NMR magnet. The damping is only used with SFG spectrometers for reducing signal losses due to non-diffusion induced position shifts, e.g., vibrations of the magnet.

Alltogether, six different spectrometers have been used for the measurements, three static field spectrometers named *Berta*, *Birgit*, and *Schering*, two FC spectrometers (FC1 and FC2), and an SFG spectrometer called *Magnex*.

4.1.1 Static field spectrometers

Schering and *Birgit* feature fixed-field superconducting magnets with 7.15 T and 8.46 T, respectively, which corresponds to ^{7}Li Larmor frequencies of $2\pi \times 118.25$ MHz and $2\pi \times 139.91$ MHz. During the time span of data aquisition for this work, the superconducting magnet of *Berta* has been de- and re-powered. Therefore, measurements at 1.64 T, 3.80 T, and 4.61 T, corresponding to ^{7}Li Larmor frequencies of $2\pi \times 27.07$ MHz, $2\pi \times 62.93$ MHz, and $2\pi \times 76.24$ MHz, have been carried out at this spectrometer. From this point on, the used frequencies of the static field spectrometers will be given as $2\pi \times 27$ MHz, $2\pi \times 63$ MHz, $2\pi \times 76$ MHz, $2\pi \times 118$ MHz, and $2\pi \times 140$ MHz.

Berta and *Schering* are equipped with nitrogen flow cryostats which are evaporing liquid nitrogen. A stable temperature is reached by heating the N_2 gas. An Oxford Instruments cryostat and an Oxford Instruments Integrated Temperature Controller (ITC)-502 are used with *Berta* while *Schering* uses a Konti cryostat from CryoVac which is controlled by a CryoVac TIC 304 MA control unit. A diaphragm pump draws liquid nitrogen through a capillary in the cryostat. A heat exchanger with an electrical heater is used to adjust the temperature. Assuming a sufficient temperature equilibration before the start of a measurement the maximal thermal drift of the cryostats was $\Delta T \leq 0.5$ K. A PT-1000 (*Schering*) or PT-100 (*Berta*) resistance thermocouple near the B_1 coil measured the sample temperature using four-terminal sensing to eliminate the contribution of the supply line to the total resistance. Cryostat equipped spectrometers allow measurements in the temperature range from 77 K to 420 K when liquid nitrogen is used for cooling. Because of possible heat induced changes of some samples and too slow lithium ion dynamics at very low temperatures, measurements have usually been restricted to the temperature range between 100 K and 400 K. At *Birgit*, the sample temperature was stabilized by a tempered gas flow, which allowed measurements in the range between 180 K and 400 K. Compressed air has been used for temperatures at and above 300 K while at temperatures below 300 K cold nitrogen gas adjusted the temperature.

Berta and *Schering* are equipped with PTS 310 frequency synthesizers and American Microwave Technology (AMT) pulse amplifiers. The pulse amplifiers are capable of delivering 1 kW (model M3425) or 2 kW (model M3445) of power. The former is used with *Schering* while *Berta* is equipped with the latter. *Birgit* is equipped with a PTS 500 frequency synthesizer and a 1 kW Kalmus 166UP amplifier. With this setups a 90° pulse length Δ_p between 2.0 µs and 2.5 µs was used. Usually, the pulse length has been kept constant for the measurements of each sample at any given spectrometer. This was achieved by an adjustable attenuation of the strength of the B_1 field. The 90° pulse length Δ_p has been determined using an FID experiment by varying the pulse length. The length of pulses other than 90° have been calculated as corresponding fractions or multiples of the 90° pulse length. This kind of pulse length measurement was done after every change of the temperature.

Home-built probe heads have been used for conducting the experiments. They consist of a series connection of the B_1-coil and an adjustable cylindrical capacitor with a shiftable dielectric medium for tuning and a parallel connected coil or adjustable capacitor for matching the resonant circuit. A more detailed description of some of the home-built probe heads are given in [Haa11, Kre10].

4.1.2 Field-cycling spectrometers

Both FC spectrometers are home-built devices. FC1 consists of several coils [Lip01], allowing it to use a very broad magnetic field range between 0.1 µT and 2 T, depending on the used current source (see below). The main coil can be run permanently with 700 A, corresponding to a magnetic field of 0.8 T, but short-term currents of 2000 A are also possible. It can be driven with one of two available current sources; the home-built source [Lip04] runs with 1000 A and 50 V. The commercial source (Siemens Healthcare) is a high-power source which is able to deliver 2000 A and 2000 V. With this setup switching times of 3 ms and 8 ms are reachable for switching down and up, respectively [Kre16]. More details about FC1 can be found in the literature [Kre16, Fuj14]. For the ^{7}Li measurements evolution fields from 20 kHz to 12 MHz and a detection field of 31 MHz have been used, corresponding to evolution fields between about 1 mT and 0.73 T and a detection field of 1.88 T. FC1 is equipped with an AMT M3525 pulse amplifier using up to 1 kW power to deliver the B_1 field.

FC2 is a dipole magnet where the field is created by an iron yoke which is magnetized by two coils as shown in Fig. 4.3a. It runs with a commercially available current source which yields a maximum magnetic field of 0.66 T at a current of 320 A and a switching time of 2 ms can be achieved [Ple09]. Advantages of FC2 are the reduced energy consumption and significantly lower operating costs and it is much less demanding relating to cooling and protection. On the other hand, the available frequency range is restricted and the SNR is lower in comparison to FC1.

Temperature control of both FC spectrometers was realized by a tempered gas flow system described above and an Eurotherm 2216e which can communicate with DAMARIS through an RS-232 connector. Therefore, it is possible to monitor and store the temperature during the measurement, q.v. Fig. 4.3b.

4.1.3 Static field gradient spectrometers

While Helmholtz coils are used to create a homogeneous magnetic field, q.v. Fig. 4.4a, the magnets of SFG spectrometers are equipped with superconducting coils in anti-Helmholtz configuration, also known as (AKA) gradient-field Maxwell coils [You05], as shown in Fig. 4.4b. With this kind of configuration, field gradients of up to 180 T/m are achieveable. The SFG magnets are placed on top of several air filled hoses to damp vibrations of the building. Additional vibrations of the turbopump are eliminated by swithing it off after reaching a suitable pressure ($p \leq 10^{-5}$) and using an ion gatter pump (IGP) to sustain the vacuum. An AMT 3445 amplifier and a PTS 310 were used to achieve pulse lengths of less than 2 µs at *Magnex* (1.4 µs ≤ P90 ≤

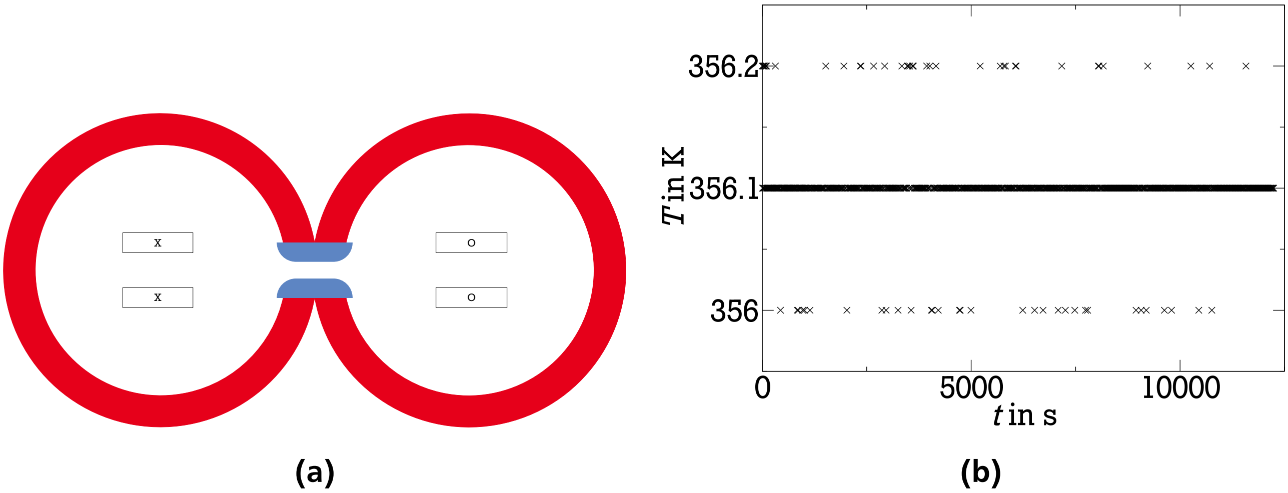

Figure 4.3.: (a) Cross section of FC2. The magnetic field is created by the coils (marked as "X" and "O") and amplified by the iron yoke (red). The sample is placed between the pole pieces (blue). Modified from [Ple09]. (b) Temperature protocol during a measurement at FC1, proofing the stability of ±0.1 K.

1.9 µs) in order to excite a layer as thick as possible for increasing the SNR. SFG measurements were carried out at a Larmor frequency of $\omega_L = 2\pi \times 63\,\text{MHz}$ to use the same frequency as is now available at *Berta*. This Larmor frequency corresponds to a gradient of 73 T/m at *Magnex*, q.v. Fig. 4.5. Temperature control was done with the cryostat-method described above. *Magnex* has a Konti cryostat (CryoVac) and temperature control is realized with a LakeShore Cryotronics 335 controller.

Table 4.1.: Devices used with the various spectrometers.

spectrometer	amplifier	PTS	cryostat	temperature controller
Berta	AMT 3445	310	Oxford Nitrogen	Oxford ITC-502
Birgit	Kalmus 166UP	500		Eurotherm 2216e
Schering	AMT 3425	310	CryoVac Konti	CryoVac TIC 304 MA
FC1	AMT M3525	310		Eurotherm 2216e
FC2	Tomco BT00500-Beta	310		Eurotherm 2216e
Magnex	AMT 3445	310	CryoVac Konti	LakeShore 335

4.2 Samples

In this section the investigated samples are shortly introduced and the respective preparation technique will be briefly discussed. All samples consist of fine powder which is placed in flame sealed, thin wall NMR sample tubes with an outer diameter of 5 mm. The length has been restricted to 3 cm to ensure a proper placement inside the cryostats. More details about the samples are presented in the chapters where the respective results are discussed and in Appx. B.

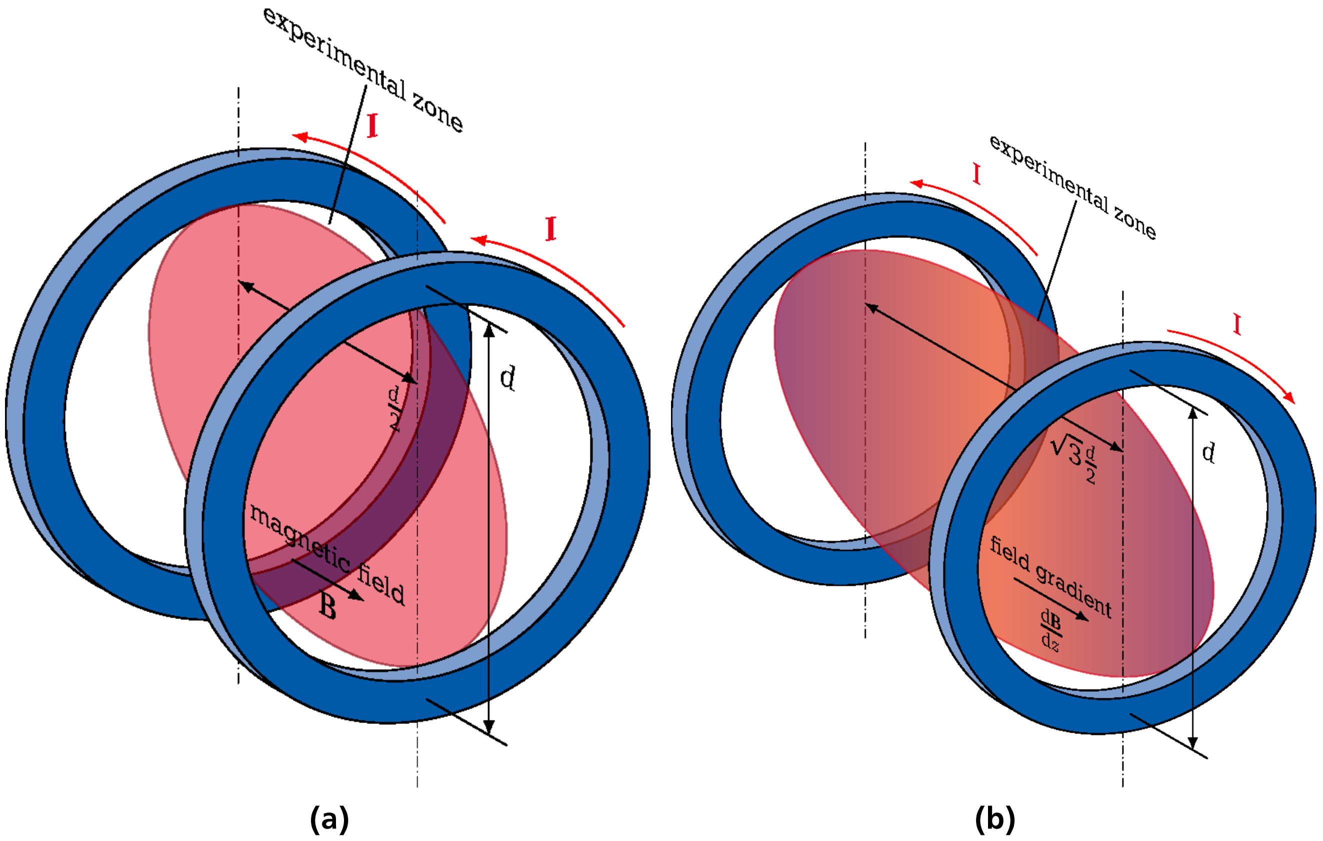

Figure 4.4.: (a) Helmholtz coils create a homogeneous magnetic field. Here, the currents of both coils are parallel. (b) To obtain a field gradient, Maxwell coils with anti-parallel currents are used.

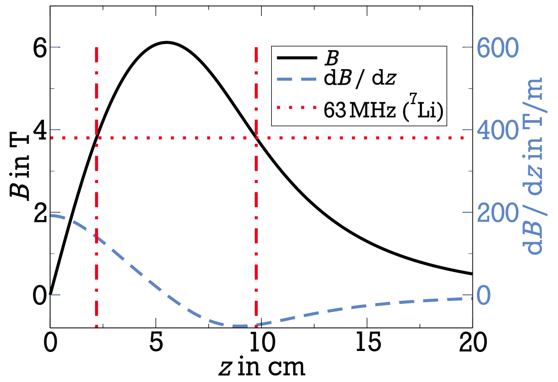

Figure 4.5.: Gradient profile of *Magnex*. The horizontal dotted line at 3.8 T gives the field of the Larmor frequency used during the ^{7}Li diffusion measurements. The intersections with the solid black line mark the positions in z-direction where these fields are available. The intersections of these dash-dotted lines with the dashed black line give the resulting field gradients at these positions. The measurements were carried out at the smaller gradient (73 T/m at 9.8 cm) using a higher SNR. The position at 2.2 cm belongs to a higher gradient of 140 T/m, which could used to measure smaller diffusion coefficients but also decreases the SNR. This profile is anti-symmetric to the center of the z-axis. Modified from [Gäd09].

4.2.1 $Li_{10}SnP_2S_{12}$

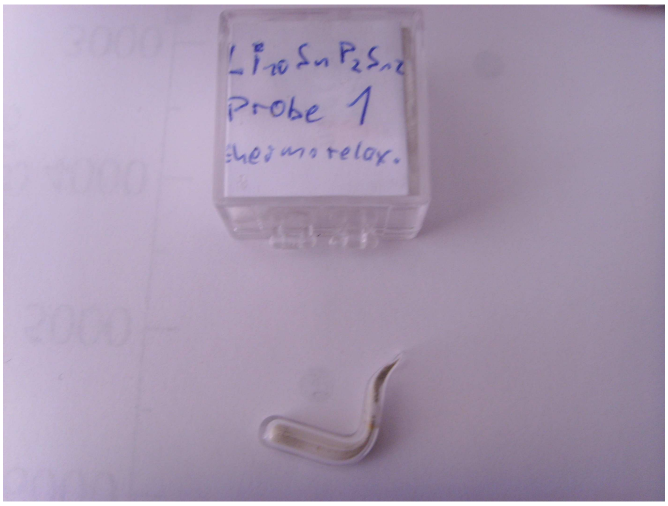

Figure 4.6.: Sample $Li_{10}SnP_2S_{12}$.

Appropriate amounts of Li_4SnS_4, Li_2S, and P_2S_5 were weighed and thoroughly mixed to obtain $Li_{10}SnP_2S_{12}$. Crystallization of the mixture was done in an evacuated, sealed quarz tube at 600° C and purity of the mixture was determined with X-ray diffraction revealing that $Li_{10}SnP_2S_{12}$ shows tetragonal symmetry according to the space group $P4_2/nmc$ (no. 137), q.v. Fig. 4.7. The preparation was done in the group of Prof. Roling (Marburg University) and a more precise documentation can be found in [Bro13]. Measurements on this samples conducted prior to this work resulted in a change of relaxation, see Chap. 5 for more details.

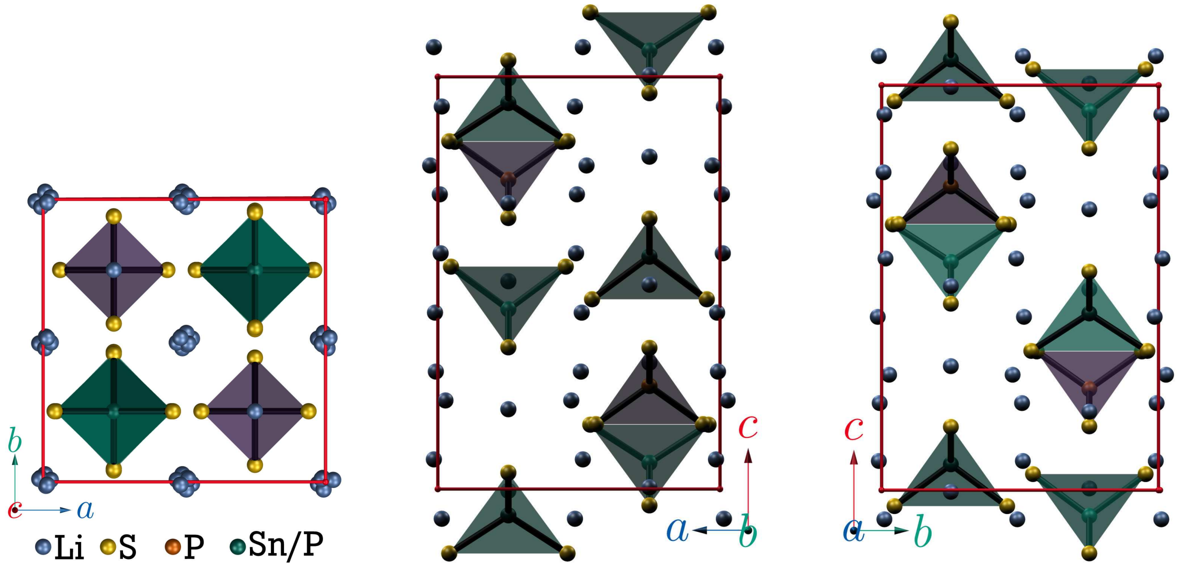

Figure 4.7.: Crystal structure of $Li_{10}SnP_2S_{12}$. Modified from [Bro13].

4.2.2 SiOC

Figure 4.8.: Lithiated SiOC.

In a first step, electrode pellets of 10 mm diameter, composed of 85 wt% SiOC active material, 5 wt% Carbon Black, and 10 wt% polyvinylidene fluoride binder were prepared and pressed onto a thin copper foil. Lithiated silicon oxycarbide (SiOC) was obtained by placing vacuum dried pellets in a two-electrode swagelok-type half-cell, which was discharged to a potential of 0.0005 V (E vs. Li^+/Li). Delithiated SiOC was prepared the same way with subsequent current reversion until a potential of 2.5 V was reached. Finally, the cells were disassembled under Ar-atmosphere and the pellets were hand-ground to fine powders which were filled into the sample tubes [Kas14]. The preparation was done by Jan Kaspar (TU Darmstadt) and more details about the samples are given in Chap. 6.

4.2.3 Li_2S–B_2S_3

Figure 4.9.: Samples $0.7Li_2S$–$0.3B_2S_3$ (right) and $0.7Li_2S$–$0.27B_2S_3$–$0.03B_2O_3$ (left).

To obtain the $0.7Li_2S$-$0.3[xB_2S_3$-$(1-x)B_2O_3]$ samples (mol-%), stoichiometric amounts of Li_2S, B_2S_3, and B_2O_3 have been weighed and thoroughly mixed. The preparation of high-purity vitrous B_2S_3 is described elsewhere [Mar90]. The mechanical milling of the mixture was conducted using a high energy planetary ball mill by the group of Prof. Steve Martin at the Iowa State University. More details about the samples are given in Chap. 7.

Figure 4.10.: Samples $0.7Li_2S$–$0.3P_2S_5$-gc (left) and $0.7Li_2S$–$0.3P_2S_5$-g (right).

The $0.7Li_2S$–$0.3P_2S_5$ glass (mol-%) was prepared by the mechanical milling method. Li_2S and P_2S_5 crystalline powders were used as starting materials. The mixture of these materials was mechanically milled at ambient temperature by a planetary ball mill. The glass was heated at 240° C for 2 h to obtain the $0.7Li_2S$–$0.3P_2S_5$ glass-ceramic [Miz05] which consists of a $Li_7P_3S_{11}$ crystal showing triclinic symmetry as depicted in Fig. 4.11. Preparation of this samples was also done by the group of Prof. Steve Martin (Iowa State University). More details about the samples are given in Chap. 8.

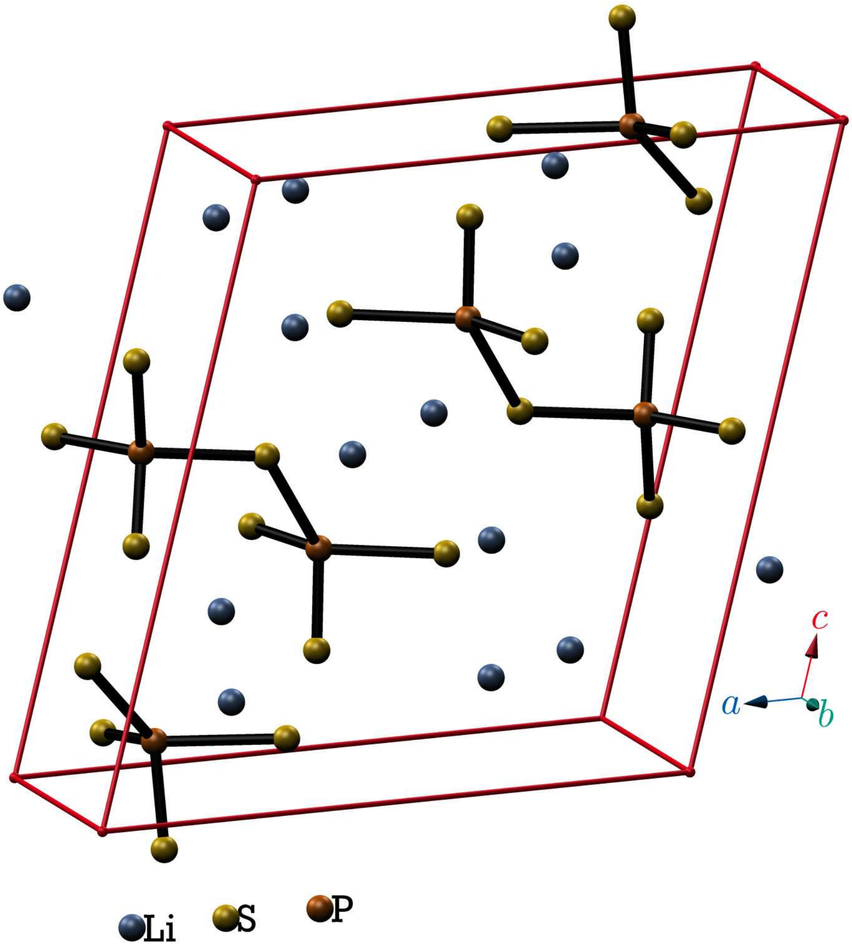

Figure 4.11.: The elementary cell of the $Li_7P_3S_{11}$ crystal contains two $Li_7P_3S_{11}$ units, which both consists of a PS_4 tetrahedron and a P_2S_7 di-tetrahedron.

5 $Li_{10}SnP_2S_{12}$

In 2011, Kamaya et al. reported a new Li superionic conductor $Li_{10}GeP_2S_{12}$, which, at that time, had the highest conductivity ever achieved among solid lithium electrolytes of 12 mS/cm at room temperature [Kam11]. This conductivity is comparable to or even higher than the conductivities of organic liquid electrolytes used in lithium-ion batteries. $Li_{10}GeP_2S_{12}$ has a tetragonal structure and Kamaya et al. proposed a 1-dimensional diffusion pathway along the c-axis. However, molecular dynamics (MD) simulations on this system also revealed significant Li hopping in the ab-plane [Mo12, Ada12], which circumvents the typical problem of 1D ion conductors of easily blocked transport channels by structural defects [Mal10]. A 3D isotropic diffusion was also found in ^{7}Li PFG measurements [Kuh13]. $Li_{10}GeP_2S_{12}$ also showed outstanding electrochemical performance in Li-ion batteries [Kam11], but the scarce deposits and high cost of germanium are drawbacks for the application in batteries. Therefore, Bron et al. synthesized the thiostannate analog of $Li_{10}GeP_2S_{12}$, namely $Li_{10}SnP_2S_{12}$, which leads to a large reduction of the raw material costs and has a similar conductivity at room temperature [Bro13]. Impedance spectroscopy and ^{7}Li PFG measurements have shown that several members of the tetragonal $Li_{10\pm1}MP_2S_{12}$ family (M = Ge, Si, Sn) show similar structures and diffusivity parameters [Ong13, Kuh14].

To get more insight into lithium ion dynamics in the solid electrolyte $Li_{10}SnP_2S_{12}$, several ^{7}Li NMR techniques have been performed and their results are presented and discussed in this chapter. It should be mentioned, that the very sample investigated in this work has been used for measurements before, where a significant change in the ^{7}Li SLR behavior has been observed after heating the sample to 410 K [Sch15, Koh15]. These changes have mainly affected the T_1 minimum. Its value nearly doubled and its position shifted to a slightly higher temperature. The combination of excellent SNR and ultra-fast relaxation proved to be helpful to establish various ^{7}Li NMR techniques. Therefore, this sample was used despite the heat induced changes in SLR mentioned above, but to prevent further changes, measurements above 380 K have been omitted. The $Li_{10}SnP_2S_{12}$ sample has been sealed in an L-shaped NMR tube, q.v. Fig. 4.6. Because of this, the probe head normally used with the spectrometer *Berta* could not be employed for the measurements, as it requires cylindrical tubes. Instead, the probe head usually working with the SFG spectrometer *Magnex* has been used for all experiments discussed in this chapter, except of the FC measurements. It turned out that the desired resonance frequency of $2\pi \times 63$ MHz is outside of the tuning range of this probe head at very low temperatures. As ^{7}Li diffusion measurements are not possible due to very short spin-spin relaxation times T_2 in this temperature range, adjustments of the probe head have been omitted and the experiments have been limited to $150\,\mathrm{K} \leq T \leq 380\,\mathrm{K}$.

5.1 Spin-lattice relaxation

SLR measurements have been performed to get insight into the fast dynamics in the high temperature regime. While Fig. 5.1a shows the magnetization recovery at the investigated temperatures for the $\mathrm{Li_{10}SnP_2S_{12}}$ sample, the resulting β_{T1} and $\langle T_1 \rangle$ values obtained from fitting the recovery curves with Eq. (3.34) and using (3.35), respectively, are presented in Fig. 5.1b. The stretching factor β_{T1}, as seen in the top of Fig. 5.1b, shows a typical behavior with values approaching $\beta_{\mathrm{T1}} = 1$ at high and low temperatures, indicating that the relaxation tends to be dominated by a common relaxation time rather than by a distribution of relaxation times in the rigid-lattice and extreme narrowing regimes. This changes in the MN regime as the value of β_{T1} decreases and reaches a minimum of approximately 0.65 at 200 K.

The resulting $\langle T_1 \rangle$ is shown at the bottom of Fig. 5.1b. The T_1 minimum of 84 ms is reached at 347 K. The low temperature slope of $\langle T_1 \rangle$ is given by an activation energy of $E_\mathrm{a} = 0.10\,\mathrm{eV}$. As the activation energy obtained from the low temperature side of the T_1 minimum is given by Eq. (3.85) the low value of this activation energy can be a result of an actual low activation energy of the lithium jump dominated diffusion process or of a broad distribution of correlation times, resulting in a highly stretched correlation function. The T_1 minimum can also be used to estimate the anisotropy parameter δ_Q with the help of Eq. (3.37). Assuming a single correlation time, the result of the square bracket in this Eq. becomes $\sqrt{2}/\omega_\mathrm{L}$ and δ_Q is calculated with

$$\delta_\mathrm{Q} = \sqrt{\frac{25 \cdot \omega_\mathrm{L}}{\sqrt{2} \cdot 8 \cdot T_{1\mathrm{min}}}} \approx 102\,\mathrm{kHz}. \tag{5.1}$$

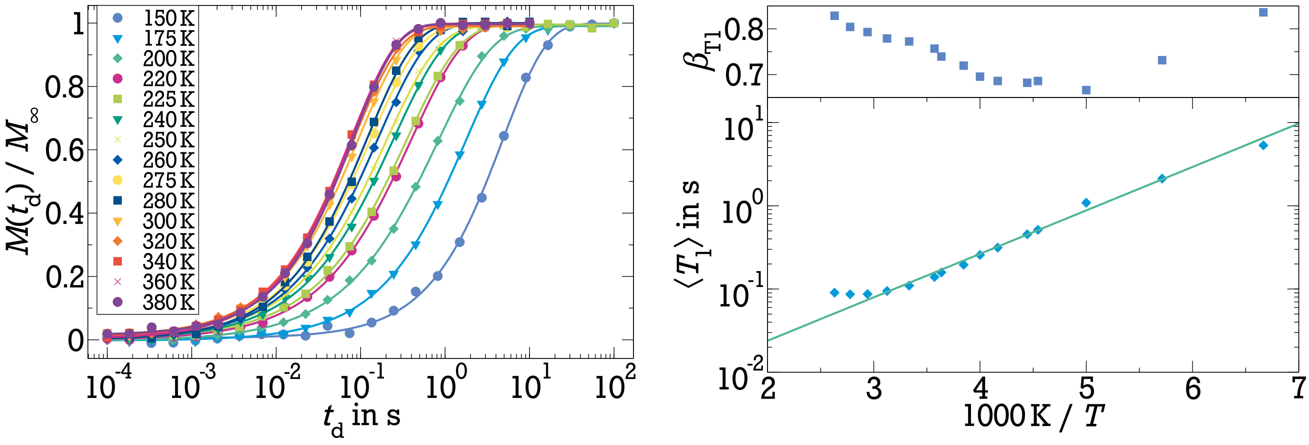

(a) **(b)**

Figure 5.1.: The saturation recovery buildup curves of $\mathrm{Li_{10}SnP_2S_{12}}$ (a) and the resulting SLR times $\langle T_1 \rangle$ and stretching factors β_{T1} (b) at various temperatures. The solid line is a fit to the Arrhenius equation (2.10) with an activation energy of $E_\mathrm{a} = 0.10\,\mathrm{eV}$. The T_1 minimum of 84 ms is reached at 347 K.

Field-cycling relaxometry was used to extend the accessible dynamics to longer correlation times. The results are presented in Fig. 5.2a. Here, frequency dependent SLR times are shown for various temperatures. FC measurements can be analyzed in many ways. First, they can be used to investigate the T_1 minimum for various Larmor frequencies, which is shown in the inset of Fig. 5.2a for a small selection of the used frequencies. The condition $\omega_\mathrm{L}\tau_\mathrm{c} \approx 1$ can then be used to determine correlation times τ_c in the ns to ms regime. The corresponding results are presented in Fig. 5.15b, together with correlation times obtained from other measurements discussed below.

Second, the relaxation rate at low frequencies can be used to calculate diffusion coefficients. So far this proved to be successful especially for protons in liquids and polymers [Mei13]. While there is indeed a linear dependence of R_1 on the square root of ω_L for $90 \leq \sqrt{\omega_\mathrm{L}/\mathrm{Hz}} \leq 500$ in $\mathrm{Li_{10}SnP_2S_{12}}$, q.v. Fig. 5.2b, the resulting difussivity of $D \approx 10^{-5}\,\mathrm{m^2/s}$ from using Eq. (3.43) is several orders of magnitude too high for lithium self-diffusion in solids at ambient temperature, q.v. Sec. 5.6. Considering that in this frequency regime the quadrupolar frequency ω_Q exceeds ω_L this finding is not surprising. Quantitative analysis of SLR data in this regime would require a more precise method than first order perturbation theory which goes beyond the scope of this thesis.

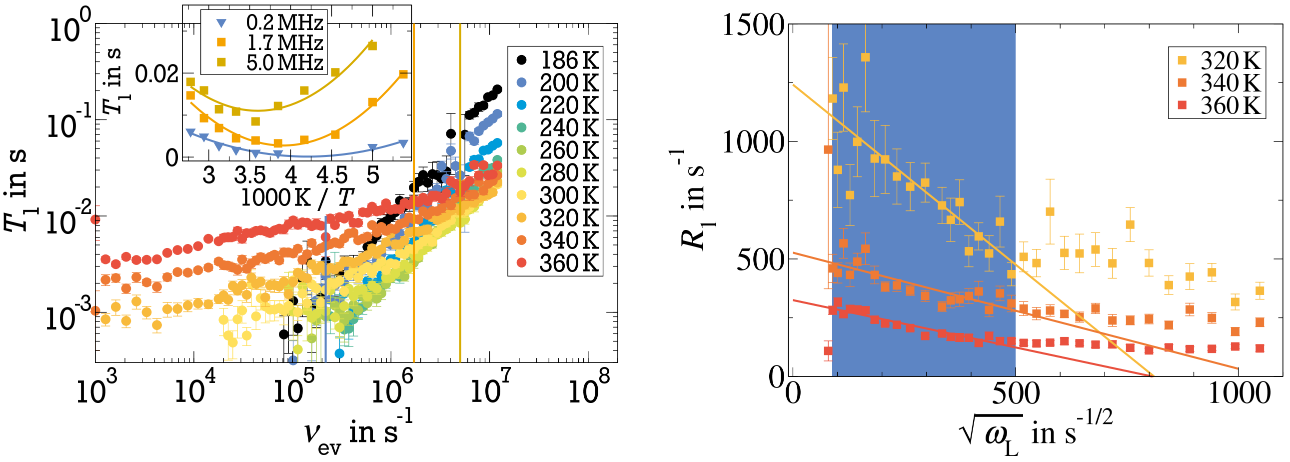

(a) (b)

Figure 5.2.: Field-cycling measurements of $\mathrm{Li_{10}SnP_2S_{12}}$. (a) SLR times as a function of frequency. The inset shows the T_1 minima for some selected frequencies represented by the solid vertical lines. (b) SLR rate of $\mathrm{Li_{10}SnP_2S_{12}}$. The solid lines are fits to Eq. (3.43); only data in the range $90 \leq \sqrt{\omega_\mathrm{L}/\mathrm{Hz}} \leq 500$ have been considered for the fit.

Last, the frequency dependent measurements are used to calculate the so called NMR susceptibility $\chi''_\mathrm{NMR} = \omega_\mathrm{L} \cdot R_1$. χ''_NMR of $\mathrm{Li_{10}SnP_2S_{12}}$ is shown in Fig. 5.3a. Here, also the data from the high frequency measurements discussed above are included on the very right. This kind of representation is helpful for recognizing the shape of both the spectral density and the distribution of correlation times. Three factors are important for the analysis of χ''_NMR, the position of the maximum, where $\omega \cdot \tau_\mathrm{c} \approx 1$ holds and the slope of the regimes $\omega \cdot \tau_\mathrm{c} \ll 1$ and $\omega \cdot \tau_\mathrm{c} \gg 1$. For example, the BPP model with just a single correlation time (δ-distribution) predicts a slope of +1 and -1, respectively. Therefore, the slopes of χ''_{NMR} have been determined as an average over the whole frequency range for each temperature (see inset in Fig. 5.3a) to observe where the slopes changes from a negative to a positive sign. Obviously, at about 250 K the maximum of χ''_{NMR} is in the middle of the accessible frequency regime and the low and high temperature limits of the slope are ca. -0.3 and 0.8, respectively. If frequency-temperature superposition (FTS) holds, it is possible to create a master curve by shifting the measurements of the individual temperatures along the frequency axis. FTS follows from the fluctuation-dissipation theorem (FDT) under the assumption that the form of the spectral density of a process in the frequency domain is the same as in the temperature domain. This form of analysis has also been successfully used for polymers [Hof12].

As there is no measurement at 250 K, the 260 K curve has been used to determine the $\omega_{\mathrm{L}} \cdot \tau_{\mathrm{c}} = 1$ condition and the other curves where shifted to create the master curve shown in Fig. 5.3b. The maximum of the susceptibility and the shift factors have been utilized to calculate correlation times for all temperatures which agree with the correlation times obtained from the T_1 minima as shown in Fig. 5.15b. A closer look at the master curve reveals that a power law with exponent 0.8 describes the data on the low frequency side very well, while an exponent of -0.3 agrees with the data on the high frequency flank. This indicates a distinct deviation from the BPP model and reveals an asymmetric frequency dependence, which eliminates symmetric spectral densities like the Cole-Cole, log-Gaussian or log-Lorentzian form. A general asymmetric spectral density is the Havriliak-Negami (HN) spectral density $J_{\mathrm{HN}}(\omega_{\mathrm{L}}, \tau_{\mathrm{c}})$ given by Eq. (3.73). Analyzing the master curve with Eq. (3.73) reveals that the distribution of correlation times is caused by a HN spectral density with $\alpha = 0.77$ and $\beta = 0.38$. The obtained anisotropy parameter $\delta_{\mathrm{Q}} = 116\,\mathrm{kHz}$ is slightly higher than the one calculated with the help of the T_1 minimum. This is expected, because for the latter a BPP spectral density has been used, which reduces the value of a calculated δ_{Q}.

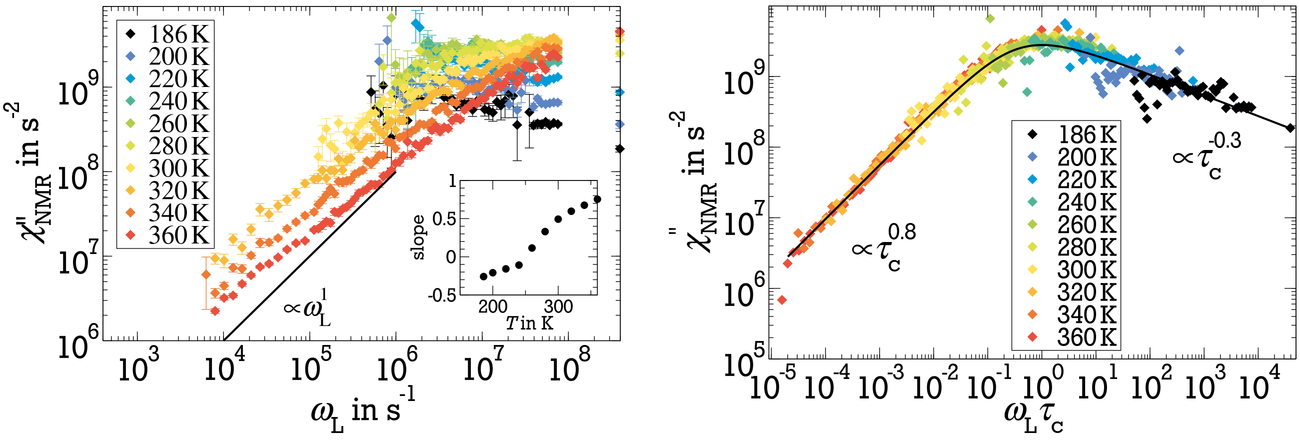

(a) **(b)**

Figure 5.3.: (a) Susceptibility χ''_{NMR} of $\mathrm{Li_{10}SnP_2S_{12}}$. The BPP model predicts a slope of 1 in the low-frequency limit which is not quite reached at high temperatures as shown in the inset. (b) The master curve obtained from the FC data reveals that the distribution of correlation times can be described with a HN spectral density. The resulting susceptibility is given by the solid line.

The *exorcycle* described in Sec. 3.3.1.2 was used to determine the spin-spin relaxation time T_2 for various temperatures. Exemplary, the measurements at 150 K and 380 K are shown in Figs. 5.4a and 5.4b, respectively. At 380 K it is clearly seen that the individual measurements of SE_+ and SE_-, as well as the sum $SE_+ + SE_-$ show an influence of quadrupolar transients for interpulse delays t_p up to about 1 ms while for the *exorcycle* SE_+-SE_- these transients are eliminated and an exponential decay with T_2 as the decay time is seen. For very short interpulse delays ($t_p <$ 20-40 µs; the exact value varies with temperature) a deviation from the exponential decay is observable.

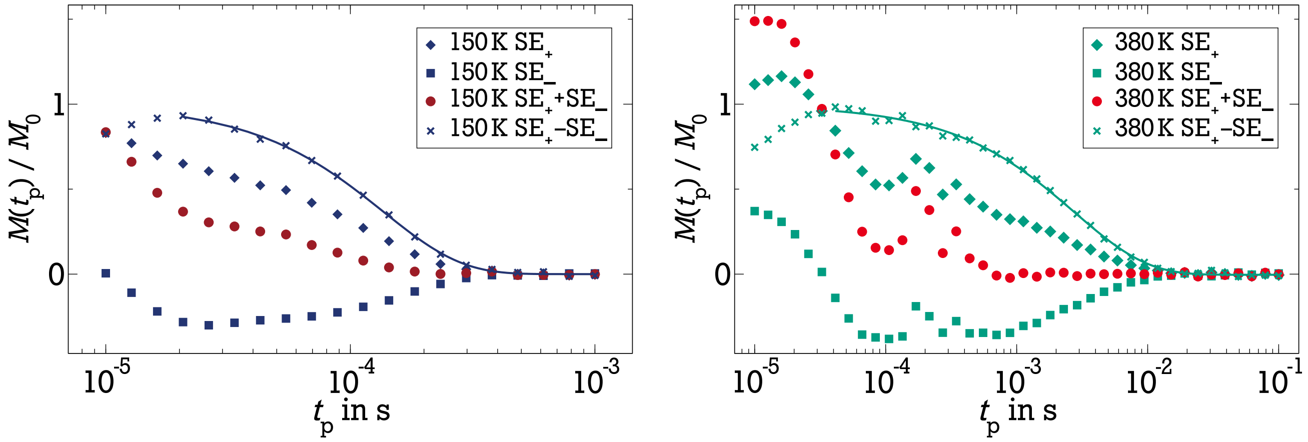

(a) **(b)**

Figure 5.4.: (a) Spin-echo measurements at 150 K and (b) at 380 K. For the *exorcycle* SE_+-SE_- the decay is free of quadrupolar transients and the spin-spin relaxation time T_2 can be measured. The sum of both measurements $SE_+ + SE_-$ shows that transients are present for interpulse delays t_p up to about 1 ms at 380 K.

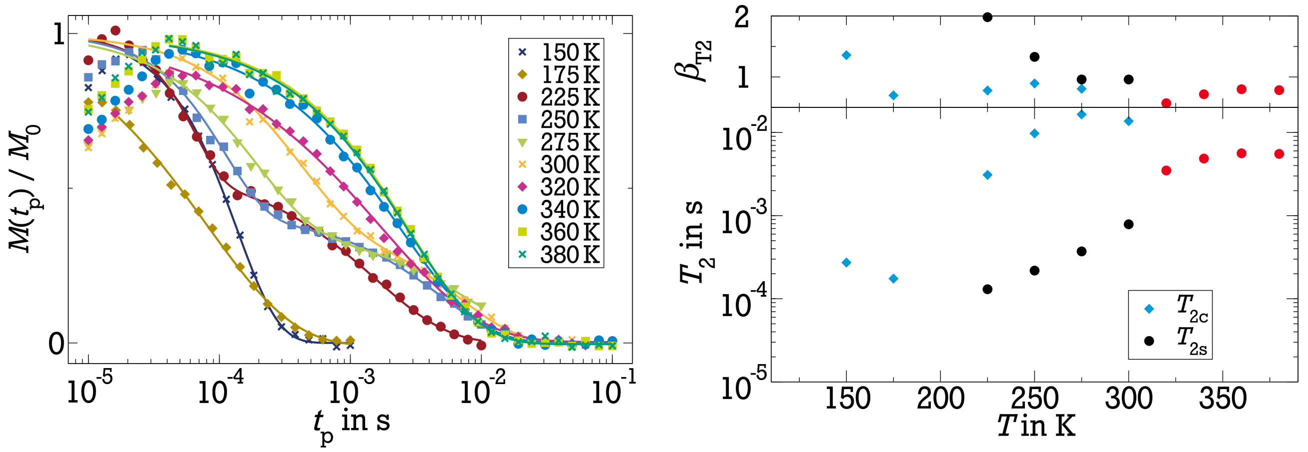

(a) **(b)**

Figure 5.5.: (a) The measured *exorcycles* show a single decay for high and low temperatures but a two-step decay for temperatures in between. (b) The resulting T_2 times.

Figure 5.5a shows all measured *exorcycles* and the resulting spin-spin relaxation times T_2 are presented in Fig. 5.5b. For high and low temperatures, a single T_2 can be used to describe the data. For intermediate temperatures, a two step decay indicates two different relaxation times. A single exponential decay at high temperatures is expected, as at short τ_c, i.e., at temperatures above the T_1 minimum, all contributions of the spectral densities are nearly equal. Therefore, all relaxation mechanisms should have the same relaxation time in this temperature regime, q.v. Fig. 3.6. However, T_2 is significantly smaller than T_1 above 350 K (see Fig. 5.8b), which could be due to the tetragonal crystalline structure of $Li_{10}SnP_2S_{12}$, preventing the ion dynamics from completely averaging out the quadrupolar interaction; see the next section for more details. For the same reason T_2 is not increasing with temperature, but rather constant above the T_1 minimum. Below the T_1 minimum the spin-spin relaxation of the central transition differs from that of the satellite transitions, resulting in two distinct relaxation times as shown in Fig. 5.5b. The T_2 of the satellite transition is continuously decreasing with increasing correlation time until the condition $\tau_c = \omega_Q^{-1}$ is reached and then becomes constant for longer correlation times. On the other hand, T_2 of the central transition first increases with correlation time, reaches a maximum for $\tau_c = \omega_Q^{-1}$, then decreases again and becomes constant for $\tau_c \geq \omega_L/\omega_Q^2$. At very low temperatures, T_2 of the satellite transition is supposed to be as low as $\omega_Q^{-1} \approx 10^{-6}$ s, which is too short to be measured with the pulse sequence used. Therefore, the single relaxation decay measured at temperatures below 200 K is given by the T_2 of the central transition, which is in the order of $\omega_L/\omega_Q^2 \approx 10^{-4}$ s in the slow motion regime, q.v. Fig. 3.6.

5.3 Line-shape analysis

Information about Li ion dynamics in the micro-second regime can be obtained from LSA of spectra. The solid echo pulse sequence was used to measure the spectra shown in Fig. 5.6. The spectrum at 150 K, which consists of two Gaussian lines with clearly distinctive FWHMs, is a typical lithium spectrum of an amorphous solid in the rigid-lattice regime (RLR). Both central and satellite transitions are narrowing in a small temperature window, when the temperature is increased. It takes roughly 75 K for the central transition to evolve from the RLR to the extreme narrowing limit (ENL) as shown in Fig. 5.7b. Even though there are no measurements in the RLR the Hendrickson and Bray (HB) fit gives a reasonable result for the FWHM Σ in the RLR. It agrees with other measurements that have been done on this very sample [Koh15] and other samples of identical composition [Kuh14]. On the other hand, the correlation time obtained from Σ deviates significantly from the correlation times calculated with the help of the FC measurements described above, see Fig. 5.15b. A better agreement of the Σ correlation time with the SLR correlation times would require either a more than one decade lower FWHM in the RLR or a shift of the line narrowing to higher temperatures. The former is unlikely, as the FWHM in the RLR is given by the density of the lithium ions and typically results in linewidths of a few kHz for ^{7}Li. As the FWHM at 175 K has already nearly reached the ENL, the latter is not very likely either and in earlier measurements of the linewidth the MN is shifted to lower rather than to higher temperatures [Koh15, Kuh14]. Therefore, the discrepancy between the SLR and LSA correlation times originates from the fact that most models assume a single correlation time when trying to convert the linewidth to a correlation time and ignore the fact that for most amorphous solids distributions of correlation times exist.

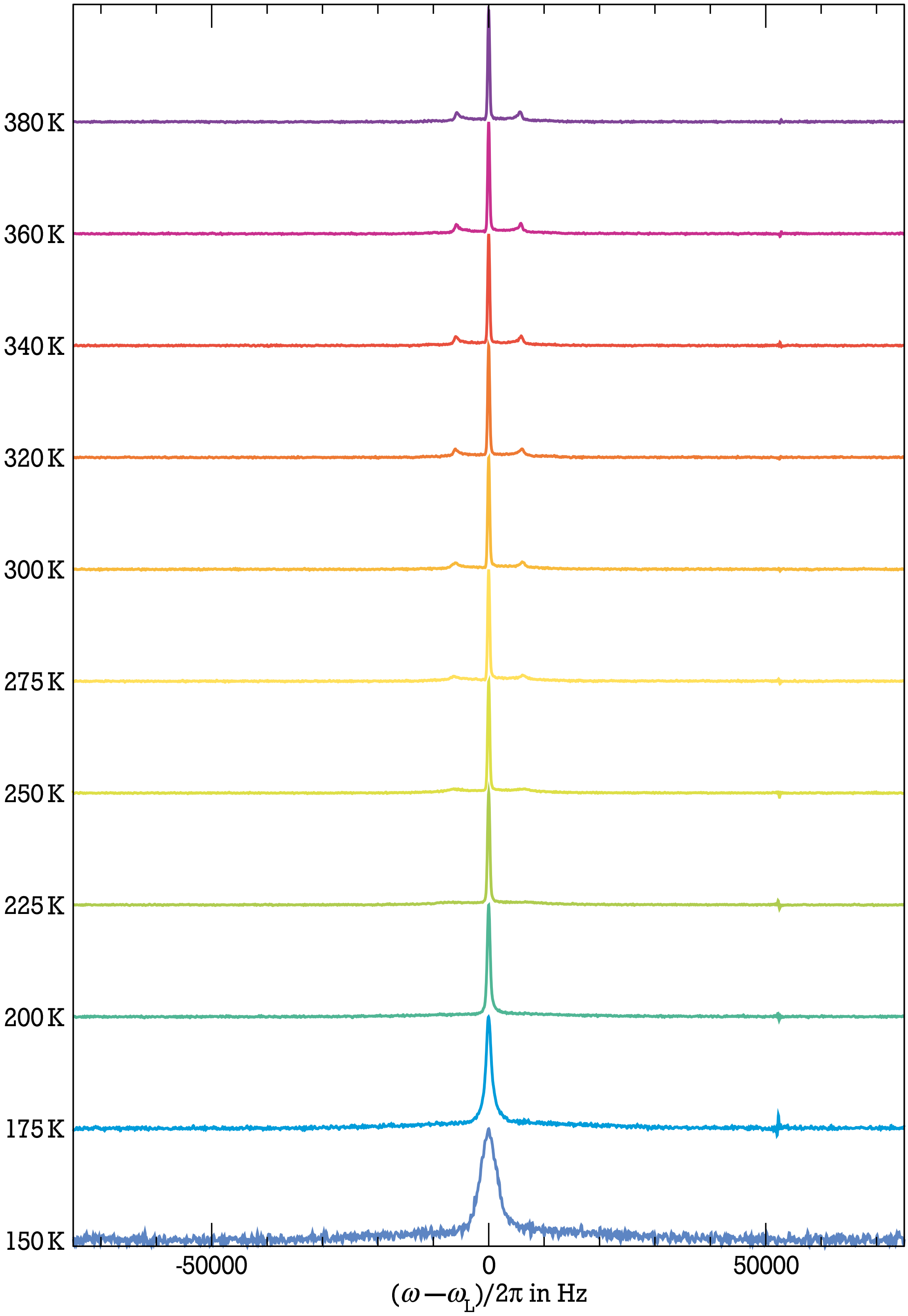

Figure 5.6.: Spectra of $Li_{10}SnP_2S_{12}$. In this representation the extremely broad satellite transition is only visible for the 150 K spectrum. The Pake pattern starts to appear at 225 K and becomes more and more pronounced with increasing temperature.

So far the analysis has been focused on the central line. A closer inspection of the satellite line reveals the transformation of a Gaussian line in the RLR to a line with shoulders and horns in the ENL. This kind of spectrum is also known as Pake spectrum [Pak48] and arises because of the tetragonal crystal structure of $Li_{10}SnP_2S_{12}$ with finite distinct lithium ion sites, preventing the ion dynamics from completely averaging out the quadrupolar interaction. The powder pattern is first observed at 225 K and becomes more prominent with increasing temperature. A zoom of the Pake spectrum at 380 K is shown in Fig. 5.7a. Throughout the whole temperature range the Pake spectrum is described by an asymmetry parameter $\eta_Q = 0$, which reflects the tetragonal symmetry, and an anisotropy paramter of the averaged solid spectrum $\bar{\delta}_Q = 2\pi \times 12\,\text{kHz} \approx 75\,\text{kHz}$. This is smaller than the δ_Q obtained from the T_1 minimum and the δ_Q calculated with the help of the HN spectral density, explaining the absence of the Pake spectrum at low temperatures.

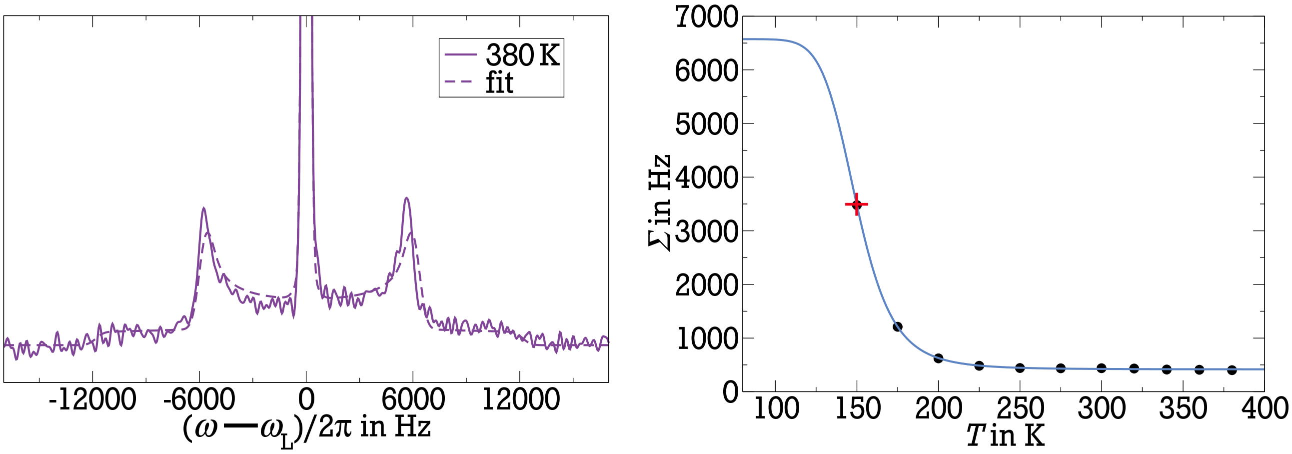

(a) **(b)**

Figure 5.7.: (a) Zoom of the spectrum at 380 K. The dashed line is a fit with a Gaussian central line and a Pake satellite line. (b) FWHM Σ of the central line of $Li_{10}SnP_2S_{12}$. The red cross marks the infliction point of the fit as obtained from the Hendrickson-Bray function (solid line).

5.4 Two-time correlation functions

Two-time correlation functions have been measured to analyze the dynamics in the slow motion regime up to a few seconds. First, the results of the sin-sin correlation function F_2^{SS} obtained by the Jeener-Broekaert sequence [Jee67] are discussed in Sec. 5.4.1. Then, the ^{7}Li cos-cos correlation function F_2^{CC} acquired by a newly developed pulse sequence [Sto15] is evaluated in Sec. 5.4.2.

5.4.1 Spin alignment

The results of the spin-alignment measurements are shown in Fig. 5.8a. Between 150 K and 175 K the decay of the signal shifts to shorter mixing times with increasing temperature, indicating an speedup in the local Li-ion dynamics. Starting with the 200 K measurement, the decay shifts to longer mixing times, indicating that the signal loss is no longer due to lithium ion dynamics but rather to an other process. This coincides with the fact, that at higher temperatures the tetragonal symmetry of the crystalline powder with its many equivalent Li-ion sites prevents the quadrupolar interaction to be averaged out, resulting in the Pake spectrum described above and preventing a further loss in a two-time correlation function. At temperatures above 250 K the decay starts to shift to shorter mixing times, again. This signal loss is generated by the SLR of the spin alignment state, the time constant of which is called T_{1Q}. The obtained T_{1Q} are presented in Fig. 5.8b, together with the T_1 already shown above. The ratio of T_1/T_{1Q} is near the expected value of 25/8 [Böh07b] at lower temperatures and increases with temperature due to the occurance of the T_1 minimum in this temperature range. Under the described circumstances, correlation times can only be determined up to 175 K. The results are in good agreement with the correlation times obtained by SLR analysis, expanding the dynamical range to lower temperatures as shown in Fig. 5.15b.

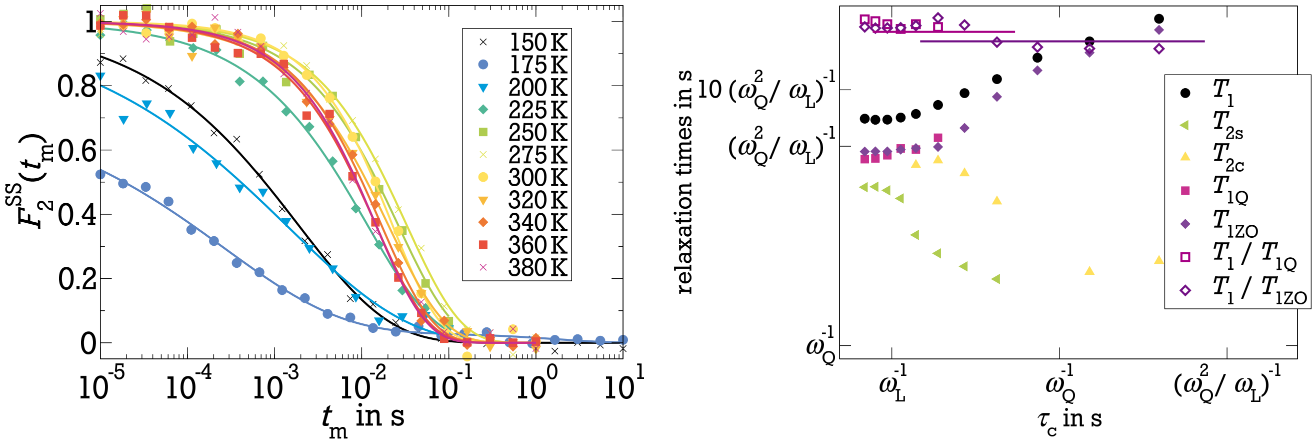

(a) **(b)**

Figure 5.8.: (a) F_2^{SS} of Li$_{10}$SnP$_2$S$_{12}$. A signal loss due to lithium dynamics is observed only up to 175 K. At higher temperatures the anisotropic solid-state spectrum prevents a faster decay resulting in a shift of the curves to longer mixing times t_m. At temperatures above 250 K the decay is most probably given by T_{1Q}. (b) Relaxation times of Li$_{10}$SnP$_2$S$_{12}$. T_{1Q} and T_{1ZO} have been obtained from the F_2^{SS} and F_2^{CC} decays, respectively. The expected ratios of T_1/T_{1Q} = 25/8 and T_1/T_{1O} = 17/8 in the high frequency regimes [Böh07b] are shown as horizontal lines. The transformation from T to τ_c on the x-axis has been done using $\omega_Q = 116$ kHz and the Arrhenius equation (2.10) with a pre-exponential factor $\tau_0 = 6.1 \times 10^{-14}$ s and an activation energy $E_m = 0.31$ eV, according to the solid line in Fig. 5.15b.

5.4.2 Zeeman order

Figure 5.9a shows the measurements of the two-time correlation function of the Zeeman order F_2^{CC}. Up to 225 K the curves can be described by two stretched exponential decays, the second one being caused by the SLR. Specifically, the decay time and stretching factor of the second decay of F_2^{CC} and of the SLR measurements are identical. The first decay of F_2^{CC} shows two characteristic features. First, the plateau value F_∞^{CC} increases linearly with temperature, as shown in the inset of Fig. 5.9a. Second, the first decay of F_2^{CC} continuously shifts to longer mixing times with increasing temperature. In general, the inverse of the plateau value F_∞^{CC} is given by the number of equally populated inequivalent crystalline sites. At 150 K F_∞^{CC} is 0.22, indicating four to five inequivalent Li sites in the tetragonal structure of $\mathrm{Li_{10}SnP_2S_{12}}$, which agrees with the four Li sites reported in the literature [Bro13]. On the other hand, an $F_\infty^{\mathrm{CC}} \approx 0.4$ is expected for the decay of F_2^{CC} due to a non-vanishing contribution of the central line, q.v. (3.56). The observed monotonical increase of F_∞^{CC} for higher temperatures is usually ascribed to "progressive motional phase averaging" [Ber05, Sto15]. The reason for the shift to longer mixing times is the same as for the shift of the SAE described above. For temperatures $T \geq 250\,\mathrm{K}$, the remaining single decay is not exactly given by the SLR but can rather be desribed by a temperature independent KWW function, which is given by the relaxation time of the mixed Zeeman and octupolar state $T_{1\mathrm{ZO}} = 34\,\mathrm{ms}$ and a stretching factor $\beta_{\mathrm{T1ZO}} = 0.66$, q.v. Eq. (3.57). $T_{1\mathrm{ZO}}$ and the other determined relaxation times are shown in Fig. 5.8b. While the general frequency dependence of the relaxation times is similar to that predicted from the BPP model, compare Figs. 3.6 and 5.8b, the exact position of minima, maxima and plateaus are shifted in x and y direction. Similar to the F_2^{SS} measurements, a two-time correlation could be measured up to 175 K, while at higher temperatures the transition from correlation to relaxation decay prevents an analysis of the lithium ion dynamics.

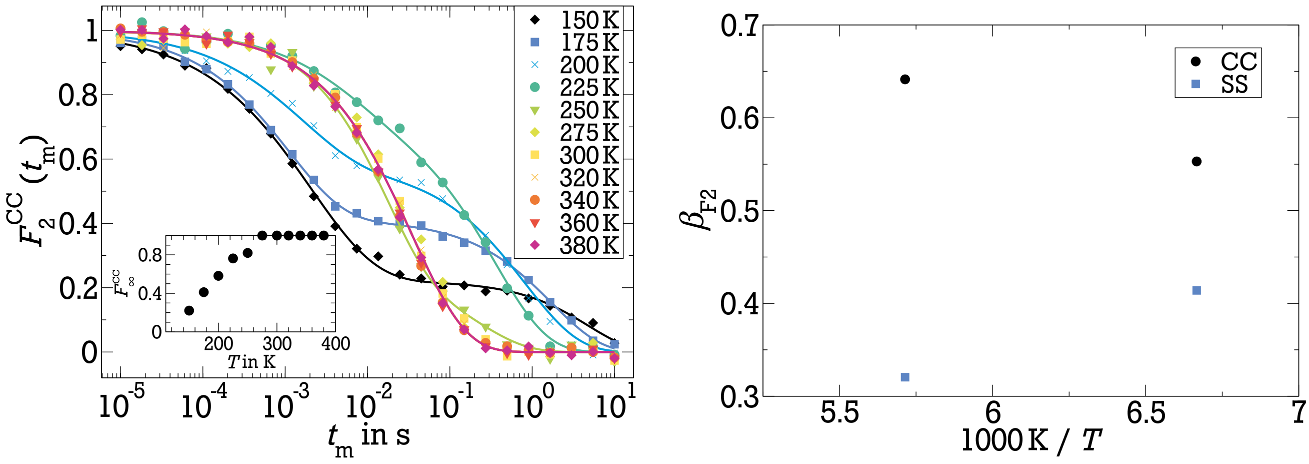

(a) (b)

Figure 5.9.: (a) F_2^{CC} of $\mathrm{Li_{10}SnP_2S_{12}}$. A signal loss due to a two-time correlation is only given up to 175 K. At higher temperatures the anisotropic solid-state spectrum prevents a faster decay resulting in a shift of the curves to longer mixing times t_m. At temperatures above 250 K the decay is temperature independent and characterized by a relaxation time $T_{1\mathrm{ZO}} = 0.03\,\mathrm{s}$ and a stretching parameter $\beta_{\mathrm{T1ZO}} = 0.66$. The plateau value F_∞^{CC} increases linearly with the temperature up to 275 K (see insert). (b) The stretching factors of the F_2^{CC} and F_2^{SS} measurements. Only the temperatures that could be connected to a correlation loss have been considered in this graph.

As shown in Sec. 5.1.1, FC measurements revealed that a distribution of correlation times exists in $Li_{10}SnP_2S_{12}$. To investigate the origin of this DCT, three- and four-time correlation functions have been measured at 175 K as seen in Fig. 5.10. The three-time correlation function F_3 has been recorded for three different first mixing times t_{m1} using a sufficiently short second mixing time of $t_{m2} = 10\,\mu s$. The data have been scaled to an initial value of $F_3(t_{m3} = 0) = 1$. Analysis of F_3 can be done in two different ways. First, comparing the complete three-time correlation function F_3 with predictions calculated for the limiting cases of purely heterogeneous and homogeneous dynamics from F_2^{SS} by using Eqs. (3.61) and (3.62). Second, determining the heterogeneous limit of F_3 from the individual KWW parameters τ_2 and β_{F2} of F_2^{SS} with Eqs. (3.64) and (3.65) and comparing the results with the KWW fit of F_3. The former method is presented in Fig. 5.10a, where predictands for F_3 in the heterogeneous limit are represented by the dashed lines, which agree quite well with the obtained data. The latter technique also reveals the heterogeneity of F_3 as presented in Fig. 5.11. Here, the parameters β_{F3} and τ_3 are given as a function of the filter efficiency (FE) in Figs. 5.11a and 5.11b, respectively. The heterogeneous limits are shown as solid lines in these figures, proving the heterogeneity of F_3.

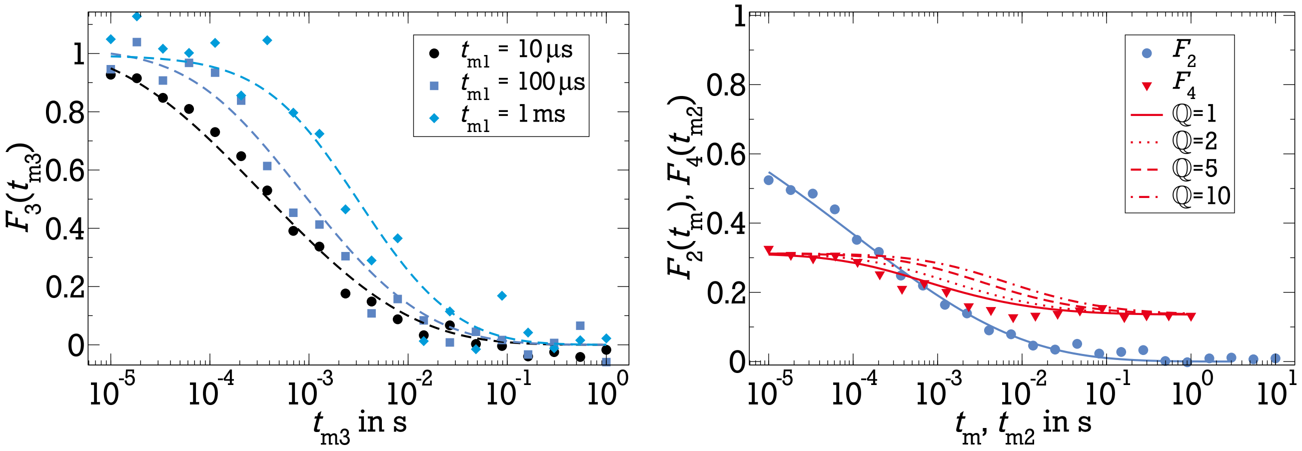

(a) **(b)**

Figure 5.10.: Multi-time correlation functions of $Li_{10}SnP_2S_{12}$. (a) The measured F_3 shows a heterogeneous character of lithium ion dynamics. Equation (3.62) has been used to describe the data. (b) The measured F_4 reveal that a rate memory parameter of $\mathbb{Q} \approx 1$ describes the heterogeneity very well, indicating that the lithium ions explore different parts of the rate distribution with nearly every jump.

To investigate on which time scale the Li ions exchange their correlation times, the four-time correlation function F_4 is presented in Fig. 5.10b. Analysis of F_4 with Eq. (3.66) shows that the set of data is best described with a rate memory parameter $\mathbb{Q} = 1$, indicating that the Li ions change their rate with every single jump.

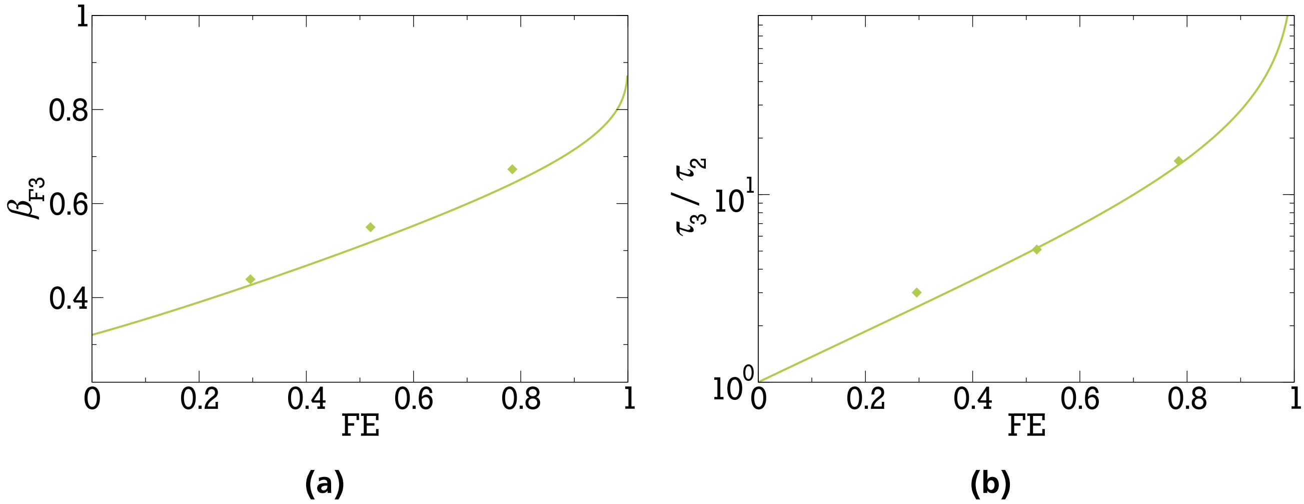

(a) (b)

Figure 5.11.: Heterogeneity of $Li_{10}SnP_2S_{12}$. The solid lines represents the theoretical values of β_{F3} and τ_3 in the heterogeneous limit due to Eq. (3.64) (a) and Eq. (3.65) (b), respectively.

5.6 Diffusion

So far, only the local dynamics of $Li_{10}SnP_2S_{12}$ has been discussed. To study the long-range transport of the Li ions, diffusion coefficients have been measured using the SFG method. Figure 5.12a shows the measurement at 360 K. Interestingly, the data for $t_p = 100\,\mu s$ and $t_p = 215\,\mu s$ are almost identical, in contradiction to the expected t_p-dependent T_2 decay given in Eq. (3.68). Consequently, the global fit of all data is insufficient in explaining the results, especially for the $t_p = 100\,\mu s$ curve. A t_p-dependent measurement at fixed $t_m = 20\,\mu s$ exhibits an oscillation with a frequency of $\omega \approx 36\,kHz$ which is overlaying the exponential decay, q.v. Fig. 5.12b. This oscillation is caused by the remaining anisotropic quadrupolar coupling as described in Sec. 5.3. As a result, the signal height is nearly the same for $t_p = 100\,\mu s$ and $t_p = 215\,\mu s$, explaining the almost identical curves observed in the t_m-dependent measurements for these two values of t_p.

In a first approach to obtain temperature-dependent diffusion coefficients the data have been rescaled to an initial value of $D(t_m = 0) = 1$, as seen in Fig. 5.13. But neither a global fit of all data, shown in Fig. 5.13a, nor a fit of only the two curves with the longest t_p, presented in Fig. 5.13b, sufficiently describes the measurements. Before considering a t_p-dependent diffusion coefficient, which would indicate a dependence on the lengthscale of the measurement, $(\gamma g t_p)^{-1}$, or a non-3D diffusion, t_m-dependent STE measurements have been performed in a homogeneous magnetic field. The normed measurement is presented in Fig. 5.14a. The gradient of the spectrometer Berta is $g \approx 0\,T/m$. Therefore, all non-diffusion induced signal losses are identified by a STE measurement at Berta. These non-diffusion induced decays are then eliminated from the SFG measurements by dividing the gradient data by the curves obtained in the homogeneous field. The result is shown in Fig. 5.14b, revealing a t_p independent diffusion coefficient. This procedure has been repeated for the other temperatures and the resulting diffusion coefficients are presented in Fig. 5.15a, indicating that the long-range transport of the Li

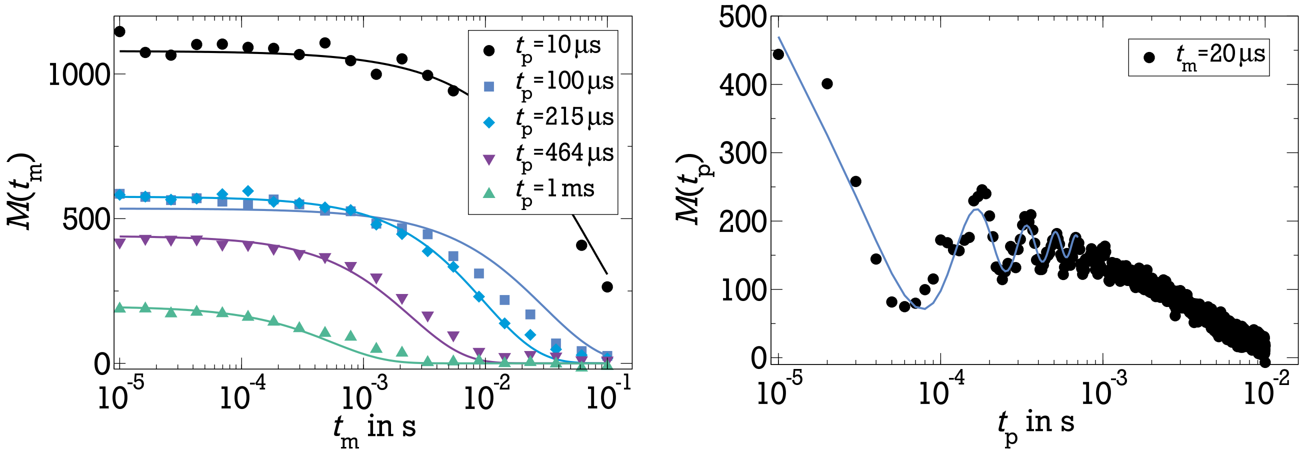

(a) **(b)**

Figure 5.12.: (a) t_m-dependent diffusion measurements for several values of t_p. Most striking is the $t_\mathrm{p} = 100\,\mu\mathrm{s}$ curve, which starts at a lower initial value than another curve with longer t_p in contradiction to the t_p-dependent T_2 decay given in Eq. (3.68). (b) The t_p-dependent measurement shows an oscillation with a frequency of about $2\pi \times 6\,\mathrm{kHz}$ due to the anisotropic quadrupolar interaction which is still present in the samples at 360 K as seen in the Pake-patterned spectrum. The signal height M is roughly the same for 100 µs and 215 µs, consistent with the findings in panel (a).

ions in $Li_{10}SnP_2S_{12}$ is due to a 3D diffusion process in the accessible temperature range on the studied time and length scales.

As shown in Fig. 5.15a, the diffusion coefficients measured with the SFG method differ from those obtained by PFG measurements [Sch15, Kuh14], especially in the activation energy represented by the slope of the data. As the diffusion activation energy agrees with the E_a obtained from correlation times, the difference between the slopes of the PFG and SFG measurements most probably arises due to the heat induced changes in the relaxation behavior mentioned in the introduction of this chapter. This is motivated by the fact that the PFG measurements in [Sch15] have been done before, and the SFG measurements after these changes. To demonstrate the consistency of the activation energies of the local jump dynamics and the long-range transport, the diffusion coefficients have been transformed into correlation times according to

$$\tau_\mathrm{c} = \frac{a^2}{6D}, \tag{5.2}$$

where a jump length of $a = 3.4\,\mathrm{\AA}$ has been used, the mean distance of the four distinct Li sites given in the supplementary material of [Bro13]. The resulting correlation times have been included in Fig. 5.15b, indicating good agreement of the results of the FC and the SFG measurements.

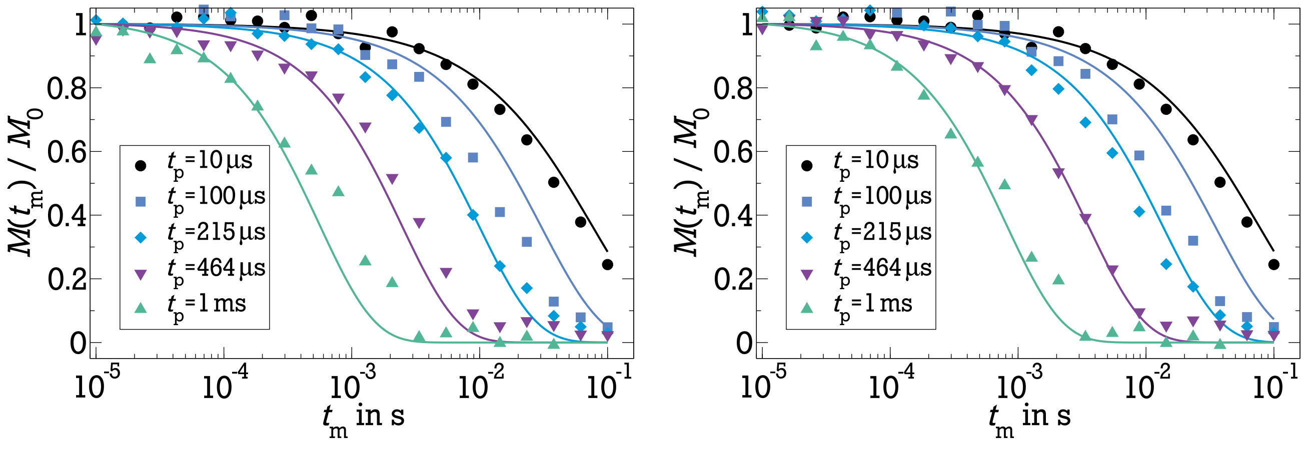

(a) **(b)**

Figure 5.13.: (a) Diffusion measurements normed to an initial value of $\mathrm{M}(t_\mathrm{m}=0)=1$. The solid lines represent a global diffusion coefficient D. (b) Same as on the left, but here, only the two measurements with the longest t_p have been considered for the global fit.

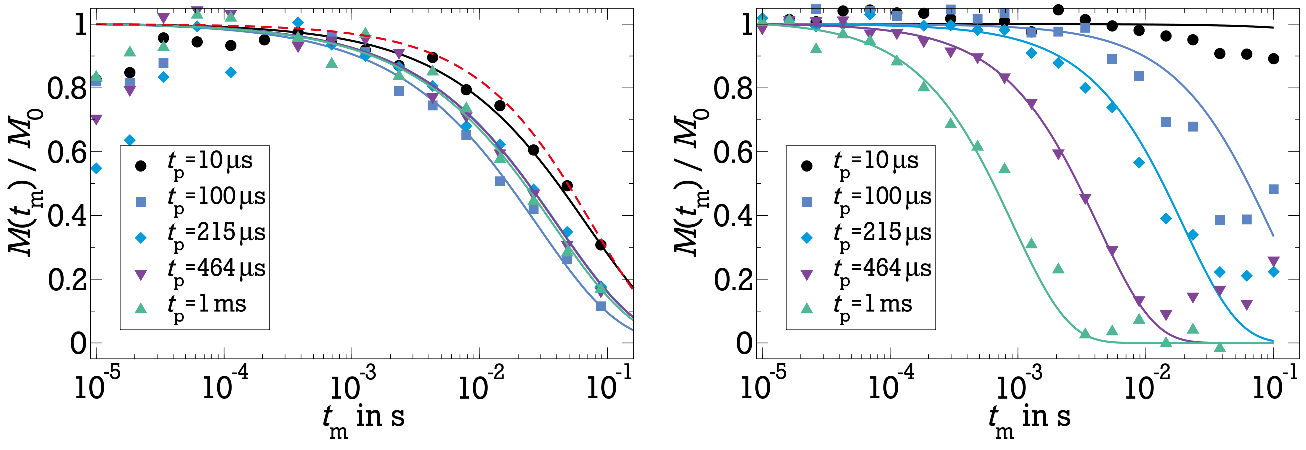

(a) **(b)**

Figure 5.14.: (a) STE measurements at a homogeneous field at *Berta*. The dashed red line represents the signal loss due to T_1. (b) The measured decays in the SFG have been divided by the STE decays to eliminate all non-diffusion related signal losses.

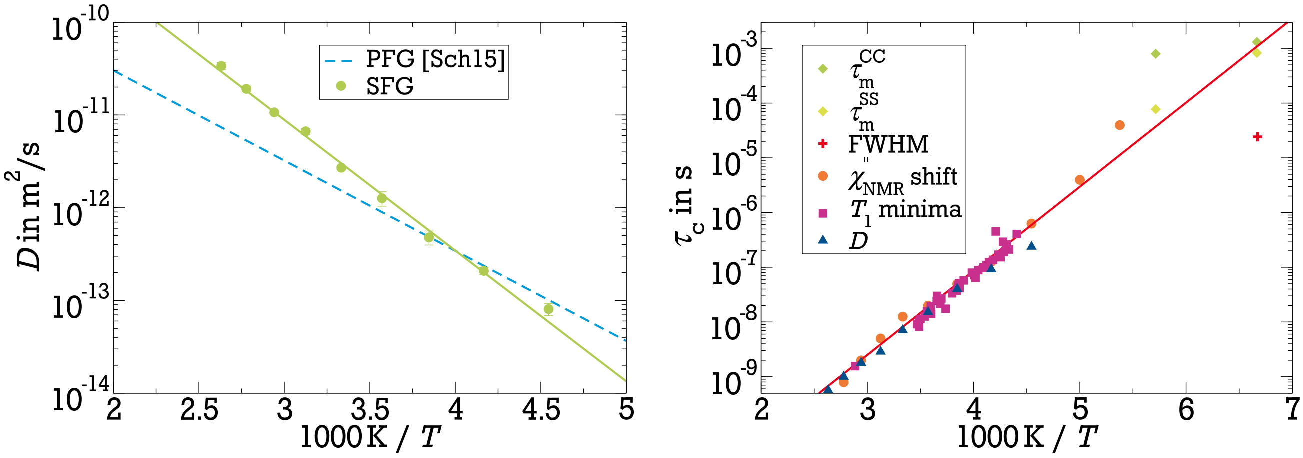

(a) **(b)**

Figure 5.15.: (a) Diffusion coefficients of $Li_{10}SnP_2S_{12}$. The solid line represents an Arrhenius fit with an activation energy of $E_a = 0.29$ eV. PFG measurements yielded $E_a = 0.19$ eV [Sch15]. (b) Correlation times τ_c of $Li_{10}SnP_2S_{12}$ obtained by different methods. The solid line is a fit to the Arrhenius equation (2.10) with an activation energy of $E_a = 0.31$ eV.

5.7 Summary and conclusion

^{7}Li NMR studies on the superionic conductor $Li_{10}SnP_2S_{12}$ have been performed. SLR measurements in a high magnetic field revealed the existence of a distribution of relaxation times ($0.65 \leq \beta_{T1} \leq 0.85$) in the whole accessible temperature range. The low temperature slope of $\langle T_1 \rangle$ is given by an activation energy of $E_a^{T_1} = 0.10$ eV. This activation energy is usually given by the product of the E_a of the lithium jump induced diffusion process and the stretching parameter β_{F2} of the correlation function. The former has been measured by various other NMR techniques and is given by $E_a = 0.31$ eV, q.v. Fig. 5.15b. The latter is between 0.3 and 0.4, see Fig. 5.9b, resulting in $0.09\,\mathrm{eV} \leq E_a^{T_1} \leq 0.12$ eV, which is in agreement with the findings of the SLR measurements. The existence of the T_1 minimum below 400 K at $\omega_L = 2\pi \times 63$ MHz is one sign of the superionic character of $Li_{10}SnP_2S_{12}$, as for most lithium ion conductors the T_1 minimum is not accessible at a regular NMR spectrometer in the MHz regime. With the help of this T_1 minimum the correlation time at the minimum temperature and the anisotropy parameter could be calculated to $\tau_c = 1.6$ ns at 347 K and $\delta_Q = 102$ kHz, respectively.

FC measurements have been used to extend the dynamic range of SLR experiments to lower frequencies, yielding temperature dependent T_1 minima, which were used to calculate correlation times revealing an activation energy of $E_a = 0.31$ eV. On the other hand, the temperature and frequency dependent SLR times T_1 have been used to calculate the NMR susceptibility χ''_{NMR}. With this susceptibility, the form and parameters of the spectral density could be determined employing a HN type with $\alpha = 0.77$, $\beta = 0.38$, and $\delta_Q = 116$ kHz.

LSA of the central line of $Li_{10}SnP_2S_{12}$ revealed, that the onset of the motional narrowing occurs below 150 K, while at 200 K it has already ended. The start of the MN at a relatively low temperature is another prove of the superionic character of $Li_{10}SnP_2S_{12}$, while the small temperature intervall between the start and the end of the MN hints at a rather narrow distribution of correlation times. The satellite transition shows a distinct quadrupolar powder pattern at high temperatures, representing an anisotropic averaged solid spectrum with $\bar{\delta}_Q = 2\pi \times 12\,\text{kHz}$ and an asymmetry parameter of the quadrupolar interaction $\eta_Q = 0$.

The fast dynamics in the sample hinders a temperature dependent analysis of the SAE, because at temperatures above 175 K the ENL is already reached, indicating that the correlation time is approaching the microsecond regime, which is outside the scope of the SAE experiments. The remaining quadrupole coupling at high temperatures prevented a two-time correlation decay, allowing to measure the relaxation time of the spin alignment state T_{1Q}, which proved to be helpful to confirm the theoretical T_1/T_{1Q} ratio.

Besides the effective operation of well established ^{7}Li NMR experiments, $Li_{10}SnP_2S_{12}$ turned out to be an ideal sample to establish some newly devloped pulse sequences [Sto15]. By using the *exorcycle* SE_+-SE_- the spin-spin relaxation time T_2 could be measured and the different behavior of the relaxation times of central and satellite transition has been observed. Additionally, the Zeeman-order correlation function F_2^{CC} has been acquired. While these measurements suffered from the same problems as the SAE, the F_2^{CC} at high temperatures could be used to determine the relaxation time of the mixed Zeeman and octupolar state T_{1ZO}.

Last, three- and four-time correlation functions have been recorded. While F_3 showed the heterogeneity of the rate distribution, F_4 revealed that a rate memory parameter of $\mathbb{Q} = 1$ describes this heterogeneity very well, indicating that the lithium ions change their jump rate with every single jump.

After eliminating all non-diffusion induced signal losses by dividing the SFG data by the corresponding measurements in a homogeneous magnetic field, temperature dependent diffusion coefficients could be obtained. By transforming these coefficients into correlation times using the mean distance of the four distinct lithium sites as the jump length $a = 3.4\,\text{Å}$, it could be shown, that the jump-diffusion induced long-range transport of $Li_{10}SnP_2S_{12}$ obeys the same Arrhenius law as the local dynamics.

With the combination of many different NMR measurements, the local dynamics could be investigated over a time scale spanning several orders of magnitude. Moreover, the combination of FC and SFG experiments is a powerful tool to relate the local dynamics of lithium ion jumps with the long-range diffusivity, the main advantage being the fact that both techniques yield results in the same temperature range.

6 SiOC

This chapter deals with lithium ion dynamics in polymer-derived silicon oxycarbide (SiOC) ceramics. SiOC compounds with various compositions have been examined since the 1990s [Wil94]. Especially stoichiometries with high content of free carbon have been identified as perspective anode materials with good gravimetric capacity, rate capability, and cycling stability [Fuk10, Liu11, Dib12, Wei14, Kas14, Fuk14]. Carbon-rich SiOC ceramics usually consist of an amorphous Si-O-C-mixed bond network, which is interpenetrated by a carbon phase, where percolating carbon networks are formed [Mer13]. Consistent with this host structure, former ^{7}Li NMR studies revealed three electrochemically active lithium sites in carbon-rich compounds [Fuk10]. The majority of lithium ions reside in interstitials or edges of the graphene layers, while minority lithium species are stored in the amorphous Si-O-C network or in micropores. In contrast to the detailed information about the structure, the knowledge about the lithium ion dynamics in these materials is still poor. To improve this insight, a combination of various ^{7}Li NMR techniques have been used in this study to observe the lithium ion dynamics in wide ranges of temperature and time scales. The local jump motion of lithium ions is proped by spin-lattice relaxation (SLR), line-shape analysis (LSA) and spin-alignment echo (SAE) measurements, which have been done at the spectrometer *Berta* where a Larmor frequency $\omega_L = 2\pi \times 76\,\text{MHz}$ has been used. Additionally, results of diffusion measurements using the static field gradient (SFG) method are shown to get insight into the long-range transport of the lithium ions. The microscopic ion motions in lithiated ($\text{SiOC}^{+\text{Li}}$) and delithiated ($\text{SiOC}^{-\text{Li}}$) compounds will be presented and discussed. The corresponding lithium contents amount to 12.9 wt% and 4.6 wt%, respectively. More details on the composition of the samples are given in Tab. B.2.

6.1 Saturation recovery

The fast dynamics in the high temperature regime is studied by SLR measurements. Figures 6.1a and 6.1b show the magnetization recovery for some representative temperatures for the two samples, $\text{SiOC}^{+\text{Li}}$ and $\text{SiOC}^{-\text{Li}}$, respectively. At low and ambient temperatures only a single exponential relaxation is observed for $\text{SiOC}^{+\text{Li}}$, while an additional relaxation process starts to appear at longer times when approaching 400 K. Therefore, the measurements have been repeated two times. During the second and third heating cycles, a two-step buildup is observed at all temperatures. For $\text{SiOC}^{-\text{Li}}$, the scenario is quite similar with the difference that a bimodal buildup is observed right from the beginning of the first heating cycle. The data have been analyzed by fitting the recovery curves with two KWW functions:

$$\frac{M(t_d)}{M_\infty} = 1 - \sum_{n=f,s} a_n \exp\left[-\left(\frac{t_d}{T_{1n}}\right)^{\beta_{T1n}}\right]. \tag{6.1}$$

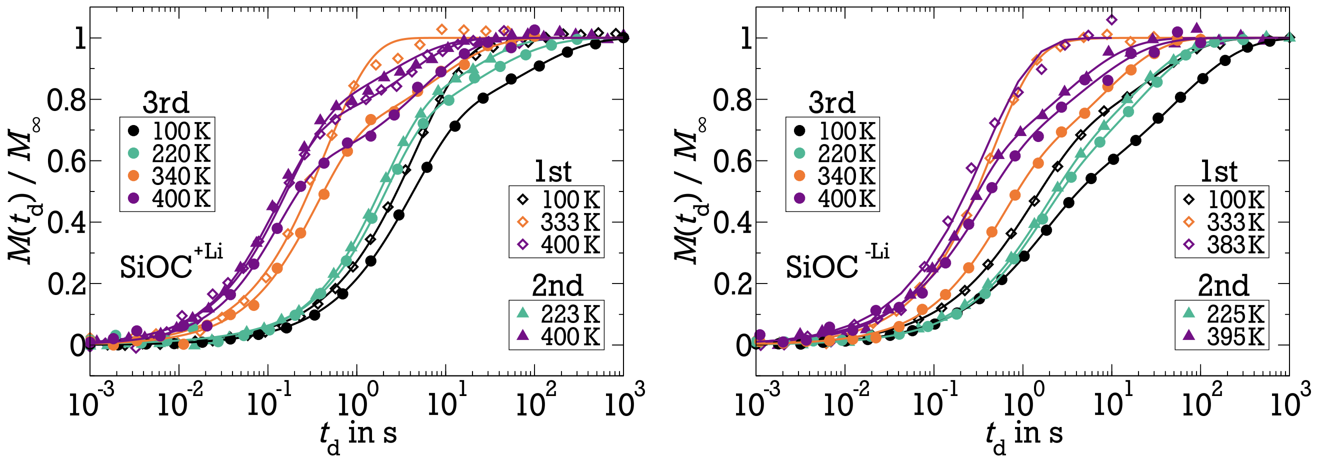

(a) **(b)**

Figure 6.1.: The saturation recovery buildup curves of SiOC$^{+\text{Li}}$ (a) and SiOC$^{-\text{Li}}$ (b) at various temperatures for three heating cycles (1st, 2nd, 3rd). The lines are fits to Eq. (6.1).

Here, M_∞ denotes the equilibrium magnetization and the index n refers to the different relaxation steps. The indices n=f and n=s are used to distinguish between the faster (f) and slower (s) SLR processes. The relative magnetizations of the different components fulfill the relation $\sum_{n=f,s} a_n = 1$. From the time constants T_{1n} and stretching parameters β_{T1n} mean SLR times $\langle T_{1n} \rangle = (T_{1n}/\beta_{T1n})\Gamma(1/\beta_{T1n})$ are calculated utilizing the gamma function Γ.

With decreasing temperature the recovery curves shift to shorter delay times, showing that the minimum of the relaxation time T_1 is not reached in the investigated temperature regime. This indicates that the lithium dynamics are characterized by correlation times $\tau_c \gg \omega_L^{-1} \approx 2\,\text{ns}$ at the studied temperatures.
To gain further insights into the ^{7}Li SLR behavior, Eq. (6.1) was used to fit the observed buildup curves. The results are displayed in Figs. 6.2, 6.3, and 6.4.

6.1.1 Stretching factor

At lower temperatures diverse local lithium environments lead to a distribution of ^{7}Li SLR times and a non-exponentiality of both ^{7}Li SLR processes, resulting in stretching factors $\beta_{T1n} < 1$ in this temperature regime (see Fig. 6.2). The short-time step becomes more exponential with increasing temperature, i.e., $\beta_{T1f} = 1$ is approached. This indicates that ion dynamics cause an exchange between various environments of the corresponding lithium species leading to an averaging of different SLR behaviors on the time scale of $\langle T_{1f} \rangle$. On the contrary, the stretching factor of the long-time step is temperature independent and characterized by $\beta_{T1s} \approx 0.6$. Obviously, for this lithium species, the dynamical averaging of diverse ^{7}Li SLR behavior is less effective. It should also be noted that the differences for the miscellaneous heating cycles and between the delithiated and lithiated samples are marginal.

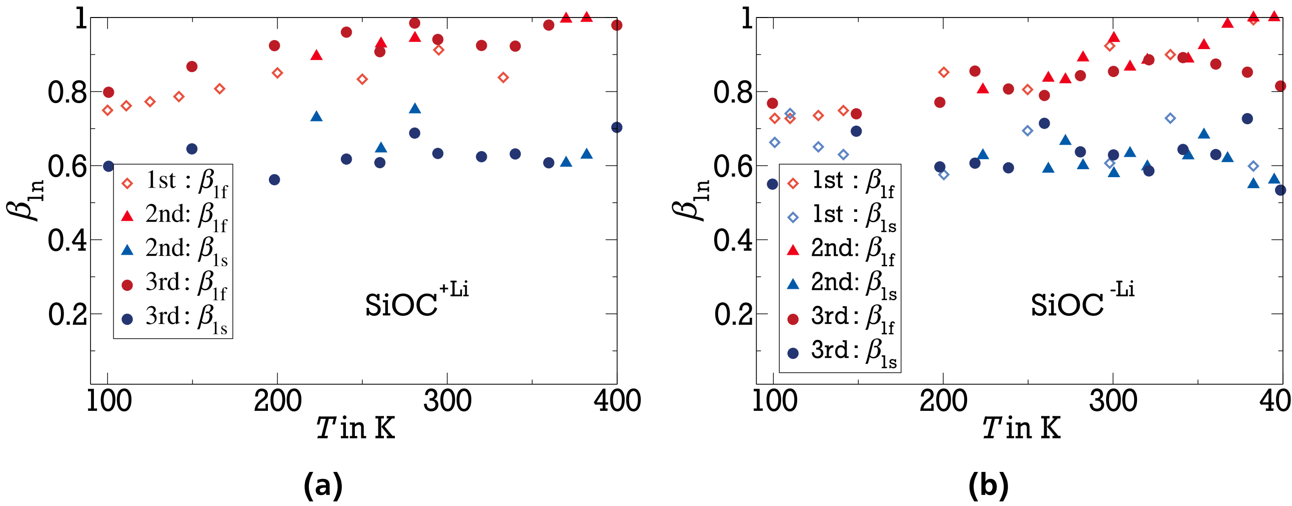

Figure 6.2.: Stretching factor of the fast (β_{T1f}) and slow process (β_{T1s}) from the saturation-recovery experiments of SiOC^{+Li} (a) and SiOC^{-Li} (b).

6.1.2 Fraction of slow relaxation process

Figure 6.3 shows the contribution of the second relaxation step, a_s, which is more or less constant during each heating cycle. While this fraction increases from the 2nd to 3rd heating cycle for SiOC^{+Li}, a_s is unchanged between these cycles for SiOC^{-Li}, suggesting that $a_s \approx 0.55$ is the final state value.

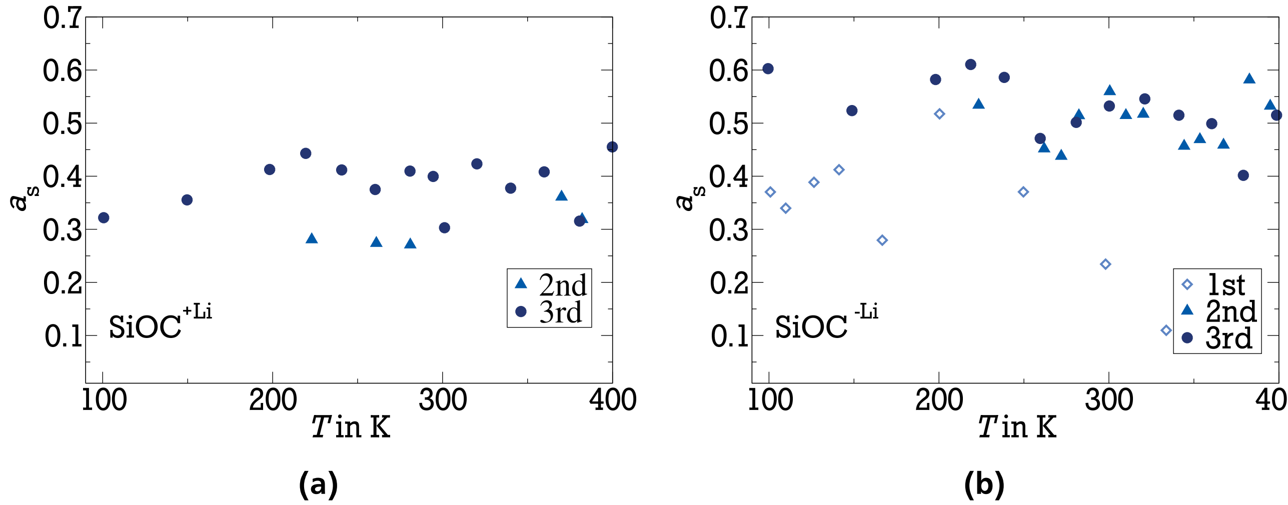

Figure 6.3.: Fraction of the second relaxation step a_s of SiOC^{+Li} (a) and SiOC^{-Li} (b).

6.1.3 Mean spin-lattice relaxation times

The mean spin-lattice relaxation times, $\langle T_{1n} \rangle$, obtained from Eq. (6.1) are presented in Fig. 6.4. Like the stretching factors β_{T1n}, the relaxation times $\langle T_{1f} \rangle$ and $\langle T_{1s} \rangle$ are similar during all heating cycles, indicating that, with the exception for $\langle T_{1s} \rangle$ of SiOC^{-Li} between the first and second cycle, heating induced changes of the sample have no influence on the rate and shape of the SLR process. These changes lead solely to the appearance of a slowly relaxing spin species the population of which grows only mindly during heating cycles, as indicated by the weak increase of a_s. The ^{7}Li SLR times $\langle T_{1f} \rangle$ and $\langle T_{1s} \rangle$ do not show a minimum in the accessible temperature range. They continuously increase upon cooling until they reach a plateau near 160 K. The finding of such a temperature independent relaxation time in the latter range implies that the hopping motion of the lithium ions becomes too slow to be effective for ^{7}Li SLR upon cooling. This kind of crossover in the temperature dependence of ^{7}Li SLR has also been found in other amorphous lithium ion conductors [Böh07a, BJ89, Kle03], but the low-temperature mechanism of ^{7}Li SLR in these materials is still unclear. Figure 6.4 shows that $\langle T_{1f} \rangle$ and $\langle T_{1s} \rangle$ of SiOC$^{+\mathrm{Li}}$ and SiOC$^{-\mathrm{Li}}$ differ by more than one order of magnitude in the plateau regime at lower temperatures, while both relaxation times depart from the plateau in a similar manner at higher temperatures. These results suggest that the heat treatment particularly affects the low-temperature mechanism of ^{7}Li SLR, which is most probably not related to lithium ion transport.

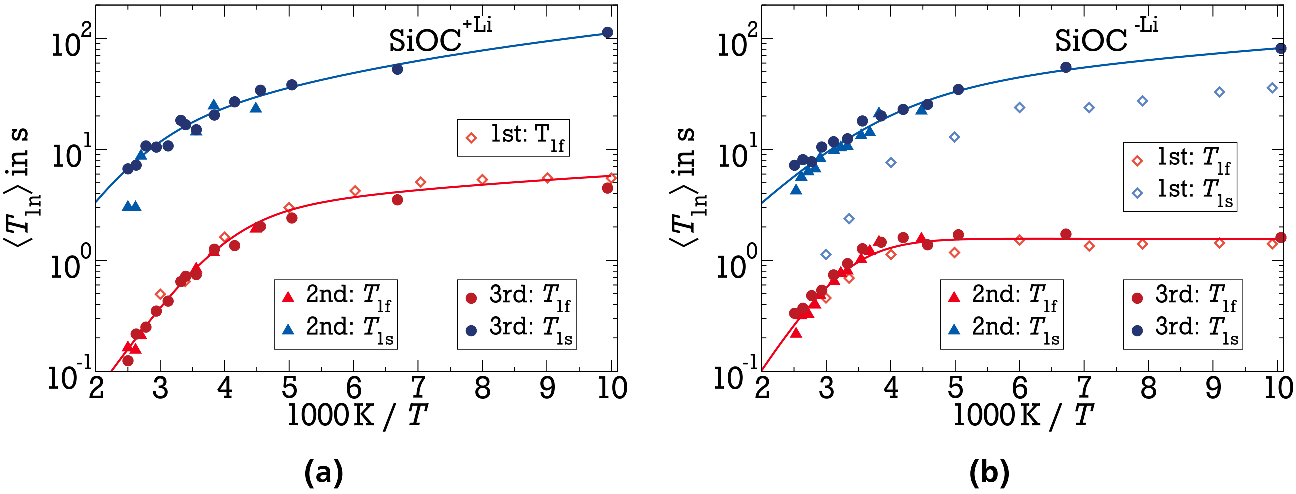

Figure 6.4.: Spin-lattice relaxation times of SiOC$^{+\mathrm{Li}}$ (a) and SiOC$^{-\mathrm{Li}}$ (b). The solid lines are fits to Eq. (6.2).

In general, the activation energy of lithium ionic jumps can be obtained from temperature dependent measurements of ^{7}Li SLR times. If ^{7}Li SLR is exponential and fully governed by lithium jumps, which are characterized by a correlation function with an exponential shape, this analysis is straightforward. However, for non-exponential buildup curves, multiple relaxation mechanisms, and pronounced dynamical heterogeneity the analysis of ^{7}Li SLR times becomes difficult. As a first approach the non-exponentiality of the buildup and, hence, differences between time and rate averages are neglected and instead of the relaxation time $\langle T_{1n} \rangle$ its inverse is used, as relaxation rates are additive. Next, the crossover in the temperature is tried to be explained by a second rate, which becomes dominant at low temperatures. Possibilities of this kind of relaxation is contributions due to paramagnetic impurities [Kle03], two-level tunneling systems

[And72, Phi72] or localized motions in non-rigid potentials [Fun97]. With these assumptions, the relaxation can be described by the following equation:

$$\frac{1}{\langle T_{1n} \rangle} = R_0 \exp[-E_a/(k_B T)] + a T^b. \tag{6.2}$$

Here, the first summand describes the relaxation due to lithium ion jumps with an activation energy E_a, while the second term denotes the relaxation due to the second relaxation process. Equation (6.2) has been used to fit the data of the different heating cycles globally. The result is shown in Fig. 6.4 as solid lines and the fitting-parameters are given in Tab. C.1. As the parameters R_0, a, and b do not yield insights into lithium ion transport, only the activation energies will be discussed in the following. While E_a of the fast process is similar for both samples (SiOC$^{+\text{Li}}$: $E_a = (0.16 \pm 0.01)$ eV; SiOC$^{-\text{Li}}$: $E_a = (0.18 \pm 0.02)$ eV), it differs for the slow process (SiOC$^{+\text{Li}}$: $E_a = (0.18 \pm 0.09)$ eV; SiOC$^{-\text{Li}}$: $E_a = (0.11 \pm 0.03)$ eV). The influence of the second term of Eq. (6.2) on the slow relaxation process is higher than that on the fast process as the relaxation rate of the slow process is significantly lower and the slope of the second term is steeper for this process. This leads to the circumstance that only a few data points have been obtained on the high temperature side of the crossover, which holds especially for the slow process. Therefore, the analysis of $\langle T_{1s} \rangle$ is more erroneous than that of $\langle T_{1f} \rangle$. At first glance, an activation energy of about 0.18 eV seems to be quite low, but E_a obtained from ^{7}Li SLR times of amorphous lithium ion conductors are often quite low, especially when broad distribution of correlation times exist, q.v. Sec. 3.4.2.

6.2 Spectra

Next, ^{7}Li LSA has been performed to investigate lithium ion dynamics in SiOC ceramics. Due to the existence of two SLR processes, both, partially relaxed (PR) and fully relaxed (FR) spectra are considered. They differ with respect to the delay t_d between the destruction of the magnetization during the saturation sequence and the signal acquisition. To distinguish the dynamics of the fast and slowly relaxing lithium species, PR spectra have to single out the behavior of the lithium species exhibiting the shorter SLR time $\langle T_{1f} \rangle$ and surpress contributions from the lithium species showing the longer SLR time $\langle T_{1s} \rangle$. Therefore, $\langle T_{1f} \rangle \ll t_d \ll \langle T_{1s} \rangle$ has been used to obtain PR spectra, ensuring that the magnetizations from the fast and slowly relaxing lithium species have recovered to major and minor extents when recording the data. For measuring FR spectra, the delay has been set to $\langle T_{1f} \rangle \ll \langle T_{1s} \rangle \ll t_d$ so that both lithium species add to the line shape. Figure 6.5a visualizes the mentioned conditions for t_d.

In Fig. 6.6, the PR and FR spectra of SiOC$^{+\text{Li}}$ at various temperatures are presented and in Fig. 6.7, the corresponding data of SiOC$^{-\text{Li}}$ are shown. The typical ^{7}Li low-temperature line shape for amorphous solids can be seen in the PR and FR spectra of both samples up to about 200 K. It can be described by a superposition of two Gaussians [Böh07a]. The central line with a width of ca. 7 kHz corresponds to the $m = +1/2 \leftrightarrow -1/2$ transition of ^{7}Li, while the satellite line with a width of ca. 100 kHz is associated with the $m = \pm 3/2 \leftrightarrow \pm 1/2$ transitions of this $I = 3/2$ nucleus, but barely visible in the chosen representation of Figs. 6.6 and 6.7. To demonstrate the existence of the satellite line, another presentation is used in Fig. 6.5b for the FR spectrum of SiOC$^{+\text{Li}}$ at 100 K. Narrowing of the ^{7}Li spectra starts above 200 K, indicating an onset of lithium ionic jumps on the microsecond time scale. This motionally narrowing (MN) occurs over a broad temperature range and is still ongoing at 400 K, the highest studied temperature. Visual inspection of Figs. 6.6 and 6.7 does not yield differences between PR and FR spectra or between SiOC$^{+\mathrm{Li}}$ and SiOC$^{-\mathrm{Li}}$. For a quantitative ^{7}Li LSA, the spectra are fitted with a pseudo-Voigt central line and a Gaussian satellite line. For the PR and FR spectra of both samples, the fits show that the Lorentzian component of the pseudo-Voigt function gains in importance with respect to the Gaussian component with increasing temperature until it fully dominates the line shape at high temperatures. The fraction R_{PV}, representing the Lorentzian part of the pseudo-Voigt function, is shown in Fig. 6.8a, indicating that the central line is given solely by an Lorentzian shape above 300 K, with the exeption of the PR spectra of SiOC$^{-\mathrm{Li}}$. Here, the central line reaches the purely Lorentzian shape, represented by a fraction of $R_{\mathrm{PV}} = 1$, only at 380 K. While the shape of the FR central line is always dominated by the Lorentzian part ($R_{\mathrm{PV}} \geq 0.8$), for the PR spectra the Lorentzian and Gaussian contributions are similar ($R_{\mathrm{PV}} \approx 0.5$) at temperatures up to 200 K, i.e., in the rigid-lattice regime. In contrast, the FWHM Σ of the central line as shown in Fig. 6.9a does not reveal such a big difference between PR and FR spectra. Also the central line FWHM of SiOC$^{+\mathrm{Li}}$ and SiOC$^{-\mathrm{Li}}$ differ hardly, implying that the lithium species related to the short-time and long-time SLR processes of SiOC$^{+\mathrm{Li}}$ and SiOC$^{-\mathrm{Li}}$ exhibit similar jump motions. In other words, the diverse SLR behaviors of the lithium species in the studied polymer-derived SiOC samples are not due to different ionic mobilities, but due to diverse SLR mechanisms. In the following, the differences of ion dynamics in SiOC$^{+\mathrm{Li}}$ and SiOC$^{-\mathrm{Li}}$ are discussed.

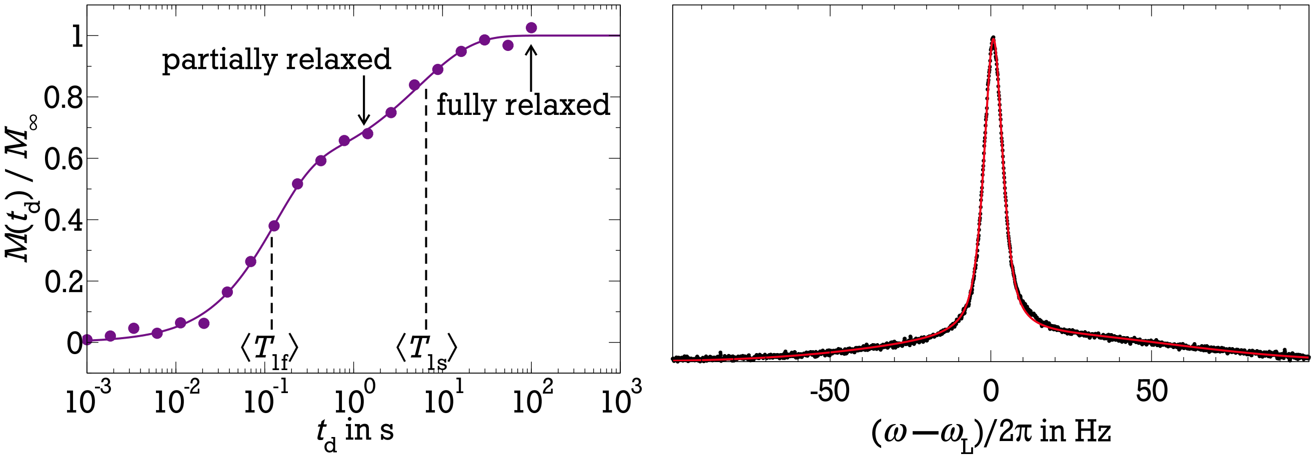

(a) **(b)**

Figure 6.5.: (a) Partially relaxed spectra have been obtained using the condition $\langle T_{1\mathrm{f}} \rangle \ll t_{\mathrm{d}} \ll \langle T_{1\mathrm{s}} \rangle$, while $\langle T_{1\mathrm{f}} \rangle \ll \langle T_{1\mathrm{s}} \rangle \ll t_{\mathrm{d}}$ has been used for the fully relaxed spectra. (b) Fully relaxed spectrum of SiOC$^{+\mathrm{Li}}$ at 100 K. In this representation the broad Gaussian satellite line is visible. The solid red line is a fit to the measured data (black dots).

With increasing temperature, line narrowing starts at $T \approx 200$ K for the lithiated sample and at $T \approx 240$ K for the delithiated sample, indicating that ionic jumps are somewhat faster in the former than in the latter sample. More precisely, lithium ionic jumps enter the microsecond regime at a lower temperature for SiOC$^{+\mathrm{Li}}$ than for SiOC$^{-\mathrm{Li}}$. As shown in Fig. 6.9a the line width decreases more rapidly for the lithiated than for the delithiated sample. When dealing

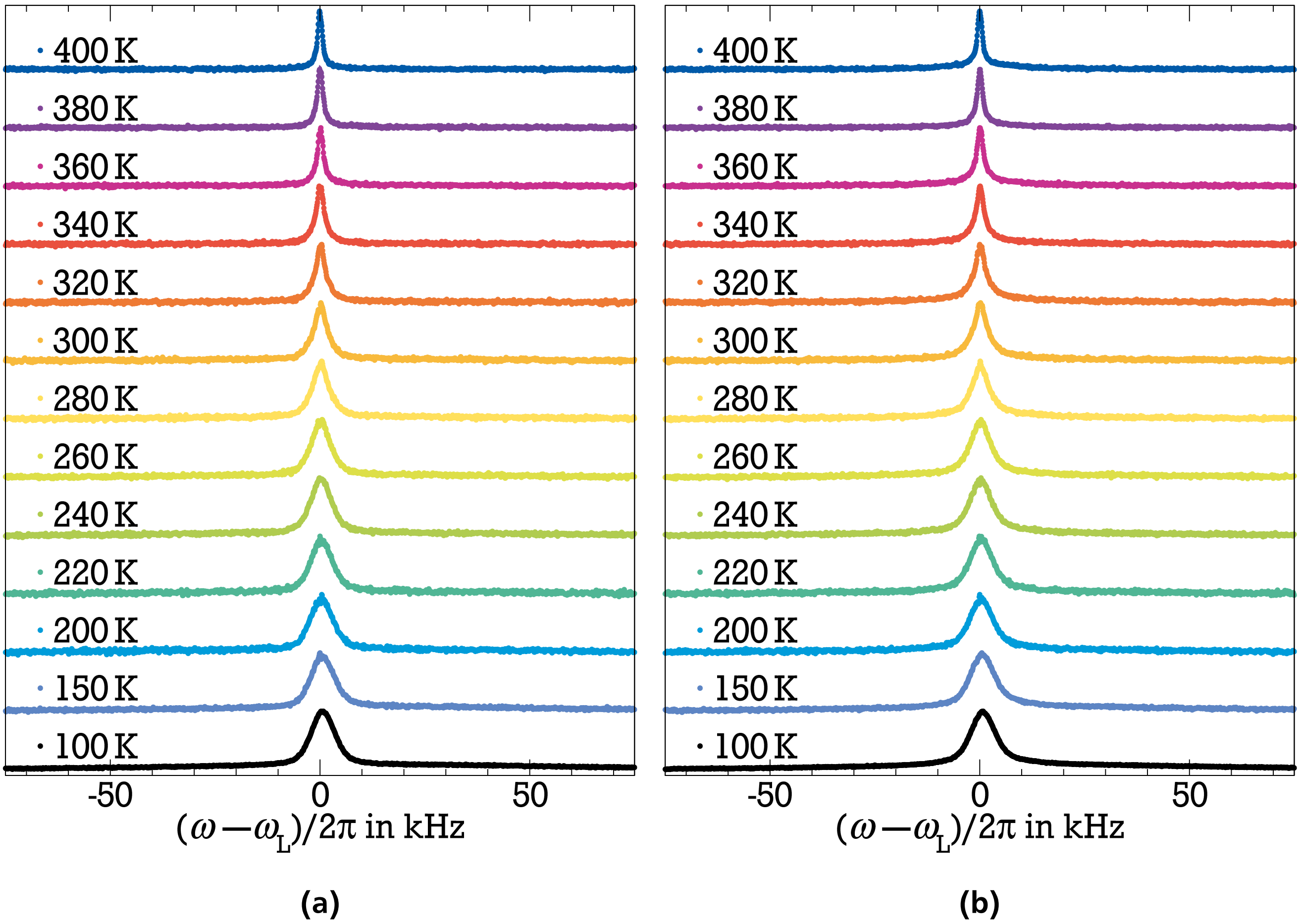

Figure 6.6.: (a) Partially and (b) fully relaxed spectra of $\mathrm{SiOC}^{+\mathrm{Li}}$.

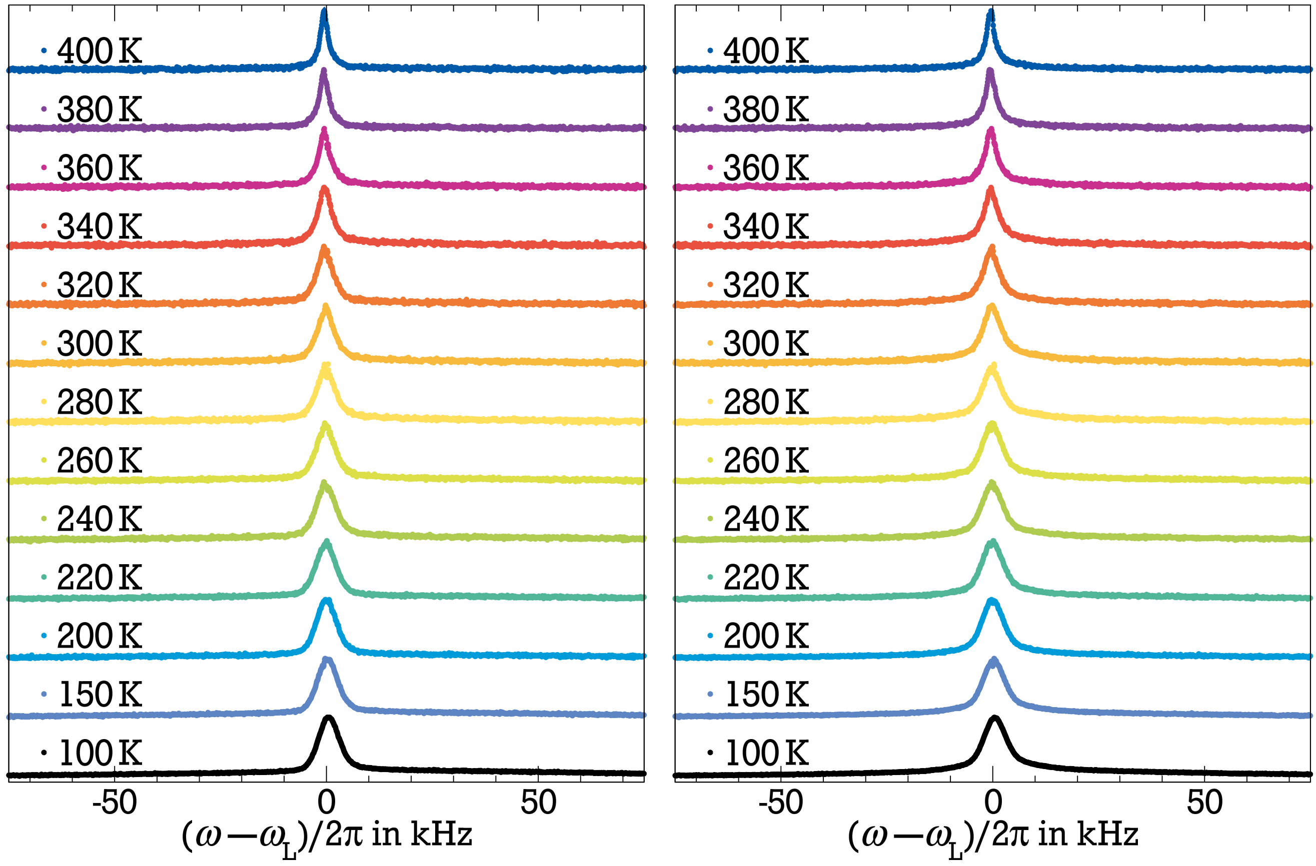

(a) **(b)**

Figure 6.7.: (a) Partially and (b) fully relaxed spectra of SiOC$^{-\mathrm{Li}}$.

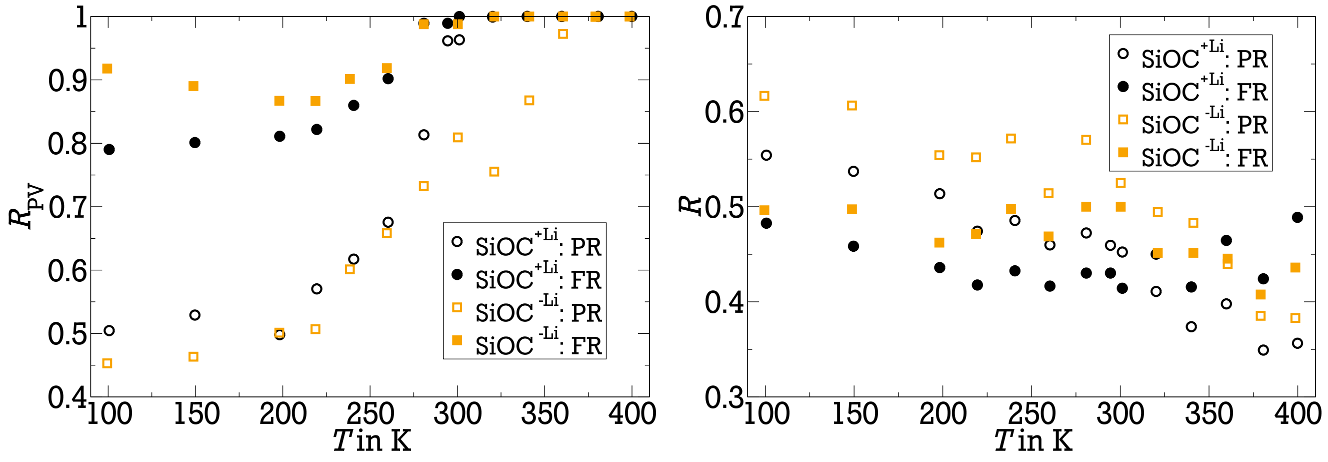

(a) **(b)**

Figure 6.8.: (a) Fraction R_{PV} of the pseudo-Voigt function used to fit the central line of partially and fully relaxed spectra of SiOC$^{+\mathrm{Li}}$ and SiOC$^{-\mathrm{Li}}$, representing the Lorentzian part of the central line. (b) Contribution of the satellite line to the total spectral intensity.

with amorphous materials, widely different lithium environments lead to broad distributions of correlation times $G(\ln \tau_c)$ [Böh07a, Bri10, Fas08, Fas11, Gra13]. Therefore, a stronger temperature dependence of the line width Σ results from a higher fraction of this distribution crossing the time window of the experiment in a certain temperature interval. This can be caused by two distinct scenarios; either $G(\ln \tau_c)$ shifts faster or it is narrower. It is extremely difficult to distinguish these two possibilities in ^{7}Li LSA. Fortunately, such information is available from ^{7}Li SAE, as will be explained below. Noticeable differences between the SiOC$^{+\mathrm{Li}}$ and SiOC$^{-\mathrm{Li}}$ samples exist relating to the central line width Σ at low temperatures as shown in Fig. 6.9a. Here, it can be seen that the central line of the static spectra is broader for the lithiated than for the delithiated SiOC ceramic. As explained in Sec. 3.2.2, the width of the central line is determined by the strength of Li–Li homonuclear dipolar interactions and, thus, by the average number and distance of neighboring lithium ions, q.v. Eq. (3.29). Applying this knowledge, the findings for the low-temperature line width indicate that the lithium density is higher in SiOC$^{+\mathrm{Li}}$ than in SiOC$^{-\mathrm{Li}}$, as expected. With the same argument, the narrower central line in PR than in FR static spectra implies that the lithium species showing faster SLR reside in environments with smaller local lithium density than the lithium species exhibiting slower SLR.

As explained in Sec. 3.3.2, there are several methods to obtain activation energies and/or correlation times from the temperature dependence of the central line width Σ. The red line in Fig. 6.9a is one example of fitting the line width with the Hendrickson and Bray formula. The respective parameters of this fit are listed in Tab. C.2. As the extreme narrowing limit is not reached in the investigated temperature regime, the values for the high-temperature line width D must be taken particularly carefully. Correlation times have been calculated using the equation suggested by BPP [Blo48] (see Eq. (3.47)) and the result is shown in Fig. 6.10. It must be noted that this analysis has been used successfully when dealing with systems where just one correlation time exists [Böh07a] while the existence of a distribution of correlation times, which is obviously the case for this amorphous SiOC ceramics, leads to results that differ from that obtained by other methods. Not surprisingly, τ_{LS} of SiOC$^{+\mathrm{Li}}$ is shorter than τ_{LS} of SiOC$^{-\mathrm{Li}}$ and the difference between PR and FR correlation times are just marginal. This result was expected from the shape of the different $\Sigma(T)$. Interestingly, the temperature dependence of τ_{LS} of SiOC$^{-\mathrm{Li}}$ is stronger than that of SiOC$^{+\mathrm{Li}}$, resulting in an approach of both τ_{LS} at higher temperatures.

The Arrhenius equation (2.10) was used to determine activation energies from these correlation times. As Eq. (3.47) is valid only in the MN regime, the Arrhenius fits have been restricted to $200\,\mathrm{K} < T < 360\,\mathrm{K}$ and $240\,\mathrm{K} < T < 410\,\mathrm{K}$ for SiOC$^{+\mathrm{Li}}$ and SiOC$^{-\mathrm{Li}}$, respectively. As the difference between PR and FR is insignificant, these fits were done globally for all data of each sample. The resulting activation energies are (0.08 ± 0.01) eV for SiOC$^{+\mathrm{Li}}$ and (0.15 ± 0.01) eV for SiOC$^{-\mathrm{Li}}$. These are even lower activation energies than the ones obtained from ^{7}Li SLR. Figure 6.10 also shows correlation times calculated from the infliction point of the HB fits for PR (stars) and FR line widths (crosses). The correlation times have been acquired using the equation

$$\tau_{\mathrm{i}} = \frac{1}{2\pi \times \Sigma\left(T_{1/2}\right)}, \tag{6.3}$$

where $T_{1/2}$ is the temperature where the HB fit of $\Sigma(T)$ reaches the value $\frac{1}{2}A + D$ which is roughly the point of infliction of the HB function. This temperature can be obtained from

$$T_{1/2} = \frac{E_{\mathrm{a}}}{k_{\mathrm{B}} \ln(A/B - 1)}. \tag{6.4}$$

The FWHM in the rigid-lattice and extreme narrowing limits are similar for all data shown in Fig. 6.9a. Consequently, the resulting correlation times τ_i are all nearly the same and only the temperatures at which this τ_i is reached is lower for SiOC$^{+\mathrm{Li}}$ and PR than for SiOC$^{-\mathrm{Li}}$ and FR, respectively. Noticeably, τ_i is continuously lower than τ_LS.

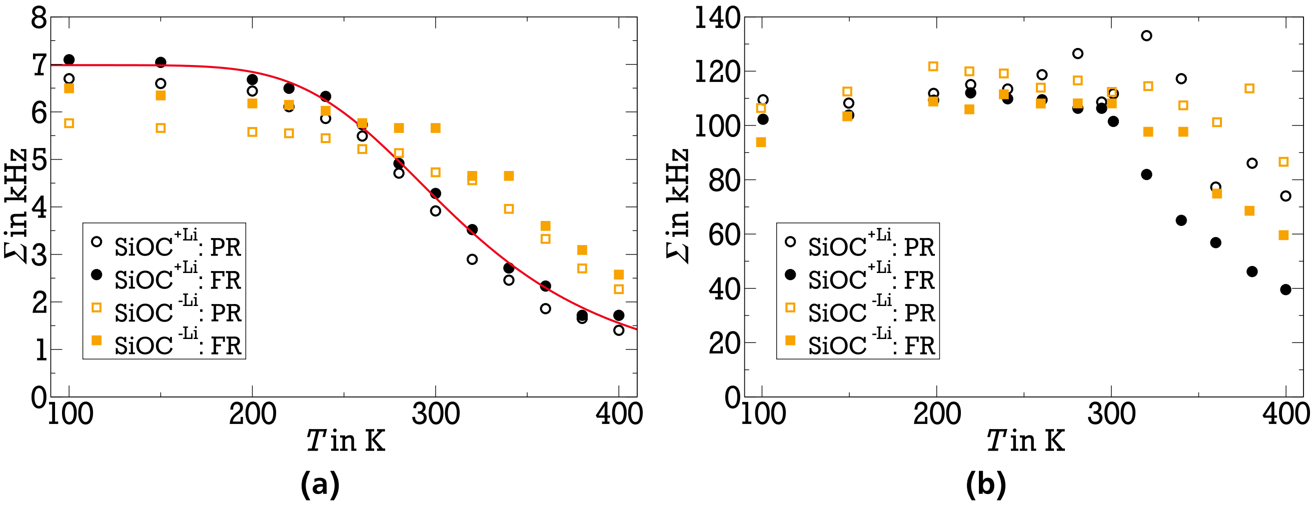

Figure 6.9.: (a) FWHM Σ of the central line of partially and fully relaxed spectra of SiOC$^{+\mathrm{Li}}$ and SiOC$^{-\mathrm{Li}}$. The red line is a fit of the SiOC$^{+\mathrm{Li}}$ fully relaxed spectra to Eq. (3.50). (b) Corresponding FWHM of the satellite line.

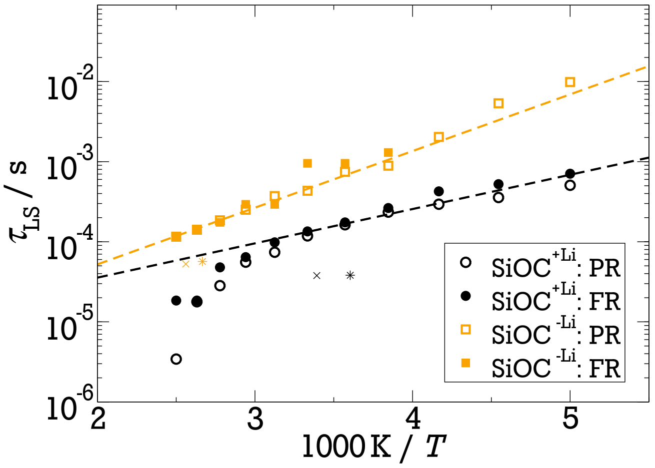

Figure 6.10.: Correlation times τ_LS obtained from the SiOC FWHM. The stars and crosses refer to the correlation times acquired from the infliction point of the HB fit for the partially and fully relaxed spectra. The dashed lines are Arrhenius fits to the FWHM in the MN regime with activation energies of E_a = (0.08 ± 0.01) eV and (0.15 ± 0.01) eV for SiOC$^{+\mathrm{Li}}$ and SiOC$^{-\mathrm{Li}}$, respectively.

Figure 6.9b shows the FWHM of the satellite lines. Here, no prominent differences at low temperatures are visible. As the satellite line arises due to the strength of the quadrupolar interaction, which is governed by the electric field gradient (see Sec. 3.2.1), the Σ of the satellite line is not related to the density but depends on the electronic environment of the lithium ions. The strength of the quadrupolar interaction is larger than that of the Li–Li homonuclear dipolar interaction, which is represented by the width of the static spectrum ($\delta_D \approx 2\pi \times 7\,\text{kHz}$, $\delta_Q \approx 2\pi \times 110\,\text{kHz}$). Consequently, the narrowing of the satellite line occurs at higher temperatures than the narrowing of the central line. Again, the narrowing starts at lower temperatures for the SiOC$^{+\text{Li}}$ sample, indicating the faster lithium ion dynamics in this compound. Further analysis of the satellite FWHM is hampered by the large statistical error of the fit of the broad Gaussian line. As can be seen in Fig. 6.8b, the contribution of the satellite line to the total spectral intensity decreases with increasing temperature. At low temperatures, the fraction starts at about 0.6, which is the theoretical value of the satellite transition of an $I = 3/2$ nucleus obtained from a FID spectrum, e.g., see Fig. 3.8 or [Böh07a]. In part, this decrease is due to the fact that line narrowing starts at a lower temperature for the central than for the satellite transition.

6.3 Spin alignment

To access slow lithium ionic dynamics in the SiOC ceramic in the ms to s regime at low temperatures, ^{7}Li SAE has been employed. Again, PR and FR measurements have been performed to distinguish between the two species with different relaxation mechanisms. Figure 6.11 displays the measured temperature-dependent correlation functions $F_2(t_m)$ for SiOC$^{+\text{Li}}$ (a) and SiOC$^{-\text{Li}}$ (b). For both samples and relaxation delays, ionic jumps cause strongly non-exponential decays of the correlation functions, consistent with the existence of broad distributions of correlation times $G(\ln \tau_c)$.

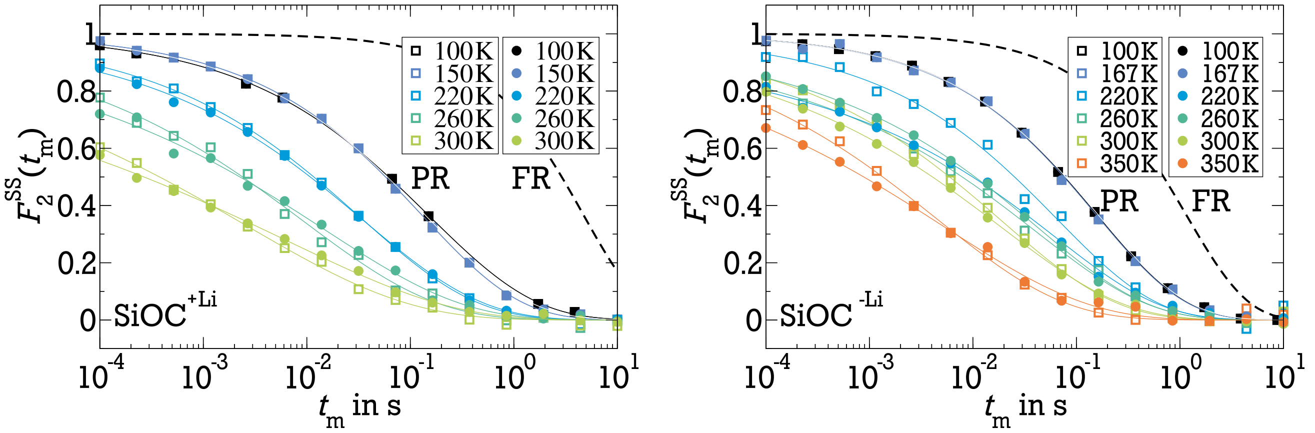

(a) (b)

Figure 6.11.: Two-time correlation function F_2^{SS} of SiOC$^{+\text{Li}}$ (a) and SiOC$^{-\text{Li}}$ (b) at $2\pi \times 76\,\text{MHz}$. The dashed black line represents the spin-lattice relaxation at 100 K, indicating that T_1 corrections have not to be taken into account.

With decreasing temperature the hopping motion slows down. Consequently, the correlation loss is shifted towards longer times. Below 200 K this shift becomes smaller and at ca. 150 K it ceases, indicating that the SAE decays are no longer caused by temperature-dependent ion dynamics, but rather by temperature-independent spin diffusion [Fas08, Fas11]. In harmony with LSA results shown above, for neither of the two samples, substantial differences between PR and FR data are observed. This confirms the conclusion that the existence of two lithium species with diverse ^{7}Li SLR behaviors does not result from a bimodality of lithium ion dynam-

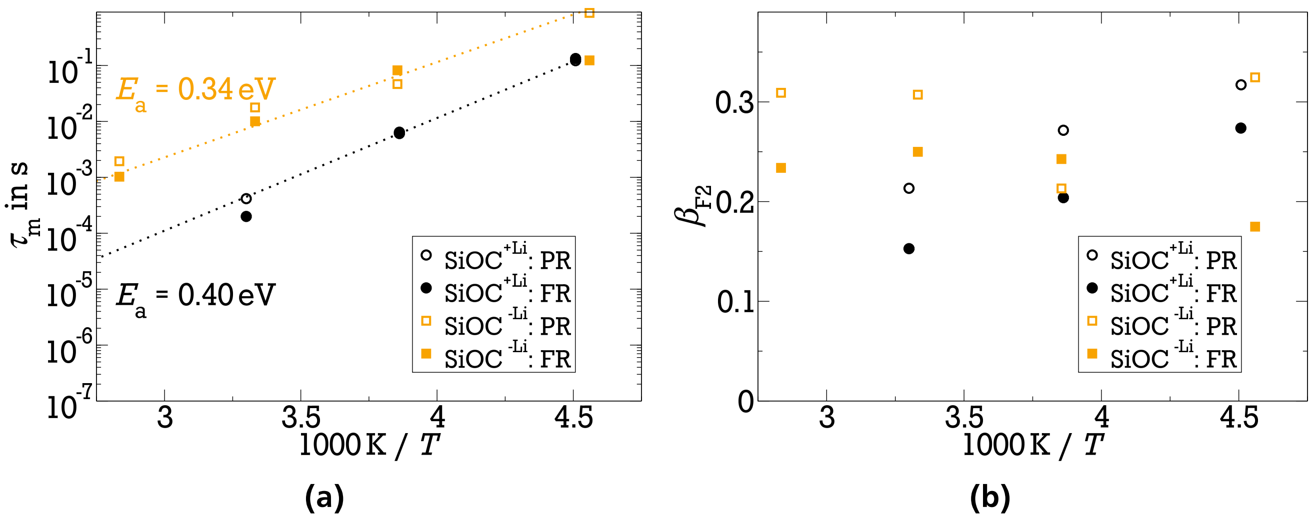

Figure 6.12.: (a) Correlation times of partially and fully relaxed spin-alignment measurements of $SiOC^{+Li}$ and $SiOC^{-Li}$ at $2\pi \times 76$ MHz. (b) Parameter β_{F2} obtained from fitting the spin-diffusion corrected data to a KWW function.

ics. Consistent with the LSA findings, $F_2(t_m)$ differs for $SiOC^{+Li}$ and $SiOC^{-Li}$. The analysis of the measured data has been carried out in two stages to obtain quantitative insights from the decays of the correlation function $F_2(t_m)$. First, the decay due to spin diffusion is determined from the low-temperature data and, then, the parameters of ion dynamics, τ_2 and β_{F2}, are calculated from fitting the high-temperature data with a fixed spin diffusion contribution. A correction due to SLR is not required, as SLR occurs at larger times at the studied temperatures as indicated by the dashed lines in Fig. 6.12a. The mean logarithmic correlation times τ_m obtained from the fit results τ_2 and β_{F2} using Eq. (3.52) are presented in Fig. 6.12a. At ambient temperatures τ_m is almost two orders of magnitude shorter for $SiOC^{+Li}$ than for $SiOC^{-Li}$. As the temperature dependence is higher for the former than for the latter sample, lithium mobilities in the lithiated and in the delithiated SiOC ceramic approach each other upon cooling. The mean logarithmic correlation times τ_m characterizing the lithium ionic jumps at low temperatures show an Arrhenius-like behavior. Therefore, activation energies could be obtained by fitting the data to Eq. (2.10) resulting in $E_a = (0.40 \pm 0.15)$ eV and $E_a = (0.34 \pm 0.03)$ eV in $SiOC^{+Li}$ and $SiOC^{-Li}$, respectively. These activation energies are higher than the energies obtained from ^{7}Li SLR and LSA studies (see above or Tab. 6.1). The strong non-exponentiality of the correlation functions is reflected by small stretching parameters of $\beta_{F2} \approx 0.20$ for $SiOC^{+Li}$ and $\beta_{F2} \approx 0.25$ for $SiOC^{-Li}$. All obtained stretching parameters β_{F2} are shown in Fig. 6.12b. As β_{F2} is lower for $SiOC^{+Li}$ than for $SiOC^{-Li}$, it is implied that $G(\ln \tau_c)$ is broader for the former than for the latter sample. Hence, the diversity of the occupied lithium sites is reduced upon delithiation. The ^{7}Li SAE results confirm the above ^{7}Li LSA findings. The shorter values of τ_m obtained from SAE for $SiOC^{+Li}$, compared to $SiOC^{-Li}$, are in harmony with the observation that line narrowing sets in at lower temperatures for this sample. Additionally, a higher activation energy for $SiOC^{+Li}$ obtained by ^{7}Li SAE mirrors the higher temperature dependence of the line width Σ in this samples. On the other side, a broader distribution $G(\ln \tau_c)$ for the lithiated sample, indicated by the smaller stretching parameter β_{F2}, negates this effect. Seemingly, the observed values $\tau_m \geq 1$ s do not suggest that lithium dynamics starts to affect the line shape at 200 K as ionic jumps in the microsecond regime are required for the observed narrowing. However, it is important to consider that τ_m

is the logarithmic mean of a, supposedly, very broad distribution $G(\ln\tau_c)$ so that fast ions from this distribution may already exhibit microsecond dynamics near 200 K. Having a closer look at the $F_2(t_m)$ plotted in Fig. 6.12a, the latter idea is confirmed. Obviously, the initial decay enters the microsecond regime when increasing the temperature through 200 K for SiOC$^{+\mathrm{Li}}$, consistent to the observed onset of motional narrowing.

6.4 Diffusion

Finally, SFG measurements have been employed to measure diffusion coefficients and get information about long-range transport of the lithium ions. A Larmor frequency of $\omega_L = 2\pi \times 63$ MHz and a gradient of $g = 73$ T/m have been used for the measurements. Due to the low signal and slow relaxation only one FR measurement for SiOC$^{+\mathrm{Li}}$ has been performed at 430 K which is shown in Fig. 6.13. The data have been fitted globally using Eq. (3.68). As no individual SLR measurement has been performed at this specific temperature, not only D but also T_1 has been used as a free parameter. As the stretching parameter has become 1 at high temperatures (see Fig. 6.2), this value has been used here as well. The factor containing T_2 has been combined with the pre-exponential factor D_0. The resulting $T_1 = 0.06$ s is a reasonable result and the corresponding SLR decay is represented by the black line in Fig. 6.13. For the diffusion coefficient a value of $D = (8.3 \pm 4.9) \cdot 10^{-11}$ m^2/s has been obtained. Taking into account the scatter of the data and the weak shift with increasing t_p the high uncertainty of D is not surprising. Calculating the correlation time τ_m according to the results of the SAE measurments for the temperature of 430 K and using the approximation

$$D = \frac{a^2}{6\tau_m} \tag{6.5}$$

with an hopping length $a = 4$ Å, D would become roughly $7 \cdot 10^{-15}$ m^2/s.

A lithium ion diffusion coefficient lower than $1 \cdot 10^{-14}$ m^2/s can hardly be measured with the SFG method. On the other hand, to measure a D in the order of $1 \cdot 10^{-10}$ m^2/s, the mean correlation time τ_m has to become lower than 1 ps. This correlation time is reached at temperatures near the T_1-minimum which is outside the measured temperature regime for the SiOC ceramics as shown above. Therefore, it is unlikely that the D obtained from the fit is an accurate value. Diffusion coefficients obtained from potentiostatic intermittent titration technique (PITT), galvanostatic intermittent titration technique (GITT), and electrochemical impedance spectroscopy (EIS) methods are in the range between 10^{-13} and 10^{-15} m^2/s at ambient temperature [Kas14], corresponding to correlation time between 10^{-7} and 10^{-5} s, which is at least one order of magnitude faster than resulting from SAE measurements. Alltogether, the results imply that diffusion of the lithium ions in SiOC ceramics is rather slow, preventing the material to be a good replacement for carbon as anode in lithium ion batteries.

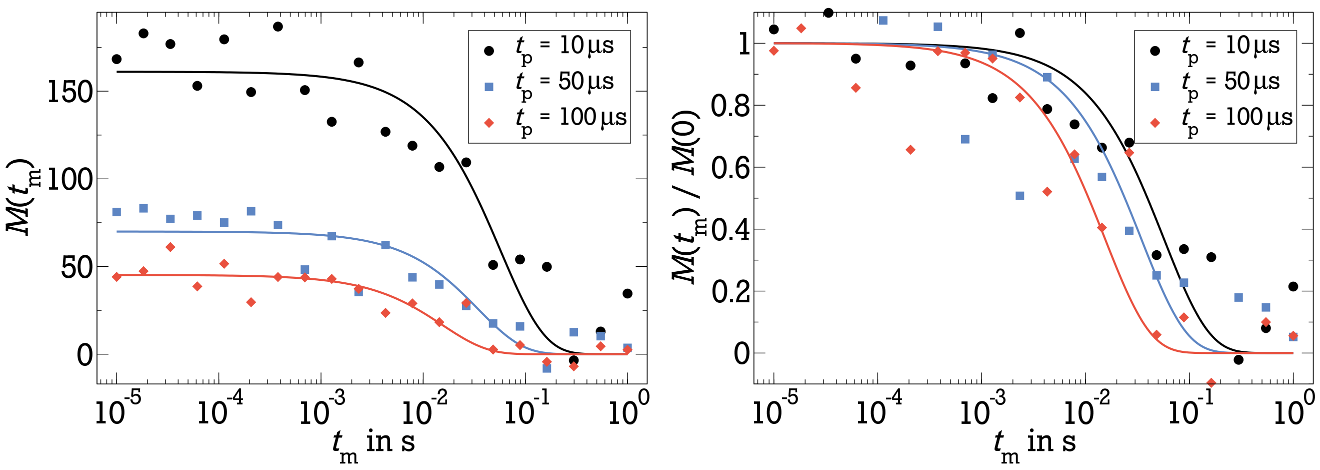

(a) **(b)**

Figure 6.13.: (a) Diffusion measurement of fully relaxed SiOC$^{+\mathrm{Li}}$ at $2\pi \times 63$ MHz. The static field gradient used during the data acquisition was g = 73 T/m. (b) Same data as in panel (a) normed to an initial value of 1 for a vanishing mixing time t_m. The solid lines are global fits with D and T_1 as the only two free parameters.

6.5 Summary and conclusion

^{7}Li SLR, LSA, SAE, and SFG studies on the lithium ionic motion in lithiated and delithiated SiOC ceramics have been performed. Irreversible changes occured to the prepared samples when heating to 400 K. Most noticeably, two lithium species with different ^{7}Li SLR are present in the samples with SLR times $\langle T_{1\mathrm{n}} \rangle$ which differ by more than an order of magnitude for the two species. The irreversible changes mentioned above cause the fraction of the slower relaxing species to increase. ^{7}Li LSA and SAE measurements reveal that the different ^{7}Li SLR behaviors of the two lithium species are not caused by different ionic jump dynamics. More likely, the different lithium species differ with respect to another mechanism for ^{7}Li SLR, specifically, the mechanism that dominates ^{7}Li SLR in various disordered solids at low temperatures, but still awaits an explanation [Böh07a, Gra13, BJ89, Kle03]. In view of this lack of knowledge, it remains unclear which kind of structural changes the heat treatment induces, e.g., whether it heals some kind of defects.

In contrast to SLR, results from ^{7}Li LSA and SAE provided detailed information regarding the lithium ionic motions in the SiOC samples. As major effects of the thermal history in this analysis should be avoided, two heating cycles have been completed to get through most aging processes before performing these measurements. ^{7}Li LSA shows that line narrowing occurs over a broad temperature interval and ^{7}Li SAE yields correlation functions extending over several orders of magnitude in time. These observations provide evidence that the large variety of lithium environments result in broad distributions of correlation times $G(\ln \tau_c)$ for the jump motion of the lithium ions. Furthermore, ^{7}Li LSA and SAE consistently showed that the lithium ionic jumps are, on average, faster in SiOC$^{+\mathrm{Li}}$ than in SiOC$^{-\mathrm{Li}}$ in the studied temperature range. The slower dynamics in the delithiated sample could arise from strongly oxygen bonded lithium ions, but further work is required to clarify this point. Correlation functions of the lithium ionic jump motion have been measured with ^{7}Li SAE. The mean logarithmic correlation times of $\tau_\mathrm{m} = 2{\cdot}10^{-4}$ s and $\tau_m = 1 \cdot 10^{-2}$ s for SiOC^{+Li} and SiOC^{-Li}, respectively, have been found at 300 K. Additionally, the correlation functions of the lithiated sample turned out to be more non-exponential. The combination of a shorter mean correlation time with a more stretched correlation function for SiOC^{+Li} than SiOC^{-Li} leads to the assumption that a higher fraction of fast ions than slow ions was removed during delithiation. On the other hand, the temperature dependence is higher for SiOC^{+Li} ($E_a = 0.40$ eV) than for SiOC^{-Li} ($E_a = 0.34$ eV) so that the difference of the lithium ionic mobilities becomes weaker upon cooling.

Activation energies obtained from different NMR techniques yielded partly quite different results making this study a perfect example for the discrepancies observed by comparing activation energies acquired by completely different methods. While it is common knowledge that activation energies from SLR and LSA are quite low, E_a resulting from STE are often considered to be the true activation energy. In the next chapters it will be shown that also the E_a from STE measurements are untrustworthy when broad distribution of correlation times are present.

^{7}Li SFG measurements have been performed only for fully relaxed SiOC^{+Li} at 430 K due to the low SNR and the slow relaxation in this SiOC ceramics. The diffusion coefficient of $D = 8 \cdot 10^{-11}\,\mathrm{m}^2/\mathrm{s}$ is somewhat smaller than coefficients obtained from other techniques, but due to the restrictions above the D resulting from ^{7}Li SFG should not be taken too seriously in this case. The only clear conclusion that can be taken from the SFG measurement is that the diffusion of lithium ions in lithiated SiOC ceramics is relatively slow preventing this material to become an adequat replacement for carbon in lithium ion batteries.

Altogether, the present ^{7}Li NMR study provided valuable insights into the temperature-dependent time scale of lithium ionic jumps in a SiOC ceramic. This approach did not provide evidence for an existence of trimodal dynamics related to three electrochemically active lithium sites associated with graphene layers, amorphous networks, and microscopic cavities proposed as main structural components of carbon-rich SiOC ceramics. However, the measurements revealed the existence of broad distribution of correlation times $G(\ln \tau_c)$. Details of the preparation scheme can have an influence on the structure of these materials. Therefore, this study gives only an exemplary picture. Hence, it may be worthwhile to study possible correlations between the properties of the lithium environments and the rates of the lithium jumps for SiOC ceramics prepared using different pyrolysis temperatures, precursor materials etc. in future work. Such knowledge will be very useful to understand the microscopic mechanism for lithium ion uptake and release of these materials during battery cycling.

Table 6.1.: Activation energies of the SiOC samples obtained from different methods. All activation energies are given in eV and are mean values of both processes combined.

sample	WF	HB	LSA	SLR	SAE
SiOC^{+Li}	0.33 ± 0.03	0.23 ± 0.03	0.08 ± 0.01	0.17 ± 0.05	0.40 ± 0.15
SiOC^{-Li}	0.39 ± 0.04	0.24 ± 0.06	0.15 ± 0.01	0.15 ± 0.05	0.34 ± 0.03

7 Li_2S–B_2S_3 glasses

Glasses containing Li_2S have been considered as promising solid electrolytes for more than three decades [Wad83]. Its low weight and high theoretical specific capacity of 1166 mAh/g make Li_2S the ideal material for being used in lithium-sulfur batteries. Usually, Li_2S is mixed with network formers, mostly also sulfide based like B_2S_3 or P_2S_5, to increase the conductivity [Zha90]. Substitution of a small amount of the sulfur atoms with oxygen leads to a further increase of the conductivity, a phenomenon known as mixed network former effect or mixed glass former effect (MGFE) [Kim06, Pra98, Rag12, Sch09] which is caused by a decrease of the potential barriers. In germanium glasses the MGFE is most effective when 10% of the sulfur is exchanged with oxygen [Kim06]. Therefore, the same amount of sulfur has been substituted in the thioborate glasses investigated in this work. Former analysis of the $x\mathrm{Li_2S}$-$(1-x)\mathrm{B_2S_3}$ binary series revealed a conductivity maximum for $x = 0.7$ [Zha90]. ^{11}B NMR measurements have shown that $0.7\mathrm{Li_2S}$–$0.3\mathrm{B_2S_3}$ is characterized by having approximately 20% tetrahedrally coordinated BS_4 groups and 80% trigonally coordinated BS_3 groups [Kim96b] and an activation energy of $E_a = 0.34\,\mathrm{eV}$ was obtained from conductivity and PFG diffusion experiments [Kim97a]. Frequency and temperature dependent ^{7}Li spin-lattice relaxation (SLR) data revealed, that two Gaussian distributions of activation energies (DAEs) are responsible for the complex local lithium jumps [Kim96b, Kim97a]. The DAEs mentioned in both references differ slightly, especially in the fractions f and $(1\text{-}f)$ supposedly representing the fractions of ^{11}B nuclei in the BS_3 and BS_4 structural groups, respectively, suggesting a close connection between the Li ion dynamics and the short-range order of the network former. Determination of the glass transition temperature with the help of differential scanning calorimetry (DSC) revealed a dependence on the quenching speed, if melt quenching is used as the preparation technique [Men91]. Adding small amounts of oxygen yielded a minor decrease of both, the conductivity activation energy E_a (from 0.34 eV [Kim97a] to 0.32 eV as shown in Fig. 7.1c) and the glass transition temperature T_g, q.v. Fig. 7.1d and Tab. B.3. Additionally, the conductivity at ambient temperatures increased, compare Figs. 2 of [Kim97a] and 7.1c. To investigate the origin of the enhanced conductivity, ^{7}Li NMR experiments have been performed and the results will be presented in this chapter.

The samples investigated in this work have been prepared by the group of Prof. Steve Martin at the Iowa State University with the ball-milling method, which is prone to creating paramagnetic impurities, e.g., iron, in the samples, which have an influence on the relaxation of ion-conducting glasses [Grü95]. Some of the experiments, for example the $T_{1\rho}$ and the T_1 measurement at $2\pi \times 155\,\mathrm{MHz}$, have been conducted at the State University Research Park of St. Petersburg, Russia by G. Dost. The results of the St. Petersburg experiments, as well as the data at the Larmor frequencies $2\pi\times144\,\mathrm{MHz}$, $2\pi\times76\,\mathrm{MHz}$, and $2\pi\times27\,\mathrm{MHz}$ have already been published in his Master's thesis [Dos16].

In the following, the $0.7\mathrm{Li_2S}$–$0.3\mathrm{B_2S_3}$ and $0.7\mathrm{Li_2S}$–$0.27\mathrm{B_2S_3}$–$0.03\mathrm{B_2O_3}$ (mol %) samples will be denoted as O0 and O1, respectively.

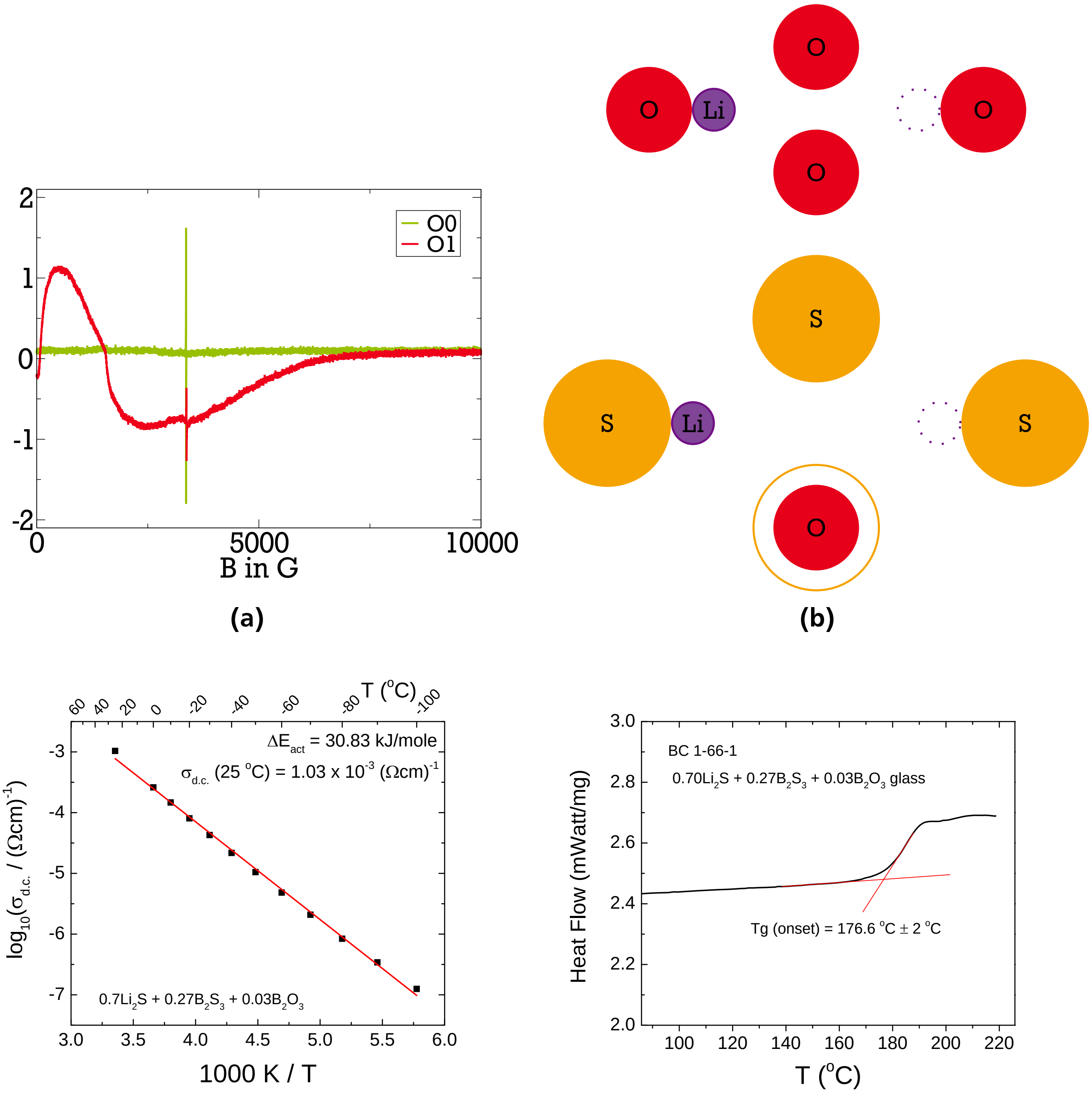

(a) **(b)**

(c) **(d)**

Figure 7.1.: (a) Electron paramagnetic resonance (EPR) spectra of O0 and O1. The distinctive peak observed for both samples is caused by iron. The additional broad peak of O1 corresponds to several other elements like nickel and cobalt. (b) Pictorial representation of the MGFE. In pure oxide based network formers (above) the relatively small atomic radius of O, 60 pm, leads to high energy barriers for the lithium ion jumps to vacant sites (dotted circle). In pure sulfide based network formers, the bigger atomic radius of S, 100 pm, causes smaller energy barriers. Partial substitution of sulfur with oxygen further widens the diffusion pathways of the lithium ions resulting in even lower energy barriers (below). Modified from [Kim06]. Conductivity (c) and DSC measurements (d), revealing a glass transition temperature $T_g = 176.6\,^\circ\mathrm{C}$ for sample O1.

7.1 Initial measurements

In this section, the measurements conducted by G. Dost will be presented, while experiments performed after the samples were sent back from St. Petersburg are discussed in Sec. 7.2.

7.1.1 Spin-lattice relaxation

The magnetization recovery of O0 and O1 at $\omega_\mathrm{L} = 2\pi \times 76\,\mathrm{MHz}$ is shown in Figs. 7.2a and 7.2b, respectively. For O0, the recovery is mono-exponential ($\beta_\mathrm{T1} = 1$) over the whole temperature range, while a mild deviation from mono-exponential relaxation is observed for O1 at temperatures above 200 K. The corresponding SLR times for various Larmor frequencies ω_L are depicted in Figs. 7.3a and 7.3b. At low temperatures the SLR times are nearly constant, indicating that the relaxation process is not dominated by lithium ion dynamics for both samples in this temperature regime, q.v. Sec. 6.1.3. Whichever process is responsible for the relaxation below 170 K must be frequency dependent, indicated by the different height of the low-temperature plateau for the differing frequencies. The most crucial difference between the SLR data of O0 and O1 is the fact that the relaxation of O1 is much faster. The relaxation times are approximately one order of magnitude lower at all frequencies and temperatures. However, the decrease of T_1 is not a sign of enhanced lithium ion dynamics in O1. With an anisotropy parameter of $\delta_\mathrm{Q} \approx 100\,\mathrm{kHz}$, the minimum of the SLR time at $\omega_\mathrm{L} = 2\pi \times 76\,\mathrm{MHz}$ should be roughly $T_{1\mathrm{min}} \approx 0.1\,\mathrm{s}$, q.v. Eq. (5.1). A quadrupolar coupling of 1 MHz would be needed to observe a minimum of T_1 at 1 ms. A quadrupolar coupling of this strength is very unlikely for ^{7}Li [Hun12] and is definitely not present in this samples as can be seen from the widths of the static spectra shown in the next section. Therefore, the relaxation, especially for O1, is too fast to be related to lithium ion dynamics. A possible explanation for the existence of relaxation times in the millisecond regime is given below.

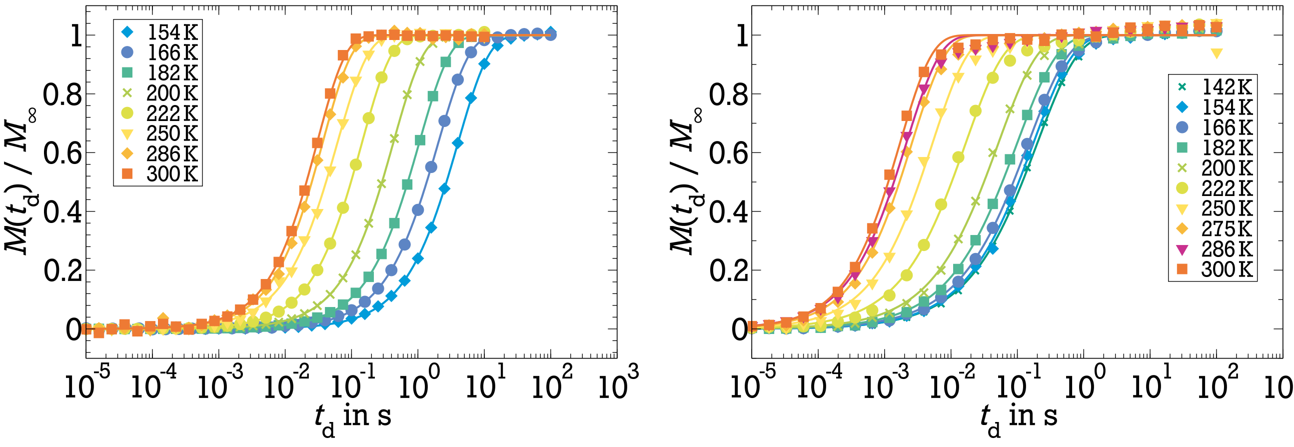

(a)

(b)

Figure 7.2.: Saturation recovery of O0 (a) and O1 (b). All curves are mono-exponential, only for sample O1 and $T > 200\,\mathrm{K}$ a mild deviation is observed.

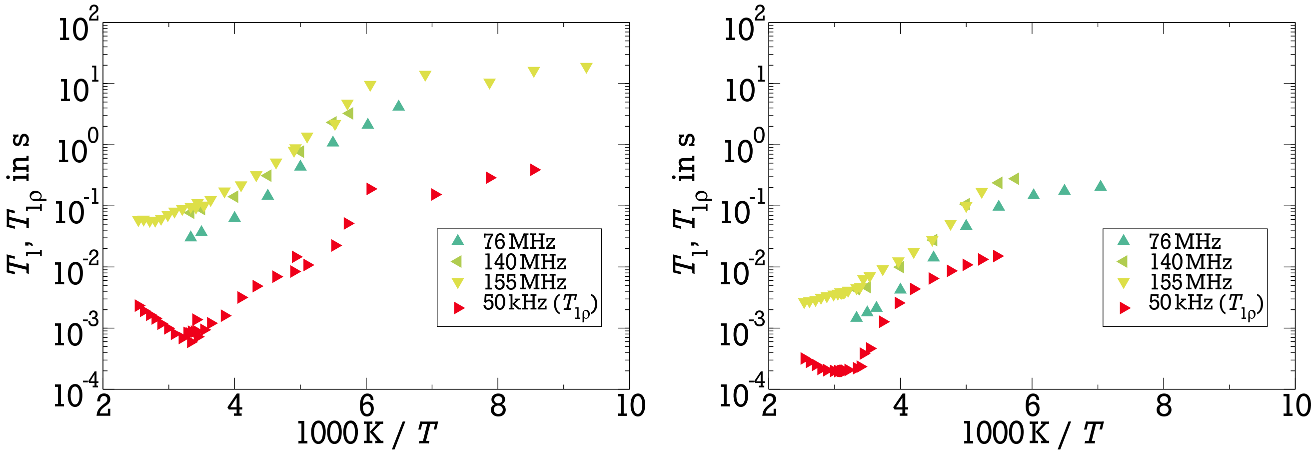

(a) **(b)**

Figure 7.3.: SLR times of O0 (a) and O1 (b). The temperature-independent plateau for $T < 170\,\mathrm{K}$ and SLR times of $T_1 < 0.1\,\mathrm{ms}$ for $T > 200\,\mathrm{K}$ indicate that lithium ion dynamics is hardly responsible for the spin-lattice relaxation, especially for sample O1.

7.1.2 Line-shape analysis

^{7}Li NMR spectra have been recorded to study the Li ion dynamics in the micro-second regime and are presented in Figs. 7.4a and 7.4b for samples O0 and O1, respectively. All spectra shown in Fig. 7.4 are two-component spectra as introduced in Sec. 3.4.5 and have been analyzed with Eq. (3.90). First, the width of the central and satellite transitions, $\Sigma^{\mathrm{c}}_{\mathrm{RL}}$ and $\Sigma^{\mathrm{s}}_{\mathrm{RL}}$, have been obtained from the static spectrum at the lowest temperature. Then, the line width of fast dynamics, Σ_∞, has been determined from the spectrum at the highest temperature. Finally, the other spectra were analyzed to get access to the weighting factor $W(T)$. It should be mentioned, that the fraction of the central line in the static spectrum, $f^{\,\mathrm{c}}$, has not been kept constant during this analysis. The FWHM of the spectral components are listed in Tab. 7.1, while the weighting factors $W(T)$ are presented in Fig. 7.5. Most striking is the relative high value of the high-temperature width ($\Sigma_\infty > 1\,\mathrm{kHz}$) for the sample O1, which is almost double of the respective value for sample O0. As the ENL has not be reached for O1 in the investigated temperature range, Σ_∞ could not be derived independently. Therefore, the given value of Σ_∞ shouldn't be taken too seriously.

The temperature dependence of $W(T)$ with its continuous increase is typical for a single Gaussian DAE. For O0, $W(T)$ increases faster and reaches its high-mobility limit ($W(T) = 1$) at a lower temperature, indicating that the corresponding DAE has its maximum E_{m} at a lower energy and its width, represented by the standard deviation σ_{E}, is narrower. This is confirmed when $W(T)$ is analyzed by means of a DAE with Eq. (3.89). The results of this analysis are also listed in Tab. 7.1. Concluding, the findings of the line-shape analysis (LSA) yields a slower dynamics in sample O1 in contradiction to the enhanced conductivity observed in this sample as mentioned above.

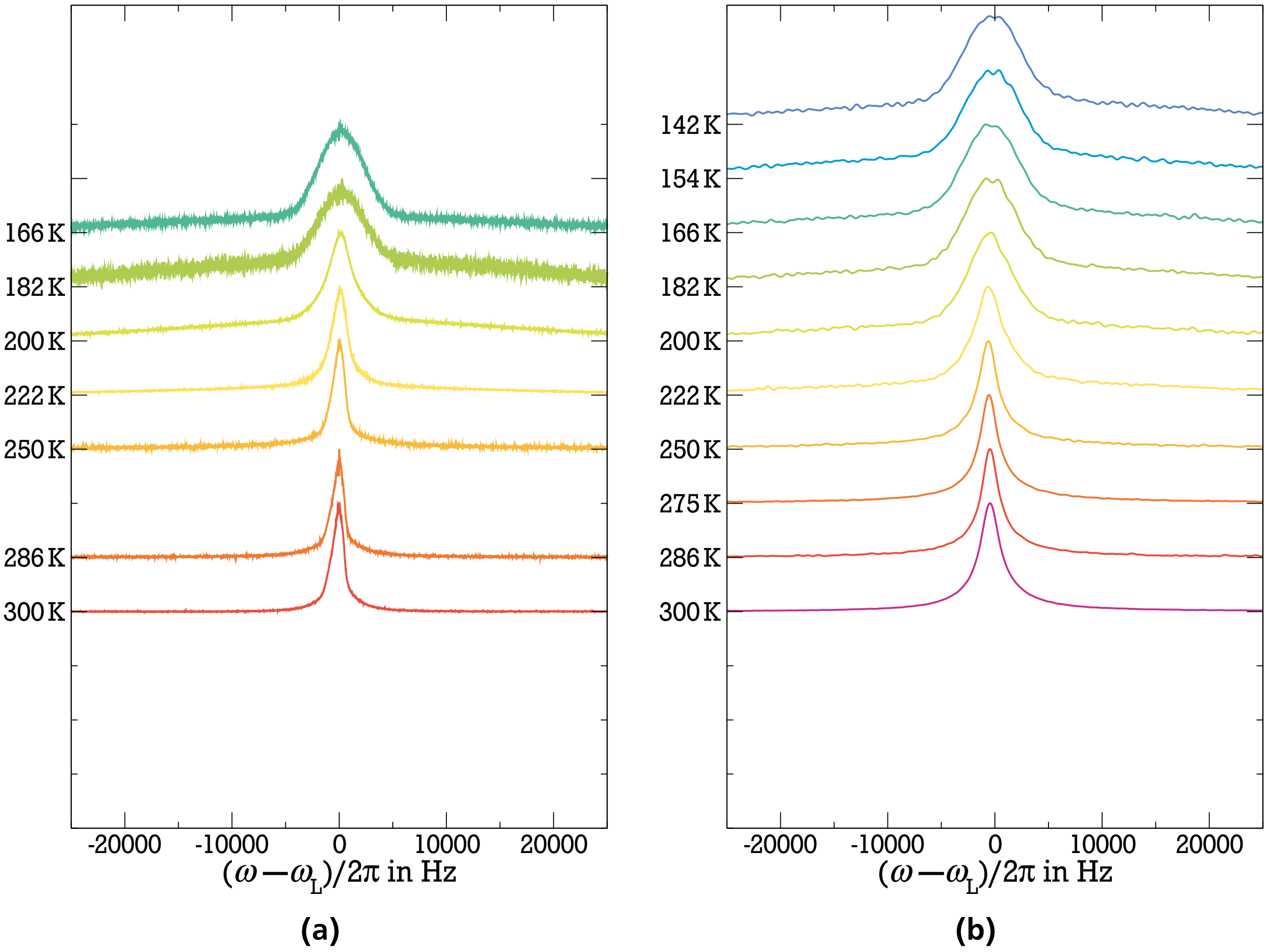

Figure 7.4.: Spectra of O0 (a) and O1 (b) obtained at $2\pi \times 76$ MHz.

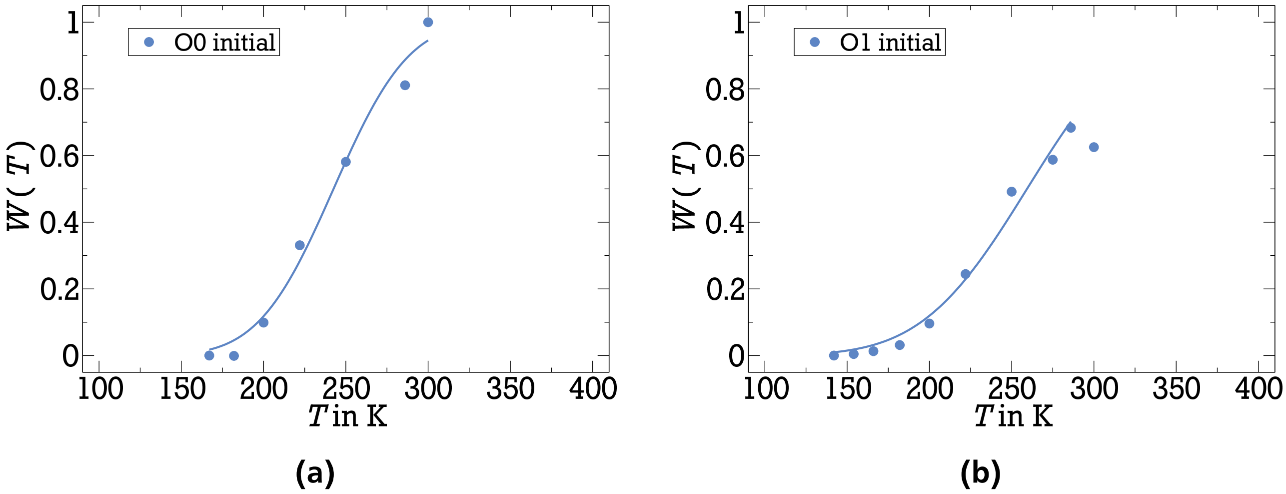

Figure 7.5.: Weighting factors of O0 (a) and O1 (b) for the initial measurement at $2\pi \times 76$ MHz. The solid lines are fits to Eq. (3.89).

7.1.3 Spin alignment

Spin-alignment echo (SAE) experiments have been performed to analyze the slow ion dynamics in the samples O0 and O1. The measured two-time correlation functions F_2^{SS} of O0 and O1 at $2\pi \times 140\,\mathrm{MHz}$ are shown in Figs. 7.6a and 7.6b, respectively. The measurement at $2\pi \times 140\,\mathrm{MHz}$ is presented here, because at $2\pi \times 76\,\mathrm{MHz}$ SAE experiments on sample O0 have not been performed on a broad temperature range. For both samples, the decays are highly stretched with stretching parameters $\beta_{F2} \leq 0.5$. This is expected as the existence of two-component spectra (see above) indicates a broad distribution of correlation times. From the decay time τ_2 and the stretching parameter β_{F2} the mean logarithmic correlation time τ_m has been calculated with Eq. (3.52) and the results are plotted in Fig. 7.7. The temperature dependence of τ_m of both samples can be described by the Arrhenius equation (2.10) with an activation energy of $E_a = 0.15\,\mathrm{eV}$. This is somewhat lower than usually observed for ^{7}Li SAE correlation times, see for example Sec. 6.3. Additionally, the temperature dependence of the SLR time T_1 is very similar for $170\,\mathrm{K} \leq T \leq 300\,\mathrm{K}$. These findings indicate that the decay of the two-time correlation function F_2^{SS} might be related to the relaxation time of the spin-alignment state T_{1Q}, although T_1 differs from the decay-time of F_2^{SS} by more than the expected factor of 25/8 [Böh07b], especially for O0.

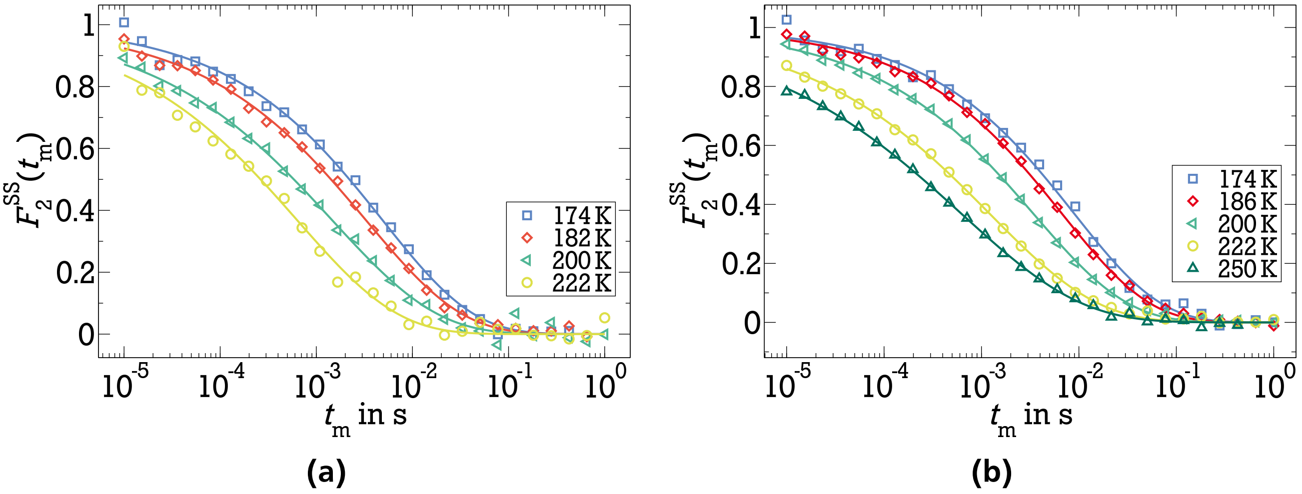

Figure 7.6.: Spin-alignment echo experiments of O0 (a) and O1 (b) at $2\pi \times 140\,\mathrm{MHz}$.

7.1.4 Interim conclusion

The SLR times, especially of sample O1, are too fast to be explained solely by lithium ion dynamics and also the two-time correlation function F_2^{SS} seems to be influenced by the extremely fast relaxation in the samples. Therefore, the purity of the samples were investigated by means of electron paramagnetic resonance (EPR) in St. Petersburg to investigate whether the fast relaxation is caused by paramagnetic impurities. Indeed, EPR spectra of $0.7Li_2S–0.3B_2S_3$ and $0.7Li_2S–0.27B_2S_3–0.03B_2O_3$ show distinctive peaks caused by iron. The additional broad peak of the $0.7Li_2S–0.27B_2S_3–0.03B_2O_3$ EPR spectrum corresponds to several other elements like

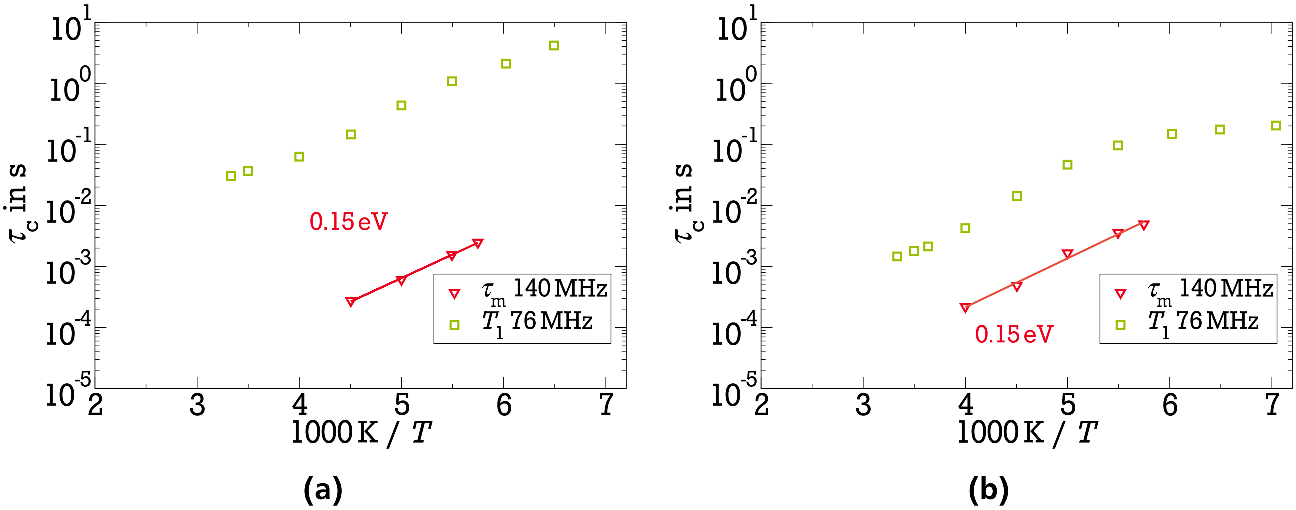

Figure 7.7.: Spin-alignment echo correlation times of O0 (a) and O1 (b). For both samples, the temperature dependence of τ_m and T_1 is similar for $170\,\mathrm{K} \leq T \leq 300\,\mathrm{K}$.

nickel and cobalt (see Fig. 7.1a). Hence, the low-temperature plateau of the SLR times T_1 is caused by iron [Grü95], while the enhanced relaxation in O1 is due to the other impurities present in this sample.

^{7}Li NMR spectra are not influenced by impurities [Grü95]. Thus, the broad distribution of correlation times indicated by the two-component spectra are caused by the numerous distinctive environments of the lithium ions in the amorphous samples. So far, no clear statement can be given whether the enhanced conductivity of O1 is caused by faster lithium ion dynamics or not.

7.2 Heat treated samples

Additional to the EPR experiments, measurements of the relaxation time in the rotating frame $T_{1\rho}$ have been conducted in St. Petersburg. The results have been included in Fig. 7.3. For these experiments, the samples had to be heated to 400 K to observe a clear $T_{1\rho}$ minimum, which is only 50 K below T_g. As a result of this heat treatment, a drastical change in the SLR of O0 and O1 is observed. As heating of glasses can lead to ceramization with enhanced dynamics, q.v. Chap. 8, the measurements have been repeated at Larmor frequencies of $2\pi \times 27$ MHz and $2\pi \times 63$ MHz to analyze the influence of this heat treatment on the $0.7\mathrm{Li_2S}$–$0.3\mathrm{B_2S_3}$ glasses. The results of the SAE experiments are not shown in this chapter as they revealed no difference between the initial and the heat treated samples. Additionally, ^{7}Li FC relaxometry and diffusometry measurements have been performed and the corresponding results are presented in this section.

7.2.1 Spin-lattice relaxation

Figure 7.8 shows the magnetization recovery of O0 and O1 at $2\pi \times 63$ MHz. Now, the recovery is bi-exponential with a stretched second step, the fraction of which, a_s, is nearly constant at low temperatures and decreases for $T > 250$ K as shown in Fig. 7.8c. For sample O0, the stretching factor of the second step scatters around $\beta_{\mathrm{T1s}} \approx 0.45$ with a distinct minimum at 275 K. The measured high-field SLR times of the heat treated sample O0 are presented in Fig. 7.8e. The data at $2\pi \times 76$ MHz have been obtained before the $T_{1\rho}$ measurements but are displayed here for comparison. Two SLR times differing by about one order of magnitude are shown for $2\pi \times 27$ MHz and $2\pi \times 63$ MHz according to the two step recovery mentioned above. A deviation from the low-temperature plateau for the slow process occurs at approximately 250 K and might be the reason for the change of β_{T1s} and a_{s} in this temperature regime. At high temperatures the fraction of the slowly relaxing species reaches 0.2. The rise of β_{T1s} for higher temperatures is due to the enhanced dynamics leading to an averaging of the corresponding SLR time and reducing its distribution. The relaxation due to lithium ion jumps kicks in at ca. 170 K for the fast process, resulting in T_1 minima occuring between 300 K and 400 K, depending on the Larmor frequency. The deviation from the low-temperature plateau takes place at approximately the same temperature as for the unheated sample. The SLR time T_1 of the unheated sample and the fast process of the heat treated sample is nearly equal for the whole investigated temperature regime when comparing the measurements at $2\pi \times 76$ MHz and $2\pi \times 63$ MHz.

The findings for the sample O1 are quite the same as the one for sample O0 described above. The heat treatment during the $T_{1\rho}$ experiments had only a minor effect on the slow relaxation process yielding a fraction of $a_{\mathrm{s}} \approx 0.3$ at low temperatures as shown in Fig. 7.8d; the fraction at high temperatures is the same for O0 and O1 ($a_{\mathrm{s}} = 0.2$). The relaxation of O1 is also much faster for both components. The relaxation times are nearly one order of magnitude lower at all frequencies and temperatures (compare Fig. 7.8e and Fig. 7.8f), which is most likely the result of the existence of nickel and cobalt in O1 as mentioned above. Consequently, the temperatures indicating the transition between both regimes are the same for both samples: 170 K and 250 K for the fast and slow relaxation process, respectively.

These results indicate that heating the samples yielded a partial crystallization of the glasses. As the fast relaxation coincides with the relaxation in the initial glasses, the slowly relaxing species reside in the crystalline regions. The fraction of the crystalline regions seems to be higher in O0 than in O1, corresponding to the fractions of the slow relaxation process a_{s} at low temperatures. For high temperatures, the decrease of a_{s} can be explained with an exchange of both relaxing species on the time scale of T_1.

For a more meaningful analysis of the frequency dependent T_1 minima, FC measurements on sample O0 have been conducted between $2\pi \times 250$ kHz and $2\pi \times 9.5$ MHz at the spectrometer FC2. To obtain the precise positions of the minima, a parabola-fit has been used as shown in Fig. 7.9a. With the minimum condition $\omega_{\mathrm{L}}\tau_{\mathrm{c}} = 1$, correlation times are acquired, q.v. Fig. 7.9b, and an activation energy $E_{\mathrm{a}} = 0.55$ eV was obtained from an Arrhenius fit. The $T_{1\rho}$ minimum has been excluded from this analysis due to the apparent deviation from the other data. Both the position and height of the $T_{1\rho}$ minimum is nearly the same as the corresponding values for the T_1 measurement at $2\pi \times 377$ kHz, a frequency almost eight times the frequency of the rotating frame ω_1 used during the $T_{1\rho}$ experiments. A diverse influence of the impurities on different relaxation times could be the reason for this apparent discrepancy.

Performing FC measurements for O1 were prevented due to the extremely short relaxation times of just a couple of ms in this sample. T_1 is as short as, or even shorter, than the switching time of the FC spectrometers, q.v. Sec. 3.3.1.4. Consequently, only two correlation times could be

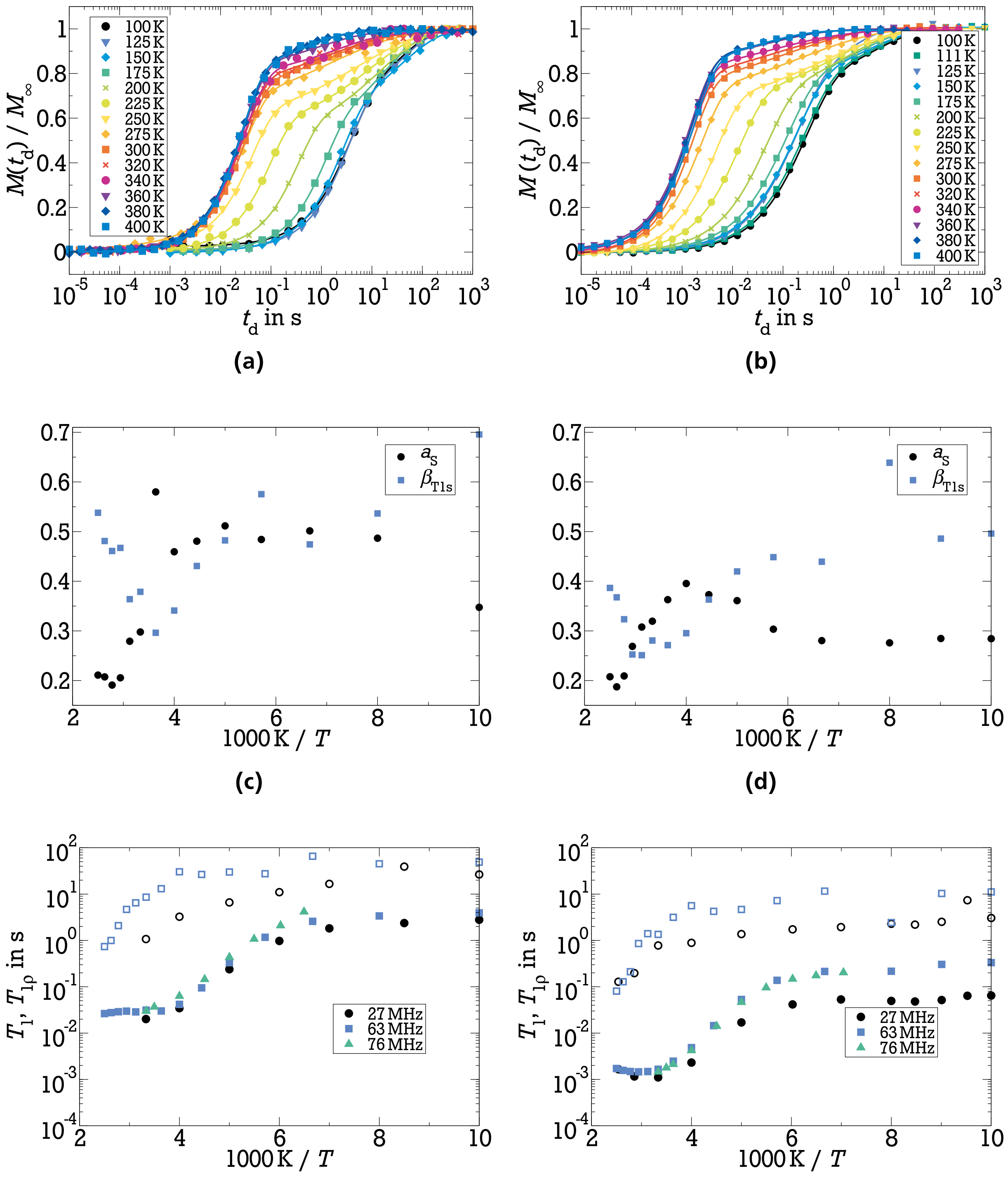

(a)

(b)

(c)

(d)

(e)

(f)

Figure 7.8.: Saturation recovery of the heat treated samples O0 (a) and O1 (b) at $2\pi \times 63$ MHz. All curves are now bimodal with an exponential first and stretched second step. The fraction a_s and stretching parameter β_{T1s} of the slow relaxation process for O0 (c) and O1 (d). For O0, a_s is aproximately 0.2 at high temperatures and 0.5 at low temperatures. The transition between those two plateaus takes place between 250 K and 350 K. In this transition regime a minimum of the stretching factor is observed. For O1, a similar behavior is observed. The main difference is a low-temperature plateau of 0.3 for a_s. SLR times of heat treated O0 (e) and O1 (f) are added to the plot. The open symbols represent the slowly relaxing species.

obtained from the T_1 minima of the $2\pi \times 27\,\mathrm{MHz}$ and $2\pi \times 63\,\mathrm{MHz}$ data, making an analysis with the Arrhenius equation obsolete.

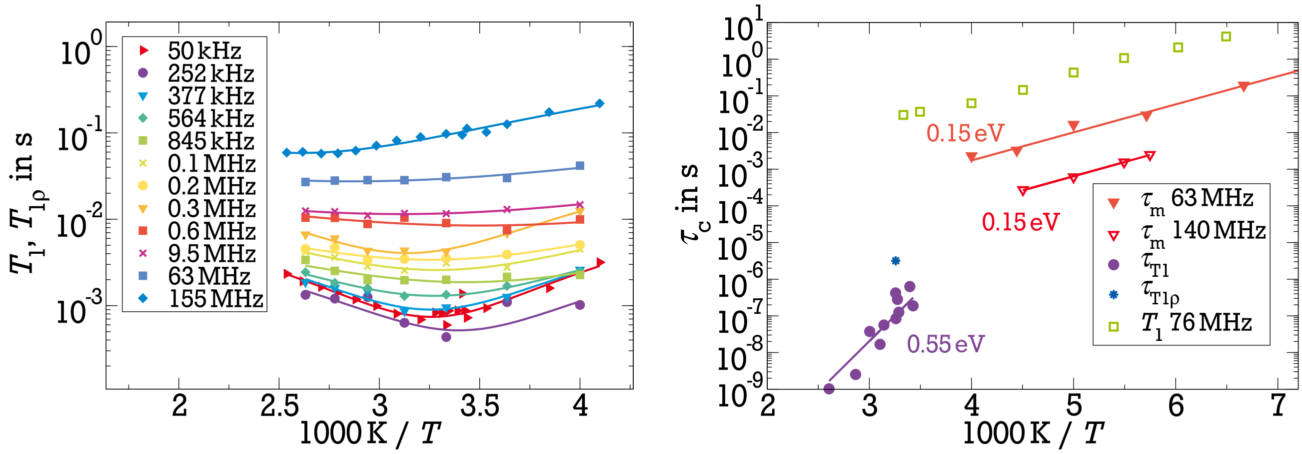

(a) **(b)**

Figure 7.9.: (a) Frequency dependent T_1 minima of heat treated O0. (b) Correlation times of heat treated O0.

7.2.2 Line-shape analysis

To analyze the dynamics of the fast and slowly relaxing species independently, partially relaxed (PR) and fully relaxed (FR) spectra have been recorded as described in Sec. 6.2. The PR spectra reflect the dynamics of the fast relaxing species directly, q.v. Figs. 7.11a and 7.11c, while the dynamics of the slowly relaxing species can be analyzed, when the PR spectrum is substracted from the FR spectrum as depicted in Figs. 7.11b and 7.11d. The poor SNR for $125\,\mathrm{K} \leq T \leq 275\,\mathrm{K}$ is caused by some temporary problems with the probe head. All spectra shown in Fig. 7.11 are two-component spectra as introduced in Sec. 3.4.5 and have been analyzed equivalent to the ^{7}Li NMR spectra of the initial samples described in Sec. 7.1.2. The FWHM of the spectral compositions are included in Tab. 7.1, while the weighting factors $W(T)$ are presented in Fig. 7.10.

For the slowly relaxing species, the motionally narrowing (MN) starts at relatively high temperatures and takes place on a broad temperature range in O0 and O1, indicating that the dynamics in the crystalline phase in both samples is slow when compared to the glassy phase. This result is in agreement with the higher temperature of the transition from the temperature independent relaxation to the relaxation dominated by lithium ion dynamics found for the crystalline phase, q.v. Sec. 7.2.1. For the fast relaxing species, the weighting factor $W(T)$ increases in two steps upon heating. Therefore, $W(T)$ has been analyzed with two DAEs with distinctive maxima (E_m^1 and E_m^2) and standard deviations (σ_E^1 and σ_E^2). For both samples, the temperature dependence of $W(T)$ of the initial measurements can be explained with the two DAEs acquired from the fast relaxing species, shown as dashed lines in Fig. 7.10. By comparing the FWHM of both samples, an increase of $\Sigma_\mathrm{RL}^\mathrm{c}$ for O1 of roughly 10% is observed, indicating the increase of the dipolar coupling and, hence, the density of the lithium ions, q.v. Eq. (3.29), by substituting a small amount

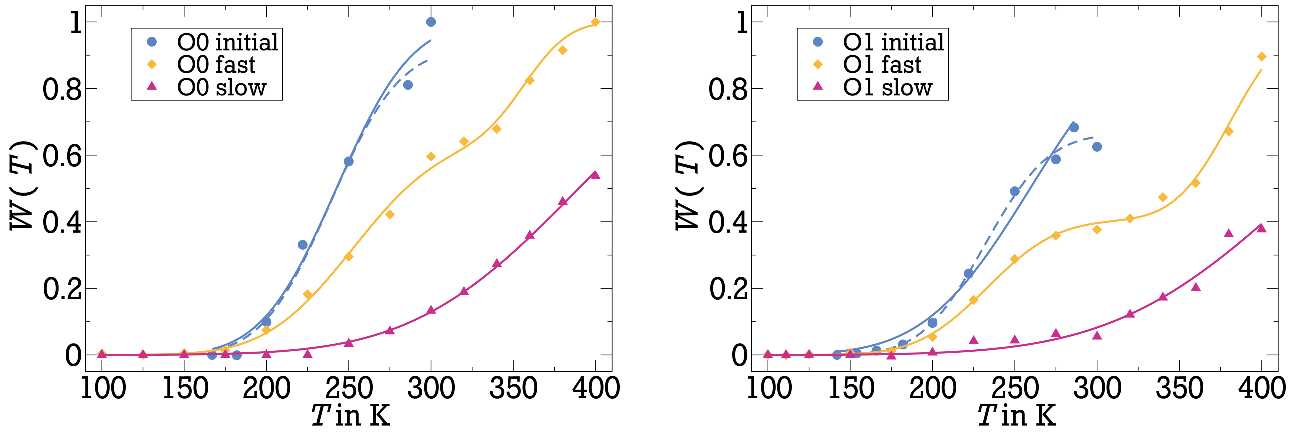

(a) **(b)**

Figure 7.10.: Weighting factors of O0 (a) and O1 (b) for the initial measurement at $2\pi \times 76$ MHz, as well as for the fast and slowly relaxing species at $2\pi \times 63$ MHz.

Table 7.1.: Line widths of the two-component spectra and parameters of the two distributions of activation energies. For the pre-exponential factor of the Arrhenius equation (2.10) $\tau_0 = 1.1 \times 10^{-16}$ s and $\tau^* = 1/\Sigma^{\mathrm{s}}_{\mathrm{RL}}$ have been used for all calculations. All Σ as introduced in Eq. (3.90) are given in Hz and all E_{m} and σ_{E} are given in eV. The values in parentheses denote the fractions of the first DAE when the $2\pi \times 76$ MHz data (initial) is analyzed with the fit of the $2\pi \times 63$ MHz measurement of the fast relaxation process, corresponding to the dashed lines in Fig. 7.10.

component	$\Sigma^{\mathrm{s}}_{\mathrm{RL}}$	$\Sigma^{\mathrm{c}}_{\mathrm{RL}}$	Σ_{∞}	E^1_{m}	σ^1_{E}	E^2_{m}	σ^2_{E}	f
O0 initial	41255	4853	665	0.51	0.08	-	-	1 (0.91)
O0 fast	46623	5677	180	0.53	0.09	0.74	0.04	0.64
O0 slow	58059	5801	225	-	-	0.80	0.16	0
O1 initial	46890	6097	1149	0.54	0.10	-	-	1 (0.66)
O1 fast	43763	6105	522	0.48	0.06	0.79	0.06	0.40
O1 slow	46378	5926	385	-	-	0.88	0.19	0

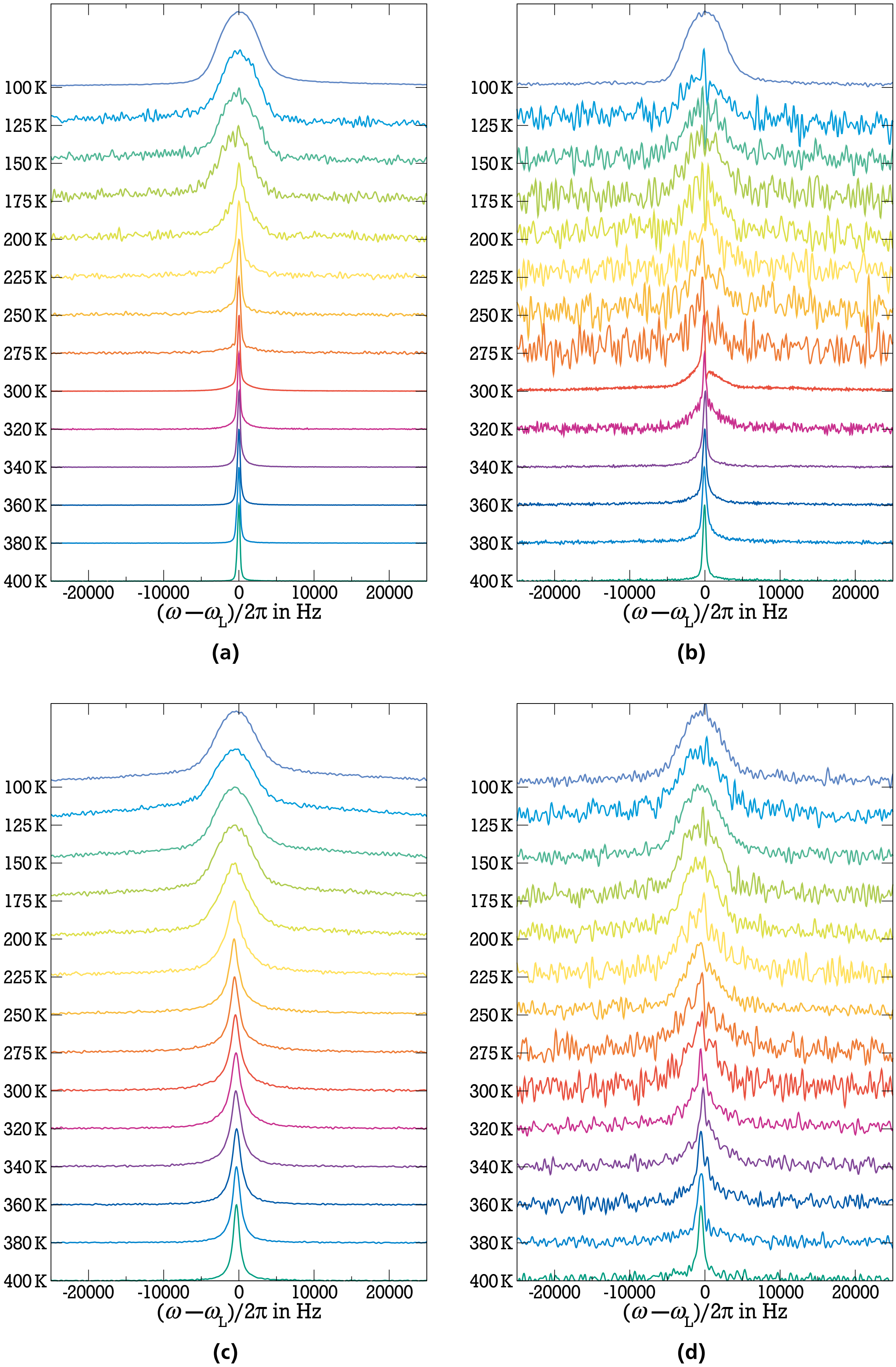

Figure 7.11.: Top: spectra of heat treated O0 at $2\pi \times 63$ MHz for fast (a) and slowly (b) relaxing species. Bottom: (c) and (d) show the corresponding spectra of O1.

of sulfur with oxygen. This increase of density is explained by the smaller atomic radius of oxygen. Most striking is the change of Σ_∞ after the heat treatment of the samples. The motionally narrowed spectra of the initial samples are more than twice as broad as the ones of the heat treated samples. Reasons for line broadening have already been listed in Sec. 3.3.2. Instrumental problems should not have effected Σ_∞ as the setup has not changed, with the exception of the strength of the magnetic field $\mathbf{B}_0$. Paramagnetic impurities can lead to line broadening, which is the reason why Σ_∞ of O1 is twice as high as Σ_∞ of O0. But the impurities do not disappear due to the heat treatment, indicated by the yet fast relaxation times of O1, as shown in Fig. 7.8f. Therefore, the line broadening of the initial samples is most probably explained by sample inhomogeneities, e.g., poor mixing or solid particles, which are eliminated by the heat treatment.

In summary, the findings of the line-shape analysis of heat treated O0 and O1 support the conclusion of the spin-lattice relaxation. Heating the samples resulted in partial crystallization with a reduced lithium ion dynamics in the crystalline phase.

7.2.3 Diffusion

To analyze the long-range transport of the Li ions in the thioborate glasses, stimulated echo (STE) measurements in a static field gradient (SFG) have been performed to obtain diffusion coefficients. This kind of experiment was conducted only after the samples were heated to 400 K. Therefore, no statement regarding the influence of the heat induced changes on the diffusion mechanism can be made. Due to the fast relaxation, especially of sample O1, only the high-temperature regime, where fast diffusion is expected, could be examined. During the measurement the evolution time t_p has been kept constant while the mixing time t_m was the variable parameter. This procedure was repeated for various evolution times as depicted in Fig. 7.12. At 440 K the decays for short t_p occur at the same mixing time, indicating that relaxation is responsible for the signal loss. For t_p longer than 100 µs, diffusion becomes the dominant mechanism for the decay resulting in a shift to shorter mixing times t_m when extending the evolution time t_p. A global analysis of all decays with Eq. (3.68) indicates a free 3D diffusion process on a length scale of $(\gamma g t_\mathrm{p})^{-1} \approx 1\,\mu\mathrm{m}$ for both samples. Therefore, the lithium ions observe the same diffusion mechanism in the glassy and crystalline phases for the investigated time and length scales.

The acquired diffusion coefficients of O0 and O1 are shown in Fig. 7.13, revealing an Arrhenius dependence for both samples. The lower activation energy and enhanced diffusivity in O0 is a clear evidence for the faster Li ion dynamics in this sample. These findings are in contradiction to the enhanced conductivity and reduced activation energy found for O1 prior to the heat treatment. The activation energy of $E_\mathrm{a} = 0.35\,\mathrm{eV}$ for O0 coincides with findings from conductivity measurements [Kim97a] but is lower than the maximum of the first DAE. As mentioned in Chap. 2, E_a obtained from conductivity measurements are often lower than the DAE maxima resulting from NMR experiments. This apparent discrepancy will be dealt with in more detail in the next chapter. For the heat treated O1, the diffusion activation energy $E_\mathrm{a} = 0.41\,\mathrm{eV}$ is higher than the conductivity activation energy of the initial O1. Therefore, the heating yielded a slow down of lithium ion dynamics in the sample 01.

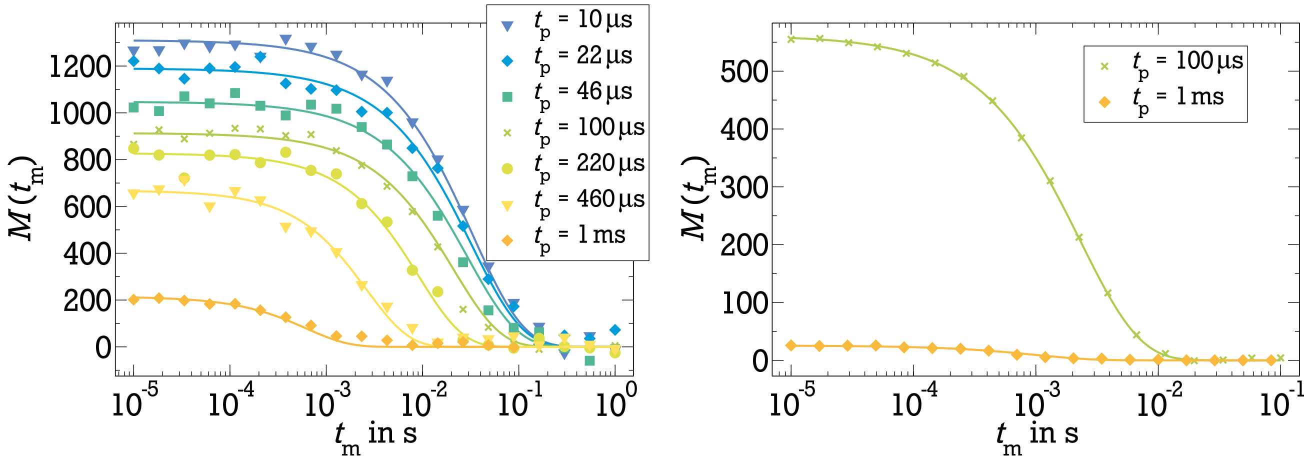

(a) **(b)**

Figure 7.12.: Diffusion measurement at 440 K for (a) O0 and (b) O1.

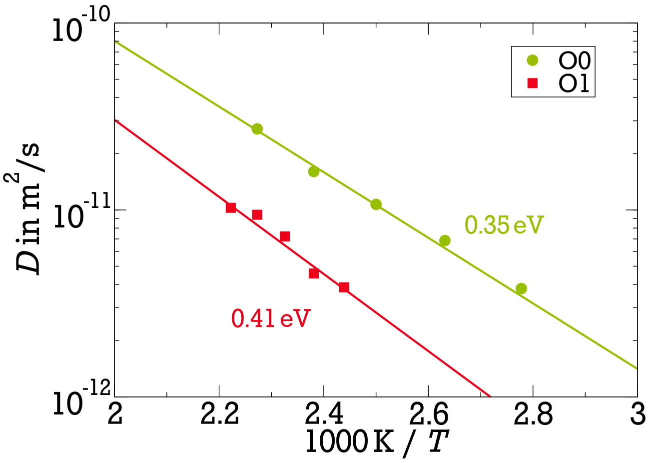

Figure 7.13.: Diffusion coefficients of O0 and O1.

7.3 Summary and conclusion

^{7}Li SLR, LSA, SAE, and SFG studies on the lithium ionic motion in glassy $0.7Li_2S$–$0.3B_2S_3$ (O0) and $0.7Li_2S$–$0.27B_2S_3$–$0.03B_2O_3$ (O1) have been performed. Irreversible changes occured to the prepared samples when heating to 400 K during the $T_{1\rho}$ measurements. Most noticeably, two lithium species with different ^{7}Li SLR are present in the samples after the heating with SLR times $\langle T_{1n} \rangle$ differing by more than an order of magnitude for the two species. The faster relaxation time $\langle T_{1f} \rangle$ is identical to the SLR time of the initial glasses. This indicates that heating the samples resulted in partial crystallization and the fast relaxing species resides in the remaining glassy phase, while the slow relaxation is caused by lithium ions in the crystalline phase. The biggest impact on the relaxation by substitution of 10% B_2S_3 with B_2O_3 is the decrease of the relaxation time for all investigated frequencies and temperatures. This is explained by the non-iron impurities present in $0.7Li_2S$–$0.27B_2S_3$–$0.03B_2O_3$, i.e., nickel and cobalt. These impurities are contaminations from the ball-milling preparation and not related to the existence of a second glass former. SAE experiments yielded correlation times with the same weak temperature dependence as the SLR time T_1, indicating that the decay of F_2^{SS} is caused by the fast relaxation in the samples. Therefore, no difference in the lithium ion dynamics of both samples could be obtained in the analysis by means of ^{7}Li SLR and SAE.

^{7}Li LSA has shown that two distributions of activation energies are present in the glassy phase. The distribution with the lower maximum position ($E_m = 0.53\,\mathrm{eV}$) is responsible for the local dynamics observed in the temperature dependent T_1 minima of O0 ($E_a = 0.55\,\mathrm{eV}$). The other distribution seems to have no effect on the local lithium ion jump dynamics.

While the investigation of the local jump dynamics did not show a significant difference between the two samples (either before or after the heat treatment), high-temperature diffusion measurements using the SFG method revealed a reduced long-range transport for the sample with two network formers. This result is in contradiction to the enhanced conductivity and reduced activation energy for conduction observed in O1. A possible explanation is the influence of the second DAE ($E_m \approx 0.79\,\mathrm{eV}$) which is shifted to higher energies and has a higher relative fraction for sample O1.

For this system of thioborate glasses, partial crystallization lead to a reduced lithium ion dynamics, especially for O1. In the next chapter it will be shown that such kind of partial crystallization by heating a sample can also lead to an enhanced dynamics of lithium ions. For a more detailed analysis of the mixed glass former effect in the presented system of thioborate glasses, samples with different relative quantities of both network formers should be investigated. Moreover, the preparation process should be optimized to enhance the purity of the samples.

8 0.7Li_2S–0.3P_2S_5 glass-ceramic

As mentioned in Chap. 7, glasses in the Li_2S-P_2S_5 system have been studied intensively because of their potential use as solid electrolytes. In 2005, Tatsumisasgo et al. have found that ceramization of 0.7Li_2S–0.3P_2S_5 (mol %) increases its conductivity [Miz05]. This glass-ceramic, a material supposedly consisting of a glassy and a crystalline phase, q.v. Fig. 8.1a, showed an extremely high conductivity of 3.2 mS/cm at ambient temperature. Analysis of XRD pattern revealed a crystalline phase in the glass-ceramic differing from Li_3PS_4 and $Li_4P_2S_6$ crystals, which are formed in the glass-ceramic heated at 823 K. This new high conductive phase has been considered metastable [Miz05]. It was identified as triclinic $Li_7P_3S_{11}$, composed of PS_4 tetrahedra, P_2S_7 ditetrahedra, and Li ions situated between them [Yam07]. In a later study, the $Li_7P_3S_{11}$ crystal could also be precipitated from the liquid phase as a primary crystal, indicating that the $Li_7P_3S_{11}$ crystal is a high-temperature phase [Min10], see Fig. 8.1b.

In recent years, many studies, experiments and simulations, of metastable $Li_7P_3S_{11}$ have been published. By varying details in the preparation a correlation between the ionic conductivity and the degree of crystallization was found [Min11, Sei15] and the conductivity could be further enhanced to 17 mS/cm, the highest conductivity of a solid electrolyte reported to date [Sei14]. An average Li-Li bond length of 4.3 Å could be obtained by quasielastic neutron scattering (QENS) [Mor15] and the body-centred cubic-like sulfur anion sublattice is claimed to allow direct Li hops between adjacent tetrahedral sites [Wan15]. Despite all these findings, no explanation for the origin of the increase of conductivity upon ceramization could be given. To investigate the short-range local dynamics and the long-range motion of lithium ions in 0.7Li_2S–0.3P_2S_5 glass and glass-ceramic, denoted as LiPS-GL and LiPS-GC in the following, respectively, several ^{7}Li NMR techniques were performed in the framework of this thesis.

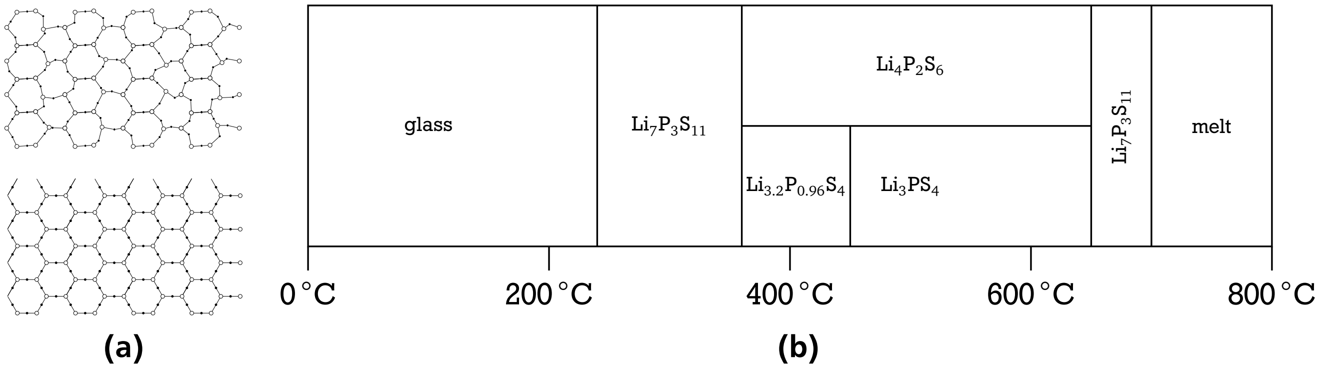

Figure 8.1.: (a) Sketch of a two dimensional glass-ceramic with glassy (top) and crystalline (bottom) phases. (b) Simple phase diagram of 0.7Li_2S–0.3P_2S_5 (mol %); adapted from [Min10].

8.1 Spin-lattice relaxation

To exploit the relation between the relaxation rate and the spectral density given in Eq. (3.37), the temperature and frequency dependence of $1/T_1$ is investigated. While a mono-exponential buildup of the magnetization is found in all ^{7}Li SLR studies on LiPS-GC, a two-step buildup is observed for LiPS-GL in the high-field measurements, as shown for the $2\pi \times 76\,\mathrm{MHz}$ experiments in Fig. 8.2. Therefore, the LiPS-GL data have been analyzed by fitting the recovery curves with two KWW functions, q.v. Eq. (6.1). As such bimodality is unusual for glasses, the structural integrity of the sample was confirmed by X-ray diffraction (XRD) and Raman spectroscopy. In the following, only the faster SLR process of LiPS-GL is focused on, which is still slower than that of LiPS-GC.

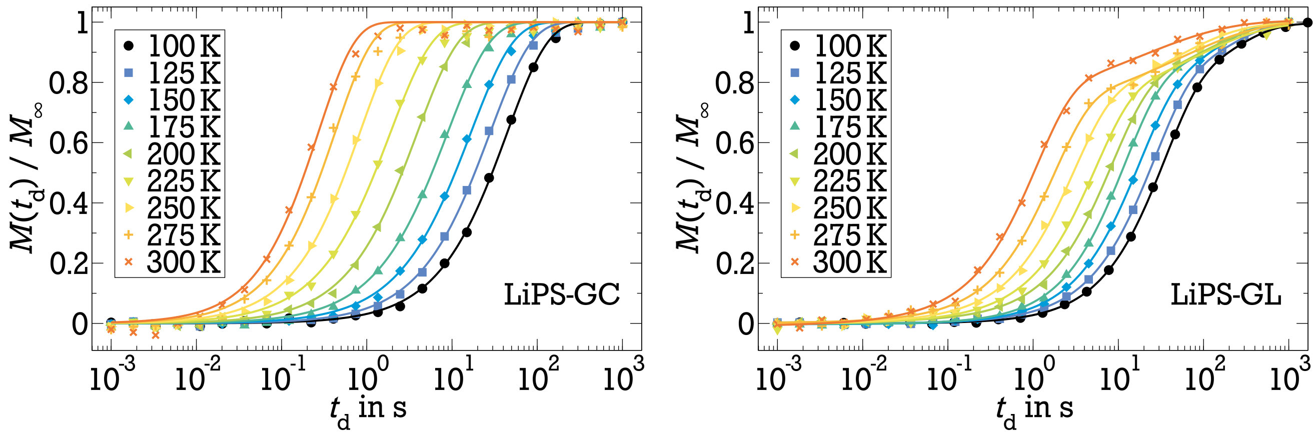

(a) **(b)**

Figure 8.2.: (a) Saturation recovery buildup curves of LiPS-GC at 76 MHz are mono-exponential in the whole temperature range. (b) Saturation recovery buildup curves of LiPS-GL at 76 MHz show bi-exponentiality with an exponential first and a non-exponential second step.

In Fig. 8.3 temperature dependent SLR rates $1/T_1$ for LiPS-GC and LiPS-GL at exemplary Larmor frequencies ω_L are shown. For LiPS-GC, the $1/T_1$ maxima indicate lithium ion dynamics on the time scale $1/\omega_\mathrm{L}$ in the studied temperature range. The speedup of the motion upon heating is reflected by the shift of the location of the maxima to higher temperatures for higher Larmor frequencies. Additionally, the maxima are lower at higher Larmor frequencies, consistent with the general expectations from SLR theory [Böh07a, Bri92]. For LiPS-GL, $1/T_1$ maxima are not observed in the whole accessible temperature range. The SLR rate monotonically decreases upon cooling, indicating that lithium ion dynamics is slow on the time scale $1/\omega_\mathrm{L}$ at temperatures below the glass transition. These findings reveal that local lithium ion dynamics is slower in LiPS-GL than in LiPS-GC. For LiPS-GC, temperature-dependent correlation times τ_c could be obtained from the observed frequency-dependent shift of the $1/T_1$ maxima. Assuming a susceptibility χ''_NMR which is symmetric on a log-scale, e.g., caused by a single exponential correlation function or a log-Gaussian distribution, the relation $\omega_\mathrm{L}\tau_\mathrm{c}(T_\mathrm{max}) = 0.616$ applies. Here, T_max denotes the temperature at which the respective $1/T_1$ is maximum. The resulting correlation times, as shown in the inset of Fig. 8.3b, are well described by an Arrhenius law (2.10) with an activation energy of $E_a = 0.49\,\text{eV}$.

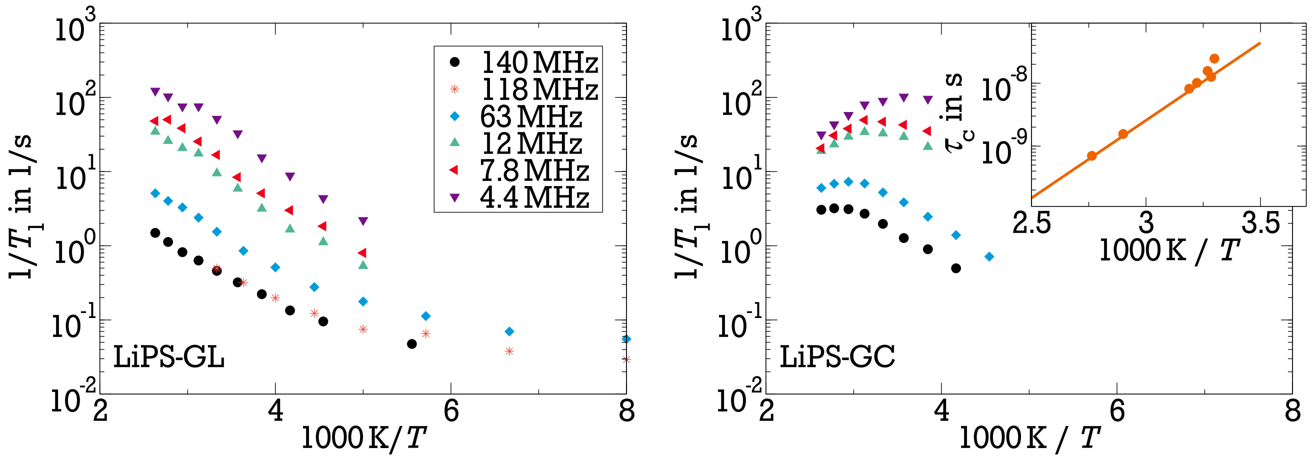

(a) **(b)**

Figure 8.3.: SLR rate $1/T_1$ for LiPS-GL (a) and LiPS-GC (b) at several Larmor frequencies. The indicated values $\omega_L/(2\pi)$ apply to both samples. In the inset of panel (b) correlation times τ_c of lithium ion dynamics in LiPS-GC are shown. These are obtained from the condition $\omega_L \tau_c(T_{\text{max}}) = 0.616$ where T_{max} denotes the temperature of the respective $1/T_1$ maximum. The straight line is an Arrhenius fit, yielding an activation energy of $E_a = 0.49$ eV.

Next, ^{7}Li FC relaxometry is used to obtain insights into the frequency dependence of the SLR rate. Therefore, the NMR susceptibility χ''_{NMR} is presented for the studied samples in Fig. 8.4, which gives directly access to the time scale of the dynamics through the condition $\omega_p \tau_c = 1$, where ω_p is the peak position of χ''_{NMR}. For LiPS-GC, a broad susceptibility maximum is observed, which shifts to higher frequencies upon heating, reflecting the speedup of the lithium motion. Additionally, the height of the susceptibility maximum weakly depends on temperature, indicating that the mechanism for ^{7}Li SLR and the strength of the quadrupolar interaction are unchanged in the studied temperature range, q.v. Eq. (3.37). A Debye peak would be observed for χ''_{NMR} with slopes ω_L^{+1} and ω_L^{-1} on the low- and high-frequency flanks, respectively, if lithium ion dynamics were described by a single exponential correlation function. Obviously, χ''_{NMR} is significantly broadened with respect to the Debye case, indicating that the correlation functions of lithium ion dynamics in LiPS-GC are strongly non-exponential. When thermally activated jumps of the lithium ions, governed by a temperature-independent Gaussian distribution of activation energies $g(E_a)$, are assumed, the broadening of χ''_{NMR} is explained by a temperature-dependent width of the distribution of correlation times $G(\ln \tau_c)$. Then, the NMR susceptibility is calculated according to Eq. (3.87). Figure 8.4a shows that this model, represented by the solid lines, accurately describes χ''_{NMR} in broad frequency and temperature ranges. The temperature-independent Gaussian distribution of activation energies $g(E_a)$ resulting from those fits is characterized by a mean energy $E_m = 0.43\,\text{eV}$ and a standard deviation $\sigma_E = 0.07\,\text{eV}$. The former value is in reasonable agreement with the temperature-dependent analysis described above. The latter value reveals that the lithium ion jump motion in LiPS-GC is caused by a distinct dynamic heterogeneity. This holds especially at low temperatures

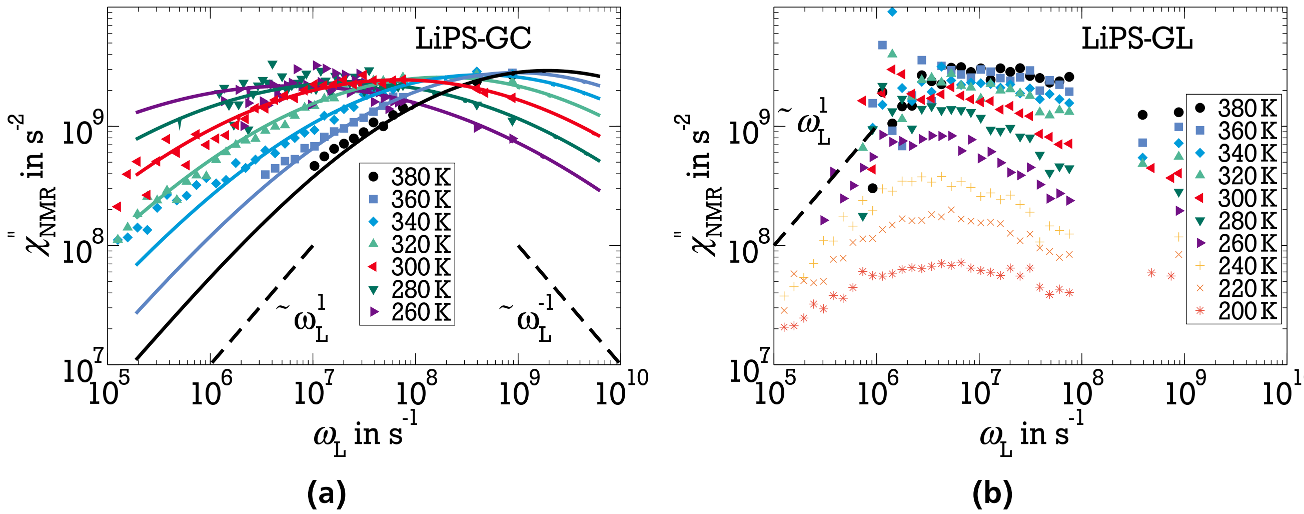

Figure 8.4.: χ''_{NMR} of LiPS-GC (a) and LiPS-GL (b). Interpretation of χ''_{NMR} with a distribution of activation energies is represented by solid lines.

where very broad distributions of correlation times result as a consequence of the fact that the width of $G(\ln \tau_c)$ increases with 1/T, q.v. Eq. (3.78) and Fig. 8.7b.

For LiPS-GL, χ''_{NMR} shows no clear maximum, which shifts through the frequency window when the temperature is varied. At $\omega_L \geq 10^6$ Hz, χ''_{NMR} weakly decreases with increasing frequency and the value at a given frequency strongly grows with increasing temperature. Consistent with the absence of $1/T_1$ maxima (see above), these results indicate that the ^{7}Li SLR of LiPS-GL is not governed by a site exchange of lithium ions in the studied frequency and temperature ranges. Rather other contributions to ^{7}Li SLR dominate, e.g., contributions from impurities [Fig78, Kle03] or two-level systems [BJ89]. At frequencies $\omega_L < 10^6$ Hz and low temperatures, ^{7}Li $1/T_1$ data should not be interpreted in terms of lithium ion motion at all [Gra13]. At such low frequencies, the Zeeman interaction is weaker than the quadrupolar one and at temperatures below 300 K, the lithium ion motion is too slow to fully average the quadrupolar interaction for LiPS-GL (see below).

8.2 Line-shape analysis

In Fig. 8.5 the temperature-dependent spectra of LiPS-GC and LiPS-GL are depicted in panel (a) and (b), respectively. The low-temperature spectra are comparable for both samples and show the broad and narrow Gaussian lines, usually observed in the rigid-lattice regime, q.v. Sec. 3.3.2. Contrarily, the motionally-narrowing schemes at high temperatures are different. For LiPS-GL, the Gaussian spectra evolve into a Lorentzian line when lithium ion dynamics becomes faster upon heating, indicating isotropic motion, consistent with the overall isotropy of glasses. For LiPS-GC, the motionally narrowing does not result in a Lorentzian line. Rather, the extreme narrowing limit spectrum consists of a narrow line and a broader foot, which has neither Lorentzian nor Gaussian shape and a width of approximately $2\pi \times 15$ kHz, as seen in the inset of Fig. 8.5a. These findings imply that a fraction of the lithium ions in LiPS-GC, most likely ions in the crystalline phase of the glass-ceramic, show anisotropic motion. By comparing ^{7}Li NMR spectra at intermediate temperatures, e.g., at 200 K, an advanced motionally narrowing in LiPS-GC as compared to LiPS-GL is observed, representing a faster lithium ion dynamics in the former than in the latter sample, consistent with the relaxometry results.

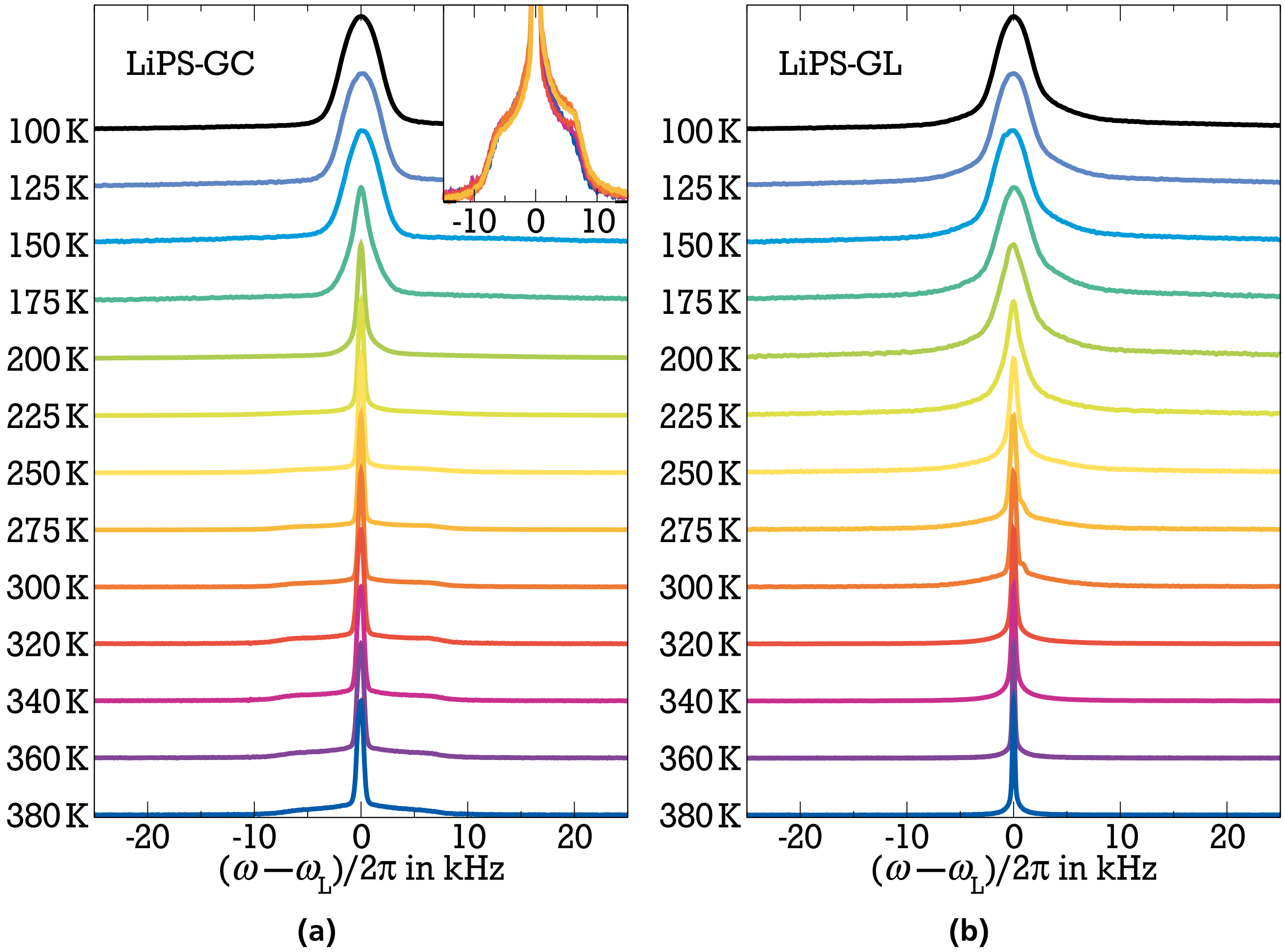

Figure 8.5.: Spectra of LiPS-GC (a) and LiPS-GL (b) at the indicated temperatures.

For a quantitative ^{7}Li line-shape analysis (LSA), the broad distribution of correlation times $G(\ln\tau_c)$ characterizing the lithium ion dynamics in LiPS-GC (see above) and, most probably, also in LiPS-GL has to be considered. As explained in Sec. 3.4.5, with a broad $G(\ln\tau_c)$, slow ($\tau_c \gg 1/\Sigma^s_{RL}$) and fast ($\tau_c \ll 1/\Sigma^s_{RL}$) lithium ions coexist at suitable temperatures. Here, Σ^s_{RL} is the static spectral width. Then, the temperature-dependent ^{7}Li NMR spectra can be described by a weighted superposition of the spectra in the limits of fast and slow dynamics, q.v. Eq. (3.91), with a weighting factor $W(T)$ as defined in Eq. (3.89). For LiPS-GC, such a weighted superposition of the high and low temperature spectra describes the ^{7}Li NMR spectra at all temperatures. Here, the low temperature spectrum consists of two Gaussian lines with widths Σ^s_{RL} and Σ^c_{RL} of the sattelite and central line, respectively. The high temperature spectrum of LiPS-GC is a superposition of a lorentzian line with a width Σ_∞ and a Pake-pattern described by an anisotropy paramter $\bar{\delta}_Q$ and an asymmetry parameter η_Q. The resulting parameters are given in Tab. 8.1. The weighting factors $W(T)$ obtained from the LSA are presented in Fig. 8.6. The transition from the rigid-lattice regime to the extreme narrowing limit takes place in a relatively broad temperature range between 150 K and 250 K. In another approach, the weighting factor $W(T)$ has been calculated based on Eq. (3.89) using the distribution of activation energies, $g(E_a)$, ac-

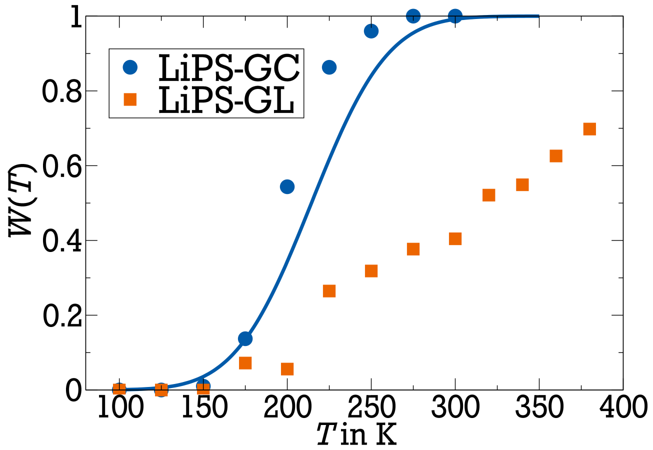

Figure 8.6.: $W(T)$ for LiPS-GC and LiPS-GL. The solid line is the $W(T)$ for LiPS-GC calculated from the distribution of activation energies obtained from the FC measurements.

quired from FC relaxometry and $\Sigma_{\mathrm{RL}}^{\mathrm{s}} = 2\pi \times 20.2\,\mathrm{kHz}$ as obtained from the spectra below 150 K. As shown in Fig. 8.6, the experimental (blue dots) and calculated (blue line) weighting factors $W(T)$ show a very similar temperature dependence. Hence, the information about local lithium ion dynamics in LiPS-GC obtained from ^{7}Li SLR and LSA are fully consistent.

For LiPS-GL, the ^{7}Li NMR spectra at intermediate temperatures cannot be described by a simple superposition of the spectra in the rigid-lattice regime and extreme narrowing limit. The ^{7}Li NMR spectra of LiPS-GL have been analyzed by a superposition of two Gaussians, reflecting the rigid-lattice regime, and a Lorentzian, which represents the extreme narrowing limit. However, different from the approach for LiPS-GC described above, temperature dependent width parameters have been allowed for the three lines for LiPS-GL, yielding good interpolations of the experimental data. The resulting weighting factors $W(T)$ are included in Fig. 8.6. Compared to LiPS-GC, the line-shape transition of LiPS-GL occurs at higher temperatures and in a broader range. While the former result confirms that ceramization speeds up local lithium ion dynamics, the latter finding implies that $G(\ln \tau_c)$ is even broader for LiPS-GL than for LiPS-GC. Therefore, a broader temperature interval is required to fully shift this distribution over the experimental time scale $1/\Sigma_{\mathrm{RL}}^{\mathrm{s}}$.

Table 8.1.: Parameter of the ^{7}Li NMR spectra used to determine the weighting factor $W(T)$. All parameters are given in kHz/2π, except η_Q.

sample	$\Sigma_{\mathrm{RL}}^{\mathrm{s}}$	$\Sigma_{\mathrm{RL}}^{\mathrm{c}}$	Σ_∞	$\bar{\delta}_Q$	η_Q
LiPS-GC	20.2	3.8	0.23	12	0.33

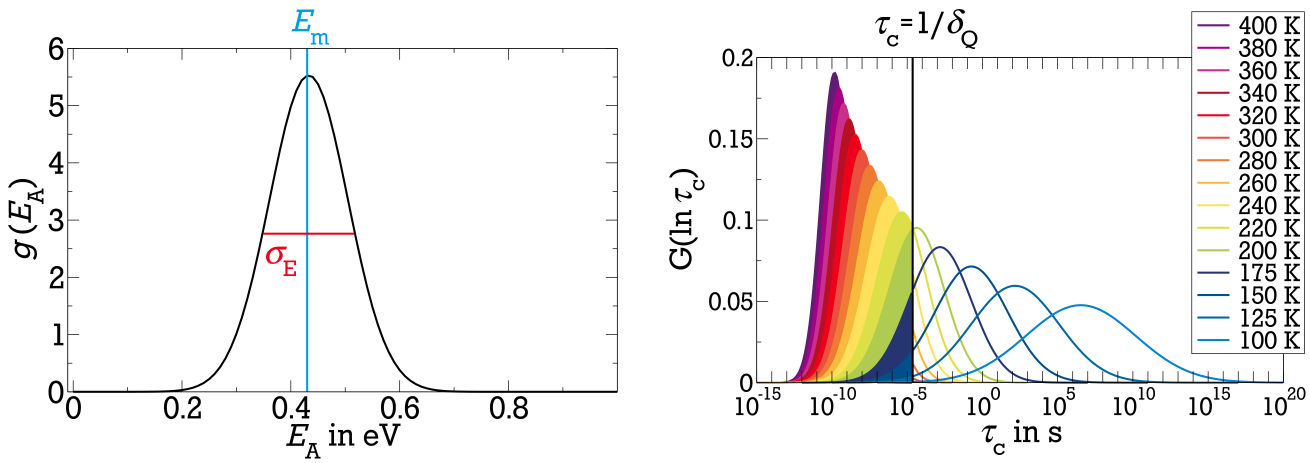

(a) **(b)**

Figure 8.7.: (a) Distribution of activation energies and (b) distribution of correlation times of LiPS-GC. The filled area of $G(\ln \tau_c)$ denotes the fraction of the fast ions representing the weighting factor $W(T)$.

8.3 Diffusion

Having characterized the lithium ion dynamics on local scales using ^{7}Li SLR and LSA, lithium ion diffusion on micrometer scale is now analyzed with the ^{7}Li SFG method described in Sec. 3.3.5. Figure 8.8a presents the results from SFG diffusometry on LiPS-GC at 360 K. It is clearly seen that, with increasing evolution time t_p, the stimulated echo amplitude $M(t_m)$ is reduced and the decay shifts to shorter mixing times t_m. The former effect is related to the spin-spin relaxation occuring during both evolution times of the stimulated echo, leading to a signal loss $\propto \exp\left[-2\left(t_p/T_2\right)^{\beta_{T2}}\right]$, q.v. Eq. (3.68). The latter is expected due to the evolution-time dependent length scale of the experiment: $\left(\gamma g t_p\right)^{-1}$. A global fit of the stimulated echo decays for all values of t_p to Eq. (3.68) reveals that a single self-diffusion coefficient D describes the data. These findings indicate that lithium ion motion in LiPS-GC on a micrometer scale is due to free diffusion in all three dimensions. In particular, possible differences of the diffusivities in the glassy and crystalline phases are not detected on the micrometer length scale of the SFG experiments. While the results of this SFG study do not agree with the outcome of a previous PFG work [Hay13], which reported anomalous diffusion with a length-scale-dependent diffusivity, it confirms findings of first principle calculations predicting widely spread three dimensional conducting paths [Kow10].

Self-diffusion coefficients D of LiPS-GL have been obtained in an analogous analysis. Here, only the fast relaxing species have been considered by conducting partially relaxed experiments. Figure 8.8b presents the results from SFG diffusometry on LiPS-GL at 360 K and the corresponding D of LiPS-GC and LiPS-GL for broad temperature ranges are shown in Fig. 8.9. In the studied temperature range, lithium ion diffusion is more than one order of magnitude faster in LiPS-GC than in LiPS-GL. The temperature dependence of the diffusion coefficients are very similar for both samples and can be described with the Arrhenius equation (2.10) using activation energies $E_a = 0.28$ eV for LiPS-GC and $E_a = 0.26$ eV for LiPS-GL. For comparison,

Fig. 8.9 displays also diffusion coefficients calculated from the dc conductivity based on the Nernst-Einstein relation (dotted lines) [Hay13] and obtained from QENS (red star) [Mor15]. The results of these different methods are in reasonable agreement. Conductivity and SFG studies reveal that the lithium ion mobility at ambient temperatures can be enhanced by ca. one order of magnitude upon ceramization. Comparison of diffusometry and relaxometry studies reveal, however, a significantly smaller activation energy for the former ($E_a = 0.28\,\mathrm{eV}$) than for the latter ($E_m = 0.43\,\mathrm{eV}$). This apparent discrepancy of activation energies is often observed when comparing results from different methods, cf. [Kim96a, Kim97a, Sva93] or [Hei03] and references therin. This holds especially for conductivity and NMR relaxometry studies and its origin will be discussed in the following.

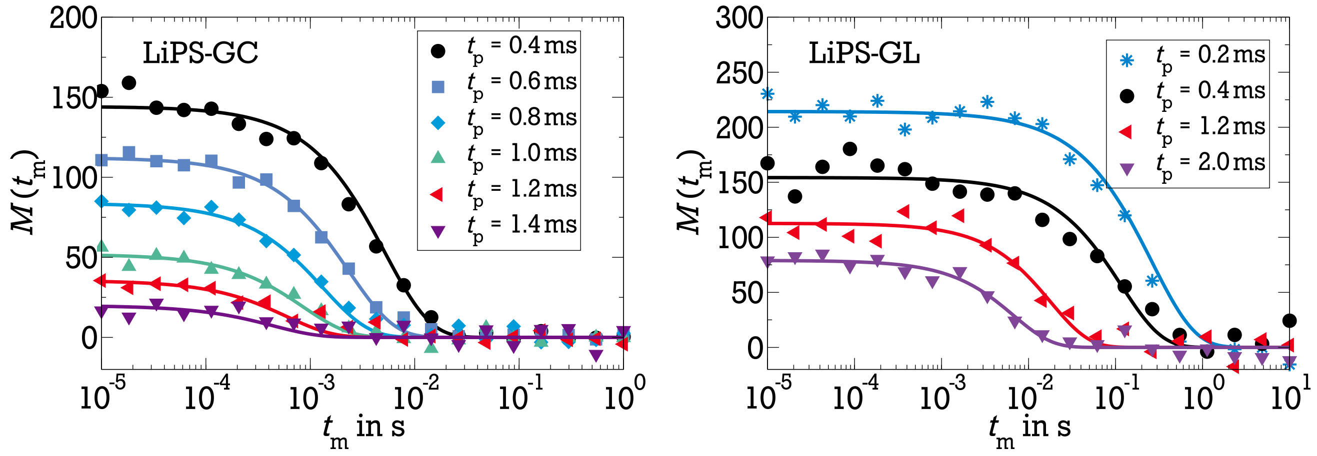

(a) **(b)**

Figure 8.8.: SFG measurements of LiPS-GC (a) and LiPS-GL (b) at 360 K. Global fits of the STE decays to Eq. (3.68) are shown as solid lines.

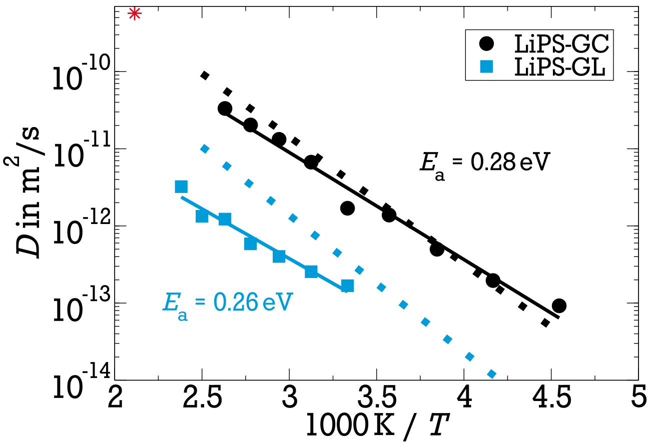

Figure 8.9.: Self-diffusion coefficients D of LiPS-GC and LiPS-GL. Solid lines are fits with an Arrhenius law, yielding activation energies of $E_a = 0.28 \pm 0.02$ eV and $E_a = 0.26 \pm 0.02$ eV, respectively. The dotted lines are diffusion coefficients obtained from dc conductivity using the Nernst-Einstein relation [Hay13]. The red star is a diffusion coefficient acquired from QENS [Mor15] using a ns time scale and nm length scale, respectively.

8.4 Relation of short-range and long-range lithium ion dynamics

Local jump dynamics of lithium ions in solids is often described by a random walk characterized by a single jump distance a and a single correlation time τ_c. Then, diffusion coefficient and correlation time are related according to [Ein05]

$$D = \frac{a^2}{6\tau_\mathrm{c}}. \tag{8.1}$$

However, if the local jump dynamics is characterized not by a single correlation time but by a broad logarithmic Gaussian distribution $G(\ln\tau_\mathrm{c})$ as described above, it is important to remember that different experiments probe different averages over this DCT. A detailed discussion of the different averages and their temperature dependences is given in Sec. 3.4.7. ^{7}Li NMR relaxometry yields the correlation time τ_m, when the maxima of $1/T_1(T)$ or $\chi''_\mathrm{NMR}(\omega)$ are observed. In the present case of symmetric distribution of correlation times, this correlation time marks the position of the peak of $G(\ln\tau_\mathrm{c})$. Therefore, τ_m corresponds to a logarithmic average, q.v. Eq. (3.99). ^{7}Li NMR diffusometry, as well as direct current (DC) conductivity, reflects the rate average of a distribution [Vog02]. The related mean correlation time is determined by the harmonic mean $\langle\tau_\Gamma\rangle$ as defined in Eq. (3.100). Note that Eqs. (3.99) and (3.100) consider the case where a temperature-independent distribution $g(E_\mathrm{a})$ yields a temperature-dependent distribution $G(\ln\tau_\mathrm{c})$ via the Arrhenius law. The temperature dependence of τ_m and $\langle\tau_\Gamma\rangle$, as calculated from the experimentally determined distribution of activation energies, see Fig. 8.7, is depicted in Fig. 8.10. It is clearly seen that τ_m is nearly two orders of magnitude longer than $\langle\tau_\Gamma\rangle$ at room temperature. This is because the rate average and, hence, the diffusion coefficient, are dominated by the fast ions of a distribution, q.v. Fig. 3.18a. Also the temperature dependences for τ_m and $\langle\tau_\Gamma\rangle$ are different. Obviously, τ_m is obtained from the Arrhenius law characterized by the mean activation energy E_m. The temperature dependence of $\langle\tau_\Gamma\rangle$ depends, however, not only on the mean energy E_m but also on the width parameter σ_E. As a consequence, the temperature dependence of $\langle\tau_\Gamma\rangle$ can be described by an apparent activation energy

$$E_\mathrm{app}(T) = E_\mathrm{m} - \frac{\sigma_\mathrm{E}^2}{2k_\mathrm{B}T}. \tag{8.2}$$

As a result, $\langle\tau_\Gamma\rangle$ has a weaker temperature dependence than τ_m. Additionally, Fig. 8.10 reveals that the broadening of $G(\ln\tau_\mathrm{c})$ upon cooling leads to a downward bending of $\langle\tau_\Gamma\rangle$ at low temperatures.

As shown in Fig. 8.10, these diverse behaviors of the various mean correlation times explain the different temperature dependences obtained from ^{7}Li SLR and SFG experiments. The calculated τ_m is in good agreement with the correlation times τ_{T_1} obtained from the $1/T_1$ maxima, q.v. Fig. 8.3b. This confirms that the frequency-dependent and the temperature-dependend SLR studies yield consistent results. A *diffusion correlation time* $\tau_D = a^2/(6D)$ has been calculated with the self-diffusion coefficients obained from the ^{7}Li SFG studies. The best agreement between τ_D and $\langle\tau_\Gamma\rangle$ is found for a jump length of $a = 0.52\,\text{Å}$, which is smaller than $4.3\,\text{Å}$, the average bond length for nearest-neighbor Li-Li bonds in LiPS-GC [Mor15]. The temperature dependence of τ_D and $\langle\tau_\Gamma\rangle$ agree well in the investigated temperature range, indicating that not only the short-range ion jumps, but also the long-range ion diffusion can be described by the same distribution of activation energies $g(E_a)$ depicted in Fig. 8.7a. In particular, the reduced temperature dependence of the self-diffusion coefficient D is explained by the fact that a rate average over the distributed dynamics is used to determine this quantity. Consequently, it depends not only on the shift of the distribution, but also on its width.

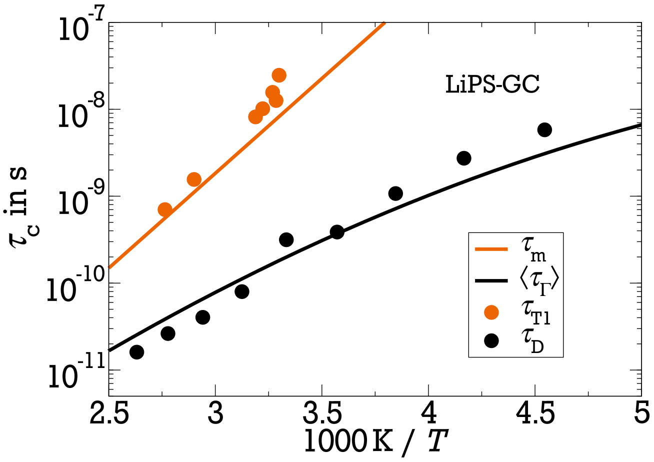

Figure 8.10.: Correlation times τ_c of LiPS-GC: τ_{T_1} denotes the correlation time obtained from the $1/T_1$ maxima and $\tau_D = a^2/(6D)$ is calculated from the self-diffusion coefficients using a = 0.52 Å. The solid lines are the correlation times τ_m and $\langle\tau_\Gamma\rangle$ calculated using the DAE obtained from the FC measurements and Eqs. (2.10) and (3.100), respectively. τ_m is the peak position of $G(\ln\tau_c)$ and $\langle\tau_\Gamma\rangle$ is the harmonic mean, i.e., the rate average.

To check the validity of this scenario for other solid electrolytes, τ_m and $\langle\tau_\Gamma\rangle$ were calculated for other systems where a Gaussian distribution $g(E_a)$ was observed in the literature. For this analysis, only data from samples of the same production batch have been used, ensuring that differences in the used preparation techniques are not responsible for the temperature dependence of correlation times.

Gabriel et al. did similar research on samples of the $0.5Li_2S+0.5[(1\text{-}x)GeS_2+xGeO_2]$ system [Gab15]. They obtained a DAE characterized by E_m = 0.49 eV and σ_E = 0.10 eV for the $x = 0$ sample, while the $x = 0.1$ sample has a Gaussian distribution $g(E_a)$ with E_m = 0.48 eV and σ_E = 0.09 eV. The diffusion coefficients of this samples were measured by the author of this thesis subsequent to the publication of [Gab15]. Analogous to the samples investigated in this work, the local dynamics in the $0.5Li_2S+0.5[(1\text{-}x)GeS_2+xGeO_2]$ system is described by τ_m while the long-range motion is dominated by $\langle\tau_\Gamma\rangle$, q.v. Figs. 8.11a and 8.11b.

When comparing ^{7}Li NMR experiments, resulting in E_m = 0.44 eV and σ_E = 0.05 eV, with conductivity measurements in the $0.7Li_2S\text{–}0.3B_2S_3$ system [Kim97a], the lower temperature dependence of the latter (E_a = 0.34 eV) is hardly distinguishable from $\langle\tau_\Gamma\rangle$ in the observed temperature range as shown in Fig. 8.12.

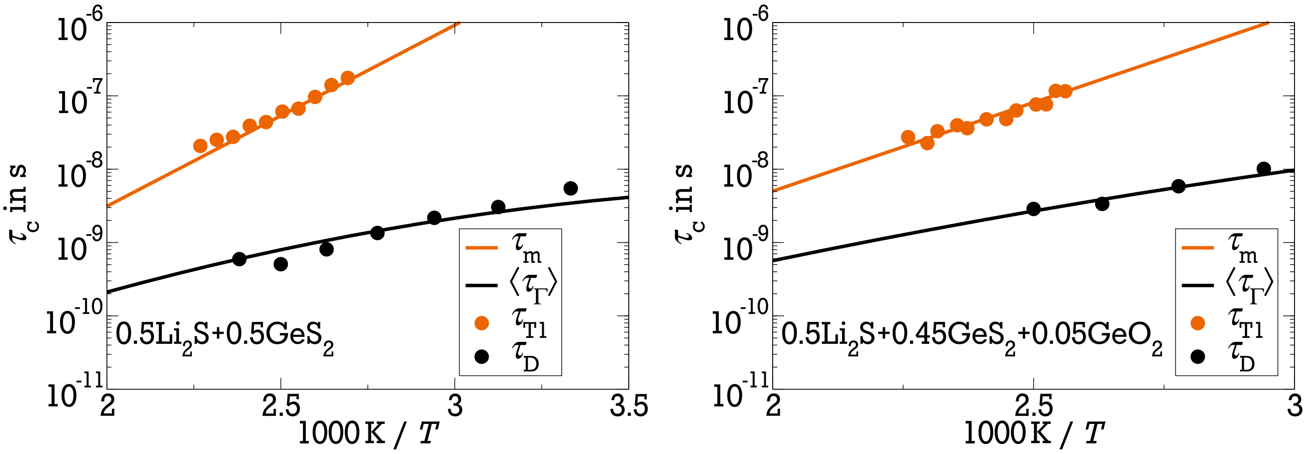

(a) **(b)**

Figure 8.11.: The different temperature dependences of ^{7}Li $1/T_1$ maxima and diffusion coefficients D in the 0.5Li$_2$S+0.5[(1-x)GeS$_2$+xGeO$_2$] system for $x = 0$ (a) and $x = 0.1$ (b) show the same behavior as τ_m and $\langle\tau_\Gamma\rangle$, respectively [Gab15].

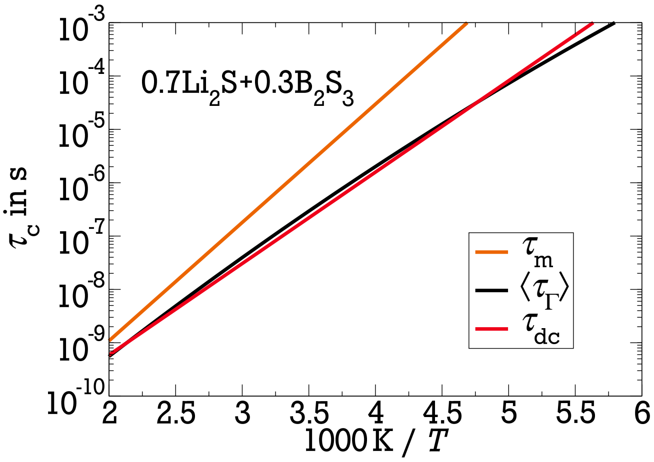

Figure 8.12.: Conductivity data also follows $\langle\tau_\Gamma\rangle$ [Kim97a]. For the sake of convenience, only the Arrhenius fits according to the activation energies given in [Kim97a] are plotted here as τ_m and τ_DC. $\langle\tau_\Gamma\rangle$ has been calculated according to Eq. (8.2).

These findings show that no theory, e.g., the coupling model or percolation theory, is needed to describe the differences of activation energies obtained from various experimental techniques. As some experiments probe a time average while other use a rate average, the corresponding temperature dependence of correlation times has to be different.

8.5 Summary and conclusion

Various ^{7}Li NMR methods were used to characterize lithium ion dynamics in LiPS-GC and LiPS-GL on different length scales. The results indicated that ceramization enhances the lithium ion dynamics on all length scales, confirming the findings of conductivity measurements. ^{7}Li SFG studies revealed that the self-diffusion coefficient D on a micrometer scale has a very similar temperature dependence for LiPS-GC and LiPS-GL, while it is about one order of magnitude higher for the former than for the latter. Speedup of the ion jump dynamics on a local scale has been shown by ^{7}Li SLR and LSA, e.g., ^{7}Li $1/T_1$ maxima were observed for LiPS-GC, indicating lithium ion dynamics on a time scale $1/\omega_L$, while these maxima are expected to occur only above the accessible temperature range for LiPS-GL. Also, the MN regime of ^{7}Li NMR spectra occurs at lower temperatures for LiPS-GC than for LiPS-GL. The anisotropic solid spectrum of LiPS-GC prevented a temperature dependent analysis of the two-time correlation function, q.v. Sec. 5.4.1. However, the corresponding measurements are briefly discussed in Appx. A.1.

No evidence for bimodal lithium dynamics, reflecting the different environments in glassy and crystalline regions in the glass-ceramics, were found for LiPS-GC, i.e., SLR and SFG data showed mono-exponential time dependence. On the other hand, ^{7}Li FC experiments revealed a broad distribution of activation energies $g(E_a)$ for local lithium ion jumps in LiPS-GC. The resulting NMR susceptibilities χ''_{NMR} in broad temperature and frequency ranges could be described by a temperature-independent Gaussian distribution, which is characterized by a mean energy $E_m = 0.43\,\mathrm{eV}$ and a standard deviation $\sigma_E = 0.07\,\mathrm{eV}$. The same Gaussian distribution could be used to explain the existence and shape of ^{7}Li two-component spectra in a broad temperature range for LiPS-GC, indicating that ^{7}Li FC relaxometry and LSA yield consistent results for lithium ion jump motion in this samples. For LiPS-GL, lithium ion dynamics turned out to be too slow to determine the distribution $g(E_a)$ below the glass-transition temperature.

Not only the short-range but also the long-range lithium ion dynamics in LiPS-GC can be rationalized in terms of the temperature-independent Gaussian distribution $g(E_a)$. It is crucial to consider that observables from different experimental techniques reflect diverse averages of the broadly distributed dynamics. NMR studies of local dynamics, e.g., FC relaxometry, are governed by the most probable correlation times of the distribution $G(\ln \tau_c)$. On the ther hand, NMR studies of diffusivities probe a rate average. Therefore, they are dominated by the fast part of the distribution, which depends not only on the position of the distribution $G(\ln \tau_c)$ but also on its width. Thus, the temperature dependence of the rate average probes both the shift and the broadening of $G(\ln \tau_c)$ upon cooling. Hence, the different activation energies obtained for short-range jumps and long-range diffusion, 0.43 eV and 0.28 eV, respectively, are explained by the diverse temperature dependence of the peak position and the harmonic mean. The apparent activation energy given in Eq. (8.2) most probably also explains the weaker temperature dependence of the self-diffusion coefficients D for LiPS-GL in comparison to LiPS-GC. Even with a higher mean energy E_m, the apparent energy E_app can be reduced, when the standard deviation σ_E of LiPS-GL is much higher than σ_E of LiPS-GC, which is assumed from the temperature dependence of the weighting factor $W(T)$. Furthermore, it could be shown that this result is not restricted to LiPS-GC and LiPS-GL, but can also be used to explain data of other systems, e.g., $0.5\mathrm{Li_2S}+0.5[(1\text{-}x)\mathrm{GeS_2}+x\mathrm{GeO_2}]$ [Gab15].

Finally, these findings are not restricted to NMR studies, but the different temperature dependences need to be considered for other observables, e.g., when comparing results from electrical conductivity and mechanical relaxation studies. This was confirmed by comparing the temperature dependence of $\langle\tau_\Gamma\rangle$ with that of conductivity measurements in the $0.7\mathrm{Li_2S}$–$0.3\mathrm{B_2S_3}$-system [Kim97a].

9 Conclusion

Quintessential goal of this thesis was establishment and application of ^{7}Li nuclear magnetic resonance (NMR) methods in terms of analyzing lithium ion dynamics in solid battery materials. These NMR methods were originally developed for $I = 1/2$ nuclei, e.g., ^{1}H, ^{13}C, and ^{31}P, or $I = 1$, e.g., ^{2}H and ^{6}Li, and could be transfered only recently to the $I = 3/2$ nucleus ^{7}Li [Gra13, Gab15, Sto16].

For the establishment of the used techniques, the fast ion conductor $Li_{10}SnP_2S_{12}$ proved to be the perfect sample. High lithium content and fast lithium ion dynamics is the ideal combination for conducting the ^{7}Li NMR methods mentioned above. Having a high amount of ^{7}Li is helpful for conducting field-cycling experiments and especially for measurements of the self-diffusion coefficient with the static field gradient method as these suffer from a relatively low signal to noise ratio. It was shown that lithium ion dynamics is accessible over a broad temperature range in terms of correlation times and self-diffusion coefficients using field-cycling and static field gradient measurements, respectively. Additionally, using $Li_{10}SnP_2S_{12}$, newly developed techniques introduced in [Sto16], including multidimensional experiments, could be successfully applied.

By combining different ^{7}Li NMR techniques, lithium ion dynamics in crystalline $Li_{10}SnP_2S_{12}$ has been obtained on a time scale of more than six orders of magnitude. The results consistently showed an Arrhenius-like temperature dependence of the correlation time with an activation energy of $E_a \approx 0.3\,\mathrm{eV}$.

In the quest for improved anode materials, polymer-derived silicon oxycarbide (SiOC) ceramics have received considerable attention as suitable hosts for lithium ions. To gain further knowledge about the dynamics of lithium ions in these heterogeneous material, lithiated and delithiated SiOC have been investigated. The measurements of SiOC ceramics have shown that irreversible changes occured to these samples when heating them to 400 K. This was indicated by the appearance of a second lithium species with a much slower spin-lattice relaxation time. Analysis of ^{7}Li NMR line shapes and correlation functions revealed that this difference in spin relaxation is not related to diverse dynamics of the lithium ions but is caused by different spin-relaxation mechanisms. Futhermore, these experiments showed that, in contrast to the situation in the crystalline ion conductor $Li_{10}SnP_2S_{12}$, broad distribution of correlation times $G(\tau_c)$ exist in amorphous lithiated and delithiated SiOC. Moreover, lithium ion jumps are, on average, faster in lithiated than in delithiated SiOC. The slower dynamics in the delithiated sample could arise from strongly oxygen bonded lithium ions, but further work is required to clarify this point.

One strategy to increase the conductivity of solid electrolytes is to take advantage of the mixed glass former effect (MGFE). Here, the substitution of a small amount of one network former with a second one leads to an enhanced dynamics. The origin of the speedup of lithium ion dynamics in mixed network former glasses has been analyzed in the $0.7Li_2S$–$0.3B_2S_3$ system. Here, the dynamics of a sample without oxygen (O0) was compared with that of a sample where a small amount of B_2S_3 was replaced by B_2O_3 (O1). Investigation of the local jump dynamics did not show a significant difference between O0 and O1. In contrast to the enhanced conductivity observed in O1, the diffusion in this sample is slowed down. Additionally, an accelerated spin-lattice relaxation was found in O1, which could be assigned to the presence of paramagnetic impurities. These impurities are contaminations from the ball-milling technique used to prepare the samples. Therefore, care has to be taken when using ball-milling for preparation of NMR samples.

Glass-ceramics are another class of systems with conductivities comparable to that of liquid electrolytes. However, the origin of enhanced ionic conductivity still awaits an explanation. In this work, the dynamics of lithium ions in glass-ceramic $0.7Li_2S–0.3P_2S_5$ (LiPS-GC) has been investigated. Analysis of NMR data of $0.7Li_2S–0.3P_2S_5$ samples confirmed that ceramization leads to an enhanced local lithium ion dynamics in this system. In the studied glass-ceramic LiPS-GC, no bimodality, corresponding to glassy and crystalline parts of the sample, could be observed. However, a Gaussian distribution of activation energies $g(E_\mathrm{a})$ is given for local lithium jumps. The exact shape of $g(E_\mathrm{a})$ could be obtained with field-cycling (FC) measurements and confirmed with line-shape analysis of ^{7}Li NMR spectra. All experimental results in broad temperature ranges are well described by the temperature independent $g(E_\mathrm{a})$ with mean $E_\mathrm{m} = 0.43\,\mathrm{eV}$ and variance $\sigma_\mathrm{E} = 0.07\,\mathrm{eV}$.

Another important question is the relation between ion dynamics on different time and length scales. In particular, the connection between elementary jumps and macroscopic transport is of interesst. Here, it was shown that the Gaussian $g(E_\mathrm{a})$ also well describes the long-range transport of lithium ions in LiPS-GC. However, it has to be considered that a rate average is responsible for the diffusion and an apparent activation energy E_app describes its temperature dependence. This E_app is related not only to the maximum of the distribution, E_m, but also to its width σ_E. It is not neccessary to use any models, i.e., the coupling model or the percolation theory, to explain the discrepancy of activation energies often found when comparing data of various analyses. This difference is a mere consequence of measurements probing distinct averages. These findings were confirmed by applying the result to literature data of other systems.

Altogether, improvements in understanding of tranport mechanisms of lithium ions requires characterization in broad dynamic and temperature ranges and, therefore, combination of various experimental methods. ^{7}Li FC and static field gradient measurements are an ideal combination, as the former probes local dynamics of lithium ions while the latter measures the long-range transport in the same temperature regime. A particular advantage of field-cycling relaxometry is the possibility to measure the distribution of activation energies $g(E_\mathrm{a})$ of the local lithium ion jump dynamics, often present in complex amorphous solids.

Appendices

A Numerical calculation of correlation functions

In Sec. 3.4 it is shown how to calculate the correlation function with the help of the distribution of correlation times, q.v. Eq. (3.88). As mentioned in Chap. 3, correlation functions are also connected to spectral densities through the fast fourier transform (FFT);

$$F_2(t) = \mathrm{Re}\,\frac{1}{\pi}\int_{-\infty}^{\infty} J(\omega_\mathrm{L},\tau_\mathrm{c})\exp(-i\omega t)\,\mathrm{d}\omega. \tag{A.1}$$

To simplify the calculation the exponent is replaced by its real part and the even character of the integrand is used, leading to the following form:

$$F_2(t) = \frac{2}{\pi}\int_{0}^{\infty} J(\omega_\mathrm{L},\tau_\mathrm{c})\cos(\omega t)\,\mathrm{d}\omega. \tag{A.2}$$

Usually, two-time correlation functions measured with NMR decay within a few decades. Nevertheless, the commonly known FFT essentially requires an equal spacing on the linear frequency axis, which makes its use inappropriate when dealing with logarithmically sampled points. The application of a simple rule of numerical integration like the Simpson rule requires replacing the integrand by a polynomial of grade n. This works quite well for small values of ωt, otherwise the oscillatory character of the integrand makes it run through several cycles between two adjacent sampling points of $J(\omega_\mathrm{L},\tau_\mathrm{c})$. As a consequence, the polynomial approximation fails. In the past, several attempts have been made to overcome this problems and properly calculate integrands of the form given in Eq. (A.2). One of the oldest method for numerical calculation of integrals with oscillating integrands was introduced by Filon [Fil30], who replaced just the slowly varying part $J(\omega_\mathrm{L},\tau_\mathrm{c})$ in parts of the interval by parabola and integrates the rapidly oscillating cosine term analytically. But also simpler Filon rules have been suggested, e.g., Tuck [Tuc67] and Blochowicz [Blo03]. Latter used just a linear interpolation of $J(\omega_\mathrm{L},\tau_\mathrm{c})$ in between two adjacent sampling points to obtain satisfying numerical results. His approach is as follows: Assuming the following approximation holds:

$$J(\omega_\mathrm{L},\tau_\mathrm{c}) \approx \begin{cases} J(\omega_0), & \omega \le \omega_0 \\ J(\omega_n) = 0, & \omega \ge \omega_n, \end{cases} \tag{A.3}$$

then the integral can be calculated with

$$\int_0^{\infty} J(\omega_\mathrm{L},\tau_\mathrm{c})\cos(\omega t)\,\mathrm{d}\omega \approx \sum_{i=0}^{n-1} \frac{J(\omega_{i+1}) - J(\omega_i)}{\omega_{i+1}-\omega_i}\,\frac{\cos(\omega_{i+1}t) - \cos(\omega_i t)}{t^2}. \tag{A.4}$$

The inverse transformation leads to an aquivalent equation:

$$\int_0^\infty F_2(t)\cos(\omega t)\,\mathrm{d}t \approx \sum_{i=0}^{n-1} \frac{F_2(t_{i+1})-F_2(t_i)}{t_{i+1}-t_i}\,\frac{\cos(\omega t_{i+1})-\cos(\omega t_i)}{\omega^2}. \tag{A.5}$$

This approach is indeed sufficient for functions where ω_0 and ω_n are within only a few decades. But this simplification fails for broad distributions as present in this work. For extremely small t the result is limited by the numerical accurancy of the calculating program. For high t the problems due to the oscillating cosine as described above occur. This effect can be seen in Fig. A.1 where the inverse of the Filon-algorithm described above was used to calculate the spectral density from the correlation function.

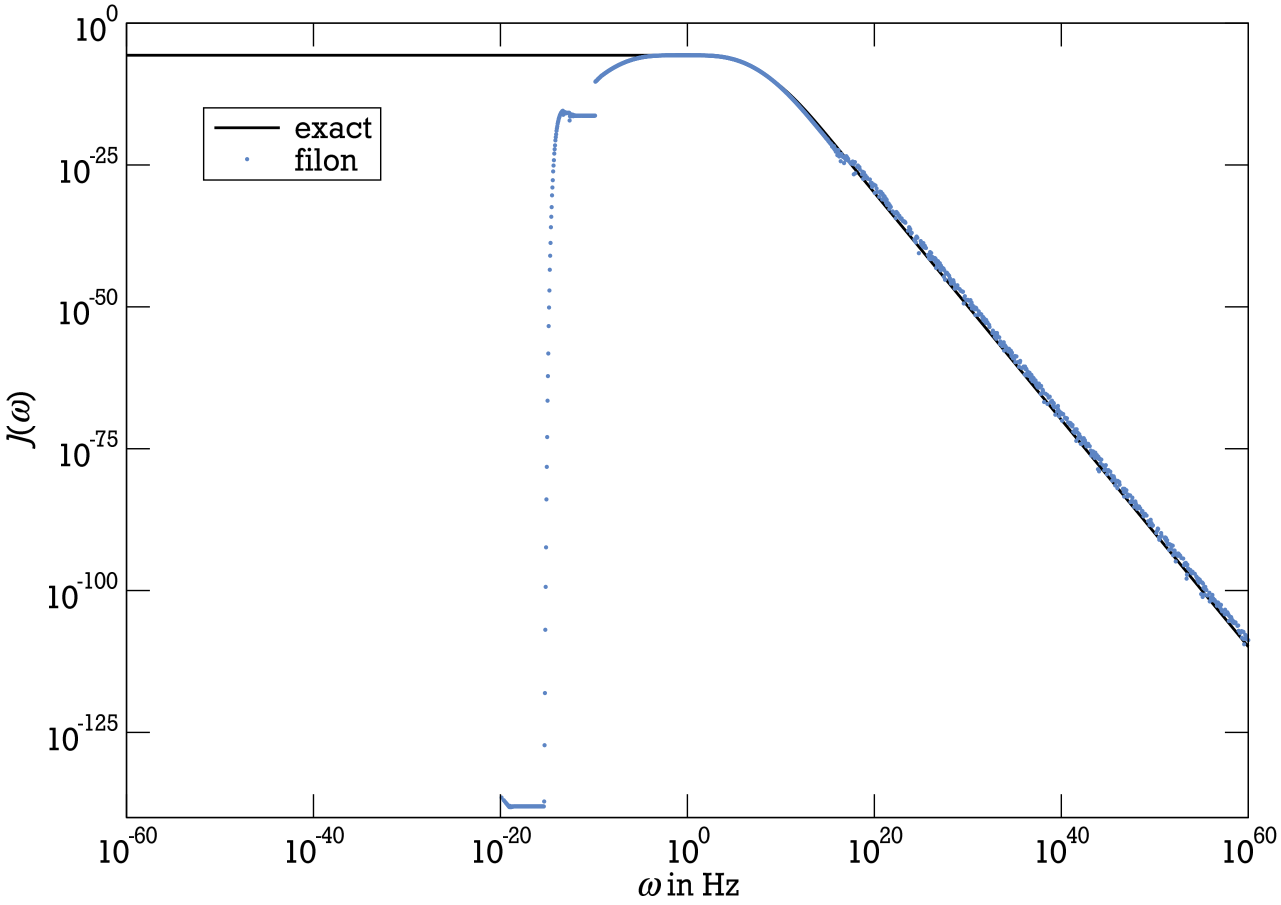

Figure A.1.: Comparison of the exact spectral density derived by Eq. (3.88) and the $J(\omega_\mathrm{L},\tau_\mathrm{c})$ calculated with the linear interpolated Filon-algorithm (A.5). For small frequencies the result fails due to the numerical accurancy of the calculation and for extremely high frequencies the oscillating character of the integrand leads to randomly distributed positive and negative values (only the positive values are shown here on the logarithmic scale).

The Problems of both ends of the frequency scale can be solved quite easily:

a) For high ω, the randomly oscillating behavior (positive and negative values change without a pattern) can be eliminated by replacing the difference of the cosines in Eq. (A.5) by the negative of its absolute value.

b) On the low end of the frequency scale improvements can be made by replacing the cosines by its series. By using just the first three terms of the cosine series the second factor of the sum in Eq. (A.5) becomes:

$$\frac{\cos(\omega t_{i+1}) - \cos(\omega t_i)}{\omega^2} \approx \frac{t_i^2 - t_{i+1}^2}{2} + \frac{\omega^2}{24}\left(t_{i+1}^4 - t_i^4\right) \overset{\omega t_{i+1}^2 \ll 1}{=} \frac{t_i^2 - t_{i+1}^2}{2}.$$

For $\omega t_{i+1}^2 \ll 1$ the spectral density is independend of ω, q.v. Fig. A.2.

As seen in Fig. A.2, the oscillating behavior can indeed be eliminated, but the results on the high frequency flank scatter around the exact values.

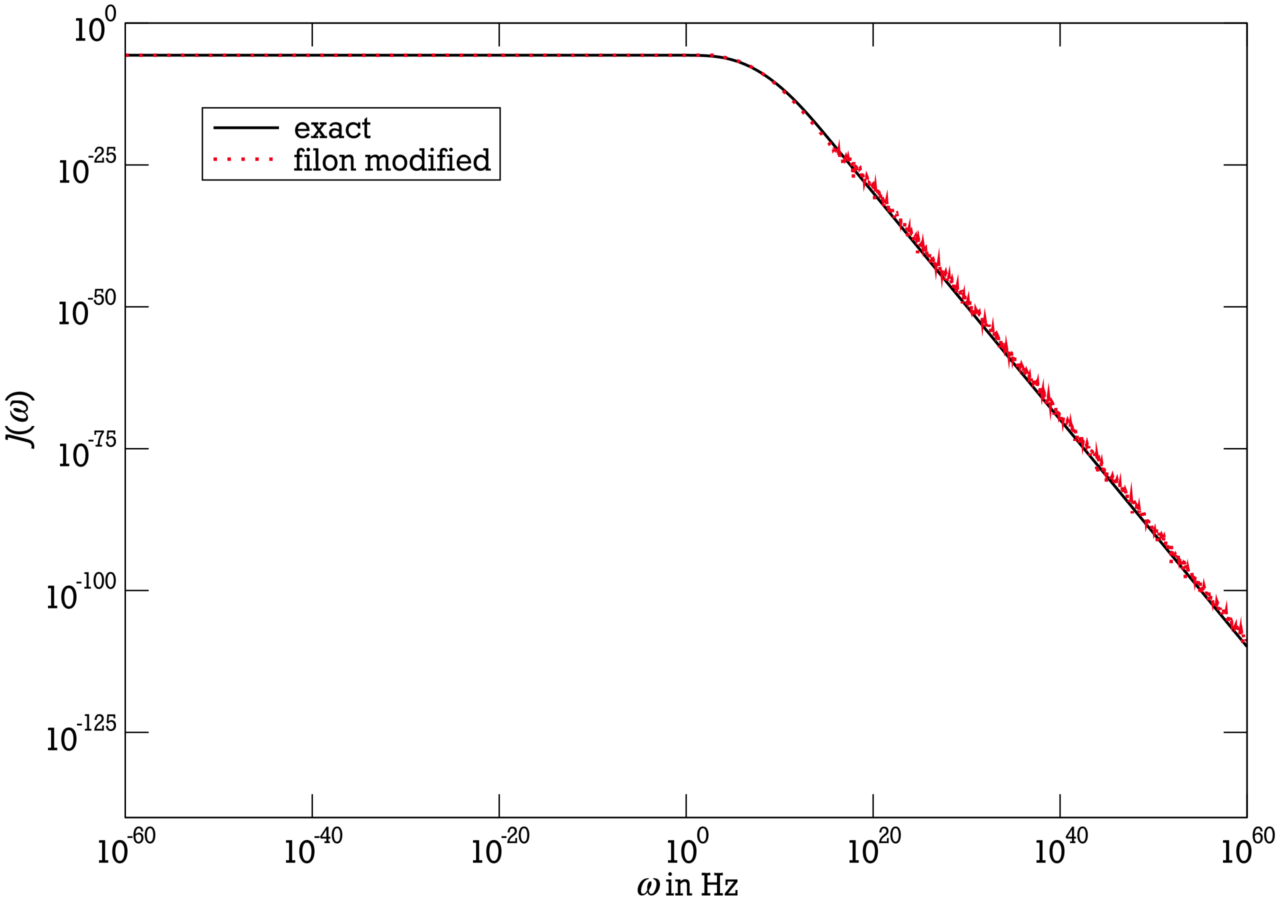

Figure A.2.: Comparison of the exact spectral density derived by Eq. (3.82) and the $J(\omega_L, \tau_c)$ calculated with the linear interpolated, modified Filon-algorithm. For small frequencies the modified Filon-algorithm yields a constant $J(\omega_L, \tau_c)$ as expected. The results at high frequencies are all positive but somewhat noisy.

A smooth curve with an ω^{-2} dependence for high frequencies is obtained, when always the absolute value of the complete sum is used. However, the result is approximately two orders of magnitude higher than the exact spectral density, q.v. Fig. A.3.

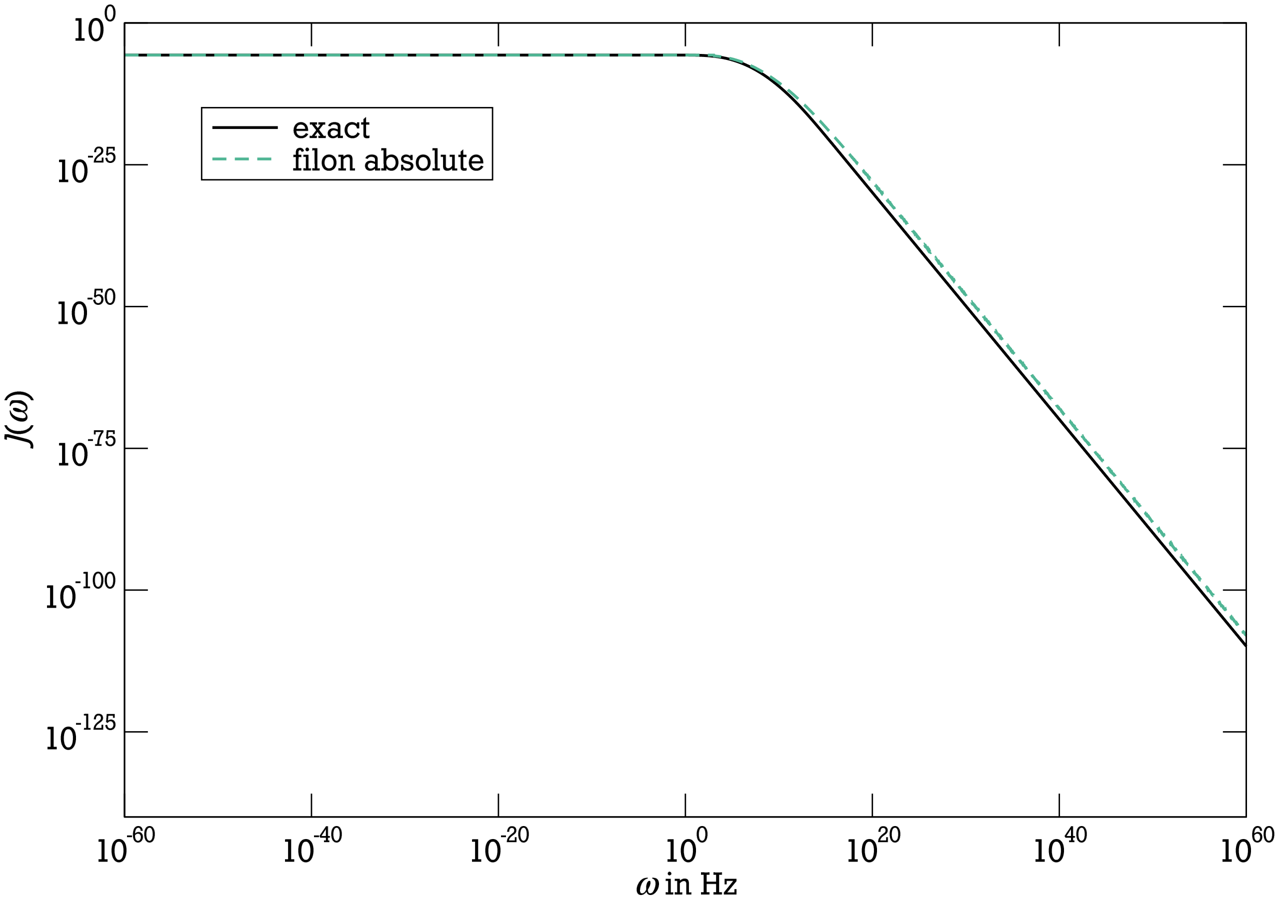

Figure A.3.: Comparison of the exact spectral density derived by Eq. (3.82) and the $J(\omega_{\mathrm{L}}, \tau_{\mathrm{c}})$ calculated with the linear interpolated, modified Filon-algorithm where the absolute values of the resulting sum has been used. The result is now a smooth curve with a ω^{-2} slope for high frequencies, but the result is almost two orders of magnitude above the exact spectral density.

So far it seems sufficient to modify the Filon algorithm introduced in [Blo03] with the corrections mentioned above to calculate the spectral density from the correlation function. But when looking at the inverse transformation, it is seen that this modification is not always working properly. Figure A.4 compares the result of calculating the correlation function directly by the DCT using Eq. (3.88), with the Filon algorithm, the modified Filon algorithm, and the trapezoidal rule. The Filon algorithm again fails on short times due to the numerical accurancy of the calculation. The oscillation for long times is not clearly seen in the linear y-scale of the graph but becomes visible in logarithmic scaling. For the modified Filon algorithm, it is not possible to find a single position on the time-axis to distinguish between both time-regimes. Improvements could be possible, when separating the short and the long time limits with an intermediate region. The trapezoidal rule works great for short times, but the noise at long times is even higher compared to the Filon algorithm. In this case a better result was achieved by combining the result of the trapezoidal rule for short times with the result of the Filon algorithm for longer times as shown in Fig. A.5. It turned out to be sufficient to use the trapezoidal rule until the correlation function has decreased to 20% of its initial value and then switch to the modified Filon algorithm to describe the correlation functions over a broad temperature range.

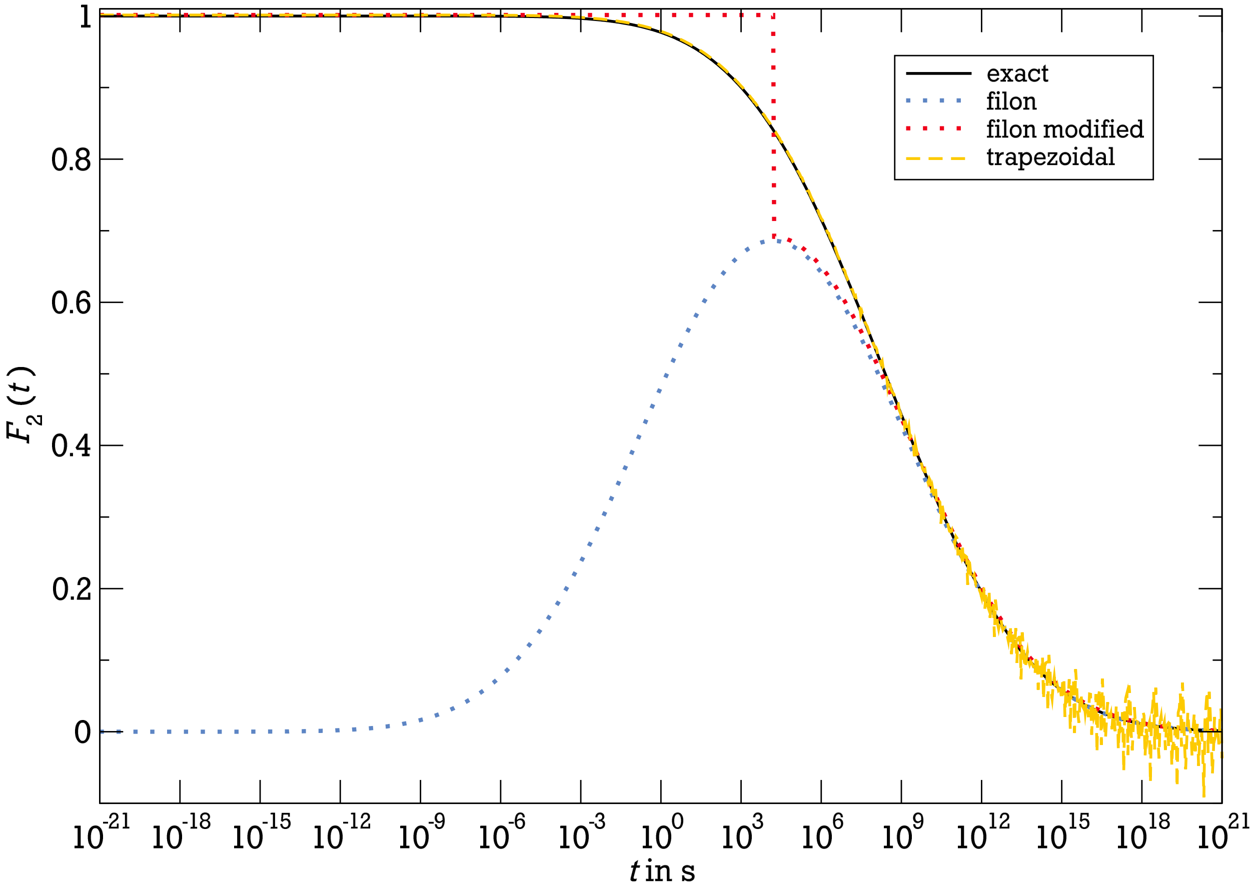

Figure A.4.: Comparison of the exact correlation function derived directly by the DCT using Eq. (3.88) and the F_2 calculated with the linear interpolated Filon-algorithm, its modified version and the trapezoidal rule.

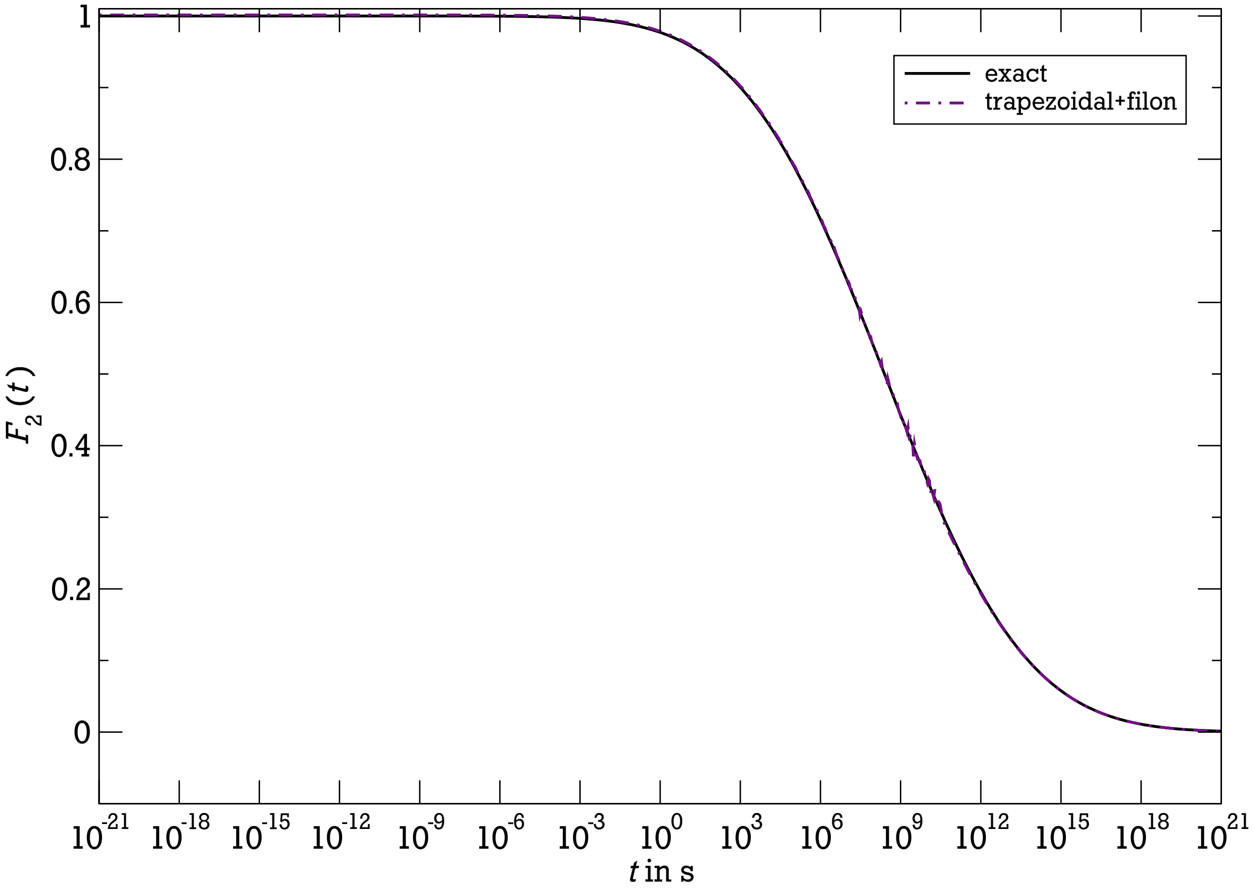

Figure A.5.: Comparison of the exact correlation function derived directly by the DCT using Eq. (3.88) and the F_2 calculated with a combination of the trapezoidal rule and the modified Filon algorithm.

A.1 Two-time correlation function of LiPS-GC

Similar to $Li_{10}SnP_2S_{12}$, the anisotropic solid spectrum of LiPS-GC at high temperatures prevents a signal loss due to two-time correlation for $T > 200\,K$, q.v. Fig. A.6a. Usually, spin diffusion is the dominant process for F_2 measurements at low temperatures. Therefore, a temperature dependent analysis of F_2 is not possible for LiPS-GC. The combination of the trapezoidal rule and the modified Filon algorithm mentioned above has been used to calculate the two-time correlation function of LiPS-GC to show the accurancy of the measurement at 180 K. Figure A.7b shows the calculated F_2 restricted to the time window of the SAE measurement. The measurement at 180 K (blue dots) is in good agreement with the calculated F_2 at the same temperature. The source code of the python program used for the calculation is given in Appx. E.

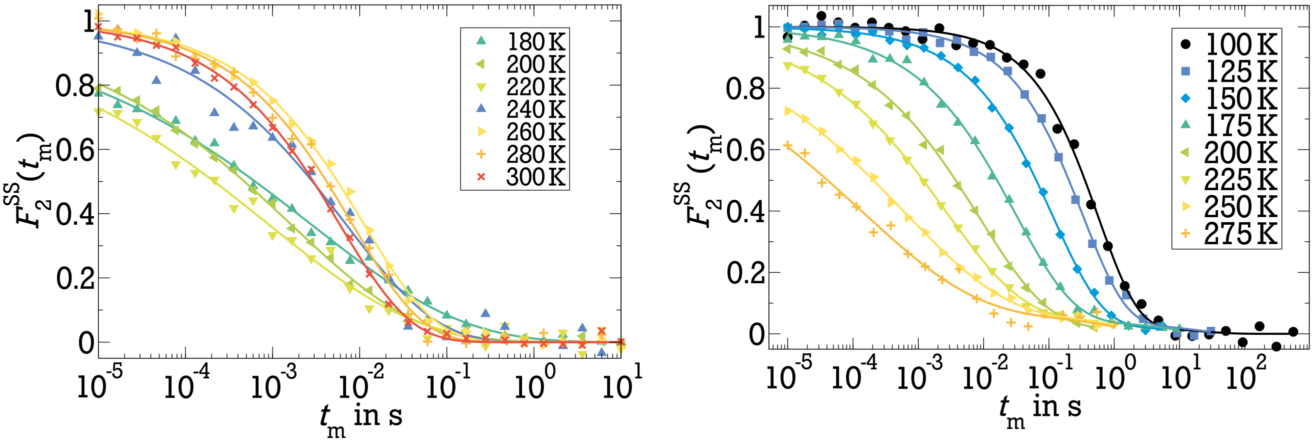

(a) (b)

Figure A.6.: Measured F_2^{SS} of LiPS-GC (a) and LiPS-GL (b). For LiPS-GC, the anisotropic spectrum ($\bar{\delta}_Q \neq 0$) prevents a signal loss due to two-time correlation for $T \geq 200\,K$.

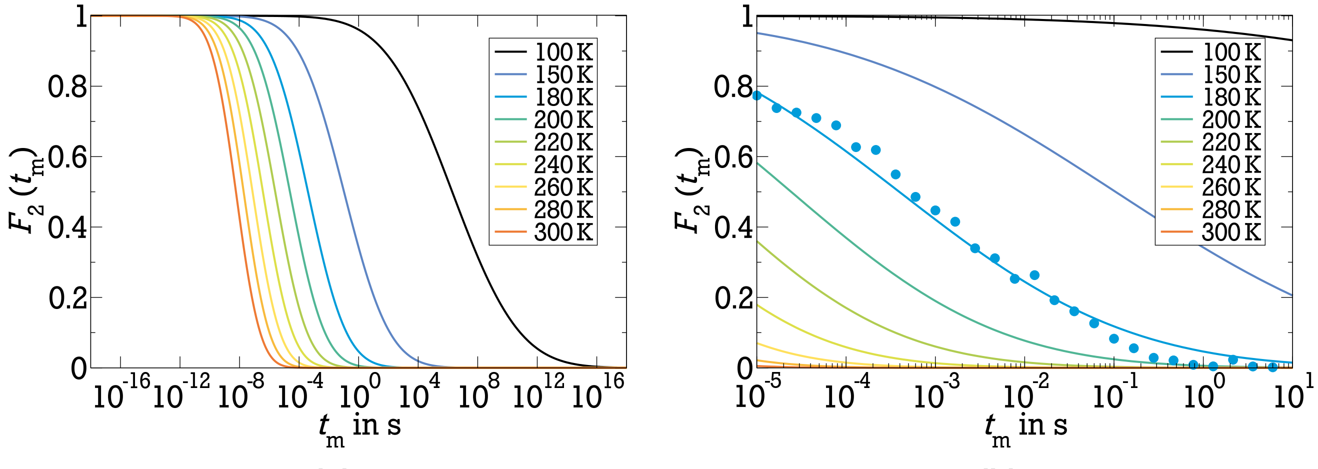

(a) **(b)**

Figure A.7.: (a) F2 of LiPS-GC calculated with the combination of the trapezoidal rule and the modified Filon algorithm. (b) Same as in panel (a) but restricted to the time window of the SAE including the measured F_2^{SS} at 180 K.

B Properties of the samples

This appendix lists the properties of the samples investigated in this work.

B.1 $Li_{10}SnP_2S_{12}$

Table B.1.: Crystal data for $Li_{10}SnP_2S_{12}$ sample (taken from supplementary material of [Bro13]).

		atom	x	y	z
Formula	$Li_{10}SnP_2S_{12}$	Sn	0.2500	0.2500	1.06369(7)
Formula weight in g/mol	634.75	P1	0.7500	0.2500	0.7500
Crystal system	tetragonal	P2	0.2500	0.2500	1.06369(7)
Space group	$P4_2/nmc$	S1	0.56023(17)	0.2500	0.84246(11)
Formular units Z	2	S2	0.2500	0.4596(2)	0.65620(13)
a in Å	8.7057(4)	S3	0.2500	0.4534(2)	0.96044(13)
b in Å	8.7057(4)	S4	0.93977	0.25000	0.84246
c in Å	12.7389(9)	S5	0.25000	0.04040	0.65620
α in °	90	S6	0.25000	0.04660	0.96044
β in °	90	S7	0.25000	0.56023	0.34246
γ in °	90	S8	0.04040	0.25000	0.15620
Lattice volume in $Å^3$	965.47(9)	S9	0.04660	0.25000	0.46044
ϱ (calc.) in g/cm^3	2.183	S10	0.25000	0.93977	0.34246
X-ray wavelength in Å	0.71073	S11	0.45960	0.25000	0.15620
		S12	0.45340	0.25000	0.46044
		Li1	0.514(2)	0.490(2)	0.9280(19)
		Li2	0.473(5)	0.493(3)	0.785(3)
		Li3	0.2500	0.2500	0.8063(13)
		Li4	0.2500	0.7500	1.0042(17)
		Li5	0.25000	0.25000	0.30630
		Li6	0.75000	0.25000	0.50420
		Li7	0.98600	0.01000	0.92800
		Li8	0.01000	0.51400	0.42800
		Li9	0.49000	0.98600	0.42800
		Li10	0.00700	0.47300	0.28500

B.2 SiOC

Table B.2.: Chemical composition of the SiOC samples.

	Si	O	C	SiO_2	SiC	Free C
wt%	31.9	17.3	50.8	32.5	23.9	43.6
mol	1.14	1.08	4.23	0.54	0.60	3.63
mol%	17.6	16.8	65.6	11.3	12.5	76.2
mol% normalized	1.00	0.95	3.72			

B.3 $Li_2S–B_2S_3$

Table B.3.: Properties of the $0.7Li_2S–0.3B_2S_3$ and $0.7Li_2S–0.27B_2S_3–0.03B_2O_3$ sample according to [Kim97a, Men91].

sample	T_g	ϱ	N_{Li}	a
$0.7Li_2S–0.3B_2S_3$	453-473 K	1800 kg/m^3	2.25×10^{28} m^{-3}	3.6 Å
$0.7Li_2S–0.27B_2S_3–0.03B_2O_3$	450 K			

B.4 $Li_2S–P_2S_5$

Table B.4.: Properties of the $0.7Li_2S–0.3P_2S_5$ samples.

property	glass	Reference	glass-ceramic	Reference
σ_{25} in mS/cm	0.05-0.34	[Miz05, Hay13]	3.2-17	[Miz05, Sei14]
E_σ in eV	0.35-0.39	[Hay13, Miz05]	0.18-0.33	[Sei14, Hay13]
T_g in K	483-518	[Uji12, Chu16]	-	-
T_c in K	543-553	[Uji12, Chu16]	-	-
D in m^2/s (at 473 K)	-	-	5.7×10^{-10}	[Mor15]
τ_c in s (at 473 K)	-	-	5.5×10^{-11}	[Mor15]
a in Å	-	-	4.3	[Mor15]
ϱ in Mg/m^3	1.938	[Oha16]	1.91	[Yam07]
E in GPa	22	[Kat14]	-	-
B in GPa	-	-	24	[Wan14]
V_{Mol} in cm^3/mol	51	[Kat14]	-	-

Table B.5.: Crystal data for $0.7Li_2S–0.3P_2S_5$ glass-ceramic (taken from [Yam07]; [Chu16] lists cell parameters from other works which are very similar, but not identical).

		atom	x	y	z
Formula	$Li_7P_3S_{11}$	P1	0.7938	0.0334	0.4654
Formula weight in g/mol	988.45	P2	0.4929	0.0380	0.2966
Crystal system	triclinic	P3	0.8400	0.2698	0.0585
Space group	$P\bar{1}$	S1	0.8606	0.2363	0.6195
Formular units Z	2	S2	0.8235	0.1052	0.3342
a in Å	12.5009(3)	S3	0.8400	0.6829	0.4680
b in Å	6.03160(17)	S4	0.6176	0.1597	0.4529
c in Å	12.5303(3)	S5	0.3306	0.2267	0.2884
α in °	102.845(3)	S6	0.5086	0.0795	0.1507
β in °	113.2024(18)	S7	0.5094	0.7001	0.3074
γ in °	74.467(3)	S8	0.8406	0.3302	0.9033
Lattice volume in $Å^3$	829.35(4)	S9	0.8279	0.9266	0.0462
ϱ (calc.) in g/cm^3	1.98	S10	0.6781	0.4874	0.0640
ϱ (meas.) in g/cm^3	1.91	S11	0.9772	0.3509	0.1876
X-ray wavelength in Å	1.49738	Li1	0.6690	0.1322	0.0920
		Li2	0.6381	0.4020	0.8657
		Li3	0.2160	0.5300	0.7400
		Li4	0.9420	0.7860	0.2700
		Li5	0.3590	0.5909	0.3368
		Li6	0.6370	0.7340	0.4980
		Li7	0.1390	0.2940	0.1340

C Fit-parameter

Table C.1.: Fit-parameter of the relaxation rates of the SiOC samples using Eq. (6.2).

sample	process	R_0 in 1/(K·s)	E_a in eV	a	b
$SiOC^{+Li}$	f	670.4 ± 264.1	0.16 ± 0.01	4.0e-03 ± 4.5e-03	0.82 ± 0.23
$SiOC^{+Li}$	s	10.6 ± 25.04	0.18 ± 0.09	5.2e-06 ± 6.7e-06	1.62 ± 0.25
$SiOC^{-Li}$	f	573.4 ± 340.0	0.18 ± 0.02	1.66 ± 1.29	-0.19 ± 0.16
$SiOC^{-Li}$	s	2.72 ± 1.77	0.11 ± 0.03	1.0e-04 ± 2.5e-04	1.04 ± 0.50

Table C.2.: Fit-parameter of the HB fits to the FWHM Σ of the central line of the SiOC samples using Eq. (3.50).

sample	process	A in Hz	B in Hz	E_a in eV	D in Hz
$SiOC^{+Li}$	PR	5671 ± 212	0.69 ± 0.55	0.24 ± 0.02	829 ± 149
$SiOC^{+Li}$	FR	6144 ± 454	2.11 ± 2.64	0.21 ± 0.03	749 ± 355
$SiOC^{-Li}$	PR	5582 ± 1079	3.94 ± 6.43	0.24 ± 0.04	0
$SiOC^{-Li}$	FR	6234 ± 2238	6.10 ± 17.6	0.23 ± 0.06	0

D Phase cycles

In this appendix the used phase cycles for every experiment are listet. The nomenclature is the same as used in the DAMARIS scripts: 0, 90, 180, and 270 instead of the more conventional use of X, Y, -X, and -Y.

FID

Table D.1.: 4-fold phase cycle for the FID used in FC experiments or to determine the legth of the 90° pulse.

pulse	0	180	90	270
receiver	0	180	90	270

Solid echo

Table D.2.: 8-fold phase cycle for the saturation recovery with solid echo detection used for T_1 measruements and recording of ^{7}Li NMR spectra.

first pulse (90°)	0	180	0	180	90	270	90	270
second pulse (64°)	90	90	270	270	0	0	180	180
receiver	0	180	0	180	90	270	90	270

Table D.3.: 8-fold phase cycle for the SE$_+$ experiment; taken from [Sto16].

first pulse (90°)	0	0	180	180	90	90	270	270
second pulse (70.5°)	90	270	90	270	180	0	180	0
receiver	90	90	270	270	180	180	0	0

Table D.4.: 8-fold phase cycle for the SE$_-$ experiment for determining T_2 by using the *exorcycle*; taken from [Sto16].

first pulse (90°)	0	0	180	180	90	90	270	270
second pulse (70.5°)	0	180	0	180	270	90	270	90
receiver	90	90	270	270	180	180	0	0

Stimulated echo

Table D.5.: 8-fold phase cycle of the SAE for eliminating single and double quantum coherences; taken from [Sto16]. This phase cycle was only used for the $Li_{10}SnP_2S_{12}$ sample.

first pulse (90°)	0	0	90	90	0	0	90	90
second pulse (45°)	90	90	0	0	270	270	180	180
third pulse (45°)	90	270	90	270	90	270	90	270
receiver	0	180	180	0	180	0	0	180

Table D.6.: 16-fold phase cycle of the SAE with an additional cycle for the third pulse; taken from [Qi04]. This phase cycle was used for all samples except $Li_{10}SnP_2S_{12}$.

1st (90°)	0	180	0	180	90	270	90	270	90	270	90	270	180	0	180	0
2nd (45°)	90	90	270	270	0	0	180	180	180	180	0	0	90	90	270	270
3rd (45°)	0	0	0	0	180	180	180	180	90	90	90	90	270	270	270	270
receiver	180	0	0	180	180	0	0	180	270	90	90	270	270	90	90	270

Table D.7.: 8-fold phase cycle of the cos-cos STE for eliminating single and double quantum coherences; taken from [Sto16].

first pulse (90°)	0	180	180	0	90	270	270	90
second pulse (45°)	0	0	0	0	90	90	90	90
third pulse (41.8°)	0	180	0	180	0	180	0	180
receiver	180	180	0	0	180	180	0	0

Table D.8.: 16-fold phase cycle of the SFG measurements; taken from [Hür02].

1st (90°)	0	180	0	180	0	180	0	180	90	270	90	270	90	270	90	270
2nd (90°)	0	0	180	180	0	0	180	180	0	0	180	180	0	0	180	180
3rd (90°)	0	0	0	0	180	180	180	180	0	0	0	0	180	180	180	180
receiver	180	0	0	180	0	180	180	0	90	270	270	90	270	90	90	270

MTCF

Table D.9.: 256-fold phase cycle for the MTCF experiments; taken from [Sto17].

1st pulse (90°)	0	0	90	90	0	0	90	90	0	0	90	90	0	0	90	90
	90	90	180	180	90	90	180	180	90	90	180	180	90	90	180	180
	0	0	90	90	0	0	90	90	0	0	90	90	0	0	90	90
	90	90	180	180	90	90	180	180	90	90	180	180	90	90	180	180
	0	0	90	90	0	0	90	90	0	0	90	90	0	0	90	90
	90	90	180	180	90	90	180	180	90	90	180	180	90	90	180	180
	0	0	90	90	0	0	90	90	0	0	90	90	0	0	90	90
	90	90	180	180	90	90	180	180	90	90	180	180	90	90	180	180
	90	90	180	180	90	90	180	180	90	90	180	180	90	90	180	180
	180	180	270	270	180	180	270	270	180	180	270	270	180	180	270	270
	90	90	180	180	90	90	180	180	90	90	180	180	90	90	180	180
	180	180	270	270	180	180	270	270	180	180	270	270	180	180	270	270
	90	90	180	180	90	90	180	180	90	90	180	180	90	90	180	180
	180	180	270	270	180	180	270	270	180	180	270	270	180	180	270	270
	90	90	180	180	90	90	180	180	90	90	180	180	90	90	180	180
	180	180	270	270	180	180	270	270	180	180	270	270	180	180	270	270
2nd pulse (45°)	90	270	180	0	90	270	180	0	90	270	180	0	90	270	180	0
	180	0	270	90	180	0	270	90	180	0	270	90	180	0	270	90
	90	270	180	0	90	270	180	0	90	270	180	0	90	270	180	0
	180	0	270	90	180	0	270	90	180	0	270	90	180	0	270	90
	90	270	180	0	90	270	180	0	90	270	180	0	90	270	180	0
	180	0	270	90	180	0	270	90	180	0	270	90	180	0	270	90
	90	270	180	0	90	270	180	0	90	270	180	0	90	270	180	0
	180	0	270	90	180	0	270	90	180	0	270	90	180	0	270	90
	180	0	270	90	180	0	270	90	180	0	270	90	180	0	270	90
	270	90	0	180	270	90	0	180	270	90	0	180	270	90	0	180
	180	0	270	90	180	0	270	90	180	0	270	90	180	0	270	90
	270	90	0	180	270	90	0	180	270	90	0	180	270	90	0	180
	180	0	270	90	180	0	270	90	180	0	270	90	180	0	270	90
	270	90	0	180	270	90	0	180	270	90	0	180	270	90	0	180
	180	0	270	90	180	0	270	90	180	0	270	90	180	0	270	90
	270	90	0	180	270	90	0	180	270	90	0	180	270	90	0	180
3rd pulse (45°)	0	0	0	0	180	180	180	180	0	0	0	0	180	180	180	180
	90	90	90	90	270	270	270	270	90	90	90	90	270	270	270	270
	0	0	0	0	180	180	180	180	0	0	0	0	180	180	180	180
	90	90	90	90	270	270	270	270	90	90	90	90	270	270	270	270
	0	0	0	0	180	180	180	180	0	0	0	0	180	180	180	180
	90	90	90	90	270	270	270	270	90	90	90	90	270	270	270	270
	0	0	0	0	180	180	180	180	0	0	0	0	180	180	180	180
	90	90	90	90	270	270	270	270	90	90	90	90	270	270	270	270
	90	90	90	90	270	270	270	270	90	90	90	90	270	270	270	270
	180	180	180	180	0	0	0	0	180	180	180	180	0	0	0	0
	90	90	90	90	270	270	270	270	90	90	90	90	270	270	270	270
	180	180	180	180	0	0	0	0	180	180	180	180	0	0	0	0
	90	90	90	90	270	270	270	270	90	90	90	90	270	270	270	270
	180	180	180	180	0	0	0	0	180	180	180	180	0	0	0	0
	90	90	90	90	270	270	270	270	90	90	90	90	270	270	270	270
	180	180	180	180	0	0	0	0	180	180	180	180	0	0	0	0
4th pulse (90°)	90	90	90	90	90	90	90	90	270	270	270	270	270	270	270	270
	180	180	180	180	180	180	180	180	0	0	0	0	0	0	0	0
	90	90	90	90	90	90	90	90	270	270	270	270	270	270	270	270
	180	180	180	180	180	180	180	180	0	0	0	0	0	0	0	0
	90	90	90	90	90	90	90	90	270	270	270	270	270	270	270	270
	180	180	180	180	180	180	180	180	0	0	0	0	0	0	0	0
	90	90	90	90	90	90	90	90	270	270	270	270	270	270	270	270
	180	180	180	180	180	180	180	180	0	0	0	0	0	0	0	0
	180	180	180	180	180	180	180	180	0	0	0	0	0	0	0	0
	270	270	270	270	270	270	270	270	90	90	90	90	90	90	90	90
	180	180	180	180	180	180	180	180	0	0	0	0	0	0	0	0

Continued on next page

Table D.9 – *Continued from previous page*

	270	270	270	270	270	270	270	270	90	90	90	90	90	90	90	90
	180	180	180	180	180	180	180	180	0	0	0	0	0	0	0	0
	270	270	270	270	270	270	270	270	90	90	90	90	90	90	90	90
	180	180	180	180	180	180	180	180	0	0	0	0	0	0	0	0
	270	270	270	270	270	270	270	270	90	90	90	90	90	90	90	90
5th pulse (90°)	0	0	0	0	0	0	0	0	0	0	0	0	0	0	0	0
	0	0	0	0	0	0	0	0	0	0	0	0	0	0	0	0
	180	180	180	180	180	180	180	180	180	180	180	180	180	180	180	180
	180	180	180	180	180	180	180	180	180	180	180	180	180	180	180	180
	0	0	0	0	0	0	0	0	0	0	0	0	0	0	0	0
	0	0	0	0	0	0	0	0	0	0	0	0	0	0	0	0
	180	180	180	180	180	180	180	180	180	180	180	180	180	180	180	180
	180	180	180	180	180	180	180	180	180	180	180	180	180	180	180	180
	90	90	90	90	90	90	90	90	90	90	90	90	90	90	90	90
	90	90	90	90	90	90	90	90	90	90	90	90	90	90	90	90
	270	270	270	270	270	270	270	270	270	270	270	270	270	270	270	270
	270	270	270	270	270	270	270	270	270	270	270	270	270	270	270	270
	90	90	90	90	90	90	90	90	90	90	90	90	90	90	90	90
	90	90	90	90	90	90	90	90	90	90	90	90	90	90	90	90
	270	270	270	270	270	270	270	270	270	270	270	270	270	270	270	270
	270	270	270	270	270	270	270	270	270	270	270	270	270	270	270	270
6th pulse (45°)	90	90	90	90	90	90	90	90	90	90	90	90	90	90	90	90
	90	90	90	90	90	90	90	90	90	90	90	90	90	90	90	90
	90	90	90	90	90	90	90	90	90	90	90	90	90	90	90	90
	90	90	90	90	90	90	90	90	90	90	90	90	90	90	90	90
	270	270	270	270	270	270	270	270	270	270	270	270	270	270	270	270
	270	270	270	270	270	270	270	270	270	270	270	270	270	270	270	270
	270	270	270	270	270	270	270	270	270	270	270	270	270	270	270	270
	270	270	270	270	270	270	270	270	270	270	270	270	270	270	270	270
	180	180	180	180	180	180	180	180	180	180	180	180	180	180	180	180
	180	180	180	180	180	180	180	180	180	180	180	180	180	180	180	180
	180	180	180	180	180	180	180	180	180	180	180	180	180	180	180	180
	180	180	180	180	180	180	180	180	180	180	180	180	180	180	180	180
	0	0	0	0	0	0	0	0	0	0	0	0	0	0	0	0
	0	0	0	0	0	0	0	0	0	0	0	0	0	0	0	0
	0	0	0	0	0	0	0	0	0	0	0	0	0	0	0	0
	0	0	0	0	0	0	0	0	0	0	0	0	0	0	0	0
7th pulse (45°)	90	90	90	90	90	90	90	90	90	90	90	90	90	90	90	90
	90	90	90	90	90	90	90	90	90	90	90	90	90	90	90	90
	90	90	90	90	90	90	90	90	90	90	90	90	90	90	90	90
	90	90	90	90	90	90	90	90	90	90	90	90	90	90	90	90
	90	90	90	90	90	90	90	90	90	90	90	90	90	90	90	90
	90	90	90	90	90	90	90	90	90	90	90	90	90	90	90	90
	90	90	90	90	90	90	90	90	90	90	90	90	90	90	90	90
	90	90	90	90	90	90	90	90	90	90	90	90	90	90	90	90
	90	90	90	90	90	90	90	90	90	90	90	90	90	90	90	90
	90	90	90	90	90	90	90	90	90	90	90	90	90	90	90	90
	90	90	90	90	90	90	90	90	90	90	90	90	90	90	90	90
	90	90	90	90	90	90	90	90	90	90	90	90	90	90	90	90
	90	90	90	90	90	90	90	90	90	90	90	90	90	90	90	90
	90	90	90	90	90	90	90	90	90	90	90	90	90	90	90	90
	90	90	90	90	90	90	90	90	90	90	90	90	90	90	90	90
	90	90	90	90	90	90	90	90	90	90	90	90	90	90	90	90
receiver	90	270	90	270	270	90	270	90	270	90	270	90	90	270	90	270
	90	270	90	270	270	90	270	90	270	90	270	90	90	270	90	270
	270	90	270	90	90	270	90	270	90	270	90	270	270	90	270	90
	270	90	270	90	90	270	90	270	90	270	90	270	270	90	270	90
	270	90	270	90	90	270	90	270	90	270	90	270	270	90	270	90
	270	90	270	90	90	270	90	270	90	270	90	270	270	90	270	90
	90	270	90	270	270	90	270	90	270	90	270	90	90	270	90	270
	90	270	90	270	270	90	270	90	270	90	270	90	90	270	90	270
	90	270	90	270	270	90	270	90	270	90	270	90	90	270	90	270
	90	270	90	270	270	90	270	90	270	90	270	90	90	270	90	270

Continued on next page

Table D.9 – *Continued from previous page*

	270	90	270	90	90	270	90	270	90	270	90	270	270	90	270	90
	270	90	270	90	90	270	90	270	90	270	90	270	270	90	270	90
	270	90	270	90	90	270	90	270	90	270	90	270	270	90	270	90
	270	90	270	90	90	270	90	270	90	270	90	270	270	90	270	90
	90	270	90	270	270	90	270	90	270	90	270	90	90	270	90	270
	90	270	90	270	270	90	270	90	270	90	270	90	90	270	90	270

E Program source codes

Pyhton script *log_gauss.py* to determine the Gaussian distribution of activation energies $g(E_\mathrm{a})$ from FC relaxometry data. Furthermore, the spectral density $J(\omega_\mathrm{L}, \tau_\mathrm{c})$, the two-time correlation function F_2, the relaxation of the spin-alignment state $T_{1\mathrm{Q}}$, and the diffusion coefficient D are derived with the obtained $g(E_\mathrm{a})$.

```
# -*- coding: utf-8 -*-
from __future__ import division
import matplotlib
matplotlib.use('Agg')
from matplotlib import rc
rc('text', usetex=True)

rc('text.latex',preamble='\usepackage[charter]{mathdesign}')
rc('font',**{'family':'serif','serif':['Charter'], 'size':20})
rc('mathtext', **{'it':'Charter', 'fontset':'custom'})

import scipy.odr as odr
import numpy as N
import pylab as pl
import glob
from math import pi
import matplotlib.pyplot as plt
import os, sys
from scipy.integrate import quad
import saveagr
import tud_colors

#script to obtain gaussian distribution of activation energies g(Ea)
#from FC measurements and use this g(Ea) to calculate T1Q, F2(t), J(w), and D

#parameter
kb=8.6173324e-5 #8.6173324e-5 #in ev/K, 1.3806488 in J/K/mol, 1 without units
#measured temperatures in K
temp = [260, 280,  300,  320, 340, 360, 380]
#p0 = [C,tau_0,E_m,sigma]
p0=[4.0e+09, 1.0e-14, 0.4, 0.0721526]

#define function for fit using z = ln(tau/tau_m)
```

```
def integrand(z,p,T,x):
    return  kb*T/((2*pi)**0.5*p[2])*p[0]/N.sqrt(p[1]/kb)*N.exp(p[1]/(kb*T))
            *N.exp(z-(z*kb*T/p[2])**2/2)/(1+(x*p[0]/N.sqrt(p[1]/kb)
            *N.exp(p[1]/(kb*T))*N.exp(z))**2)

def Jlg(p,T,x):
    ret_val = N.empty(N.shape(x))
    for i, xval in enumerate(x):
ret_val[i] = quad(integrand, -N.inf, N.inf, args=(p,T,xval))[0]
    return ret_val

def lg(p,x,n):
    ret_val = []
    ret_val = N.append(ret_val, x[    :n[0]]*p[0]*(Jlg([p[1],p[2],p[3]],temp[0],
              x[    :n[0]])+4*Jlg([p[1],p[2],p[3]],temp[0],2*x[    :n[0]]))
    for i in range(len(temp)-1):
        ret_val = N.append(ret_val, x[n[i]:n[i+1]]*p[0]*(Jlg([p[1],p[2],p[3]],
                  temp[i+1],x[n[i]:n[i+1]])+4*Jlg([p[1],p[2],p[3]],
  temp[i+1],2*x[n[i]:n[i+1]])))
    return N.log10(ret_val)#change to ret_val if fit on log-scale is desired


#load data and parameter
laenge=[]
x=[]
y=[]
sd=[]

dic = {}

#!!!!!!!! Here the filenames have to be adjusted !!!!!!!!
for i in range(len(temp)):
    dic['data%i'%i] = N.loadtxt("data/data.dat"%temp[i])


for k,v in sorted(dic.iteritems()):
    print k
    laenge = N.append(laenge,len(v[:,1]))
    x = N.append(x,2*N.pi*v[:,0])
    y = N.append(y,v[:,0]*2*N.pi/v[:,1])
    sd = N.append(sd,v[:,2]*2*N.pi/v[:,1]**2)

y = N.log10(y) #delete this line if fit on log-scale is desired

for k,v in enumerate(laenge):
    if k==0:
```

```
continue
    else:
laenge[k] = v+laenge[k-1]

results = N.array([])

print p0

#fit
model = odr.Model(lg, extra_args=([laenge]))
odrdata = odr.RealData(x=x,y=y,sy=sd,sx=5e-9*x)
myodr = odr.ODR(odrdata, model, beta0=p0)
result = myodr.run()

p2=result.beta

results = N.append(results, result.beta)

#save data
p_final = result.beta
std_final = result.sd_beta
N.savetxt('lga_fit-parameter.dat', N.column_stack((p_final[0], std_final[0],
          p_final[1], std_final[1], p_final[2], std_final[2], p_final[3],
          std_final[3])), fmt = '%.18e', header="C C_err tau_0
          tau_0_err E_m E_m_err sigma sigma_err")
N.savetxt('Constant.dat', N.array(p_final[0]).reshape(1,), fmt = '%.18e')
N.savetxt('Tau.dat', N.array(p_final[1]).reshape(1,), fmt = '%.18e')
N.savetxt('Mean.dat', N.array(p_final[2]).reshape(1,), fmt = '%.18e')
N.savetxt('Sigma.dat', N.array(0.0721526).reshape(1,), fmt = '%.18e')

print p_final

#create the plot

def lgplot(p,T,x):
    return x*p[0]*(Jlg([p[1],p[2],p[3]],T,x)+4*Jlg([p[1],p[2],p[3]],T,2*x))

colors=['k', 'tud1a', 'tud2a', 'tud3a', 'tud4a', 'tud5a', 'tud6a', 'tud7a',
        'tud8a', 'tud9a', 'tud10a', 'tud11a', 'tud1b', 'tud2b', 'tud3b',
        'tud4b', 'tud5b', 'tud6b', 'tud7b', 'tud8b', 'tud9b', 'tud10b',
        'tud11b', 'tud1c', 'tud2c', 'tud3c', 'tud4c', 'tud5c', 'tud6c',
        'tud7c', 'tud8c', 'tud9c', 'tud10c', 'tud11c', 'tud1d', 'tud2d',
        'tud3d', 'tud4d', 'tud5d', 'tud6d', 'tud7d', 'tud8d', 'tud9d',
        'tud10d', 'tud11d']
fig = pl.figure(frameon=False)
ax1 = fig.add_subplot(111)
```

```
timeaxis = N.logspace(5.275,N.log10(10**9*2*N.pi),num=1000)[::-1]

ax1.plot(x[:laenge[0]], 10**y[:laenge[0]], colors[0]+'o', markersize=10.0,
         markeredgecolor=colors[0], label = str(temp[0])+' K')
ax1.plot(timeaxis, lgplot(p_final,temp[0], timeaxis), color=colors[0])
for i in range(len(temp)-1):
    ax1.plot(x[laenge[i]:laenge[i+1]], 10**y[laenge[i]:laenge[i+1]],
             color=colors[i+1], marker='o', markersize=10.0,
             markeredgecolor=colors[i+1], linestyle='None', label =
             str(temp[i+1])+' K')
    ax1.plot(timeaxis, lgplot(p_final,temp[i+1], timeaxis), color=colors[i+1])

ax1.loglog()
ax1.set_xlabel(r'$\omega/\mathrm{s}^{-1}$')
ax1.set_ylabel(r'$\omega T_1^{-1}/\mathrm{s}^{-2}$')
ax1.legend(loc=4, ncol=2, labelspacing=.1, numpoints=1, handlelength=.5,
           columnspacing = .5, handletextpad = 0.2)
fig.savefig('lga.pdf', format='pdf', facecolor='none', edgecolor='none')

bla1 = saveagr.SaveAGR()
bla1.saveagr('lga.agr', fig=fig, ax=ax1)
plt.clf()

#FC calculation is done here, see below for T1Q, J(w), F2, and D calculations
#parameter of g(Ea) (kb has been defined at the beginning of this script):
C = p_final[0]
tau0 = p_final[1]
Em = p_final[2]
sigma = p_final[3]
#Temperatures in K
T = [100, 150, 180, 200, 220, 240, 260, 280, 300]
#larmor frequency (in MHz/(2*pi)) for which T1Q should be calculated
omega=76.0

#calculate J(w) = int_0^inf G(tau)*tau/(1+w^2*tau^2)d_tau using z=ln(tau/tau_m)
def integrand_t1q(z,p,omega):
    _tau, _em, _sigma, _temp = p
    ret_val = kb*p[3]/((2*pi)**0.5*p[2])*p[0]/N.sqrt(p[1]/kb)*
              N.exp(p[1]/(kb*p[3]))*N.exp(z-(z*kb*p[3]/p[2])**2/2)/
              (1+((omega*1e6*2*pi)*p[0]/N.sqrt(p[1]/kb)*N.exp(p[1]/(kb*p[3]))*
              N.exp(z))**2)
    x.append(z)
    y.append(ret_val)
    return ret_val

def Jlg(p,x):
```

```
    #getting J(w) by integration from -N.inf to +N.inf
    return quad(integrand_t1q, -N.inf, N.inf, args=(p,omega), epsabs=1e-21)[0]

#calculate F2 using z = ln(tau/tau_m)
#version 1: F2 = int_0^inf G(tau)*exp(-t/tau) dtau

def integrand_f2(z, p, tm):
    _tau, _em, _sigma, _temp = p
    ret_val = kb*p[3]/((2*pi)**0.5*p[2])*N.exp(-(z*kb*p[3]/p[2])**2/2)*
              N.exp(-tm/(p[0]/N.sqrt(p[1]/kb)*N.exp(p[1]/(kb*p[3]))*N.exp(z)))
    return ret_val

def F2(p, tm):
    ww = tm + 0
    ret_val = [quad(integrand_f2, -N.inf, N.inf, args=(p, tm_i), epsabs=1e-21)
               [0] for tm_i in ww]
    return N.array(ret_val)

#T1Q correction

def integrand_f2_t1q(z, p, tm):
    _tau, _em, _sigma, _temp, _t1q = p
    ret_val = kb*p[3]/((2*pi)**0.5*p[2])*N.exp(-(z*kb*p[3]/p[2])**2/2)*
              N.exp(-tm/(p[0]/N.sqrt(p[1]/kb)*N.exp(p[1]/(kb*p[3]))*N.exp(z)))*
              N.exp(-tm*p[4])
    return ret_val

def F2_t1q(p, tm):
    ww = tm + 0
    ret_val = [quad(integrand_f2_t1q, -N.inf, N.inf, args=(p, tm_i),
               epsabs=1e-21)[0] for tm_i in ww]
    return N.array(ret_val)

#version 2: F2 = 2/pi*int_{0}^{inf} J(w)*cos(w*t) dw = FFT(J(w))
#using filon-algorithm:
def integrand_filon(z,p,w):
    _tau, _em, _sigma, _temp = p
    ret_val = kb*p[3]/((2*pi)**0.5*p[2])*p[0]/N.sqrt(p[1]/kb)*
              N.exp(p[1]/(kb*p[3]))*N.exp(z-(z*kb*p[3]/p[2])**2/2)/(1+(w*
              p[0]/N.sqrt(p[1]/kb)*N.exp(p[1]/(kb*p[3]))*N.exp(z))**2)
    return ret_val

def J(p, w, intlimit):
    ww = w + 0
    print w[0]
    ret_val = [quad(integrand_filon, -N.inf, intlimit, args=(p, w_i),
```

```
               epsabs=1e-21)[0] for w_i in ww]
    print w[0]
    return N.array(ret_val)

def filon(omega, omega_limit, jw, t_start=1e-60, t_stop=1e60, t_num=3001):
#
#    Filon-Algorithmus (see Dissertation Blochowicz, p.33),
#    calculate F(t) = int_0^\infty J(w) cos(w*t) dw.
#
    t = N.logspace(N.log10(t_start), N.log10(t_stop), num=t_num)
    ret_val = N.zeros_like(t)
    wl = omega_limit
    t_low = t[t < 1e-01/wl**2]
    t_high = t[t > 1e-01/wl**2]
    ret_val_low = N.zeros_like(t_low)
    ret_val_high = N.zeros_like(t_high)
    for i in xrange(len(omega)-1):
        ret_val_low += ((jw[i+1]-jw[i])*(omega[i+1]+omega[i]))/(-2)*t_low/t_low
        ret_val_high += ((jw[i+1]-jw[i])/(omega[i+1]-omega[i]))*(N.cos(t_high*
                        omega[i+1])-N.cos(t_high*omega[i]))/t_high**2
    return N.concatenate((ret_val_low,ret_val_high), axis=0)

def F2_filon(p, w, w_limit, t_limits, intlimit):
    j_w = J(p, w, intlimit)
    return 2/pi*filon(w, w_limit, j_w, t_start=t_limits[0], t_stop=t_limits[1],
           t_num=t_limits[2])

#using trapezoidal rule
def trapez(w,y,x):
    ret_val = N.zeros(w.shape)
    for i in range(len(ret_val)):
        ret_val[i] = 2/pi*N.trapz(y*N.cos(w[i]*x),x)
    return ret_val

#calculate diffusion-coefficient from DCT:
def integrand_D(z, p):
    _tau, _em, _sigma, _temp, _a = p
    ret_val = kb*p[3]/((2*pi)**0.5*p[2])*N.exp(-(z*kb*p[3]/p[2])**2/2)*p[4]**2/
              (6*p[0]/N.sqrt(p[1]/kb)*N.exp(p[1]/(kb*p[3]))*N.exp(z))
    return ret_val

def D(p):
    ret_val = quad(integrand_D, -25, 25, args=(p), epsabs=1e-21)[0]
    return ret_val

#control calculation of int_0^infty G(t) dt = int_-infty^infty G(z) dz = 1
```

```
def integrand_DCT(z,p):
    _tau, _em, _sigma, _temp = p
    ret_val = kb*p[3]/((2*pi)**0.5*p[2])*N.exp(-(z*kb*p[3]/p[2])**2/2)
    return ret_val

def DCT(p):
    ret_val = quad(integrand_DCT, -N.inf, N.inf, args=(p), epsabs=1e-21)[0]
    return ret_val

#building an array with calculated 1/T1Q and one with calculated D
t1qarray = list()
Darray = list()
DCTarray = list()
#array of temperatures at which diffusion coefficient is calculated
tempD = [200, 220, 240, 260, 280,  300,  320, 340, 360, 380, 400, 420, 440]
#array with frequencies to separate the calculation of the FFT with trapezoidal
#and Filon-rule
omega_limits = [1.01e-4, 1.01e-1, 1.01e2, 3e2, 1.01e3, 3e4, 1.01e5, 5e5, 8e5]
if __name__ == '__main__':
    fig, ax = plt.subplots(2, 3,figsize=(23.38,16.54),dpi=300)
    vv = N.logspace(-60, 60, num=3001)
    for j in range(len(T)):
        print T[j]
        x = list()
        y = list()
        t1q = 3*C*(Jlg([tau0,Em,sigma,T[j]],omega))
        t1qarray.append(t1q)
        s = N.argsort(x)
        x = N.array(x)[s]
        y = N.array(y)[s]
        ax[0,1].set_xlim([-25,25])
        ax[0,1].plot(x, y, color=colors[j], linestyle='-', linewidth=3.0,
                     label='T=%i K'%T[j])
        ax[0,1].set_xlabel(r'$z=\ln(\tau/\tau_\mathrm{m})$')
        ax[0,1].set_ylabel('G(z)')
        parameter = [tau0, Em, sigma, T[j]]
        parameter2 = [tau0, Em, sigma, T[j], t1qarray[j]]
        f2_time = F2(parameter, vv)
        f2_t1q = F2_t1q(parameter2, vv)
        f2_time_filon = F2_filon(parameter, vv, omega_limits[j],
                        (1e-60, 1e60, 3001), N.inf)
        f2_trapez = trapez(vv, J(parameter, vv, N.inf), vv)
        trapez_low = f2_trapez[f2_trapez > 0.176]
        f2_filon_high = f2_time_filon[len(trapez_low):]
        f2_trapez_filon = N.concatenate((trapez_low, f2_filon_high), axis=0)
        ax[1,0].semilogx(vv, f2_time, color=colors[j], linestyle='-',
```

```
                     linewidth=3.0, label='T = %i K'%T[j])
    ax[1,0].semilogx(vv, f2_t1q, color=colors[j], linestyle='--',
                     linewidth=3.0, label='T = %i K, Q'%T[j])
    ax[1,0].semilogx(vv, f2_trapez, color=colors[j], linestyle='-.',
                     linewidth=3.0, label='T = %i K, T'%T[j])
    ax[1,0].semilogx(vv, f2_time_filon, color=colors[j], linestyle=':',
                     linewidth=3.0, label='T = %i K, f'%T[j])
    ax[1,0].semilogx(vv, f2_trapez_filon, color=colors[j], linestyle=':',
                     linewidth=3.0, label='T = %i K, T+f'%T[j])
    ax[1,0].set_xbound([1e-18,1e+18])
    ax[1,0].set_xlabel('t in s')
    ax[1,0].set_ylabel('F2')
    ax[1,1].loglog(vv, J(parameter, vv, N.inf), color=colors[j],
                   linestyle='-', linewidth=3.0, label='T = %i K'%T[j])
    ax[1,1].set_xlabel(r'$\omega$')
    ax[1,1].set_ylabel(r'$J(\omega)$')
for i in range(len(tempD)):
    parameter = [tau0, Em, sigma, tempD[i], 3.763e-10]
    parameterDCT = [tau0, Em, sigma, tempD[i]]
    DCT_T = DCT(parameterDCT)
    DCTarray.append(DCT_T)
    diff = D(parameter)
    Darray.append(diff)

inv = [1./x for x in t1qarray]
inv2 = [1000./x for x in T]
inv3 = [1000./x for x in tempD]
ax[0,0].semilogy(inv2, t1qarray, color='tud9b', marker='o',
                 markersize=10.0, markeredgecolor='tud9b', linestyle='None')
ax[0,0].set_ybound([1e-04,1e+01])
ax[0,0].set_xlabel('1000 K / T')
ax[0,0].set_ylabel(r'$1/T_\mathrm{1Q}$')
ax[0,2].semilogy(inv3, Darray, color='tud1b', marker='s', markersize=10.0,
                 markeredgecolor='tud1b', linestyle='None')
ax[0,2].set_xlabel('1000 K/T')
ax[0,2].set_ylabel(r'D in $m^2/s$')
ax[1,2].plot(inv3, DCTarray, color='tud11b', marker='d', markersize=10.0,
             markeredgecolor='tud11b', linestyle='None')
ax[1,2].set_ybound([0.9,1.1])
ax[1,2].set_xlabel('1000 K/T')
ax[1,2].set_ylabel(r'$\int_0^\infty G(\tau) \mathrm{d}\,\tau$')

fig.savefig('log_gauss.pdf', format='pdf', facecolor='none', edgecolor='none')
a = saveagr.SaveAGR()
b = saveagr.SaveAGR()
c = saveagr.SaveAGR()
```

```
    d = saveagr.SaveAGR()
    e = saveagr.SaveAGR()
    f = saveagr.SaveAGR()
    a.saveagr(’T1Q.agr’, fig=fig, ax=ax[0,0])
    b.saveagr(’Jlg.agr’, fig=fig, ax=ax[0,1])
    c.saveagr(’F2.agr’, fig=fig, ax=ax[1,0])
    d.saveagr(’J.agr’, fig=fig, ax=ax[1,1])
    e.saveagr(’Diffusioncoefficient.agr’, fig=fig, ax=ax[0,2])
    f.saveagr(’DCT.agr’, fig=fig, ax=ax[1,2])

data = N.array(N.column_stack((T, t1qarray, inv, inv2)))
N.savetxt(’T1Q.dat’, data, fmt = ’%.18e’, header="T 1/T1Q T1Q 1000K/T")
data2 = N.array(N.column_stack((inv3, Darray, tempD)))
N.savetxt(’Diffusioncoefficient.dat’, data2, fmt=’%.18e’, header="1000K/T D T")

import subprocess
bashCommands = ["xmgrace F2.agr -param F2.par -saveall F2.agr -noask",
                "xmgrace J.agr -param J.par -saveall J.agr -noask",
                "xmgrace Jlg.agr -param Jlg.par -saveall Jlg.agr -noask",
                "xmgrace lga.agr -param lga.par -saveall lga.agr -noask",
                "xmgrace T1Q.agr -param T1Q.par -saveall T1Q.agr -noask",
                "xmgrace D.agr -param D.par -saveall D.agr -noask",
                "xmgrace DCT.agr -param DCT.par -saveall DCT.agr -noask"]
for i in range(len(bashCommands)):
    process = subprocess.Popen(bashCommands[i].split(), stdout=subprocess.PIPE)
    output, error = process.communicate()
```

Python script *relax_from_tau.py* to calculate the correlation time dependence of various relaxation times. The result is shown in Fig. 3.6.

```
# -*- coding: utf-8 -*-
from __future__ import division
import matplotlib
matplotlib.use('Agg')
from matplotlib import rc
rc('text', usetex=True)

rc('text.latex',preamble='\usepackage[charter]{mathdesign}')
rc('font',**{'family':'serif','serif':['Charter'], 'size':20})
rc('mathtext', **{'it':'Charter', 'fontset':'custom'})

import scipy.odr as odr
import numpy as N
import pylab as pl
import glob
from math import pi
import matplotlib.pyplot as plt
import os, sys
from scipy.integrate import quad
import saveagr
import tud_colors

#script to calculate different relaxation times from J_BPP and with gaussian
#distribution of activation energies g(Ea); plot relax. time vs tau included

#parameter
kb=8.6173324e-5 #Boltzmann's constant
a=3./10. #pre-factor
deltaQ=50e+03 #coupling strength; vertical shift
omega=2*N.pi*63e+6 #Larmor frequency; diagonal shift
omega1=2*N.pi*1e+5 #frequency of soft pulse (rotating frame); diagonal shift
tau0=1e-14 #pre-exponential factor; inverse of hopping freq.; horizontal shift
Em=1. #maximum of g(Ea); change of slope
sigma=[0.05,0.1,0.2] #width of g(Ea)
colors=['k', 'tud1a', 'tud2a', 'tud3a', 'tud4a', 'tud5a', 'tud6a', 'tud7a',
        'tud8a', 'tud9a', 'tud10a', 'tud11a', 'tud1b', 'tud2b', 'tud3b',
        'tud4b', 'tud5b', 'tud6b', 'tud7b', 'tud8b', 'tud9b', 'tud10b',
        'tud11b', 'tud1c', 'tud2c', 'tud3c', 'tud4c', 'tud5c', 'tud6c',
        'tud7c', 'tud8c', 'tud9c', 'tud10c', 'tud11c', 'tud1d', 'tud2d',
        'tud3d', 'tud4d', 'tud5d', 'tud6d', 'tud7d', 'tud8d', 'tud9d',
        'tud10d', 'tud11d']

#z = ln(tau/tau_m)
```

```
def integrand(z,p,T):
    _kb,_omega,_tau0, _Em, _sigma = p
    ret_val = p[0]*T/((2*N.pi)**0.5*p[4])*p[2]*N.exp(p[3]/(p[0]*T))*
              N.exp(z-(z*p[0]*T/p[4])**2/2)/(1+(p[1]*p[2]*N.exp(p[3]/
              (p[0]*T))*N.exp(z))**2)
    return ret_val

#integration over all z
def Jlg(p,T):
    #getting J(w) by integration from -N.inf to +N.inf
    return quad(integrand, -N.inf, N.inf, args=(p,T), epsabs=1e-21)[0]

T=range(300,10000)
#x-axis will be in tau
tau=N.logspace(-14,4,num=1801)

#if __name__ == '__main__':
fig = pl.figure(frameon=False)
ax1 = fig.add_subplot(111)
#first, T_1 with g(Ea) will be calculated
for i in range(len(sigma)):
    t1array = list()
    for j in range(len(T)):
        x = list()
        y = list()
        t1 = a*deltaQ**2*(Jlg([kb,omega,tau0,Em,sigma[i]],T[j]) +
             4*Jlg([kb,2.*omega,tau0,Em,sigma[i]],T[j]))
        t1array.append(t1)
        s = N.argsort(x)
        x = N.array(x)[s]
        y = N.array(y)[s]
        inv1 = [tau0*N.exp(Em/(kb*x)) for x in T]
        inv = [1./y for y in t1array]
    print sigma[i]
    ax1.plot(inv1, inv, color=colors[i], linestyle='--', linewidth=3.0,
             label=r'$\sigma_\mathrm{E}=%i$ eV'%sigma[i])

#second, relaxaion times with J_BPP are plotted
#t1altarray = list()
t1array = list()
t11array = list()
t2sarray = list()
t2carray = list()
t1rarray = list()
t1qarray = list()
t1oarray = list()
```

```
t1Zqarray = list()
t1Zoarray = list()

for i in range(len(tau)):
    x = list()
    y = list()
    t1 = a*deltaQ**2*tau[i]*(1/(1+(omega*tau[i])**2)+4/(1+(2*omega*tau[i])**2))
    t1array.append(t1)
    t11 = a*deltaQ**2*tau[i]*(1/(1+(2*omega*tau[i])**2)+4/
          (1+(4*omega*tau[i])**2))
    t11array.append(t11)
    t2s = a*deltaQ**2/4*tau[i]*(10/(1+(omega*tau[i])**2)+4/
          (1+(2*omega*tau[i])**2) + 6/(1+(0*omega*tau[i])**2))
    t2sarray.append(t2s)
    t1r = a*deltaQ**2/4*tau[i]*(10/(1+(omega*tau[i])**2)+4/
          (1+(2*omega*tau[i])**2) + 6/(1+(2*omega1*tau[i])**2))
    t1rarray.append(t1r)
    t2c = a*deltaQ**2*tau[i]*(1/(1+(omega*tau[i])**2)+4/(1+(2*omega*tau[i])**2))
          + (0.25*deltaQ**2/omega)**2*tau[i]
    t2carray.append(t2c)
    t1q = a*deltaQ**2*tau[i]*(5/(1+(omega*tau[i])**2)+5/(1+(2*omega*tau[i])**2))
    t1qarray.append(t1q)
    t1o = a*deltaQ**2*tau[i]*(4/(1+(omega*tau[i])**2)+1/(1+(2*omega*tau[i])**2))
    t1oarray.append(t1o)
    t1Zq = t1/t1q
    t1Zqarray.append(t1Zq)
    t1Zo = t1/t1o
    t1Zoarray.append(t1Zo)
    s = N.argsort(x)
    x = N.array(x)[s]
    y = N.array(y)[s]

inv = [1./y for y in t1array]
inv11 = [1./y for y in t11array]
inv2s = [1./y + 0.5/deltaQ for y in t2sarray] #constant value for rigid-lattice
inv1r = [1./y for y in t1rarray]
inv2c = [1./y for y in t2carray]
for i, element in enumerate(inv2c):
    if i > 900:
        inv2c[i] = inv2c[i] + 0.25*omega/deltaQ**2
inv1q = [1./y for y in t1qarray]
inv1o = [1./y for y in t1oarray]
inv1Zq = [1./y for y in t1Zqarray]
inv1Zo = [1./y for y in t1Zoarray]

ax1.plot(tau, inv, color=colors[0], linestyle='-',
```

```
         linewidth=3.0,label=r'$\sigma_\mathrm{E}=0$ eV')
ax1.plot(tau, inv11, color=colors[1], linestyle='-',
         linewidth=3.0,label=r'$2\omega_\mathrm{L}$')
ax1.plot(tau, inv2s, color=colors[2], linestyle='-',
         linewidth=3.0,label=r'T$_{2s}$')
ax1.plot(tau, inv2c, color=colors[3], linestyle='-',
         linewidth=3.0,label=r'T$_{2c}$')
ax1.plot(tau, inv1r, color=colors[4], linestyle='-',
         linewidth=3.0,label=r'T$_{1\varrho}$')
ax1.plot(tau, inv1q, color=colors[5], linestyle='-',
         linewidth=3.0,label=r'T$_{1Q}$')
ax1.plot(tau, inv1o, color=colors[6], linestyle='-',
         linewidth=3.0,label=r'T$_{1O}$')
ax1.plot(tau, inv1Zq, color=colors[7], linestyle='-',
         linewidth=3.0,label=r'T$_1$/T$_{1Q}$')
ax1.plot(tau, inv1Zo, color=colors[8], linestyle='-',
         linewidth=3.0,label=r'T$_1$/T$_{1O}$')
ax1.loglog()
ax1.set_xlim([1e-14,1e+4])
ax1.set_xlabel(r'$\tau$ / s')
ax1.set_ylabel(r'$T_1$/$T_2$/$T_{1\varrho}$ / s')

fig.savefig('T1.pdf', format='pdf', facecolor='none', edgecolor='none')
a = saveagr.SaveAGR()
a.saveagr('T1.agr', fig=fig, ax=ax1)

import subprocess
bashCommands = ["xmgrace T1.agr -param T1.par -saveall T1.agr -noask"]

for i in range(len(bashCommands)):
    process = subprocess.Popen(bashCommands[i].split(), stdout=subprocess.PIPE)
    output, error = process.communicate()
```

References

[Abr61] Abragam, A. *The principles of nuclear magnetism*. 32. Oxford university press, 1961.

[Ada12] Adams, S. and Prasada Rao, R. Structural requirements for fast lithium ion migration in $Li_{10}GeP_2S_{12}$. *J. Mater. Chem.*, 22:7687, 2012.

[Alv91] Alvarez, F.; Alegría, A.; and Colmenero, J. Relationship between the time-domain Kohlrausch-Williams-Watts and frequency-domain Havriliak-Negami relaxation functions. *Phys. Rev. B*, 44:7306, 1991.

[And72] Anderson, P.W.; Halperin, B.I.; and Varma, C.M. Anomalous low-temperature thermal properties of glasses and spin glasses. *The Philosophical Magazine: A Journal of Theoretical, Experimental and Applied Physics*, 25(1):1, 1972.

[Ash07] Ashbrook, S.E. and Wimperis, S. *Quadrupolar Coupling: An Introduction and Crystallographic Aspects*. John Wiley & Sons, Ltd, 2007. ISBN 9780470034590.

[Bar73] Baram, A.; Luz, Z.; and Alexander, S. Resonance line shapes for semi-integer spins in liquids. *The Journal of Chemical Physics*, 58(10):4558, 1973.

[Bec88] Beckmann, P.A. Spectral densities and nuclear spin relaxation in solids. *Physics reports*, 171(3):85, 1988.

[Ber05] Berndt, S.; Jeffrey, K.; Küchler, R.; and Böhmer, R. Silver ion dynamics in silver borate glasses: spectra and multiple-time correlation functions from ^{109}Ag-NMR. *Solid State Nuclear Magnetic Resonance*, 27(1):122, 2005.

[BJ89] Balzer-Jöllenbeck, G.; Kanert, O.; Jain, H.; and Ngai, K.L. New interpretation of activation enthalpies for electrical conductivity and nuclear spin relaxation in glassy ionic conductors. *Phys. Rev. B*, 39:6071, 1989.

[Bjo85] Bjorkstam, J.L.; Listerud, J.; Villa, M.; and Massara, C.I. Motional narrowing of a gaussian NMR line. *Journal of Magnetic Resonance*, 65(3):383, 1985.

[Bla07] Blanc, F.; Spencer, L.; and Goward, G.R. *Quadrupolar NMR of Ionic Conductors, Batteries, and Other Energy-related Materials*. John Wiley & Sons, Ltd, 2007. ISBN 9780470034590.

[Blo46] Bloch, F. Nuclear Induction. *Phys. Rev.*, 70:460, 1946.

[Blo48] Bloembergen, N.; Purcell, E.; and Pound, R. Relaxation Effects in Nuclear Magnetic Resonance Absorption. *Phys. Rev.*, 73:679, 1948.

[Blo99] Blochowicz, T.; Kudlik, A.; Benkhof, S.; Senker, J.; Rössler, E.; and Hinze, G. The spectral density in simple organic glass formers: Comparison of dielectric and spin-lattice relaxation. *The Journal of Chemical Physics*, 110(24):12011, 1999.

[Blo03] Blochowicz, T. *Broadband Dielectric Spectroscopy in Neat and Binary Molecular Glass Formers*. Ph.D. thesis, Universität Bayreuth, 2003.

[Blo17] Blomgren, G.E. The Development and Future of Lithium Ion Batteries. *Journal of The Electrochemical Society*, 164(1):A5019, 2017.

[Boc12] Bock, D.C.; Marschilok, A.C.; Takeuchi, K.J.; and Takeuchi, E.S. Batteries used to power implantable biomedical devices. *Electrochimica Acta*, 84:155, 2012.

[Böh96] Böhmer, R.; Hinze, G.; Diezemann, G.; Geil, B.; and Sillescu, H. Dynamic heterogeneity in supercooled ortho-terphenyl studied by multidimensional deuteron NMR. *EPL (Europhysics Letters)*, 36(1):55, 1996.

[Böh98] Böhmer, R.; Chamberlin, R.; Diezemann, G.; Geil, B.; Heuer, A.; Hinze, G.; Kuebler, S.; Richert, R.; Schiener, B.; Sillescu, H.; Spiess, H.; Tracht, U.; and Wilhelm, M. Nature of the non-exponential primary relaxation in structural glass-formers probed by dynamically selective experiments. *Journal of Non-Crystalline Solids*, 235-237:1, 1998.

[Böh00] Böhmer, R. Multiple-Time Correlation Functions in Spin-3/2 Solid-State NMR Spectroscopy. *Journal of Magnetic Resonance*, 147(1):78, 2000.

[Böh07a] Böhmer, R.; Jeffrey, K.; and Vogel, M. Solid-state Li NMR with applications to the translational dynamics in ion conductors. *Progress in Nuclear Magnetic Resonance Spectroscopy*, 50(2):87, 2007.

[Böh07b] Böhmer, R. and Qi, F. Spin relaxation and ultra-slow Li motion in an aluminosilicate glass ceramic. *Solid State Nuclear Magnetic Resonance*, 31(1):28, 2007.

[Böh17] Böhmer, R.; Storek, M.; and Vogel, M. *Heterogeneous Rotational and Translational Dynamics in Glasses and Other Disordered Materials Studied by NMR*, 1–20. Springer International Publishing, Cham, 2017. ISBN 978-3-319-28275-6.

[Böh18] Böhmer, R.; Storek, M.; and Vogel, M. *NMR studies of ionic dynamics in solids*. Modern Methods in Solid-State NMR: A Practitioner's Guide. The Royal Society of Chemistry, 2018. ISBN 9781782628545. In press.

[Bow86] Bowden, G.; Hutchison, W.; and Khachan, J. Tensor operator formalism for multiple-quantum NMR. 2. Spins $\frac{3}{2}$, 2, and $\frac{5}{2}$ and general I. *Journal of Magnetic Resonance (1969)*, 67(3):415, 1986.

[Bri92] Brinkmann, D. NMR studies of superionic conductors. *Progress in Nuclear Magnetic Resonance Spectroscopy*, 24(6):527, 1992. Nuclear Magnetic Resonance Spectroscopy.

[Bri10] Brinkmann, C.; Faske, S.; Koch, B.; and Vogel, M. NMR multi-time correlation functions of ion dynamics in solids. *Zeitschrift für Physikalische Chemie*, 224(10-12):1535, 2010.

[Bro13] Bron, P.; Johansson, S.; Zick, K.; Schmedt auf der Günne, J.; Dehnen, S.; and Roling, B. $Li_{10}SnP_2S_{12}$: An Affordable Lithium Superionic Conductor. *Journal of the American Chemical Society*, 135(42):15694, 2013.

[Car99] Carper, W.R. Direct Determination of Quadrupolar and Dipolar NMR Correlation Times from Spin–Lattice and Spin–Spin Relaxation Rates. *Concepts in Magnetic Resonance*, 11(1):51, 1999.

[Chu16] Chu, I.H.; Nguyen, H.; Hy, S.; Lin, Y.C.; Wang, Z.; Xu, Z.; Deng, Z.; Meng, Y.S.; and Ong, S.P. Insights into the Performance Limits of the $Li_7P_3S_{11}$ Superionic Conductor: A Combined First-Principles and Experimental Study. *ACS Applied Materials & Interfaces*, 8(12):7843, 2016.

[Cot07] Cotts, R.M. *Diffusion in Solids*. John Wiley & Sons, Ltd, 2007. ISBN 9780470034590.

[DAM] DAMARIS online documentation. `https://element.fkp.physik.tu-darmstadt.de/damaris_cms/`. Accessed: 2017-05-17.

[Dib12] Dibandjo, P.; Graczyk-Zajac, M.; Riedel, R.; Pradeep, V.; and Soraru, G. Lithium insertion into dense and porous carbon-rich polymer-derived SiOC ceramics. *Journal of the European Ceramic Society*, 32(10):2495, 2012.

[Dos16] Dost, G. *^{7}Li NMR study of lithium borate glasses*. Master's thesis, TU Darmstadt, 2016.

[Dyr88] Dyre, J.C. The random free-energy barrier model for ac conduction in disordered solids. *Journal of Applied Physics*, 64(5):2456, 1988.

[Dyr00] Dyre, J.C. and Schrøder, T.B. Universality of ac conduction in disordered solids. *Reviews of Modern Physics*, 72:873, 2000.

[EIA16] International Energy Outlook 2016. Technical report, Energy Information Administration, 2016.

[Ein05] Einstein, A. Über die von der molekularkinetischen Theorie der Wärme geforderte Bewegung von in ruhenden Flüssigkeiten suspendierten Teilchen. *Annalen der Physik*, 322(8):549, 1905.

[Fas08] Faske, S.; Eckert, H.; and Vogel, M. ^{6}Li and ^{7}Li NMR line-shape and stimulated echo studies of lithium ionic hopping in $LiPO_3$ glass. *Phys. Rev. B*, 77:104301, 2008.

[Fas11] Faske, S.; Koch, B.; Murawski, S.; Küchler, R.; Böhmer, R.; Melchior, J.; and Vogel, M. Mixed-cation $Li_xAg_{1-x}PO_3$ glasses studied by ^{6}Li, ^{7}Li, and ^{109}Ag stimulated-echo NMR spectroscopy. *Phys. Rev. B*, 84:024202, 2011.

[Fic55] Fick, A. Ueber Diffusion. *Annalen der Physik*, 170(1):59, 1855.

[Fig78] Figueroa, D.R.; Chadwick, A.V.; and Strange, J.H. NMR relaxation, ionic conductivity and the self-diffusion process in barium fluoride. *Journal of Physics C: Solid State Physics*, 11(1):55, 1978.

[Fil30] Filon, L.N.G. On a Quadrature Formula for Trigonometric Integrals. *Proceedings of the Royal Society of Edinburgh*, 49:38, 1930.

[Fuj14] Fujara, F.; Kruk, D.; and Privalov, A.F. Solid state Field-Cycling NMR relaxometry: Instrumental improvements and new applications. *Progress in Nuclear Magnetic Resonance Spectroscopy*, 82:39, 2014.

[Fuk81] Fukushima, E. and Roeder, S. *Experimental Pulse NMR: A Nuts And Bolts Approach*. The Advanced Book Program. Addison-Wesley Pub. Co., Advanced Book Program, 1981.

[Fuk10] Fukui, H.; Ohsuka, H.; Hino, T.; and Kanamura, K. A Si-O-C Composite Anode: High Capability and Proposed Mechanism of Lithium Storage Associated with Microstructural Characteristics. *ACS Applied Materials & Interfaces*, 2(4):998, 2010.

[Fuk14] Fukui, H.; Harimoto, Y.; Akasaka, M.; and Eguchi, K. Lithium Species in Electrochemically Lithiated and Delithiated Silicon Oxycarbides. *ACS Applied Materials & Interfaces*, 6(15):12827, 2014.

[Fun97] Funke, K. Ion transport in fast ion conductors — spectra and models. *Solid State Ionics*, 94(1):27, 1997.

[Gab15] Gabriel, J.; Petrov, O.V.; Kim, Y.; Martin, S.W.; and Vogel, M. Lithium ion dynamics in $Li_2S+GeS_2+GeO_2$ glasses studied using ^{7}Li NMR field-cycling relaxometry and line-shape analysis. *Solid State Nuclear Magnetic Resonance*, 70:53, 2015.

[Gäd07] Gädke, A.; Schmitt, C.; Stork, H.; and Nestle, N. DAMARIS — a flexible and open software platform for NMR spectrometer control. *Magnetic Resonance Imaging*, 25(4):576, 2007.

[Gäd09] Gädke, A. *Diffusionseffekte in volumenselektiver NMR auf kleinen Längenskalen*. Ph.D. thesis, TU Darmstadt, 2009.

[Gao16] Gao, J.; Zhao, Y.S.; Shi, S.Q.; and Li, H. Lithium-ion transport in inorganic solid state electrolyte. *Chinese Physics B*, 25(1):018211, 2016.

[Gei93] Geil, B. and Hinze, G. Influence of data treatment on the shape of ^{2}H NMR T_1 curves. *Chemical Physics Letters*, 216(1):51, 1993.

[Gei98] Geil, B. Measurement of translational molecular diffusion using ultrahigh magnetic field gradient NMR. *Concepts in Magnetic Resonance*, 10(5):299, 1998.

[Göb79] Göbel, E.; Müller-Warmuth, W.; Olyschläger, H.; and Dutz, H. ^{7}Li NMR spectra, nuclear relaxation, and lithium ion motion in alkali silicate, borate, and phosphate glasses. *Journal of Magnetic Resonance*, 36(3):371, 1979.

[Gra13] Graf, M.; Kresse, B.; Privalov, A.F.; and Vogel, M. Combining ^{7}Li NMR field-cycling relaxometry and stimulated-echo experiments: A powerful approach to lithium ion dynamics in solid-state electrolytes. *Solid State Nuclear Magnetic Resonance*, 51:25, 2013.

[Grü95] Grüne, M. and Müller-Warmuth, W. The importance of paramagnetic impurities to the nuclear magnetic resonance relaxation of ion-conducting glasses. *Solid State Nuclear Magnetic Resonance*, 5(1):145, 1995.

[Haa11] Haaks, M. *Aufbau eines ^{7}Li NMR-Probenkopfes und Messungen am Ionenleiter $xLi_2S+(1-x)GeS_2$*. Bachelor's thesis, TU Darmstadt, 2011.

[Hah50] Hahn, E.L. Spin Echoes. *Phys. Rev.*, 80:580, 1950.

[Har69] Harmon, J.F. and Muller, B.H. Nuclear Spin Relaxation by Translational Diffusion in Liquid Ethane. *Phys. Rev.*, 182:400, 1969.

[Har07] Harris, R.K.; Becker, E.D.; Cabral de Menezes, S.M.; Goodfellow, R.; and Granger, P. *Nuclear Spin Properties and Conventions for Chemical Shifts (IUPAC Recommendations 2001)*. John Wiley & Sons, Ltd, 2007. ISBN 9780470034590.

[Hau87] Haus, J. and Kehr, K. Diffusion in regular and disordered lattices. *Physics Reports*, 150(5):263, 1987.

[Hay13] Hayamizu, K. and Aihara, Y. Lithium ion diffusion in solid electrolyte $(Li_2S)_7(P_2S_5)_3$ measured by pulsed-gradient spin-echo ^{7}Li NMR spectroscopy. *Solid State Ionics*, 238:7, 2013.

[Hei03] Heitjans, P. and Indris, S. Diffusion and ionic conduction in nanocrystalline ceramics. *Journal of Physics: Condensed Matter*, 15(30):R1257, 2003.

[Hei05] Heitjans, P. and Kärger, J. *Diffusion in condensed matter: methods, materials, models*. Springer, 2005.

[Hen73] Hendrickson, J. and Bray, P. A phenomenological equation for NMR motional narrowing in solids. *Journal of Magnetic Resonance*, 9(3):341, 1973.

[Heu95] Heuer, A.; Wilhelm, M.; Zimmermann, H.; and Spiess, H.W. Rate Memory of Structural Relaxation in Glasses and Its Detection by Multidimensional NMR. *Phys. Rev. Lett.*, 75:2851, 1995.

[Heu97] Heuer, A. Information content of multitime correlation functions for the interpretation of structural relaxation in glass-forming systems. *Phys. Rev. E*, 56:730, 1997.

[Hin98a] Hinze, G. Geometry and time scale of the rotational dynamics in supercooled toluene. *Phys. Rev. E*, 57:2010, 1998.

[Hin98b] Hinze, G.; Böhmer, R.; Diezemann, G.; and Sillescu, H. Experimental Determination of Four-Time Stimulated Echoes in Liquids, Colloidal Suspensions, and Crystals.

Journal of Magnetic Resonance, 131(2):218, 1998.

[Hof12] Hofmann, M.; Herrmann, A.; Abou Elfadl, A.; Kruk, D.; Wohlfahrt, M.; and Rössler, E.A. Glassy, Rouse, and Entanglement Dynamics As Revealed by Field Cycling ^{1}H NMR Relaxometry. *Macromolecules*, 45(5):2390, 2012.

[Hol07] Holmes, C. The Lithium/Iodine-Polyvinylpyridine Pacemaker Battery - 35 years of Successful Clinical Use. *Meeting Abstracts*, MA2007-01(6):377, 2007.

[Hub69] Hubbard, P.S. Some Properties of Correlation Functions of Irreducible Tensor Operators. *Phys. Rev.*, 180:319, 1969.

[Hun12] Hung, I.; Zhou, L.; Pourpoint, F.; Grey, C.P.; and Gan, Z. Isotropic High Field NMR Spectra of Li-Ion Battery Materials with Anisotropy >1 MHz. *Journal of the American Chemical Society*, 134(4):1898, 2012.

[Hür02] Hürlimann, M. and Venkataramanan, L. Quantitative Measurement of Two-Dimensional Distribution Functions of Diffusion and Relaxation in Grossly Inhomogeneous Fields. *Journal of Magnetic Resonance*, 157(1):31, 2002.

[Imr07] Imre, Á.W.; Staesche, H.; Voss, S.; Ingram, M.D.; Funke, K.; and Mehrer, H. Pressure-Dependent Diffusion Coefficients and Haven Ratios in Cation-Conducting Glasses. *The Journal of Physical Chemistry B*, 111(19):5301, 2007.

[Jee67] Jeener, J. and Broekaert, P. Nuclear Magnetic Resonance in Solids: Thermodynamic Effects of a Pair of rf Pulses. *Phys. Rev.*, 157:232, 1967.

[Jon66] Jones, G.P. Spin-Lattice Relaxation in the Rotating Frame: Weak-Collision Case. *Phys. Rev.*, 148:332, 1966.

[Kam11] Kamaya, N.; Homma, K.; Yamakawa, Y.; Hirayama, M.; Kanno, R.; Yonemura, M.; Kamiyama, T.; Kato, Y.; Hama, S.; Kawamoto, K.; and Mitsui, A. A lithium superionic conductor. *Nature Materials*, 10(9):682, 2011.

[Kan71] Kanert, O. and Mehring, M. *Static quadrupole effects in disordered cubic solids*, 1–81. Springer, 1971.

[Kan82] Kanert, O. Dynamical properties of defects in solids. *Physics Reports*, 91(4):183, 1982.

[Kas14] Kaspar, J.; Graczyk-Zajac, M.; and Riedel, R. Determination of the chemical diffusion coefficient of Li-ions in carbon-rich silicon oxycarbide anodes by electro-analytical methods. *Electrochimica Acta*, 115:665, 2014.

[Kat14] Kato, A.; Nagao, M.; Sakuda, A.; Hayashi, A.; and Tatsumisago, M. Evaluation of young's modulus of Li_2S-P_2S_5-P_2O_5 oxysulfide glass solid electrolytes. *Journal of the Ceramic Society of Japan*, 122(1427):552, 2014.

[Kim96a] Kim, K.; Torgeson, D.; Borsa, F.; Cho, J.; Martin, S.; and Svare, I. Distribution of activation energies explains ionic motion in glassy fast ion conductors: ^{7}Li NMR spin-lattice relaxation and ionic conductivity in xLi_2S + (1-x)GeS_2. *Solid State Ionics*, 91(1–2):7, 1996.

[Kim96b] KIM, K.; TORGESON, D.; BORSA, F.; and MARTIN, S. Two separate Li^+ ionic motions observed by ^{7}Li and ^{11}B NMR in xLi_2S + (1 - x)B_2S_3 glassy fast ionic conductors. *Solid State Ionics*, 90(1):29, 1996.

[Kim97a] KIM, K.; TORGESON, D.; BORSA, F.; CHO, J.; MARTIN, S.; SVARE, I.; and MAJER, G. Evidence of complex ionic motion in xLi_2S + (1 - x)B_2S_3 glassy fast ionic conductors from ^{7}Li and ^{11}B NMR and ionic conductivity measurements. *Journal of Non-Crystalline Solids*, 211(1):112, 1997.

[Kim97b] KIMMICH, R. *NMR: Tomography, Diffusometry, Relaxometry*. Springer Science & Business Media, 1997.

[Kim06] KIM, Y.; SAIENGA, J.; and MARTIN, S.W. Anomalous Ionic Conductivity Increase in Li_2S + GeS_2 + GeO_2 Glasses. *The Journal of Physical Chemistry B*, 110(33):16318, 2006.

[Kle03] KLEMPT, T.; KANERT, O.; and SUTER, D. F centers in LiF: A nuclear magnetic resonance study. *physica status solidi (b)*, 236(1):151, 2003.

[Koh54] KOHLRAUSCH, R. Theorie des elektrischen Rückstandes in der Leidener Flasche. *Annalen der Physik und Chemie*, 167:56, 1854.

[Koh15] KOHLMANN, D. *^{7}Li-NMR-Untersuchungen der Ionendynamik des Superionenleiters $Li_{10}SnP_2S_{12}$*. Master's thesis, TU Dortmund, 2015.

[Kow10] KOWADA, Y.; HAYASHI, A.; and TATSUMISAGO, M. Chemical bonding of Li ions in $Li_7P_3S_{11}$ crystal. *Journal of the Physical Society of Japan*, 79:65, 2010.

[Kre10] KRESSE, B. *Weiterentwicklung der Field-Cycling-Relaxometrie zu kleinen Larmorfrequenzen*. Master's thesis, TU Darmstadt, 2010.

[Kre16] KRESSE, B. *Field-Cycling NMR bei extrem kleinen Larmor-Frequenzen – Entwicklung und Anwendungen*. Ph.D. thesis, TU Darmstadt, 2016.

[Kru12] KRUK, D.; HERRMANN, A.; and RÖSSLER, E. Field-cycling NMR relaxometry of viscous liquids and polymers. *Progress in Nuclear Magnetic Resonance Spectroscopy*, 63:33, 2012.

[Kuh13] KUHN, A.; DUPPEL, V.; and LOTSCH, B.V. Tetragonal $Li_{10}GeP_2S_{12}$ and Li_7GePS_8 - exploring the Li ion dynamics in LGPS Li electrolytes. *Energy Environ. Sci.*, 6:3548, 2013.

[Kuh14] KUHN, A.; GERBIG, O.; ZHU, C.; FALKENBERG, F.; MAIER, J.; and LOTSCH, B.V. A new ultrafast superionic Li-conductor: ion dynamics in $Li_{11}Si_2PS_{12}$ and comparison with other tetragonal LGPS-type electrolytes. *Phys. Chem. Chem. Phys.*, 16:14669, 2014.

[Lev01] LEVITT, M.H. *Spin dynamics: basics of nuclear magnetic resonance*. John Wiley & Sons, 2001.

[Lip01] Lips, O.; Privalov, A.; Dvinskikh, S.; and Fujara, F. Magnet Design with High B_0 Homogeneity for Fast-Field-Cycling NMR Applications. *Journal of Magnetic Resonance*, 149(1):22, 2001.

[Lip04] Lips, O. *NMR-Untersuchungen an schnellen Ionenleitern vom LaF_3-Typ*. Ph.D. thesis, TU Darmstadt, 2004.

[Liu11] Liu, X.; Zheng, M.C.; and Xie, K. Mechanism of lithium storage in Si–O–C composite anodes. *Journal of Power Sources*, 196(24):10667, 2011.

[Maa03a] van der Maarel, J.R. Thermal relaxation and coherence dynamics of spin 3/2. I. Static and fluctuating quadrupolar interactions in the multipole basis. *Concepts in Magnetic Resonance Part A*, 19A(2):97, 2003.

[Maa03b] van der Maarel, J.R. Thermal relaxation and coherence dynamics of spin 3/2. II. Strong radio-frequency field. *Concepts in Magnetic Resonance Part A*, 19A(2):117, 2003.

[Mal10] Malik, R.; Burch, D.; Bazant, M.; and Ceder, G. Particle Size Dependence of the Ionic Diffusivity. *Nano Letters*, 10(10):4123, 2010.

[Man07] Man, P.P. *Quadrupolar Interactions*. John Wiley & Sons, Ltd, 2007. ISBN 9780470034590.

[Mar90] Martin, S.W. and Bloyer, D.R. Preparation of High-Purity Vitreous B2S3. *Journal of the American Ceramic Society*, 73(11):3481, 1990.

[Meh07] Mehrer, H. *Diffusion in solids: fundamentals, methods, materials, diffusion-controlled processes*. Springer Science & Business Media, 2007.

[Mei13] Meier, R.; Kruk, D.; and Rössler, E.A. Intermolecular Spin Relaxation and Translation Diffusion in Liquids and Polymer Melts: Insight from Field-Cycling ^{1}H NMR Relaxometry. *ChemPhysChem*, 14(13):3071, 2013.

[Men91] Menetrier, M.; Hojjaji, A.; Estournes, C.; and Levasseur, A. Ionic conduction in the B_2S_3-Li_2S glass system. *Solid State Ionics*, 48(3):325, 1991.

[Mer13] Mera, G.; Navrotsky, A.; Sen, S.; Kleebe, H.J.; and Riedel, R. Polymer-derived SiCN and SiOC ceramics - structure and energetics at the nanoscale. *Journal of Materials Chemistry A*, 1:3826, 2013.

[Min10] Minami, K.; Hayashi, A.; and Tatsumisago, M. Preparation and characterization of superionic conducting $Li_7P_3S_{11}$ crystal from glassy liquids. *Journal of the Ceramic Society of Japan*, 118(1376):305, 2010.

[Min11] Minami, K.; Hayashi, A.; Ujiie, S.; and Tatsumisago, M. Electrical and electrochemical properties of glass–ceramic electrolytes in the systems Li_2S–P_2S_5–P_2S_3 and Li_2S–P_2S_5–P_2O_5. *Solid State Ionics*, 192(1):122, 2011. Proceedings of the 17th International Conference on Solid State Ionics.

[Miz81] Mizushima, K.; Jones, P.; Wiseman, P.; and Goodenough, J. Li_xCoO_2 ($0 < x \leq 1$): A new cathode material for batteries of high energy density. *Solid State Ionics*, 3:171, 1981.

[Miz05] Mizuno, F.; Hayashi, A.; Tadanaga, K.; and Tatsumisago, M. New, Highly Ion-Conductive Crystals Precipitated from Li_2S–P_2S_5 Glasses. *Advanced Materials*, 17(7):918, 2005.

[Mo12] Mo, Y.; Ong, S.P.; and Ceder, G. First Principles Study of the $Li_{10}GeP_2S_{12}$ Lithium Super Ionic Conductor Material. *Chemistry of Materials*, 24(1):15, 2012.

[Mor15] Mori, K.; Enjuji, K.; Murata, S.; Shibata, K.; Kawakita, Y.; Yonemura, M.; Onodera, Y.; and Fukunaga, T. Direct Observation of Fast Lithium-Ion Diffusion in a Superionic Conductor: $Li_7P_3S_{11}$ Metastable Crystal. *Phys. Rev. Applied*, 4:054008, 2015.

[Mur82] Murch, G.E. The haven ratio in fast ionic conductors. *Solid State Ionics*, 7(3):177, 1982.

[Mur06] Murch, G.E. *Diffusion Kinetics in Solids*, chapter 3. Wiley-VCH Verlag GmbH & Co. KGaA, 2006. ISBN 9783527603978.

[Nga93] Ngai, K.L. Analysis of NMR and conductivity-relaxation measurements in glassy Li_2S-SiS_2 fast-ion conductors. *Phys. Rev. B*, 48:13481, 1993.

[Oha16] Ohara, K.; Mitsui, A.; Mori, M.; Onodera, Y.; Shiotani, S.; Koyama, Y.; Orikasa, Y.; Murakami, M.; Shimoda, K.; Mori, K.; Fukunaga, T.; Arai, H.; Uchimoto, Y.; and Ogumi, Z. Structural and electronic features of binary Li_2S-P_2S_5 glasses. *Scientific Reports*, 6:21302, 2016.

[Ong13] Ong, S.P.; Mo, Y.; Richards, W.D.; Miara, L.; Lee, H.S.; and Ceder, G. Phase stability, electrochemical stability and ionic conductivity of the Li10+/-1MP2X12 (M = Ge, Si, Sn, Al or P, and X = O, S or Se) family of superionic conductors. *Energy Environ. Sci.*, 6:148, 2013.

[Pak48] Pake, G.E. Nuclear Resonance Absorption in Hydrated Crystals: Fine Structure of the Proton Line. *The Journal of Chemical Physics*, 16(4):327, 1948.

[Pet13] Petrov, O. *NMR-Spektroskopie*. IFP, TU Darmstadt, 2013. Lab course manual.

[Phi72] Phillips, W.A. Tunneling states in amorphous solids. *Journal of Low Temperature Physics*, 7(3):351, 1972.

[Ple09] Plendl, D.; Fujara, M.; Privalov, A.F.; and Fujara, F. Energy efficient iron based electronic field cycling magnet. *Journal of Magnetic Resonance*, 198(2):183, 2009.

[Pra98] Pradel, A.; Rau, C.; Bittencourt, D.; Armand, P.; Philippot, E.; and Ribes, M. Mixed Glass Former Effect in the System $0.3Li_2S$-$0.7[(1\text{-}x)SiS_2\text{-}xGeS_2]$: A Structural Explanation. *Chemistry of Materials*, 10(8):2162, 1998.

[Pri02] Privalov, A.F.; Lips, O.; and Fujara, F. Dynamic processes in the superionic conductor LaF_3 at high temperatures as studied by spin-lattice relaxation dispersion. *Journal of Physics: Condensed Matter*, 14(17):4515, 2002.

[Qi04] Qi, F.; Diezemann, G.; Böhm, H.; Lambert, J.; and Böhmer, R. Simple modeling of dipolar coupled ^{7}Li spins and stimulated-echo spectroscopy of single-crystalline β-eucryptite. *Journal of Magnetic Resonance*, 169(2):225, 2004.

[Rag12] Raguenet, B.; Tricot, G.; Silly, G.; Ribes, M.; and Pradel, A. The mixed glass former effect in twin-roller quenched lithium borophosphate glasses. *Solid State Ionics*, 208:25, 2012.

[Ric90] Richert, R. and Bässler, H. Dynamics of supercooled melts treated in terms of the random-walk concept. *Journal of Physics: Condensed Matter*, 2(9):2273, 1990.

[Ric93] Richert, R. Origin of dispersion in dipolar relaxations of glasses. *Chemical Physics Letters*, 216(1-2):223, 1993.

[Ros12] Rosenstihl, M. *Untersuchung der Translationsdynamik von Wasser in Proteinmatrizen mit Hilfe von Feldgradienten-NMR*. Ph.D. thesis, TU Darmstadt, 2012.

[Sch09] Schuch, M.; Müller, C.R.; Maass, P.; and Martin, S.W. Mixed Barrier Model for the Mixed Glass Former Effect in Ion Conducting Glasses. *Phys. Rev. Lett.*, 102:145902, 2009.

[Sch15] Schmedt auf der Günne, J. 2015. Unpublished data.

[Scr95] Scrosati, B. Challenge of portable power. *Nature*, 373(6515):557, 1995.

[Sei14] Seino, Y.; Ota, T.; Takada, K.; Hayashi, A.; and Tatsumisago, M. A sulphide lithium super ion conductor is superior to liquid ion conductors for use in rechargeable batteries. *Energy & Environmental Science*, 7(2):627, 2014.

[Sei15] Seino, Y.; Nakagawa, M.; Senga, M.; Higuchi, H.; Takada, K.; and Sasaki, T. Analysis of the structure and degree of crystallisation of $70Li_2S$–$30P_2S_5$ glass ceramic. *Journal of Materials Chemistry A*, 3(6):2756, 2015.

[Sha15] Shakhovoy, R. *Structural Properties and Dynamics of Alkali Sulfates*. Ph.D. thesis, 2015.

[Sho81] Sholl, C.A. Nuclear spin relaxation by translational diffusion in liquids and solids: high- and low-frequency limits. *Journal of Physics C: Solid State Physics*, 14(4):447, 1981.

[Sou81] Souquet, J. Ionic Transport in Amorphous Solid Electrolytes. *Annual Review of Materials Science*, 11(1):211, 1981.

[SR94] Schmidt-Rohr, K. and Spiess, H.W. *Multidimensional solid-state NMR and polymers*. Academic Press, 1994.

[Sto12] Storek, M.; Böhmer, R.; Martin, S.W.; Larink, D.; and Eckert, H. NMR and conductivity studies of the mixed glass former effect in lithium borophosphate glasses. *The Journal of Chemical Physics*, 137(12):124507, 2012.

[Sto15] Storek, M. and Böhmer, R. Quadrupolar transients, cosine correlation functions, and two-dimensional exchange spectra of non-selectively excited spin-3/2 nuclei: A ^{7}Li NMR study of the superionic conductor lithium indium phosphate. *Journal of Magnetic Resonance*, 260:116, 2015.

[Sto16] Storek, M. *Kernmagnetische ^{7}Li-, ^{23}Na- und ^{17}O-Resonanz-Untersuchungen zu atomaren Austauschprozessen in Festkörpern*. Ph.D. thesis, TU Dortmund, 2016.

[Sto17] Storek, M.; Tilly, J.; Jeffrey, K.; and Böhmer, R. Four-time ^{7}Li stimulated-echo spectroscopy for the study of dynamic heterogeneities: Application to lithium borate glass. *Journal of Magnetic Resonance*, 282:1, 2017.

[Sva93] Svare, I.; Borsa, F.; Torgeson, D.R.; and Martin, S.W. Correlation functions for ionic motion from NMR relaxation and electrical conductivity in the glassy fast-ion conductor $(Li_2S)_{0.56}(SiS_2)_{0.44}$. *Phys. Rev. B*, 48:9336, 1993.

[Sva00] Svare, I.; Martin, S.W.; and Borsa, F. Stretched exponentials with T-dependent exponents from fixed distributions of energy barriers for relaxation times in fast-ion conductors. *Phys. Rev. B*, 61:228, 2000.

[Tar01] Tarascon, J.M. and Armand, M. Issues and challenges facing rechargeable lithium batteries. *Nature*, 414(6861):359, 2001.

[Tuc67] Tuck, E.O. A Simple "Filon-Trapezoidal" Rule. *Mathematics of Computation*, 21(98):239, 1967.

[Uji12] Ujiie, S.; Hayashi, A.; and Tatsumisago, M. Structure, ionic conductivity and electrochemical stability of Li_2S–P_2S_5–LiI glass and glass–ceramic electrolytes. *Solid State Ionics*, 211:42, 2012.

[Veg07] Vega, A.J. *Quadrupolar Nuclei in Solids*. John Wiley & Sons, Ltd, 2007. ISBN 9780470034590.

[Vog02] Vogel, M.; Brinkmann, C.; Eckert, H.; and Heuer, A. Silver dynamics in silver iodide/silver phosphate glasses studied by multi-dimensional ^{1}09Ag NMR. *Phys. Chem. Chem. Phys.*, 4:3237, 2002.

[Vog04] Vogel, M.; Brinkmann, C.; Eckert, H.; and Heuer, A. Origin of nonexponential relaxation in a crystalline ionic conductor: A multidimensional ^{109}Ag NMR study. *Phys. Rev. B*, 69:094302, 2004.

[Vog06] Vogel, M.; Brinkmann, C.; Eckert, H.; and Heuer, A. On the lifetime of dynamical heterogeneities associated with the ionic jump motion in glasses: Results from molecular dynamics simulations and NMR experiments. *Journal of Non-Crystalline Solids*, 352(42):5156, 2006.

[Wad83] Wada, H.; Menetrier, M.; Levasseur, A.; and Hagenmuller, P. Preparation and ionic conductivity of new B_2S_3-Li_2S-LiI glasses. *Materials Research Bulletin*, 18(2):189, 1983.

[Wan14] Wang, Z.; Wu, M.; Liu, G.; Lei, X.; Xu, B.; and Ouyang, C. Elastic properties of new solid state electrolyte material $Li_{10}GeP_2S_{12}$: A study from first-principles calculations. *Int. J. Electrochem. Sci.*, 9:562, 2014.

[Wan15] Wang, Y.; Richards, W.D.; Ong, S.P.; Miara, L.J.; Kim, J.C.; Mo, Y.; and Ceder, G. Design principles for solid-state lithium superionic conductors. *Nature materials*, 14(10), 2015.

[Wau63] Waugh, J. and Fedin, E. On determination of rotation activation barriers in solids. *Solid State Physics*, 4(8):1633, 1963.

[Wei14] Weidman, P.; Ahn, D.; and Raj, R. Diffusive relaxation of Li in particles of silicon oxycarbide measured by galvanostatic titrations. *Journal of Power Sources*, 249:219, 2014.

[Wil70] Williams, G. and Watts, D. Non-Symmetrical Dielectric Relaxation Behaviour Arising from a Simple Empirical Decay Function. *Transactions of the Faraday Society*, 66:80, 1970.

[Wil94] Wilson, A.; Reimers, J.; Fuller, E.; and Dahn, J. Lithium insertion in pyrolyzed siloxane polymers. *Solid State Ionics*, 74(3):249, 1994.

[Yam07] Yamane, H.; Shibata, M.; Shimane, Y.; Junke, T.; Seino, Y.; Adams, S.; Minami, K.; Hayashi, A.; and Tatsumisago, M. Crystal structure of a superionic conductor, $Li_7P_3S_{11}$. *Solid State Ionics*, 178(15–18):1163, 2007.

[You05] Youk, H. Numerical study of quadrupole magnetic traps for neutral atoms: anti-Helmholtz coils and a U-chip. *Canadian Undergraduate Physics Journal*, 3(2):13, 2005.

[Zha90] Zhang, Z. and Kennedy, J.H. Synthesis and characterization of the B_2S_3-Li_2S, the P_2S_5-Li_2S and the B_2S_3-P_2S_5-Li_2S glass systems. *Solid State Ionics*, 38(3):217, 1990.

[Zor02] Zorn, R. Logarithmic moments of relaxation time distributions. *The Journal of Chemical Physics*, 116(8):3204, 2002.

List of Figures

List of Tables

List of Symbols

Å	Ångström, $1\,\text{Å} = 10^{-10}\,\mathrm{m}$
B	bulk modulus
C_Q	quadrupolar coupling constant
D_0	pre-exponential factor of the self-diffusion coefficient
D_σ	diffusion coefficient of conduction
D	self-diffusion coefficient
E_σ	activation energy from DC conductivity
E_app	apparent activation energy
E_a	activation energy
E_m	mean activation energy (center of $g(E_\mathrm{a})$)
E	Young's modulus
F_2^CC	Zeeman-order correlation function
F_2^SS	spin-alignment correlation function
F_2	two-time correlation function
F_3^het	three-time correlation function in the heterogeneous limit
F_3^hom	three-time correlation function in the homogeneous limit
F_3	three-time correlation function
F_4	four-time correlation function
F_∞^CC	F_2^CC decay for $t_\mathrm{m} \to \infty$
F_∞^SS	F_2^SS decay for $t_\mathrm{m} \to \infty$
$F_{l,m}(\lvert\tau\rvert)$	correlation function
$G(T_1)$	distribution of relaxation times
$G(\ln \tau_\mathrm{c})$	logarithmic distribution of correlation times
$G(\tau_\mathrm{c})$	distribution of correlation times
H_R	Haven ratio
$J(\omega_\mathrm{L}, \tau_\mathrm{c})$	spectral density
$J_\mathrm{BPP}(\omega_\mathrm{L}, \tau_\mathrm{c})$	BPP spectral density
$J_\mathrm{Gauss}(\omega_\mathrm{L}, \tau_\mathrm{c})$	log-Gaussian spectral density
$J_\mathrm{HN}(\omega_\mathrm{L}, \tau_\mathrm{c})$	Havriliak-Negami spectral density
$M(t_\mathrm{d})$	magnetization after saturation at delay time t_d
$M(t_\mathrm{p})$	magnetization after the evolution time t_p
M_0	initial magnetization
M_∞	equilibrium magnetization
M_Mol	molar mass
P_lock	spinlock pulse
R_1	spin-lattice relaxation rate
R_PV	Lorentzian fraction of the pseudo-Voigt profile
T_1	spin-lattice relaxation time
T_2	spin-spin relaxation time

$T_{1\mathrm{O}}$	spin-lattice relaxation time of the octupolar state
$T_{1\mathrm{Q}}$	spin-lattice relaxation time of the quadrupolar state
$T_{1\mathrm{ZO}}$	spin-lattice relaxation time of a mixture of Zeeman and octupolar state
$T_{1\mathrm{min}}$	minimum of the spin-lattice relaxation time
$T_{1\mathrm{n}}$	spin-lattice relaxation time of process n
$T_{2\mathrm{c}}$	spin-spin relaxation time of the central transition
$T_{2\mathrm{s}}$	spin-spin relaxation time of the satellite transition
T_{c}	crystallization temperature
T_{g}	glass-transition temperature
T_{onset}	onset temperature of the MN
$T_{1/2}$	temperature, where the HB fit reaches the middle of both plateus values which is roughly the temperature of the infliction point of $\Sigma(T)$
$T_{1\rho}$	spin-lattice relaxation time in the rotating frame
$T_{l,m}$	spherical tensor operator
T	temperature
V_{Mol}	molar volume
$W(T)$	weighting factor
$\hat{I}_{\mathrm{z}}$	cartesian component of the spin angular momentum
$\langle T_1 \rangle$	mean spin-lattice relaxation time
$\langle T_1^{-1} \rangle$	harmonic mean spin-lattice relaxation rate
$\langle T_{1\mathrm{f}} \rangle$	mean spin-lattice relaxation time of the fast process f
$\langle T_{1\mathrm{n}} \rangle$	mean spin-lattice relaxation time of process n
$\langle T_{1\mathrm{s}} \rangle$	mean spin-lattice relaxation time of the fast process s
$\langle r^2(\mathrm{t}) \rangle$	mean square displacement
$\mathbb{Q}$	rate memory parameter
$\mathbf{B}_0$	external magnetic field
$\mathbf{B}_1$	field of the RF pulse
$\mathbf{B}_{\mathrm{det}}$	detection field
$\mathbf{B}_{\mathrm{pol}}$	polarization field
$\mathbf{B}_{\mathrm{rel}}$	relaxation field
$\mathbf{D}$	tensor representing the dipolar interaction
$\mathbf{M}$	magnetization of the samples
$\mathbf{V}$	symmetrical, treaceless EFG tensor
$\mathbf{j}(\mathbf{r}, t)$	flux of particles
$\mathscr{H}_{\mathrm{D}}$	Hamiltonian of the dipolar interaction
$\mathscr{H}_{\mathrm{Q}}$	Hamiltonian of the quadrupolar interaction
$\mathscr{H}_{\mathrm{RF}}$	Hamiltonian of radio frequency pulses
$\mathscr{H}_{\mathrm{Z}}$	Hamiltonian of the Zeeman interaction
$\mathfrak{D}$	diffusivity tensor
SE_+	spin echo with phase shift of 90° between the two pulses
SE_-	spin echo without phase shift between the two pulses
a_{n}	fraction of relaxation process n
a_{s}	fraction of the slow relaxation process s
a	mean jump length of an ion
c	particle concentration
f^{c}	fraction of the central line in the rigid-lattice ^{7}Li spectrum

$g(E_{\mathrm{a}})$	distribution of activation energies
g	static field gradient
l	lattice parameter
m_I	magnetic quantum number
n	spin density
$p(\mathbf{r},t)$	probability distribution
p_{c}	percolation limit
q_D	generalized scattering vector of diffusion experiments
q	strength of the EFG tensor
s	shift factor
t_{d}	delay time
t_{f}	filter time in MTCF experiments
t_{lock}	duration of spinlock pulse
t_{m}	mixing time
t_{p}	evolution time in pulse sequences
t_{rel}	relaxation time in FC experiments
t	time
z	unitless integration parameter, $z = \ln\left(\frac{\tau_{\mathrm{c}}}{\tau_{\mathrm{m}}}\right)$
$\langle\omega^2\rangle$	second moment of a resonance line
Γ_0	temperature independent part of the hopping rate
Γ_{m}	maximum of $g(\ln\Gamma_{\mathrm{r}})$
$\langle\Gamma_{\mathrm{r}}\rangle$	mean hopping rate
Γ_{r}	hopping rate
Γ	Gamma function
Δ	Laplace operator
$\Sigma^{\mathrm{c}}_{\mathrm{RL}}$	FWHM of the central line in the rigid lattice (RL) regime
$\Sigma^{\mathrm{s}}_{\mathrm{RL}}$	FWHM of the satellite line in the RL regime
Σ_{RL}	FWHM of a spectral line in the RL regime
Σ_{∞}	FWHM of a spectral line in the ENL
Σ	FWHM of a spectral line
β_{T1f}	stretching factor of the fast process f from T_1 measurement
β_{T1n}	stretching factor of process n from T_1 measurement
β_{T1s}	stretching factor of the slow process s from T_1 measurement
β_{F2}	stretching factor from F_2 measurement
β_{F3}	stretching factor from F_3 measurement
β_{T1Q}	stretching factor from $T_{1\mathrm{Q}}$ measurement
β_{T1ZO}	stretching factor from $T_{1\mathrm{ZO}}$ measurement
β_{T1}	stretching factor from T_1 measurement
β_{T2c}	stretching factor of the central transition from T_2 measurement
β_{T2s}	stretching factor of the satellite transition from T_2 measurement
β_{T2}	stretching factor from T_2 measurement
β	stretching factor
χ''_{NMR}	NMR susceptibility ω_{L}/T_1
$\bar{\delta}_{\mathrm{Q}}$	anisotropy parameter of anisotropic averaged spectrum

δ	Dirac delta function
σ_Γ	root mean square deviation of $\mathrm{g}(\ln \Gamma)$
δ_Q	strength of quadrupolar coupling; anisotropy parameter
ϱ	density of mass
η_Q	asymmetry parameter of the quadrupolar interaction
μ	mobility of an ion
μ_PV	position of the maximum of the pseudo-Voigt function
ν_0	hopping attempt frequency of an ion in sinusodial energy barriers
ω_1	frequency of applied RF pulses
ω_D	frequency of dipolar coupling
ω_L	Larmor frequency
ω_p	loss peak frequency
ω_Q	frequency of quadrupolar coupling
ω_R	reference frequency
ω	frequency
φ	flipangle of an RF pulse
$\Delta\nu_\mathrm{p}$	width of the excitation spectrum resulting from an RF pulse
Δ_p	duration of an RF pulse
$\rho(t)$	density operator
σ_{25}	DC conductivity at room temperature (RT)
σ_E	root meat square deviation of $g(E_\mathrm{a})$
σ_τ	root meat square deviation of $G(\ln\tau_\mathrm{c})$
σ	conductivity
τ_0	inverse of the hopping attempt frequency of an ion in sinusodial energy barriers
τ_2	decay time of F_2
τ_3	decay time of F_3
τ_DC	correlation time of DC conductivity
$\langle\tau_\Gamma\rangle$	inverse of the mean hopping rate Γ_r
τ_i	correlation time obtained from the infliction point of the temperature dependent FWHM
$\langle\tau\rangle$	mean linear correlation time (center of $G(\tau_\mathrm{c})$)
τ_LS	correlation time obtained from the temperature dependent FWHM
τ_m	mean logarithmic correlation time (log. center of $G(\tau_\mathrm{c})$; center of $G(\ln\tau_\mathrm{c})$)
τ_c	correlation time

Physical constants

$\hbar$	reduced Planck's constant, 1.055×10^{-34} Js
μ_0	vacuum permeability, $4\pi \times 10^{-7}$ H/m
Eu	Euler's constant, 0.5772
e	charge of an electron, 1.602×10^{-19} C
h	Planck's constant, 6.626×10^{-34} Js
k_B	Boltzmann constant, 1.38054×10^{-23} J/K

Properties of ^{7}Li

I	spin, $\frac{3}{2}$
Q	quadrupole moment, -40 mb
γ	gyromagnetic ratio, 103.962 MHz/T

Samples

B_2O_3	boron trioxide
B_2S_3	boron sulfide
Li_2S	lithium sulfide
P_2S_5	phosphorus pentasulfide

PVP	polyvinylpyridine

Abbreviations

ca.	circa (lat.): "approximately"; used only before a date or measure
cf.	confer (lat.): "copare"; used to refer to other materials or ideas which may provide different information or arguments
e.g.	exempli gratia (lat.): "for example": used before a noun or to introduce another sentence
et al.	et alii (lat.): "and others"; used when refering to groups of people, not things
etc.	et cetera (lat.): "and the rest"; used when the ’rest’ is unclear or ambiguous, used when refering to things and not to people
i.e.	id est (lat.): "that is"; used to introduce a word or sentence which makes what you have just said clearer or gives details
q.v.	quod vide (lat.): which (you should) see; used to direct a reader to another part of an article for further information
z. B.	zum Beispiel (ger.): "for example"

Initialisms

3TCF	Three-Time Correlation Function
4TCF	Four-Time Correlation Function
AC	Alternating Current
ADC	Analog to Digital Converter
AKA	Also Known As
AMT	American Microwave Technology
ASSB	All-Solid State Battery
BPP	Bloembergen, Purcell, and Pound
DAE	Distribution of Activation Energies
DAMARIS	Darmstadt Magnetic Resonance Instrument(ation) Software
DC	Direct Current
DCT	Distribution of Correlation Times
DSC	Differential Scanning Calorimetry
EEG	Renewable Energies Act (Erneuerbare-Energien-Gesetz)
EFG	Electric Field Gradient
EIA	Energy Information Administration
EIS	Electrochemical Impedance Spectroscopy
ENL	Extreme Narrowing Limit
EPR	Electron Paramagnetic Resonance
FC	Field-Cycling
FDT	Fluctuation-Dissipation Theorem
FE	Filter Efficiency
FFT	Fast Fourier Transform
FIC	Fast Ion Conductor
FID	Free Induction Decay
FR	Fully Relaxed
FTS	Frequency-Temperature Superposition
FWHM	Full Width at Half Maximum
GITT	Galvanostatic Intermittent Titration Technique
HB	Hendrickson and Bray
HN	Havriliak-Negami

IEO	International Energy Outlook
IGP	Ion Gatter Pump
ITC	Integrated Temperature Controller
KWW	Kohlrausch, Williams, and Watts
Li-SPE	Lithium Solid Polymer Electrolyte
LIB	Lithium Ion Battery
LSA	Line-Shape Analysis
MD	Molecular Dynamics
MGFE	Mixed Glass Former Effect
MN	Motionally Narrowing
MSD	Mean Square Displacement
MTCF	Multi-Time Correlation Function
NMR	Nuclear Magnetic Resonance
PAS	Principal Axis System
PFG	Pulsed Field Gradient
PITT	Potentiostatic Intermittent Titration Technique
PR	Partially Relaxed
PTS	Programmed Test Sources
PV	Pseudo-Voigt
QCC	Quadrupolar Coupling Constant
QENS	Quasielastic Neutron Scattering
RCF	Rotating Coordinate Frame
RF	Radio Frequency
RL	Rigid Lattice
RLR	Rigid-Lattice Regime
RT	Room Temperature
SAE	Spin-Alignment Echo
SFG	Static Field Gradient
SiOC	Silicon Oxycarbide
SLR	Spin-Lattice Relaxation
SNR	Signal to Noise Ratio
SSR	Spin-Spin Relaxation
STE	Stimulated Echo
WF	Waugh and Fedin
XRD	X-Ray Diffraction

Publications and Contributions

[I] Michael Haaks, Jan Kaspar, Anjuli Franz, Magdalena Graczyk-Zajac, Ralf Riedel, and Michael Vogel. ^{7}Li NMR studies of lithium ion dynamics in polymer-derived silicon oxycarbide ceramics. *Solid State Ionics*, 287:28–35, 2016.

[II] Michael Haaks, Steve W. Martin, and Michael Vogel. Relation of short-range and long-range lithium ion dynamics in glass-ceramics: Insights from ^{7}Li NMR field-cycling and field-gradient studies. *Phys. Rev. B*, 96:104301, 2017.

[A] Analysis of Solid-State Electrolyte Dynamics With ^{7}Li NMR. *AK Meeting Hohenberg*, Talk, 2013.

[B] ^{7}Li NMR Studies of Lithium Ion Dynamics in Ceramics. *GOMD Miami*, Invited Talk, 2015.

[C] ^{7}Li NMR Studies of Lithium Ion Dynamics in Ceramics. *GdCH Darmstadt*, Poster, 2015.

[D] ^{7}Li NMR Studies of Lithium Ion Dynamics in SiOC anode materials. *DPG Regensburg*, Talk, 2016.

[E] ^{7}Li NMR Analysis of Ion Dynamics in Amorphous Solids. *AK Meeting Heldrungen*, Talk, 2016.

[F] ^{7}Li NMR Studies of Lithium Ion Dynamics in $0.7(Li_2S)0.3(P_2S_5)$ Materials. *DPG Dresden*, Talk, 2017.

[G] ^{7}Li NMR Studien an Ionen leitenden Gläsern: von lokaler Sprungdynamik zu langreichweitigem Transport. *FKP Kolloquium TU Darmstadt*, Talk, 2017.

[H] ^{7}Li NMR Studies on ion-conducting glasses: from local ionic jumps to long-range transport. *IDMRCS8 Wisla,* Invited Talk, 2017.

Curriculum vitae

Michael Haaks

Education

10/2013–02/2018	**Doctorate Physics**, *TU Darmstadt*.
10/2011–09/2013	**Master of Science Physics**, *TU Darmstadt*.
04/2008–09/2011	**Bachelor of Science Physics**, *TU Darmstadt*.
10/2001–09/2007	**Diploma Physics (non-degreed)**, *Heidelberg University*.
06/2000	**Abitur**, *Carl-Friedrich-Gauss-Gymnasium*, Hockenheim.

06.11.1980 • *Schwetzingen* • *Germany*

Danksagung

Ohne die Mitarbeit vieler Personen wäre diese Promotionsarbeit nicht möglich gewesen.

Als erstes möchte ich mich bei meiner Familie für die andauernde Unterstüzung bedanken; besonderer Dank geht dabei an meine Eltern.

Großem Dank verpflichtet bin ich auch Prof. Dr. Michael Vogel, der diese Arbeit nicht nur ermöglicht hat, sondern auch immer ein offenes Ohr hatte. Ebenfalls danken möchte ich Prof. Dr. Roland Böhmer, der sich dazu bereit erklärt hat, das Zweitgutachten zu erstellen.

Dank geht auch an die vielen Bachelor- und Masterstudenten, deren Wirken zumindest zu einem kleinen Teil in diese Dissertation eingeflossen ist. Namentlich sind dies Anjuli Franz, Rolf Samsinger, Fabian Zentner, Georg Dost und Eva Wirth.

Gleichfalls danken möchte ich auch den anderen Mitlgiedern der AG Vogel für die jahrelange Zusamenarbeit in einem äußerst angenehmen Umfeld. Besonders erwähnen möchte ich hier Dr. Markus Rosenstihl, Dr. Oleg Petrov, Dr. Benjamin Kresse, Dr. Alexei Privalov, Dominik Demuth und Stefan Schmidt für die Unterstützung vor allem in experimenteller und technischer Hinsicht. Dank geht auch an einige ehemalige Mitglieder und Bürokollegen Jan Gabriel, Michael Lannert und Simon Becker für viele Diskussionen auch abseits der Physik.

Für das Korrekturlesen dieses Werkes gebührt mein Dank Edda Klotz, Sarah Schneider und vor allem meinem Bruder Christian, der sich durch das physikalische Kauderwelsch gekämpft hat.

Vielen Dank auch an die Arbeitsgruppen von Prof. Steve Martin und Prof. Bernhard Roling für die Herstellung und das zur Verfügungstellen der Proben.

Zu guter Letzt möchte ich mich bei allen bedanken, die ich hier evtl. vergessen habe zu erwähnen. Dies war keine Absicht, sondern ist vielmehr der Erschöpfung geschuldet.